Optical injection dynamics and polarization properties of semiconductor lasers frequency combs

Yaya Doumbia

NNT : 2021CSUP0008

THÈSE DE DOCTORAT
CentraleSupélec

Ecole Doctorale C2MP
« Chimie Mécanique. Matériaux Physique » - n° 606

Spécialité de doctorat : Physique

Laboratoire Matériaux, Optique, Photonique et Système LMOPS EA-4423
Chaire Photonique

Soutenue le 18 octobre 2021

par :

Yaya Doumbia

Optical injection dynamics and polarization properties of semiconductor lasers frequency combs

Composition du jury :

Directeur de thèse :	Marc Sciamanna	Professeur, CentraleSupélec	France
Co-directrice de thèse :	Delphine Wolfersberger	Professeur, CentraleSupélec	France
Président du jury :	Frédéric Grillot	Professeur, Télécom ParisTech	France
Rapporteurs :	Angel Valle	Professeur, Universidad de Cantabria	Espagne
	Frédéric Grillot	Professeur, Télécom ParisTech	France
Examinateurs :	Mariangela Gioannini	Professeur, Politecnico di Torino	Italie
	Krassimir Panajotov	Professeur, Vrije Universiteit Brussel	Belgique

CentraleSupélec

CentraleSupélec

Ecole Doctorale C2MP

Chimie Mécanique Matériaux Physique

Chaire Photonique

Laboratoire MOPS

Matériaux Optique Photonique et Systèmes

Philosophiæ Doctor (PhD) thesis dissertation

Specialisation : Physics

Yaya Doumbia

Optical injection dynamics and polarization properties of semiconductor lasers frequency combs

Jury members

PhD supervisor :	Pr. Marc Sciamanna	CentraleSupélec, France
PhD co-supervisor:	Pr. Delphine Wolfersberger	CentraleSupélec, France
Reviewer:	Pr. Frédéric Grillot	Télécom ParisTech, France
Reviewer:	Pr. Angel Valle	Universidad de Cantabria, Spain
Examiner:	Ass. Pr. Mariangela Gioannini	Politecnico di Torino, Italy
Examiner:	Pr. Krassimir Panajotov	Vrije Universiteit Brussel, Belgium

defended the : 18/10/2021

Acknowledgements

At this stage of my life, doing a PhD at CentraleSupélec in the Chair Photonics was the best decision I have made. Thesis work is a team effort, so I won't be able to do all the work independently without certain people's support and continued presence. First of all, I would like to thank my PhD supervisor Marc Sciamanna and my co-supervisor, Delphine Wolfersberger. Honestly, I think that beyond the excellent framework offered by CentraleSupelec and the photonics chair, doing the thesis with both of you was a very decisive factor in completing the thesis.

I would like to extend my sincere thanks to Marc Sciamanna, a very passionate researcher. I am very grateful to him for the trust he placed in me. I am also grateful to him for his advice which has constantly stimulated my research activities. He helped me to have confidence in myself. I learned a lot from him scientifically and from his leadership, professionalism, pedagogy, and organizational ability. Delphine Wolfersberger was the first to place her complete trust in me and supervised my master's internship with a very particular attention. I am very grateful for your advice. Honestly, the presence of Delphine during the meetings at the beginning of my thesis was a stabilizing factor for me. This thesis was reported and examined by Angel Valle (Universidad de Cantabria, Spain), Mariangela Gioaninni (Politecnico di Torino, Italy), Krassimir Panajotov (Vrije Universiteit Brussel, Belgium), and Frédéric Grillot (Télécom ParisTech, and Institut Polytechnique de Paris, France). I would like to thank all of you for your interesting comments and reviews of my PhD thesis manuscript.

The thesis was carried out in a stimulating environment, Chair Photonics. I met exceptional people both from a scientific and human point of view. I would like to thank the chair of photonics through its Leader Marc Sciamanna and his secretary Mary Fall. Mary helped us very enormously with the administration procedure. I also would like to thank all the postdoctoral, PhD researcher and colleague for their rich discussion. I can't mention everyone here, but I can't pass without saying a word to Mario Fernandes and Laurence Fernandes for their presence and multiple invitations. Beyond the outings, Mario was always available to assist us. Mario's skills and experience had a significant impact on this thesis.

Finally, I would like to thank my family for their support, advice, and motivation. You were present during my long nights of work. You have always dreamed of having a PhD

in your family. Today the dream has come true. Thanks for motivating me on this path. I had a pious thought for my brother Salifou Doumbia who passed away when I was writing the conclusion and perspectives of my PhD thesis. He was my brother and most importantly my best friend in everything and everywhere. He was the one who knew the most about me. He has always been my favorite advisor. The void you left in me will never go away, my brother. May your soul rest in peace.

I dedicate this thesis exclusively to you, Dear brother **Salifou Doumbia.**

Abstract

Satisfying the demand for large bandwidth in high-optical data communication is becoming a challenge. In parallel, the maximum information rate that can be transmitted through conventional optical communication systems, based on wavelength division multiplexing (WDM) with an array of single-mode lasers, is almost reached. In modern high-capacity optical data communication, an optical frequency comb is used to transmit information. The use of an optical frequency comb requires a demultiplexing of each comb line leading to the optical injection in laser diodes. In this work, we study the nonlinear dynamics of laser diodes optically injected with frequency combs.

We first theoretically and experimentally analyze the nonlinear dynamics of edge-emitting lasers (EELs) from an optical injection of frequency combs. The injection parameters (injection strength and detuning frequency) and injected comb properties (comb spacing, number of comb lines, and power per comb lines) are varied to unveil several locked and unlocked dynamics. At low injection strength, the injected laser output achieves the optical injection locking with selective amplification of the less detuned comb line. We observe as many injection locking regions as the number of the injected comb lines. At the boundary of the injection locking areas, the saddle node bifurcation leads to a modulation resulting from nonlinear wave mixing involving the detuning frequency and a new frequency that depends on the injected comb spacing. For large enough injection strength and over a large detuning range, the injection locking bifurcates to a time-periodic dynamics corresponding to an optical frequency comb that extends the injected comb to a much broader optical spectrum. A bifurcation analysis reveals a cascade harmonic frequency comb dynamics leading to a significant increase in the output comb lines. The size of the time-periodic dynamics regions depends on the amplitude of the injected comb lines. We have also used the injection parameters, comb properties, and injection current to control the new comb properties.

We secondly analyze the nonlinear dynamics and polarization properties in vertical-cavity surface-emitting lasers (VCSELs) subject to orthogonal optical injection with frequency combs experimentally. When varying the injection parameters, we enable several bifurcations scenarios leading to polarization switching accompanied by optical injection locking that bifurcates to polarized frequency comb generation. Most importantly, the VCSEL shows two frequency combs with orthogonal polarization from a single device for some

injection parameters. We also demonstrate the possibility to control the single or two polarizations comb repetition rate through harmonic frequency combs generation. Harmonic frequency combs with repetition rates of hundreds of MHz are indeed demonstrated. The polarization switching and the related bistability are also analyzed. We observe that the power required to switch the VCSEL increases with the injected comb spacing, and there is no linear dependence between the increase in the comb spacing and the increase in the switching power.

We finally present experimentally and theoretically the VCSEL injection dynamics from parallel optical frequency comb injection. We show that the two polarizations comb performance is restricted to high current injection in the case of parallel optical injection. For fixed bias current, the two polarization comb dynamics disappear when increasing the injected comb spacing. In contrast, the orthogonal optical injection can induce the two polarization comb whatever is the bias current and is not limited by the increase in the injected comb spacing. In parallel optical injection, the decrease in the linear dichroism eliminates the comb dynamics in the normally depressed polarization mode. In contrast, in the orthogonal optical injection case, the size of the comb regions in both polarization modes increases slightly when decreasing the linear dichroism.

This thesis therefore demonstrates besides its interest for nonlinear laser dynamics, optical injection is a technique to harness the comb properties in laser diodes.

Résumé

Satisfaire la demande de large bande passante dans les systèmes de communication optique devient de plus en plus un défi énorme. Parallèlement, la limite de bande passante utilisable par les systèmes de communication optique classique basé sur le multiplexage par répartition en longueur d'onde (WDM) est presque atteinte. Dans les systèmes de communication optique moderne, un peigne de fréquences optiques est utilisé à la place d'une série de lasers pour transmettre l'information. L'utilisation des peignes de fréquences optiques nécessite un démultiplexage de chaque ligne du peigne conduisant à l'injection optique dans une diode laser. Dans ce travail, nous étudions la dynamique non linéaire de diode lasers injectés optiquement avec des peignes de fréquences optiques.

Nous analysons d'abord théoriquement et expérimentalement la dynamique non linéaire de lasers émettant par la tranche (EELs) à partir d'une injection optique de peigne de fréquences. Nous faisons varier les paramètres d'injection (force d'injection et fréquence de désaccord) et les propriétés des peignes injectés (espacement des fréquences du peigne, nombre de lignes de peigne et puissance par ligne de peigne) pour dévoiler plusieurs dynamiques verrouillées et déverrouillées. A faible force d'injection, la sortie du laser injectée présente une dynamique de verrouillage d'injection optique avec une amplification sélective de la ligne de peigne la moins désaccordée. Nous observons autant de régions de verrouillage par injection que de lignes de peigne injectées. À la limite des zones de verrouillage par injection, la bifurcation du Saddle Node conduit à une modulation résultant du mélange d'ondes non linéaires impliquant la fréquence de désaccord et une nouvelle fréquence qui dépend de l'espacement des peignes injectés. Pour une force d'injection et un désaccord considérable, le verrouillage par injection bifurque vers une dynamique temporelle-périodique correspondant à un peigne de fréquences optiques qui étend le peigne injecté à un spectre optique beaucoup plus large. Une analyse de bifurcation révèle une dynamique de peigne de fréquence harmonique conduisant à une augmentation significative des lignes de peigne à la sortie du laser. La taille des régions de dynamiques périodiques dépend de l'amplitude des lignes de peigne injectées. Nous avons également utilisé les paramètres d'injection, les propriétés du peigne et le courant d'injection pour contrôler les propriétés des nouvelles solutions de peigne.

Nous analysons ensuite la dynamique non linéaire et les propriétés de polarisation des lasers émettant par la surface (VCSEL) soumis à une injection optique orthogonale avec des peignes de fréquence de manière expérimentale. En faisant varier les paramètres d'injection,

nous activons plusieurs scénarios de bifurcation menant à une commutation de polarisation accompagnée d'un verrouillage d'injection optique qui bifurque vers la génération de peignes de fréquences polarisés. De plus, pour certains paramètres d'injection, le VCSEL présente deux peignes de fréquence avec une polarisation orthogonale à partir d'un seul dispositif. Nous démontrons également la possibilité de contrôler le taux de répétition du peigne à une ou deux polarisations par la génération de peignes de fréquences harmoniques. Des peignes de fréquences harmoniques avec des taux de répétition de centaines de MHz sont en effet démontrés. La commutation de polarisation et la bistabilité associée sont également analysées. Nous avons observé que la puissance requise pour commuter le VCSEL augmente avec l'espacement du peigne injecté, et qu'il n'y a pas de dépendance linéaire entre l'augmentation de l'espacement du peigne et l'augmentation de la puissance de commutation.

Nous présentons enfin expérimentalement et théoriquement la dynamique d'injection du VCSEL à partir d'une injection optique parallèle avec peigne de fréquences. Nous montrons que les performances du peigne à deux polarisations sont limitées à une injection de courant élevée dans le cas de l'injection optique parallèle. Pour un courant d'alimentation fixe, la dynamique du peigne à deux polarisations disparaît lorsque l'espacement du peigne injecté augmente. En revanche, l'injection optique orthogonale peut induire le peigne à deux polarisations quel que soit le courant de polarisation et n'est pas limitée par l'augmentation de l'espacement des peignes injectés. Dans l'injection optique parallèle, la diminution du dichroïsme linéaire conduit à l'élimination de la dynamique du peigne dans le mode de polarisation normalement déprimé. En revanche, dans le cas de l'injection optique orthogonale, la taille des régions en peigne dans les deux modes de polarisation augmente légèrement lorsque l'on diminue le dichroïsme linéaire.

Cette thèse démontre donc qu'outre son intérêt pour la dynamique non linéaire des lasers, l'injection optique est une technique permettant d'exploiter les propriétés des peignes dans les diodes laser.

Contents

List of Figures ix

1 General introduction 1

1.1 Conventional fibre optic communication system . . . 2
1.2 Frequency comb for optical communication systems . . . 4
1.3 Optical demultiplexing using optical injection . . . 5
1.4 PhD motivations . . . 6
1.5 Outline . . . 8

2 Fundamentals of semiconductor lasers and applications 13

2.1 Principle of lasers . . . 14
2.2 Dynamical classification of lasers . . . 17
2.2.1 Class A lasers . . . 17
2.2.2 Class B lasers . . . 18
2.2.3 Class C lasers . . . 19
2.3 Semiconductor lasers . . . 20
2.4 Edge-emitting lasers (EELs) . . . 21
2.4.1 Mechanisms underlying the laser operation . . . 22
2.4.2 Mathematical Modelling of Edge-emitting semiconductor lasers . . . 22
2.5 Vertical-Cavity Surface-Emitting Lasers (VCSEL) . . . 25
2.5.1 Polarization properties of the VCSEL . . . 26
2.5.2 Polarization switching . . . 27
2.5.3 Modelling of VCSEL polarization dynamics . . . 28
2.6 Nonlinear dynamics induced by external perturbation . . . 33
2.6.1 External optical injection in EEL . . . 37
2.6.2 Polarization dynamics in VCSEL with optical injection . . . 39
2.7 Applications of semiconductor laser nonlinear dynamics . . . 41
2.7.1 Optical secure communication . . . 41
2.7.2 Random number generation . . . 41
2.8 Conclusion . . . 42

3 Optical frequency comb 43

3.1 Principle of optical frequency comb . . . 44

3.2 Physical systems generating frequency comb 48
3.2.1 Electro-optics modulators 49
3.2.2 Microresonators 52
3.2.3 Semiconductor lasers-based frequency comb 55
3.2.4 Gain Switching lasers 56
3.3 Application of frequency combs 58
3.3.1 Distance measurements and laser ranging: LIDARs 58
3.3.2 Dual-comb spectroscopy 59
3.3.3 Optical frequency comb as communication sources 61
3.4 Conclusion 61

4 Theoretical analysis of optical injection dynamics of frequency combs 63
4.1 Tailoring the frequency comb dynamics 64
4.2 Modelling of the EEL with frequency comb injection 66
4.3 Numerical mapping of nonlinear dynamics 70
4.3.1 Three comb lines injection 70
4.3.2 Seven comb lines injection 72
4.4 Bifurcation analysis 74
4.4.1 Bifurcations diagram 74
4.4.2 Nonlinear wave mixing 76
4.4.3 Injection locking with selective amplification 76
4.4.4 Chaos bandwidth analysis 77
4.4.5 Broadened comb dynamics 79
4.5 Tailoring of the comb properties 83
4.5.1 Pulse width and time bandwidth product 83
4.5.2 Number of resulting comb lines 84
4.6 Phase of comb lines analysis 85
4.7 Conclusion 86

5 Experimental optical nonlinear dynamics of diode laser frequency combs 87
5.1 Experimental setup 88
5.2 Mapping of nonlinear dynamics 91
5.2.1 Injected comb spacing>ROF 92
5.2.2 Injected comb spacing<ROF 94

5.3 Comparison between theory and experiments 95
5.3.1 Asymmetric comb injection 95
5.3.2 Symmetric comb injection 97
5.4 Nonlinear wave mixing leading to comb dynamics 99
5.4.1 Unlocked time-periodic dynamics for increasing injection strength . 99
5.4.2 Unlocked time-periodic dynamics when varying the detuning 100
5.5 Comb performance analysis 104
5.5.1 Number of lines versus the injection parameters 105
5.5.2 Time bandwidth product and phase dynamics 106
5.5.3 Impact of the bias current on the comb dynamics 106
5.5.4 Tailoring the comb dynamics 107
5.6 Conclusion 109

6 Tailoring the frequency comb properties through VCSEL polarization dynamics 111
6.1 Motivations 112
6.2 Setup for VCSEL injection 113
6.3 Polarization switching and bistability 116
6.4 Bifurcation scenarios leading to polarized harmonics comb 118
6.4.1 Detuning induced harmonics comb 118
6.4.2 Injected power induced harmonics comb 119
6.4.3 Polarization resolved optical spectra 125
6.5 Bifurcation scenarios leading to two polarization comb 126
6.5.1 Detuning close to zero 126
6.5.2 Detuning close to the birefringence 128
6.5.3 Polarization resolved analysis of two polarization comb dynamics . 128
6.5.4 Coherence of the two polarization comb lines 129
6.6 Tailoring the polarization frequency comb 130
6.6.1 General case 130
6.6.2 Central comb line close to Y-PM 131
6.6.3 Central comb line close to X-PM 132
6.7 Conclusion 133

7 Contrasting the case of parallel and orthogonal injection in VCSEL frequency comb **135**
7.1 Modelling the VCSEL with parallel comb injection 136
7.2 Theoretical results: Bifurcation diagrams analysis 139
7.2.1 Parallel optical injection 140
7.2.2 Orthogonal optical injection 144
7.3 Experimental results: VCSEL with parallel injection 146
7.3.1 Bias current close to the threshold 147
7.3.2 Bias current far from the threshold 149
7.3.3 Comb performance analysis 151
7.4 Conclusion 153

8 Conclusions and perspectives **155**
8.1 Summary of the dissertation 156
8.2 Perspective for future work 159

9 Bibliography **161**

List of Figures

1.1 Global internet traffic in exabytes. Measured (2017-2020) and predicted (2021-2022) of data traffic per month for 5 main categories. Adapted from [1]. 2
1.2 Principle of copnventional optical fiber communication using wavelength division multiplexing (WDM). 3
1.3 Principle of wavelength division multiplexing (WDM) optical fiber communication system using optical frequency comb. 4
1.4 Optical frequency comb demultiplexing circuit using optical injection locking technique. 6

2.1 Light-Matter interaction mechanism in 2-energy levels system with E_1 and E_2 the energy of the ground state and excited state, respectively. (a) an electron leaves the ground state to the excited state after the absorption of a photon with energy $h\nu = E_2 - E_1$. (b) the electron in the excited level goes down accompanied by the emission of a photon with energy $h\nu = E_2 - E_1$. (c) stimulated emission, emission of two photons with the same energy after interaction between an electron in the excited state and a photon. (d) amplification based on stimulated emission. 15
2.2 Laser output as a function of the pump characteristic. Before the threshold, the laser output is dominated by spontaneous emission. In other words, the losses are higher than the gain. The gain equalizes the losses at the threshold, and then the laser effect starts thanks to the stimulated emission. Beyond the threshold, a coherent and directional beam is created. 16
2.3 Route to chaos in a single-mode laser driven by external modulation. (a), (b) and (c) are obtained for fixed parameters when increasing only the amplitude of modulation. Taken from [32] 18
2.4 Analysis of the dynamics of class C when the injection strength ranges from zero to the locking threshold. (a) irregular self-pulsing behavior, (b) chaotic dynamics, (c) period-doubling bifurcation, (d) regular oscillatory self-pulsing. Taken from [40]. 19
2.5 Diagram showing the relationship between the lattice constant, the bandgap, and the emission wavelength. The left and right vertical axis correspond to the bandgap and the wavelength. Taken from[41] 20

2.6 (a) Simplified illustration of a double heterostructure. (b) the corresponding band gap representation. 21

2.7 Simplified illustration of edge emitting laser. 22

2.8 Fabry-Perot resonator consisting of a medium of length L confined between two mirrors with the reflection coefficient R_1 and R_2. 23

2.9 Simplified illustration of VCSEL. 26

2.10 Polarization resolved power evolution when increasing (solid line) and decreasing (dashed line) the injection currents. Taken from [68]. 28

2.11 Polarization resolved power evolution when increasing (solid line) and decreasing (dashed line) the injection currents at different substrate temperatures. (a) $T_{sub} = 10$ °C, (b) $T_{sub} = 15$ °C, and (c) $T_{sub} = 55$ °C. The full and dashed curves correspond to the lower and higher energy mode. Taken from [71] 29

2.12 Band structure of a quantum well (left) and the four-level model energy transitions (right bottom). Taken from[75]. 30

2.13 Semiconductor laser with external perturbation. (a) current modulation, (b) optical feedback, (c) optoelectronic feedback, and (d) optical injection. 34

2.14 Dynamical regime of the laser response from optical feedback when varying the feedback ratio and the external cavity length. Taken from [105]. 36

2.15 Mapping of nonlinear dynamics of EEL induced by single-mode optical injection. The laser output exhibits a variety of nonlinear dynamics, including optical injection locking, periodic dynamics, wave mixing, and chaotic dynamics. Taken from [117]. 38

2.16 Mapping of nonlinear dynamics VCSEL induced by orthogonal optical injection. This mapping was obtained for fixed detuning frequency ($\Delta\nu = \nu_{ML} - \nu_{SL}$) when increasing the injected power. ν_{ML} and, ν_{SL} are the frequency of the master and slave laser respectively. Taken from [77]. . . . 40

3.1 Frequency comb development from the femtosecond laser. Taken from [148]. 45

3.2 Principle of the optical frequency comb. The time-domain representation of the mode-locked laser output is ultra-short pulses with period T. The Fourier transformation in the frequency domain corresponds to a frequency comb with repetition rate $f_r = \frac{1}{T}$. A phase shift between the envelope of the electrical field and its corresponding carrier induces an offset in the frequency domain, $f_{ceo} = \frac{\Delta\phi_{ceo}}{2\pi} f_r$. This carried-envelope offset is a translation of all the comb lines from their harmonics frequencies nf_r. . . . 46

3.3 A single pulse in the time domain and the corresponding Fourier transformation in the frequency domain. The time-bandwidth product is computed using the pulse duration and the corresponding spectral width both at half maximum. 46

3.4 Basic experimental setup for optical frequency comb generation with an Electro-optic modulator. The output of a high quality cw laser is injected into the modulator driven with an external RF signal. 49

3.5 Schematic of the different experimental setup for optical frequency comb generation based on Electro-Optic Modulator. (a) Phase modulator (PM), (b) Intensity modulator (IM), and (c) Association of several phase modulators with an intensity modulator. 50

3.6 Principle of optical frequency comb generation using a microresonator. (a) high quality-factor (Q) microresonator is injected with a CW tunable laser. High power injection and the coupling of the pump laser with a resonant mode of microresonator mode allow producing the parametric conversion process. The parametric conversion process occurs through the degenerate and non-degenerate Four-Wave Mixing. (b) Optical frequency comb characterized by the repetition rate f_r (free spectral range of the microresonator) and the carrier-envelope offset (f_0) (see section 3.1), taken from [161]. The comb is generated by combining degenerate and non-degenerate four-wave mixing processes. The degenerate FWM refers to a situation where two photons from the pump source at the same frequency are converted into a pair of photons equally spaced with respect to the pump sources. In contrast, in the non-degenerate FWM, all the photons have different frequencies. The cascade FWM leads to strong sideband generation at the phase relation phase between them. 54

3.7 Principle of gain switching of semiconductor lasers. A single-mode laser diode's output is externally driven with an RF source to generate short pulses corresponding to an in the frequency domain. The generated comb can be further controlled by injecting optical field from a tunable laser (TL). 57

3.8 Principle of LIDAR-based dual-comb. Two phase-locked comb (Comb 1 and comb 2) at slightly repetition rate (f_r and $f_r + \Delta f$) are used to measure a distance of an obstacle with a photodiode. Comb 1 is used to interact with the obstacle, while comb 2 acts as a local oscillator. A beam splitter allows separating the signal comb (comb 1) in two-part, red and green. 59

3.9 Principle of dual-comb spectroscopy measurement. Comb 1 interrogates the sample while comb 2 is used as a local oscillator. The sample information (the absorption and dispersion) is then measured. 60

4.1 Mapping of optical injection locking with selective amplification of a semiconductor laser subject to optical frequency comb injection. IL correspond to the injection locking and NI to non injection locking. The injected comb had three lines separated by 1.2 GHz. Taken from [17] 66

4.2 Optical spectra shown (a) and (c) correspond to the injected comb for three comb lines and the corresponding time series, respectively, (b) shows the free running output of the injected laser, and (d) the injected laser under injection locking condition. $\Omega = 5$ GHz is the comb spacing and $\Delta\nu = 10$ MHz is the detuning. 69

4.3 Numerical mapping of the semiconductor laser dynamics when subject to optical injection with frequency combs is shown by varying κ as a function of detuning frequency for comb spacing of 1, 3, 5 and 10 GHz respectively for (a)-(d) 3 comb lines injection. Different regions are observed: Injection locking (IL), unlocked time-periodic dynamics (Comb1, Comb2, Comb3, and Comb4). The green color corresponds to the limit of the injection locking region. 71

4.4 Numerical mapping of the semiconductor laser dynamics when subject to optical injection with frequency combs is shown by varying κ as a function of detuning frequency for comb spacing of 1, 3, 5 and 10 GHz respectively for (a)-(d) 7 comb lines injection. Different regions are observed: Injection locking (IL), unlocked time-periodic dynamics (Comb1, Comb2, Comb3, Comb4 and Comb5). The green color corresponds to the limit of the injection locking region. 73

4.5 Bifurcation diagram of the injected laser output when varying the injection ratio and detuning. These diagrams are obtained for fixed injected comb spacing $\Omega = 5$ GHz. The left and the right panels correspond to 3 and 7 comb lines injection respectively. (a_1, b_1), (a_2, b_2) and (a_3, b_3) are obtained for detuning $\Delta\nu = -5$ GHz, $\Delta\nu = 0$ GHz, and $\Delta\nu = 5$ GHz, respectively. The surround area in the bifurcations diagrams corresponding to the complex pulse generation at very low intensity. 75

4.6 Optical spectra of nonlinear wave mixing between the detuning frequency and the injected comb spacing and their corresponding times series. (a) and (b) correspond to the three and seven comb lines injected and are obtained for $\Delta\nu = 0.2$ GHz $\kappa = 0.006$, and $\Omega = 5$ GHz. 77

4.7 Optical spectra of injection locking with selective amplification and their corresponding times series. (a) and (b) correspond to the three and seven comb lines injected and are obtained for, $\Delta\nu = 0.2$ GHz $\kappa = 0.012$, and $\Omega = 5$ GHz. 78

4.8 (a_1, b_1), (a_2, b_2), and (a_3, b_3), corresponds to the optical spectra, the times series and the power spectra of a chaotic dynamics, respectively. The top and bottom correspond to the three and seven comb lines injection and are obtained for $\Delta\nu = 0.2$ GHz, $\kappa = 0.1$ and $\Omega = 5$ GHz. 79

4.9 (Unlocked times-periodic dynamics induced by optical comb injection in the comb 1 region [Fig. 4.3 (c) and Fig. 4.4] (c)]. (a_1, b_1), (a_2, b_2), and (a_3, b_3), correspond to the optical spectra, the times series and the power spectra, respectively. The top and bottom correspond to the three and seven comb lines injection, respectively and are obtained for $\Delta\nu = 0.2$ GHz and $\Omega = 5$ GHz. The top and bottom cases are obtained for $\kappa = 0.202$ and $\kappa = 0.284$, respectively. 80

4.10 (a_1, b_1), (a_2, b_2), and (a_3, b_3), corresponds to the optical spectra, the times series and the power spectra, respectively, in the comb 2 region [Fig. 4.3 (c) and Fig. 4.4] (c)]. The top and bottom correspond to the three and seven comb lines injection and are obtained for $\Delta\nu = 0.2$ GHz and $\Delta\nu = 10$ GHz, respectively. They are obtained for $\kappa = 0.6$, and $\Omega = 5$ GHz. 81

4.11 Bifurcation sequences leading to unlocked time-periodic dynamics for 3-comb lines injection. (a), (c), (d), (e), (f) and (h),harmonics comb dynamics corresponding to a new frequency comb with comb spacing a fractional integer of the injected one. (b) and (g) corresponds to the new comb dynamics in the region of "comb 1" and "comb 2", respectively. These optical spectra are obtained for fixed injection ratio $\kappa = 0.5$, and injected comb spacing $\Omega = 5$ GHz. (a), (b), (c), (d), (e), (f) (g) and (h) are recorded for $\Delta\nu = -8.8$ GHz, $\Delta\nu = -6.8$ GHz, $\Delta\nu = -5.1$ GHz, $\Delta\nu = -4$ GHz, $\Delta\nu = -3.3$ GHz, $\Delta\nu = -2.9$ GHz, $\Delta\nu = 1.4$ GHz, and $\Delta\nu = 1.8$ GHz. . . 82

4.12 Optimization of the new comb dynamics for $\Omega = 5$ GHz for 3-comb lines injection. (a) pulse width in comb 1 and comb 2 for $\Delta\nu = 0.2$ GHz, $\kappa = 0.35$ (red), and $\kappa = 0.6$ (blue), respectively. (b) Full width at half maximum (FWHM) of the comb1 on the left vertical axis and time-bandwidth product (TBP) on the right vertical axis when increasing the injection ratio κ. . . . 83

4.13 Number of comb lines and comb bandwidth analysis for $\Omega = 5$ for 3- comb lines injection. (a) number of comb lines on the left vertical axis and comb bandwidth on the right vertical axis when scanning the detuning frequency $\Delta\nu$ across the comb regions for fixed injection ratio $\kappa = 0.5$. (b) number of output comb lines in the injected laser as a function of the number of lines of the injected comb for $\Delta\nu = 0$ GHz and $\kappa = 0.8$. 84

4.14 Optical spectra and phase for each comb line for $\Delta\nu = 0$ GHz, $\kappa = 0.8$ and $\Omega = 5$ GHz. (a) and (b), optical spectra (left vertical axis), phase (right vertical axis) for 3 and 7 comb line, respectively. (c) fitting of the linear part of the phase dependence for 3 comb lines (red) and 7 comb lines (blue). 85

5.1 (a) Experimental setup for frequency comb injection. TL: Tunable Laser, EDFA: Amplifier, P.C: Polarization Controller, AWG: Arbitrary Waveform Generator, MZM: Mach-Zehnder Modulator, VOA: Variable Optical Attenuator, BOSA: Brillouin Optical Spectrum Analyser, PD: photodiode, OSC: Oscilloscope. 89

5.2 Evolution of the emitted power by the injected laser as a function of the injection current. We use a linear fit to determine the threshold current: $I_{th} = 6.9$ mA. 90

5.3 (a) Optical spectrum of the injected laser in free-running and, (b) optical spectrum of the injected comb for fixed comb spacing $\Omega = 5$ GHz. 91

5.4 Experimental dynamical mapping of single frequency laser subject to an optical injection from a frequency comb for $\Omega = 5$ GHz. Several regions are observed: SA: Selective amplification, Unlocked time periodic dynamics (Comb 1, Comb 2, Comb 3 and Comb 4) and complex dynamics. 92

5.5 Nonlinear dynamics mapping of single frequency laser subject to a frequency comb injection for $\Omega = 2$ GHz. We observe Several regions: SA, Unlocked time periodic dynamics (Comb 1, Comb 2 and Comb 3) and complex dynamics. 94

5.6 Numerical mapping of a semiconductor laser subject to optical frequency comb injection. (a) and (b) correspond to an asymmetric comb injection similar to the experimental conditions for $\Omega = 5$ GHz and $\Omega = 2$ GHz, respectively. The blue and gray part correspond to the time periodic dynamics and unlocked chaotic dynamics, respectively. Different regions observed: SA, Comb 1, comb 2, comb 3, comb 4 and comb 5 unlocked time periodic dynamics. 97

5.7 Numerical mapping of nonlinear dynamics of a semiconductor laser subject to a flat optical frequency comb injection. (a) and (b), should be compared to Fig. 5.6 (a) and (b) when all injected comb lines have now the same amplitude. The blue and gray part correspond to the time periodic dynamics and unlocked chaotic dynamics, respectively. Different regions observed: SA, Comb 1, comb 2, comb 3, comb 4 and comb 5 unlocked time periodic dynamics. 98

5.8 Optical spectra when varying the injection strength κ for fixed comb spacing $\Omega = 5$ GHz and detuning $\Delta\nu = -0.5$ GHz. The injected laser output shows the following dynamics: (a) Injection locking at $\kappa = 0.0045$, (b) Wave mixing at $\kappa = 0.025$, (c) complex dynamics at $\kappa = 0.061$ and (d) frequency comb at $\kappa = 0.15$. The red arrow in each optical spectra indicated the position of the central injected comb line. 100

5.9 (a), (b), (c) and (d) times series corresponding to the optical spectra (a), (b), (c) and (d) of Fig. 5.8, respectively. 101

5.10 Optical spectra and corresponding times series when varying the detuning $\Delta\nu$ for fixed comb spacing $\Omega = 5$ GHz and injection strength $\kappa = 0.36$ GHz. We observe: (e) and (g) Wave mixing at $\Delta\nu = 5.4$ GHz and $\Delta\nu = 9.1$ GHz, respectively, (f) new frequency comb at $\Delta\nu = 8$ GHz. The letters (e), (f) and (g) are indicated on the map of Fig. 5.4 102

5.11 Optical spectra for fixed comb spacing to $\Omega = 2$ GHz: (a) Unlocked time periodic dynamics in "comb 1" region at $\kappa = 0.3686$ and $\Delta\nu = -15$ GHz, (b) Unlocked time periodic dynamics in "comb 2" region at $\kappa = 0.3686$ and $\Delta\nu = -10.2$ GHz, (c) Unlocked time periodic dynamics in "comb 3" region at $\kappa = 0.3686$ and $\Delta\nu = -3.8$ GHz and (d) complex dynamics at $\kappa = 0.3177$ and $\Delta\nu = 5.7$ GHz. 103

5.12 (a), (b), (c) and (d) times series corresponding to the optical spectra (a), (b), (c) and (d) of Fig. 5.11, respectively. 104

5.13 Analysis method of the output comb properties. (a) and (b) optical spectrum in comb 2 region in the map of Fig. 5.4 at $\kappa = 0.1398$ and the corresponding time series of the output power. 105

5.14 Control of the number of total comb lines with the injection parameters. (a) pulse width at half maximum (left vertical axis) and number of output comb lines of the injected laser (right vertical axis) for fixed $\Omega = 5$ GHz and detuning $\Delta\nu = -3$ GHz when varying the injection strength and (b) number of output lines and Carrier to Noise ratio (CNR) on the left and right vertical axis, respectively for fixed comb spacing $\Omega = 2$ GHz and injection strength $\kappa = 0.46$. 106

5.15 Tailoring of the frequency comb properties through injection parameters. Time-bandwidth product for fixed comb spacing $\Omega = 5$ GHZ detuning $\Delta\nu = -3$ GHz. 107

5.16 Control of the number of resulting comb lines with the injection current. These figures are obtained for fixed injected comb spacing $\Omega = 2$ GHz. (a) and (b) optical spectra for $\Delta\nu = 0$ GHz and $\kappa = 0.22$ when varying the injection current from $I_{th} = 14$ mA to $I_{th} = 16$ mA. (c) evolution of the number of total line on the left vertical axis and the CNR on the right vertical axis for $\Delta\nu = 0$ GHz and $\kappa = 0.22$ when varying the injection current. (d) number of output lines as a function of the injection strength for $\Delta\nu = -9.4$ GHz. The red and blue curves are obtained for $I_{th} = 12$ mA and $I_{th} = 15$ mA, respectively. 108

5.17 Number of output comb lines in different comb regions as a function of detuning frequency for fixed $\Omega = 2$ GHz. The blue and red curves are obtained for $\kappa = 0.2542$ and $\kappa = 0.3813$, respectively. 109

6.1 Set up for frequency comb injection into a VCSEL. TL: Tunable Laser, EDFA: amplifier, P.C: Polarization Controller, AWG: Arbitrary Waveform Generator, MZM: Mach-Zehnder Modulator, VOA: Variable Optical Attenuator, BOSA: Brillouin Optical Spectrum Analyser, PD: photodiode. 114

6.2 (a) Optical spectra of the injected comb with a comb spacing of $\Omega = 2$ GHz. (b), (c) and (d) correspond to the polarization resolved optical spectra of Y-PM, X-PM and the total output, respectively. 115

6.3 Mapping of polarization switching bistability in the plane of injection parameters for single and frequency comb injection. In the map, we analyse the switching curves when increasing the injected comb spacing. (a) single-mode and 500 MHz comb injection , (b) 500 MHz and 2 GHz comb injection, and (c) 2 GHz and 4 GHz comb injection. 117

6.4 Nonlinear dynamics when varying the detuning frequency for fixed comb spacing $\Omega = 2$ GHz and injected power $P_{inj} = 150$ µW. The VCSEL output shows: (a_1) new frequency comb at $\Delta\nu = -9.8$ GHz, (a_2) complex dynamics at $\Delta\nu = -10.8$ GHz,(a_3) harmonic comb at half of the injected comb spacing at $\Delta\nu = -11$ GHz, (a_4) harmonic comb at third of the injected comb spacing at $\Delta\nu = -11.4$ GHz. The optical spectra in (b_1), (b_2), (b_3), and (b_4) correspond to the zoom in of the spectra in (a_1), (a_2), (a_3), and (a_4), respectively 119

6.5 Scenario A: Optical spectra for fixed comb spacing $\Omega = 2$ GHz and detuning $\Delta\nu = -10.78$ GHz when varying the injected power P_{inj}. (a), (b) unlocked dynamics at $P_{inj} = 0.3$ µW, $P_{inj} = 64$ µW, respectively, (c) PS with complex dynamics at $P_{inj} = 95.7$ µW , (d) and (e) Unlocked time-periodic dynamics corresponding to a frequency comb at $P_{inj} = 100.5$ µW and $P_{inj} = 113.1$ µW, respectively, (f) and (g) harmonics at third and half of the comb spacing in both polarization modes at $P_{inj} = 352$ µW, and $P_{inj} = 440$ µW, and (h) Unlocked time-periodic dynamics in both polarization modes corresponding to a frequency comb at $P_{inj} = 688$ µW. The optical spectra in (i), (j), (k), and (l) represent zooms of the optical spectra in (e), (f), (g), and (h), respectively. The red arrows in the optical spectrum of (a) and (i) indicate the position of the central injected comb line and the residue of X-polarization mode after PS due to the spontaneous emission noise. . . . 120

6.6 (a) the power spectrum of the comb shown in Fig. 6.5 (e) and the corresponding zoom in (b). 122

6.7 Scenario B: Route to polarization switching with harmonics frequency comb generation for detuning close to the birefringence, i.e, frequency position of Y-PM, $\Delta\nu = -17.7$ GHz and for fixed $\Omega = 2$ GHz. When increasing the injected power, the VCSEL output shows the following dynamics: (a) Unlocked dynamics at $P_{inj} = 0.3$ µW, (b) and (c) PS with new frequency lines generations at $P_{inj} = 16$ µW and $P_{inj} = 32$ µW, respectively, (d) complex dynamics in both polarization modes at $P_{inj} = 40$ µW, (e) and (f) Unlocked time-periodic corresponding to a harmonics comb and comb at repetition of $\Omega = 2$ GHz in Y-PM at $P_{inj} = 56$ µW, and $P_{inj} = 64$ µW, respectively, (g) complex dynamics at $P_{inj} = 376$ µW, (h) frequency comb at $P_{inj} = 400$ µW, and (i) complex dynamics with comb lines at $P_{inj} = 696$ µW. The red arrow in optical spectrum of (a) indicated the position of the central injected comb line. 123

6.8 Optical spectra for each polarization and total output power of the VCSEL showing the sequence of bifurcation leading to a broad frequency comb generation for fixed $\Omega = 2$ GHz and detuning $\Delta\nu = -10.53$ GHz. (a), (b) and (c) polarization resolved comb for X-PM, Y-PM, and the total output, respectively at $P_{inj} = 183.3$ µW. (d), (e) and (f) polarization resolved optical spectra of X-PM, Y-PM, and the total output, respectively at $P_{inj} = 680$ µW. 125

6.9 Scenario C: Optical spectra of two polarization frequency comb dynamics for fixed comb spacing to $\Omega = 2$ GHz, and detuning $\Delta\nu = -6.5$ GHz. (a), (b) and (c), unlocked dynamics at $P_{inj} = 0.3$ µW, $P_{inj} = 80$ µw and $P_{inj} = 216$ µw, respectively, (d) incomplete PS at $P_{inj} = 224$ µW, (e) complex harmonic comb in both polarization modes at $P_{inj} = 408$ µW, (f) and (g) complex comb in both polarization modes at $P_{inj} = 520$ µW and $P_{inj} = 576$ µW, respectively, (h) and (i) comb in both polarization modes $P_{inj} = 600$ µW and $P_{inj} = 640$ µW, respectively. The red arrow in optical spectrum of (a) indicated the position of the central injected comb line. . . 127

6.10 Optical spectra revealing the nonlinear dynamics of two polarization frequency comb when varying both the comb properties and the injection parameters. (a), (b), ad (c) are obtained for $\Omega = 500$ MHz, $\Omega = 2$ GHz, and $\Omega = 4$ GHz. The injected light parameters are (a) $\Delta\nu = -23.2$ GHz and $P_{inj} = 54$ µW, (b) $\Delta\nu = -15.7$ GHz and $P_{inj} = 72$ µW, and (c) $\Delta\nu = -16.9$ GHz and $P_{inj} = 96$ µW. 128

6.11 Polarization resolved spectra corresponding to the comb evolution in scenarios C. (a), (b), (c), optical spectra of X-PM, Y-PM and total output power, respectively for fixed $P_{inj} = 552.8$ µW and $\Delta\nu = -6.8$ GHz. 129

6.12 (a) the power spectrum of the comb in Fig. 6.11 (c) and the corresponding zoom in (b). 130

6.13 Control of frequency comb properties with the injection parameters for a fixed comb spacing of $\Omega = 2$ GHz . The curves in blue and red in each map correspond to the bandwidth on the left vertical axis and the CNR on the right vertical axis, respectively. (a) is obtained for fixed detuning $\Delta\nu = -11.2$ GHz when varying the injected power. (b) is obtained for fixed injected power $P_{inj} = 608$ µW when varying the detuning frequency. . 131

6.14 Comb performance with the injection parameters for a fixed comb spacing of $\Omega = 2$ GHz . The curves in blue and red in each map correspond to the bandwidth on the left vertical axis and the CNR on the right vertical axis, respectively. (a) is obtained for fixed detuning $\Delta\nu = -18.8$ GHz when varying the injected power. (b) is obtained for fixed injected power $P_{inj} = 120$ µW. 132

6.15 Tailoring the comb properties for a fixed injected comb spacing of $\Omega = 2$ GHz . The blue and red in each map correspond to the bandwidth on the left vertical axis and the CNR on the right vertical axis, respectively. (a) is obtained for fixed detuning $\Delta\nu = -6.5$ GHz when varying the injected power. (b) is obtained for fixed injected power $P_{inj} = 640$ µW. 133

7.1 Diagram of detuning frequency for SFM. γ_p, the birefringence, ω_x, the angular frequency of the X-PM, $\Delta\omega_x$, the detuning angular frequency between the X-PM and the central injected comb lines and $\Delta\omega_x$, the detuning angular frequency between $\frac{\omega_x+\omega_y}{2}$ and the central injected comb line. 138

7.2 Polarization resolved optical spectra of the VCSEL in free-running. (a) and (b) correspond to the X-polarization mode (X-PM) and Y-polarization mode (Y-PM). These optical spectra are obtained using the SFM parameters of table 7.1. 140

7.3 Bifurcation diagrams for fixed injected comb spacing $\Omega = 2$ GHz and detuning $\Delta\nu_x = -9$ GHz. The left and right panels correspond to X-polarization mode (X-PM) and Y-polarization mode (Y-PM). (a_1, b_1), (a_2, b_2), (a_3, b_3) and (a_4, b_4), are obtained for $\gamma_a = -0.1\ ns^{-1}$, $\gamma_a = -0.2\ ns^{-1}$, $\gamma_a = -0.6\ ns^{-1}$, and $\gamma_a = -0.8\ ns^{-1}$ 141

7.4 Optical spectra for fixed $\Omega = 2$ GHz, $\Delta\nu_x = -9$ GHz, and $\gamma_a = -0.6\ ns^{-1}$. The left and right panels correspond to X-PM and Y-PM, respectively. (a) and (b) correspond to the two polarization comb dynamics and are obtained for $\kappa = 0.525$. (a) and (b) correspond to the complex polarization dynamics obtained for $\kappa = 0.6$. 143

7.5 Bifurcation diagrams for fixed injected comb spacing $\Omega = 2$ GHz and $\gamma_a = -0.8\ ns^{-1}$. The left and right panels correspond to X-PM and Y-PM, respectively. (a) and (b) are obtained for $\mu = 4.2$ and (c) and (d) for $\mu = 5.29$. 144

7.6 Bifurcation diagram for fixed injected comb spacing $\Omega = 2$ GHz and detuning $\Delta\nu_y = -9$ GHz for orthogonal optical injection. The left and right panels correspond to X-polarization mode (X-PM) and Y-polarization mode (Y-PM). (a_1, b_1), (a_2, b_2), (a_3, b_3) and (a_4, b_4), are obtained for $\gamma_a = -0.1$ ns^{-1}, $\gamma_a = -0.2$ ns^{-1}, $\gamma_a = -0.6$ ns^{-1}, and $\gamma_a = -0.8$ ns^{-1} 145

7.7 Bifurcation scenarios leading to the excitation of the depressed polarization mode. These optical spectra are obtained for detuning $\Delta\nu = 1.6$ GHz and injected comb spacing $\Omega = 1$ GHz. (a) stable output at $P_{inj} = 3$ µW, (b) and (c) wave mixing at $P_{inj} = 16$ µW and $P_{inj} = 32$ µW, respectively, (d) two polarization comb at $P_{inj} = 48$ µW, (e) and (f) two polarization harmonics comb, at $P_{inj} = 80$ µW and $P_{inj} = 96$ µW,respectively, (g) two polarization complex dynamics at $P_{inj} = 128$ µW, and (h) and (i) X-polarization comb at $P_{inj} = 144$ µW, and $P_{inj} = 240$ µW, respectively. . 148

7.8 Bifurcation scenarios leading to the excitation of the depressed polarization mode. These optical spectra are obtained for detuning $\Delta\nu = 1.6$ GHz and injected comb spacing $\Omega = 2$ GHz. (a) stable output at $P_{inj} = 3$ µW, (b) wave mixing at $P_{inj} = 16$ µW, (c) two polarizations comb at $P_{inj} = 48$ µW, (d) two polarization harmonics comb at $P_{inj} = 112$ µW, (e) two polarization complex dynamics at $P_{inj} = 208$ µW, and (f) X-polarization comb at $P_{inj} = 240$ µW. 150

7.9 Bifurcation scenarios leading to the excitation of the depressed polarization mode. These optical spectra are obtained for detuning $\Delta\nu = -0.9$ GHz and injected comb spacing $\Omega = 4$ GHz. (a) and (b) wave mixing at $P_{inj} = 3$ µW, and $P_{inj} = 32$ µW, respectively, (c) and (d) single polarization comb at $P_{inj} = 48$ µW and $P_{inj} = 228$ µW, respectively, (e), (h) and (i) two polarizations comb at $P_{inj} = 304$ µW, $P_{inj} = 560$ µW and $P_{inj} = 704$ µW, respectively, (f) two polarization harmonics comb at $P_{inj} = 376$ µW, (g) two polarization complex dynamics at $P_{inj} = 448$ µW. 151

7.10 Comb performance for fixed bias current $I = 8$ mA, injected comb spacing $\Omega = 4$ GHz and detuning frequency $\Delta\nu = -0.9$ GHz. The left and right vertical axis show the number of resulting comb line (bandwidth) and the Carrier to Noise Ratio, respectively. 152

1

General introduction

Whatever the mind can conceive and believe, it can achieve it. Our only limitations are those we set up in our minds.

Napoleon Hill

Contents

1.1 Conventional fibre optic communication system 2

1.2 Frequency comb for optical communication systems 4

1.3 Optical demultiplexing using optical injection 5

1.4 PhD motivations 6

1.5 Outline 8

Humanity is increasingly depending on the internet due to the advances in new technologies. The rapid growth of data traffic characterizes this internet dependence. For example, more than two decades ago, in 1992, the global internet networks traffic per day was approximately 100 Gb/day, but in 2017 (twenty-five years later), the global internet traffic has exponentially grown from 100 Gb/day to 46600 Gb/s [1]. It is worth noticing that the amount of global internet networks traffic data is expected to be 150700 Gb/s in 2022 because a large portion of humanity still does not have access to the internet [1]. The number of users of connected objects such as computers, smartphones, and TV is increasing in every country in the world. Figure 1.1 shows the global monthly internet traffic measured (2017-2020) and expected (2021-2022). In four years, the traffic data transmitted have almost doubled. As seen in Fig. 1.1, more than 100 exabytes (10^{20} bytes) of global data are transmitted over the network communication systems. These data are mainly used for several purposes, such as file sharing, gaming, and video. In parallel, internet connectivity speeds have exponentially increased over the last decade. For example, the mobile connectivity speed was 8.7 Mbps in 2017, while it is expected to be more than triple, i.e., 28.5 Mbps by 2022 [1].

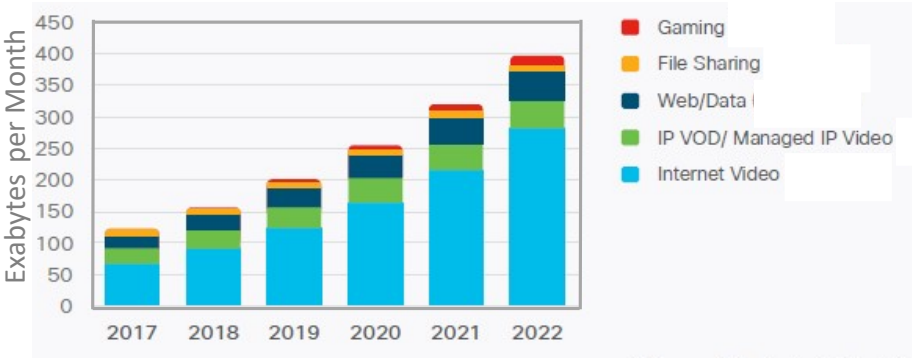

Figure 1.1: Global internet traffic in exabytes. Measured (2017-2020) and predicted (2021-2022) of data traffic per month for 5 main categories. Adapted from [1].

That rapid growth in data consumption has been made possible due to the improvement of optical communication systems.

1.1 Conventional fibre optic communication system

Conventional fibre optic communication systems are based on wavelength division multiplexing technology (WDM). Figure 1.2 shows the principle of WDM. As seen in Fig.

1.2, in the WDM technology, the outputs of several lasers (N lasers) of slightly different wavelengths are modulated in amplitude [2], in phase [3] or a combination of amplitude and phase [4]. The output of each laser corresponds to one channel of transmission. The channels are then combined into a single optical fiber using a multiplexer and then transmitted. As the information is sent over several thousand kilometers, the transmission process requires several steps of amplification. When the information arrives at the receiver side, the optical fiber output is splitted into several individual channels with respect to the initial lasers using a demultiplexer. Once the demultiplexing is completed, the data of each channel is detected separately on a photodiode. The speed and amount of data transmitted over the optical communication systems reach a fundamental limit in bandwidth known as nonlinear Shannon limit [5]. However, the frequency jitter (instability in the frequency of the lasers) in the output of each laser can lead to a strong overlap in the communication system.

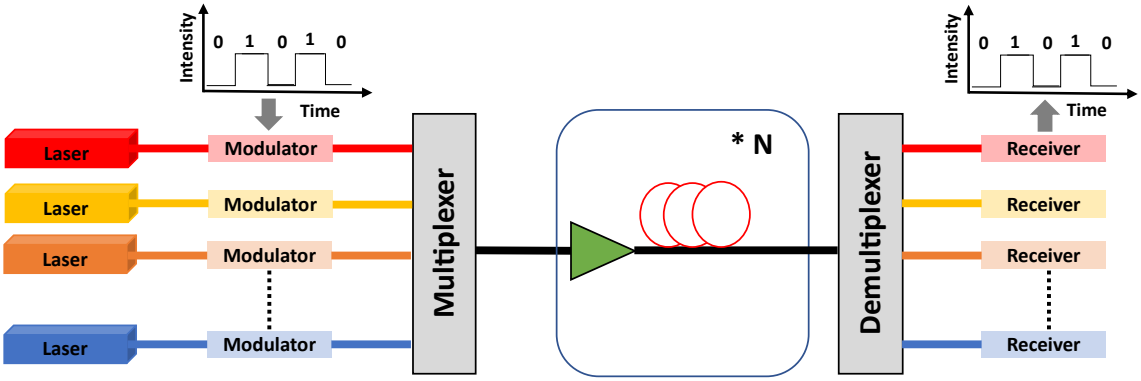

Figure 1.2: Principle of copnventional optical fiber communication using wavelength division multiplexing (WDM).

In order to suppress the overlaps, large guard bands are introduced in the WDM communication system. Unfortunately, these guards bands occupy a large portion of the transmission bandwidth. Hence, the nonlinear Shannon capacity limit is reached very quickly [5]. Currently, new optical communication systems in which a frequency comb replaces the lasers array is in development [6]. The benefice of the optical frequency comb includes low-frequency jitter due to the stable comb spacing, phase coherence of the comb lines leading to the phase noise reduction, improved spectral efficiency of transmission, and reduction of energy consumption of the communication system. This new platform of communication is very promising for high-capacity optical communication.

1.2 Frequency comb for optical communication systems

- **Frequency combs as multiple channel**

An optical frequency comb can be used to replace the array of single-frequency lasers in the WDM communication system. An optical frequency comb is a coherent spectrum composed of a set of frequency lines that are regularly spaced and whose modes have a well-defined phase relationship. In the conventional WDM communication system, the heterodyne beat between two single-mode lasers with similar linewidth δf gives rise to a beat note signal in the power spectrum with linewidth $\delta f_R = \sqrt{2}\delta f$ [7], which decreases the transmission efficiency. Whereas, due to the correlation between the noise of the comb lines, the same heterodyne beat between two comb lines will yield a beat note with linewidth much lower than the one of the individual comb lines [7]. Figure 1.3 shows the simplified schematic of the future wavelength division multiplexing (WDM) communication system. As seen, the array of laser is replaced by an optical frequency comb. Each comb line is used as one channel, i.e., each comb line takes the place of one single-mode laser. This new configuration allows reducing the size of the WDM communication system and the energy consumption. Interestingly, the narrow linewidth and the common phase relation between the comb lines, together with the fixed comb spacing, lead to the reduction of the size of the WDM communication systems through partial or total suppression of the guard bands.

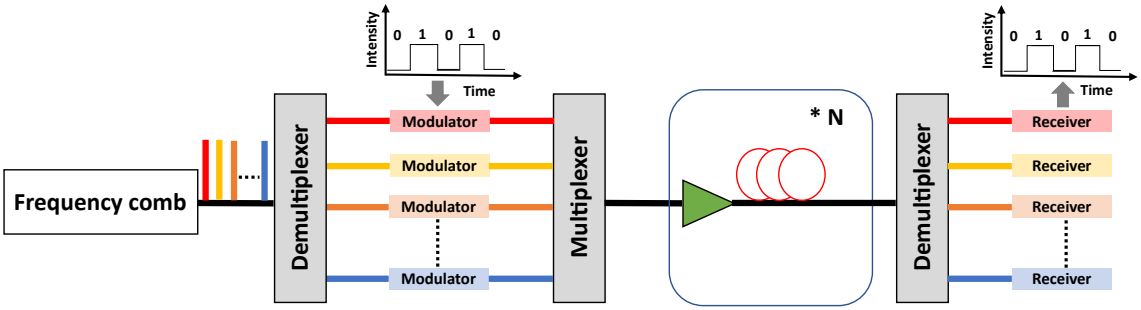

Figure 1.3: Principle of wavelength division multiplexing (WDM) optical fiber communication system using optical frequency comb.

- **Requirement to the frequency combs**

The WDM-based optical comb imposes strict requirements for the optical frequency comb concerning the linewidth, comb spacing, and power per comb line. Advanced modulation

formats in the communication system are strongly affected by the phase noise. The decrease in the linewidth decreases the phase noise variation from one channel to another. Recently, it has been shown that the modulation performances decrease with the increase in the optical linewidth [8]. Linewidths of 100 kHz are perfectly adequate for some modulation systems. The optical communication system requires a stable comb spacing to suppress the guard band used in the conventional WDM systems. In conventional WDM systems, power per channel must be higher than 1 mW. In the WDM system-based optical frequency comb, as each comb line is used as a channel, the power per comb line must be higher than 1 mW.

As seen in Fig. 1.2 and Fig. 1.3, one of the key differences is that the WDM-based frequency comb requires an extra demultiplexing method before modulation and transmission.

1.3 Optical demultiplexing using optical injection

Recent development in the WDM using an optical frequency comb has been accompanied by extensive research on the demultiplexing method of the narrow-spaced optical frequency comb. Figure 1.4 shows one of the main demultiplexing methods using the optical injection technique. The optical injection consists of injecting the light from a laser called *master laser* into the cavity of a laser called *slave laser*. When the two lasers are sufficiently close in terms of frequency, the master laser forces the slave laser to emit at its frequency, giving rise to the so-called *optical injection locking*. The next Chapter will provide more detail on the optical injection. As seen in Fig. 1.4, the N comb lines are used as the master laser, i.e., all the N comb lines are simultaneously injected into each slave laser. In the demultiplexing experiments, the slave laser is usually a single-mode diode laser. When fine-tuning the detuning frequency between the comb lines and the slave laser, the comb line that shows the smallest detuning from the slave laser is selected as shown in the output side in Fig. 1.4. In contrast to the optical amplifier (erbium-doped fiber amplifiers and semiconductor optical amplifier), which add additional noise, the selective amplification through the optical injection locking technique can amplify a comb line with a very high signal to noise ratio. The injection locking and selective amplification of the desire comb line can completely suppress the non-selected comb lines when varying the injected power and the detuning. Although modern WDM uses as many lasers as conventional WDM, the main advantage of modern WDM is the consistency of the comb lines, which leads

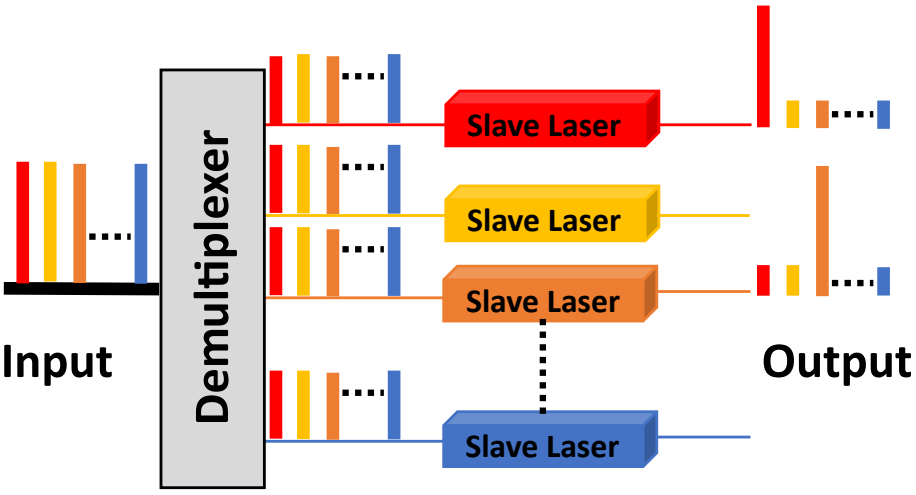

Figure 1.4: Optical frequency comb demultiplexing circuit using optical injection locking technique.

to a drastic reduction in phase noise. It has been shown that the comb lines keep their coherence after demultiplexing. Also, it is known that injection locking is a technique to stabilize the slave laser. Modern WDM technologies provide the transfer of coherence and stability between the comb and the injected laser through the optical injection, thus eliminating the guard band used in conventional WDMs leading to an increase in the total transmission bandwidth.

1.4 PhD motivations

The optimization of the suppression ratio of the unlocked comb lines under injection locking and selective amplification conditions has attracted much attention since the proposition of optical frequency comb as a powerful tool to replace the array of single-mode lasers [9–17] in the WDM communication systems. Optical injection locking using an optical frequency comb has been extensively investigated during the last decade [9, 10]. More specifically, experimental and theoretical studies of the injection locking properties have shown a gradual increase in the suppression ratio of the unlocked comb lines when the detuning frequency is varied toward zero value [13]. The influence of the injected comb spacing on the optimization of the suppression ratio has been recently reported [10]. In 2014, Gavrielides confirmed analytically the experimental results reported in [13], where the amplification seen by the unlocked comb lines is controlled with the injected power and the detuning [12]. He also demonstrated that beyond the injection locking and

selective amplification, the Hopf bifurcation can lead to the excitation of the relaxation oscillation frequency. Some recent works have addressed the nonlinear dynamics of a single mode-diode laser under modulated signal [18–20]. More specifically, they have demonstrated several harmonics frequency locking dynamics close to the Hopf bifurcation when injecting large comb spacing [18, 20]. These results suggest that the slave lasers used in the demultiplexing circuit can be destabilized and then bifurcate to a wide variety of nonlinear dynamics in the plane of the injection parameters. Yet to date, the nonlinear dynamics of a single-mode laser diode optically injected with a frequency comb (as in the demultiplexing circuit) is not fully addressed and is of significant interest.

The motivation for this thesis is to investigate the nonlinear dynamics of a single-mode laser diode in such a demultiplexing circuit. The introduction shows that current WDM is becoming limited in bandwidth due to the demand for higher bandwidths in the networks communication system. By replacing the array of single-mode lasers with an optical frequency comb, the amount of information transmitted can be increased by reducing or suppressing guard bands and decreasing the phase noise due to the perfect phase relationship between the comb lines. The laser being a nonlinear system, the injection of a frequency comb into its cavity will destabilize its output depending on the injection parameters (injected power and detuning frequency).

This thesis is mainly devoted to the external optical injection in semiconductor lasers. We want to analyze the nonlinear dynamics of semiconductor lasers under a narrow optical frequency comb injection when varying the injection parameters (injected power and detuning frequency) and the comb properties (number of comb lines, comb spacing, and amplitude of the comb lines). The motivation of this thesis is twofold. On the one hand, based on the experiments and theoretical results [10, 13, 21], we use a simple model of edge-emitting lasers (EELs) without noise contribution to describe the laser dynamics under optical comb injection. Despite the simplicity of our model, we will see strong agreement between experiment and numerical simulation as in [10, 13]. On the other hand, due to the advantage of the vertical-cavity surface-emitting lasers (VCSELs) compared to the edge-emitting lasers (EELs), we will investigate experimentally and numerically their nonlinear dynamics and polarization properties when subjected to an optical comb injection. Besides the selective amplification through injection locking, which is of interest for WDM, this thesis shows also that optical injection can be used to greatly enhance the performance of the injected optical comb, e.g., increase number of comb lines and tune

the comb spacing, bandwidth, flatness and power per lines.

1.5 Outline

Based on the motivation, the present work is organized as follows:

In Chapter 2, the fundamentals of semiconductor lasers are presented. We first present the common principle giving rise to the emission of all lasers system. We briefly expose the physical mechanism underlying the semiconductor laser's operation. We begin first with the edge-emitting lasers (ELLs) before moving to the polarization properties of the vertical-cavity surface-emitting lasers (VCSELs). In both cases, particular attention is paid to their modeling based on their gain medium. We finally discuss some techniques to induce nonlinear dynamics in a diode laser and the related applications.

Chapter 3 focuses on the optical frequency comb properties. We begin first with the principle of the optical frequency comb generation. We review different physical systems generating an optical frequency comb. We provide a broad view of the physical mechanism underlying each comb generation system and the influence on the comb properties such as bandwidth, comb spacing, and flatness. Finally, we discuss the application of the optical frequency related to the physical system generating optical comb.

Chapter 4 is devoted to the theoretical and numerical analysis of a single-mode diode laser with optical injection from frequency combs. We first model an EEL with optical frequency comb injection. The rate equations are simulated using a Runge-Kutta fourth-order numerical method. The nonlinear dynamics of the diode are then mapped in the plane of the injection parameters when varying the number of injected comb lines and the injected comb spacing. Furthermore, we observe as many injected comb lines as the number of injection locking regions. More interestingly, we show that the injection locking can bifurcate to an unlocked time-periodic dynamics corresponding to a broad optical spectrum whose frequencies lines are perfectly spaced with the same repetition rate as the injected comb lines. Their phase analysis has shown a common relationship between them, suggesting that the unlocked time-periodic dynamics are indeed optical frequency combs (new comb). The injection parameters (detuning frequency and injection ratio), the comb properties (number of lines and comb spacing), and the laser parameters are then used to control the new comb properties.

The theoretical results of Chapter 4 are confirmed experimentally in Chapter 5. The experimental configuration imposed an asymmetric frequency comb injection, i.e., the injected comb lines do not have the same amplitude. We categorize the nonlinear dynamics of a single-mode laser diode under asymmetric optical comb injection for injected comb spacing below or above the relaxation oscillation frequency of the laser diode in free-running. This chapter includes some numerical simulations to highlight the impact of the asymmetric comb injection on the laser diode dynamics. We find a strong agreement between experiments and the numerical simulations when varying both the parameters.

As we will see in the following chapters, due to their cavity structure, vertical-cavity surface-emitting lasers (VCSELs) provide many advantages compared to the EEL. The motivation of this thesis being based on the optical communication system, the polarization properties in VCSELs are beneficial for high-capacity optical communication. Chapter 6 focuses on the polarization dynamics in a single-mode VCSEL optically injected with frequency combs. We first analyze the impact of the injected comb spacing on the polarization switching and the related bistability in the plane of the injection parameters. Also, when the polarization of the injected comb is tuned to be orthogonal to that of the VCSEL, several bifurcation scenarios lead to a significantly extended output comb with the number of lines up to 15 times that of the injected comb. When varying the injection parameters, we analyze the possibility to control the comb spacing through harmonic frequency comb generation. Harmonic frequency combs with repetition rates of hundreds of MHz are indeed demonstrated. Most importantly, for some injection parameters, the VCSEL shows two frequency combs with orthogonal polarization from a single device, which may be very useful for polarization division multiplexing by suppressing several optical devices. As stated above, a requirement imposed by the modern WDM to the frequency comb to replace the array of lasers is to achieve sufficient power per comb line. We show that the power of the individual output comb lines above the noise pedestal (Carrier to Noise Ratio (CNR)) can be increased to as high as 60 dB.

Chapter 7 is mainly focused on the comparison between parallel and orthogonal optical injections from a frequency comb. We show that the two polarization combs observed in Chapter 6 can be induced in the same VCSEL when the polarization of the injected comb is parallel to that of the VCSEL. We further show through bifurcation analysis that for fixed SFM and optical injection parameters, the linear dichroism can be used to suppress the comb lines in the nonlasing polarization mode of the VCSEL (normally

depressed polarization mode). In contrast, the two polarizations comb in the orthogonal injection case is not eliminated when varying the linear dichroism. We also show that the two polarizations comb dynamics are limited by the increased in the injected comb spacing in the case of parallel optical injection. We experimentally proved that this limit can be overcome with the increase in the bias current of the VCSEL. In general, the two polarizations comb generation using orthogonal optical injection is more efficient than the parallel optical injection, but at very high bias current (around three times the threshold current), orthogonal and parallel optical injection lead to comparable comb bandwidth.

Publications and proceedings

This thesis has been the subject of scientific publications and various international conference proceedings listed below:

- Y. Doumbia, T. Malica, D. Wolfersberger, K. Panajotov, and M. Sciamanna, "Optical injection dynamics of frequency combs", **Optics Letters**, 45(2), 435-438 (2020) [22].
- Y. Doumbia, T. Malica, D. Wolfersberger, K. Panajotov, and M. Sciamanna, "Nonlinear dynamics of a laser diode with an injection of an optical frequency comb", **Optics Express**, 45(2), 435-438 (2020) [23].
- Y. Doumbia, T. Malica, D. Wolfersberger, K. Panajotov, and M. Sciamanna "Frequency comb customization by controlling the optical injection dynamics", **In Semiconductor Lasers and Laser Dynamics IX** (Vol. 11356, p. 113560G), International Society for Optics and Photonics, 45(2), 435-438 (2020) [24].
- Y. Doumbia, D. Wolfersberger, K. Panajotov, and M. Sciamanna, "Tailoring frequency combs through VCSEL polarization dynamics",**Optics Express**, 29(21), 33976-33991 (2021), [25].
- Y. Doumbia, D. Wolfersberger, K. Panajotov, and M. Sciamanna, "Two Polarization Comb Dynamics in VCSELs Subject to Optical Injection",**Photonics**, 29(21), 33976-33991 (2021), [26].
- Y. Doumbia, D. Wolfersberger, K. Panajotov, and M. Sciamanna, "Optical Injection Dynamics of VCSEL Frequency Combs", Conference on Lasers and Electro-Optics Europe and European Quantum Electronics Conference (CLEO/Europe-EQEC), 2021 [27].
- Y. Doumbia, D. Wolfersberger, K. Panajotov, and M. Sciamanna, "Nonlinear Polarization Dynamics of VCSEL with Frequency Comb Injection", OSA Advanced Photonics Congress 2021, [28].

Conferences

- Y. Doumbia, D. Wolfersberger, T. Malica, K. Panajotov, and M. Sciamanna, “Optical injection dynamics of frequency combs in diode lasers” **International Symposium on Physics and Applications of Laser Dynamics, 2021** (**Invited talk**).

- Y. Doumbia, T. Malica, D. Wolfersberger, K. Panajotov, and M. Sciamanna, "Broad optical spectrum generation and tailoring the comb properties by injection of a frequency comb.", **International Symposium on Physics and Applications of Laser Dynamics 2019** (Oral), Metz, France.

- Y. Doumbia, T. Malica, D. Wolfersberger, K. Panajotov, and M. Sciamanna, "Frequency comb customization by controlling the optical injection dynamics," **SPIE Photonics Europe,2020** (Oral) Strasbourg, France.

- Y. Doumbia, T. Malica, D. Wolfersberger, K. Panajotov, and M. Sciamanna," Nonlinear dynamics induced by optical injection with a frequency comb" **European Semiconductor Laser Workshop**, (2020) (Poster) Eindhoven, Netherlands.

- Y. Doumbia, D. Wolfersberger, K. Panajotov, and M. Sciamanna," Optical Injection Dynamics of VCSEL Frequency Combs" **CLEO Europe**, (2021) (Poster), Munich, Germany.

- Y. Doumbia, D. Wolfersberger, K. Panajotov, and M. Sciamanna," Nonlinear dynamics and polarization properties of VCSEL subject to polarized optical frequency comb injection" **Nonlinear Dynamics in Semiconductor Lasers** (2021) (Oral) Berlin, Germany.

- Y. Doumbia, D. Wolfersberger, K. Panajotov, and M. Sciamanna,"Nonlinear Polarization Dynamics of VCSEL with Frequency Comb Injection" **Advanced Photonics Congress**, 2021, (Oral) Montreal, Canada.

2

Fundamentals of semiconductor lasers and applications

Contents

2.1 Principle of lasers . . . 14

2.2 Dynamical classification of lasers . . . 17

2.2.1 Class A lasers . . . 17

2.2.2 Class B lasers . . . 18

2.2.3 Class C lasers . . . 19

2.3 Semiconductor lasers . . . 20

2.4 Edge-emitting lasers (EELs) . . . 21

2.4.1 Mechanisms underlying the laser operation . . . 22

2.4.2 Mathematical Modelling of Edge-emitting semiconductor lasers . 22

2.5 Vertical-Cavity Surface-Emitting Lasers (VCSEL) . . . 25

2.5.1 Polarization properties of the VCSEL . . . 26

2.5.2 Polarization switching . . . 27

2.5.3 Modelling of VCSEL polarization dynamics . . . 28

2.6 Nonlinear dynamics induced by external perturbation . . . 33

2.6.1 External optical injection in EEL . . . 37

2.6.2 Polarization dynamics in VCSEL with optical injection . . . 39

2.7 Applications of semiconductor laser nonlinear dynamics . . . 41

2.7.1 Optical secure communication . . . 41

2.7.2 Random number generation . . . 41

2.8 Conclusion . . . 42

This Chapter presents the fundamentals concept of lasers in general, and more specifically of semiconductor lasers. The conditions for laser emission related to the cavity structure are explained. We analyze both Edge-Emitting lasers (EELs) and Vertical-Cavity Surface-Emitting Lasers (VCSELs) geometrical's designs. The fundamental differences between the EELs and VCSELs in their structures and output emission properties are presented. We finally survey some nonlinear basics of lasers dynamics, including periodic dynamics, chaotic dynamics, and the polarization properties in VCSELs and their promising applications.

2.1 Principle of lasers

The end of the Second World War has focused much attention on developing new technologies, including powerful light sources. In 1960, powerful sources based on Light Amplification by Stimulated Emission of Radiation (LASER) have been proposed [29] using a ruby crystal. The mechanism of the stimulated emission is based on the prediction of Albert Einstein in 1917 [30]. The laser operation results from a competition between 3 main processes: absorption, spontaneous emission, and stimulated emission. Although the laser is not a two-level energy system, we use it in Fig. 2.1 describes the three mechanisms of light-matter interaction.

- **Absorption**: This process is presented in Fig. 2.1 (a) where an electron in the lower energy state, due to the absorption of a photon, moves to a higher energy state. This process is possible only if the photon has enough energy ($h\nu$) for the electron to reach the next excited state.

- **Spontaneous emission** [Fig. 2.1 (b)]: Being in the excited state, the electron relaxes a photon randomly and moves down to a lower energy state. The relaxed photon has an energy corresponding to the transition between the excited and the lower energy state, $h\nu = E_2 - E_1$. The phase of the emitted photon is random.

- **Stimulated emission** [Fig. 2.1 (c)]: A photon with energy $h\nu = E_2 - E_1$ stimulates an electron to move down to a lower energy state. The electron falls from the excited energy level to the lower energy level, accompanied by the emission of another photon with the same energy as the incoming one. The two photons created have

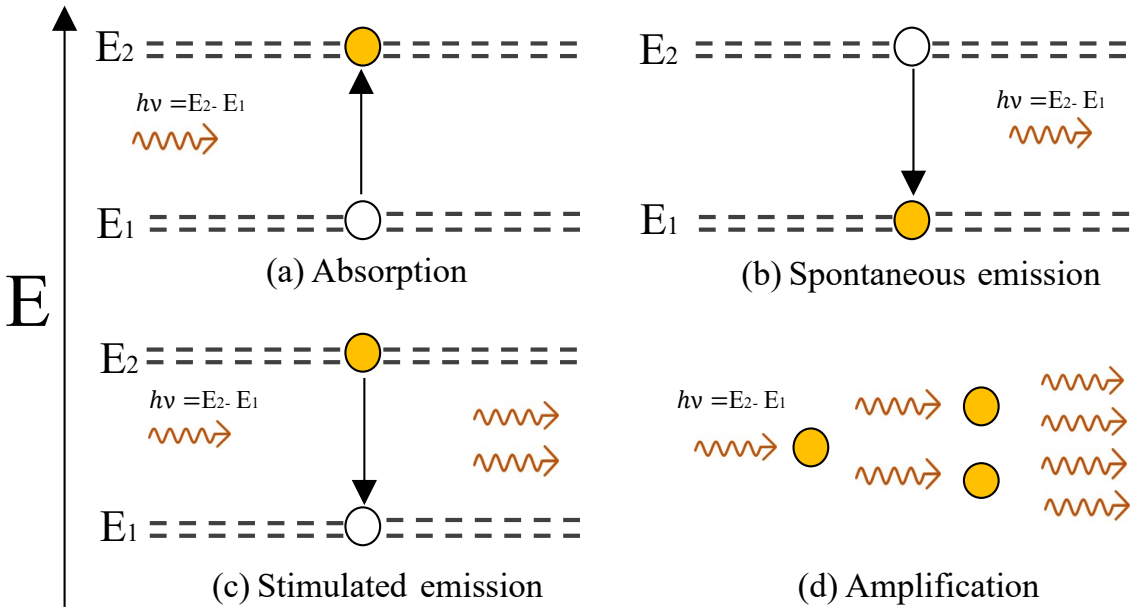

Figure 2.1: Light-Matter interaction mechanism in 2-energy levels system with E_1 and E_2 the energy of the ground state and excited state, respectively. (a) an electron leaves the ground state to the excited state after the absorption of a photon with energy $h\nu = E_2 - E_1$. (b) the electron in the excited level goes down accompanied by the emission of a photon with energy $h\nu = E_2 - E_1$. (c) stimulated emission, emission of two photons with the same energy after interaction between an electron in the excited state and a photon. (d) amplification based on stimulated emission.

the same energy (same wavelength or frequency) as the incident one. They also propagate in the same direction, i.e., exhibit the same phase.

- **Amplification** [Fig. 2.1 (d)]: The amplification is not a process of light-matter interaction but a consequence of the stimulated emission. It is only possible if there is enough electron in the excited state. The amplification by stimulated emission must be dominant to observe the lasing effect, but the spontaneous emission decreases its efficiency.

An external pump source (optical pump or electrical injection current) increases the stimulated emission efficiency. When the pump rate is enough to reach the *population inversion*, i.e., the electrons in the excited level are more numerous than the electrons in the ground level, then a net rate of stimulated emission (stimulated emission minus absorption) is achieved leading to a so-called *optical gain*. Although a population inversion can help to increase the amplification through stimulated emission, most excited electrons emit

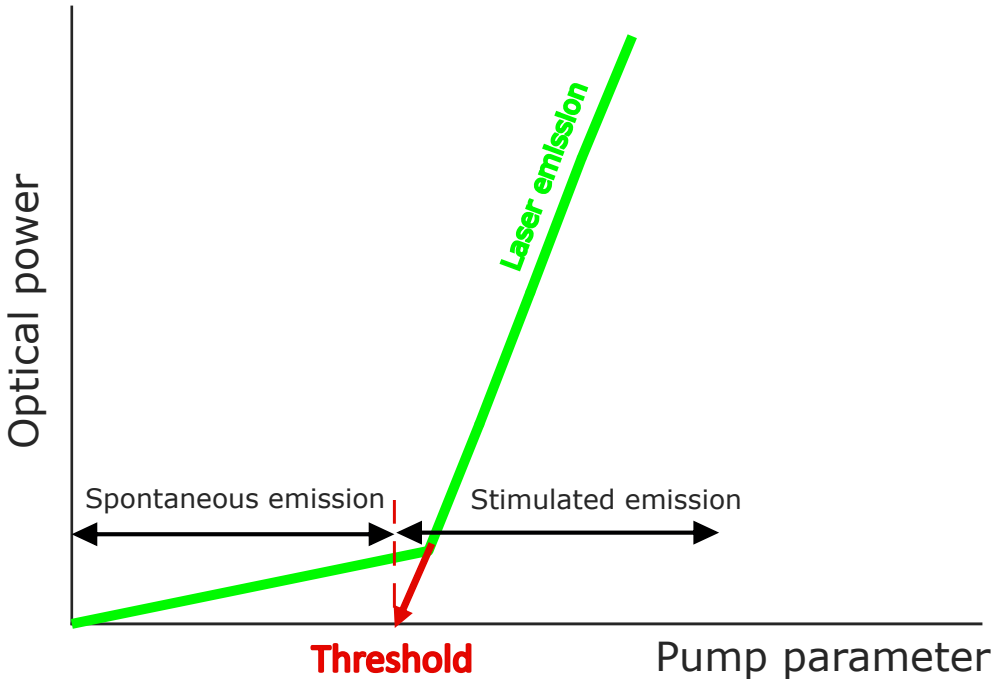

Figure 2.2: Laser output as a function of the pump characteristic. Before the threshold, the laser output is dominated by spontaneous emission. In other words, the losses are higher than the gain. The gain equalizes the losses at the threshold, and then the laser effect starts thanks to the stimulated emission. Beyond the threshold, a coherent and directional beam is created.

spontaneously and do not contribute to the lasing effect. An optical resonator formed by two mirrors is usually used to confine the gain medium and create the so-called *laser cavity*. The reflection of the photons inside the laser cavity helps for the stimulated emission. However, several electromagnetic waves are created inside the optical resonator. Only the electromagnetic waves that satisfy the boundary conditions of the optical resonator will be selected. They are called *longitudinal modes* of the laser cavity. The difference in frequency between two consecutive longitudinal modes is called free spectral range. The free spectral range is fixed by the distance between the two mirrors L and the nonlinear medium properties n_g. It is given by:

$$\omega_{FSR} = \frac{c}{2Ln_g} \tag{2.1}$$

where $c = 299792458$ m/s is the speed of the light and n_g the group refractive index. Furthermore, during the pumping, a competition between the losses and amplification

occurs inside the cavity. The losses in the laser cavity are due to the photons that escape from the mirrors and that are absorbed in the cavity medium. Figure 2.2 shows the typical light pump characteristic. For a low pump rate, the laser output is governed by spontaneous emission. An increase in the pump rate allows achieving that particular well-known operation point called laser *threshold* as shown in Fig. 2.2, where the gain overcomes the losses.

Beyond the threshold point, the dominant mechanism is the stimulated emission, and then the laser starts emitting a coherent and directional beam. The operation conditions can be summarized in three steps:

- a gain medium to provide spontaneous and stimulated emission at the desired wavelength.
- an optical or electrical pump to achieve population inversion
- a cavity controls the losses and select frequencies.

2.2 Dynamical classification of lasers

The previous section has discussed the principle underlying the laser operation and reveal stationary output power characteristics. Since the discovery of the laser, several types of lasers have been proposed depending on their dynamical properties. The equations that describe lasers dynamics have been obtained by analogy with Lorentz's system [31]. Lasers can be categorized into different classes using a simple comparison between the field decay rate κ, the dipolar polarization relaxation rate γ_d and the carrier decay rate γ_e [31], since the relationship between these three time-scales determines the laser dynamical properties.

2.2.1 Class A lasers

The class A lasers are characterized by a long photons lifetime, i.e., field decay rate κ is much less than the dipolar polarization relaxation rate γ_d and the carrier decay rate γ_e.

Based on the difference between κ, γ_d and γ_e, an adiabatic elimination can be applied to reduce the number of the equation. The laser system is then described with only one

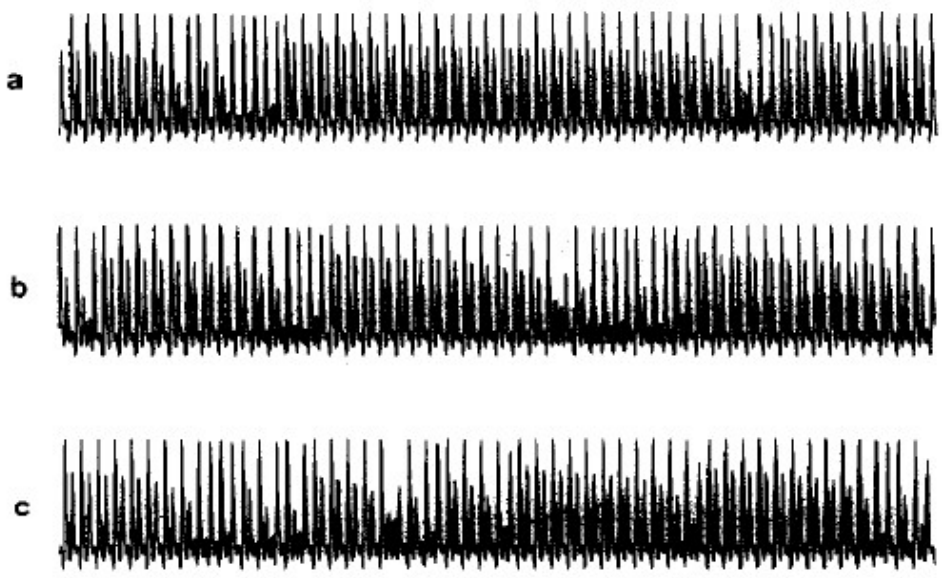

Figure 2.3: Route to chaos in a single-mode laser driven by external modulation. (a), (b) and (c) are obtained for fixed parameters when increasing only the amplitude of modulation. Taken from [32]

equation, the one of the field E. This type of laser includes atomic gas lasers (He-Ne (0.633 µm), Ar^+, Kr^+) and the dye lasers [33]. It has been shown that Class A lasers can lead to locking and regular pulsation under external fields perturbation. Most importantly, chaotic dynamics may be observed when modulating the external field, the pump rate, or the cavity losses [32, 34]. Figure 2.3 shows the bifurcation to the chaos through intermittency. Figure 2.3 (a), (b), and (c) show that chaotic bursts that interrupt the periodic evolution of the times series increase with the amplitude of modulation.

2.2.2 Class B lasers

In this type of laser, the field decay rate κ and the carrier decay rate γ_e are much smaller than the dipolar polarization relaxation rate γ_d. Adiabatical elimination allows describing the system with two coupled nonlinear equations: the field and the inversion population. The Class B lasers include the Ruby, Nd: YAG, CO_2 and semiconductor lasers. These lasers are very stable in free-running. As we will see in the following section, they can exhibit a wide variety of nonlinear behavior in the presence of external perturbation.

2.2.3 Class C lasers

For this type of laser, the three equations from the analogy between Lorentz's system and the laser (see [31]) must be considered because the times constant, κ, γ_d, and γ_e are in the same order. Among the class C laser we denote, HN_3 laser [35, 36], He-Ne lasers (3.39m) [37, 38] and Ne-Xe lasers (3.51m) [39]. We show in Fig. 2.4 an example of periodic and complex dynamics of the class C lasers with external signal injection. It was shown that when increasing the injection strength, the laser output shows an irregular self-pulsing behavior as shown in Fig. 2.4 (a). When the injection strength increases again, the laser output displays chaotic dynamics in Fig. 2.4 (b). A further increase in the injection strength leads a period-doubling bifurcation Fig. 2.4 (c). An increase in the injection strength brings the system again to the regular oscillatory self-pulsing, as shown in Fig. 2.4 (d).

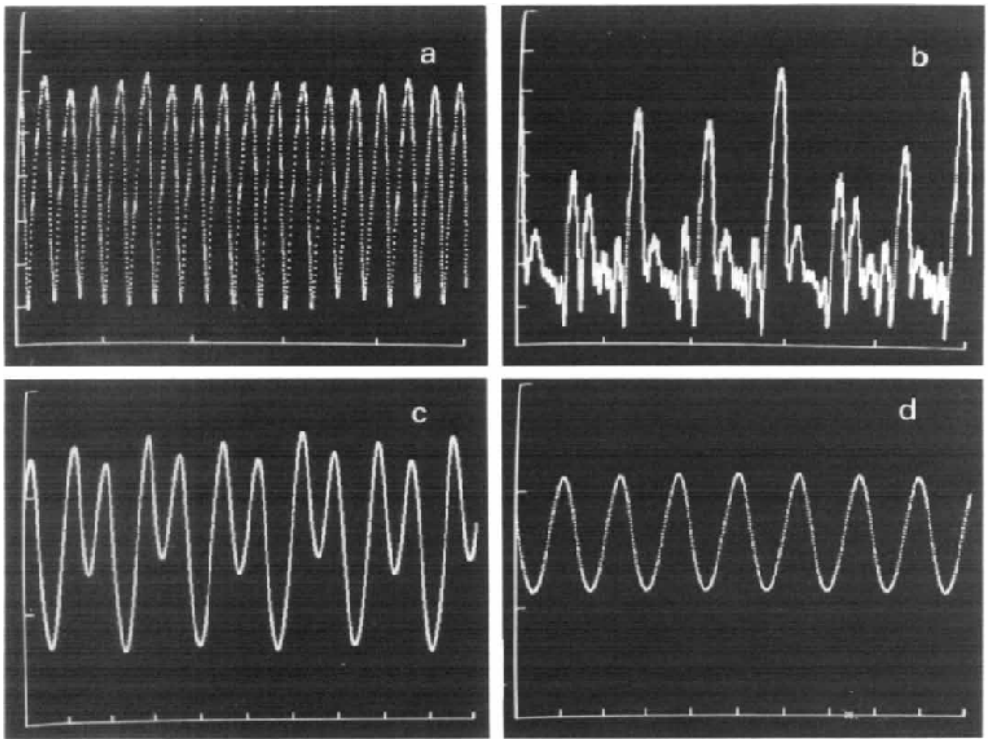

Figure 2.4: Analysis of the dynamics of class C when the injection strength ranges from zero to the locking threshold. (a) irregular self-pulsing behavior, (b) chaotic dynamics, (c) period-doubling bifurcation, (d) regular oscillatory self-pulsing. Taken from [40].

2.3 Semiconductor lasers

The previous section has shown that the semiconductor lasers behave dynamically as class B lasers. Physically, their active regions (gain medium) are made of semiconductor materials that determine the emission wavelength. Indeed, the photon energy ($E = h\frac{c}{\lambda}$) is linked to the Planck constant h and λ the wavelength. Figure 2.5 shows the diagram that summarizes the relation between the lattice constant, the bandgap, and the emission wavelength. The left and right vertical axis correspond to the bandgap and the wavelength. For some medium, photons with sufficient gain can be generated with an adequate span of wavelength. This diagram shows that a range of band gaps and wavelength can be obtained when changing the composition of the material system for a fixed lattice constant. Initially, semiconductor lasers were proposed from a so-called p-n homojunction. When two semiconductor materials are in contact, we have the so-called *p-n junction*. The type of doping characterizes the p-semiconductor and n-semiconductor. In the p(n)-semiconductor material, the doping creates an excess of holes (electrons).

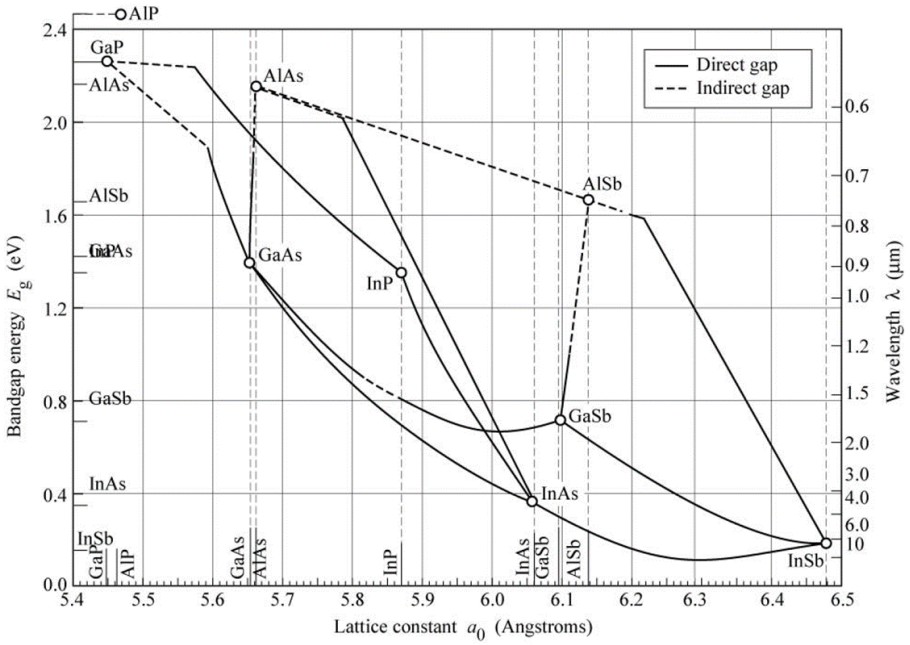

Figure 2.5: Diagram showing the relationship between the lattice constant, the bandgap, and the emission wavelength. The left and right vertical axis correspond to the bandgap and the wavelength. Taken from[41]

A p-n junction is also named as *homojunction* because the bandgap in both types of doped

materials is similar. The inversion of the population can be observed in this junction leading to the laser effect. It is not satisfactory because it requires low temperatures, high pumping current, and continuous-wave operation is challenging [42]. A new configuration called *double heterostructure* is proposed in 1963 by Herbet Kroemer, Nobel Laureate in 2000 [43] to overcome these limitations. Figure 2.6 (a) and (b) show the simplified double heterostructure and the corresponding bandgap, respectively. In such a structure, a material with a small bandgap is placed between the two strongly-doped p-type (P^+ region) and n-type (N^+ region) semiconductor materials. Electrical pumping can bring additional electrons and holes to the conduction band and valence band, respectively. The electrons and the holes are then confined in the active region, leading to photons generation by spontaneous or stimulated emission. It is worth noticing that this structure reduces the threshold current and improves the gain uniformity in the active region. In addition, the P^+ region and N^+ region have a refractive index smaller than the active region. The active region, therefore, acts as a waveguide for the laser beam.

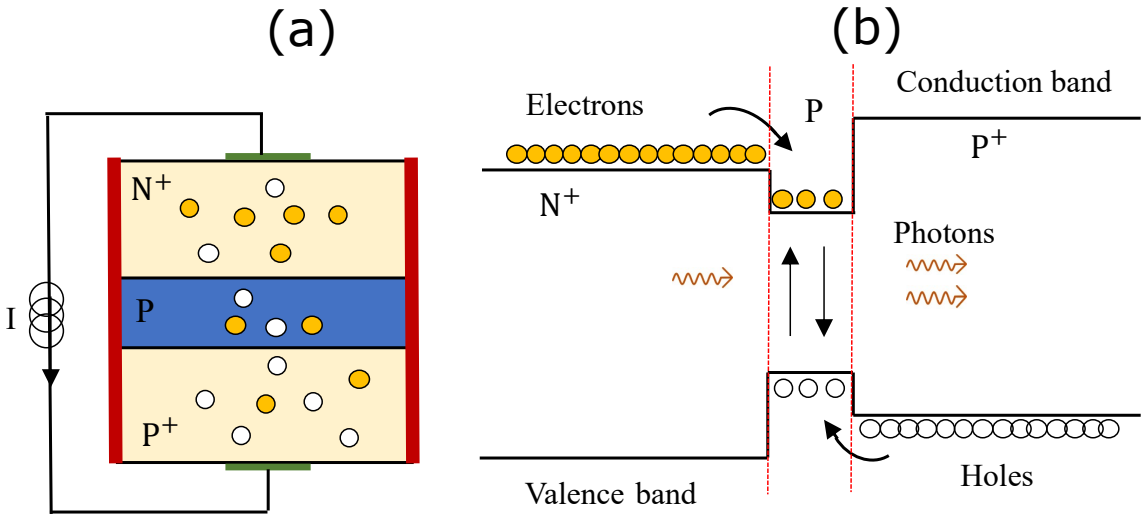

Figure 2.6: (a) Simplified illustration of a double heterostructure. (b) the corresponding band gap representation.

2.4 Edge-emitting lasers (EELs)

This section provides details of the physical mechanism underlying the edge-emitting laser and the mathematical model resulting from the different interaction processes.

2.4.1 Mechanisms underlying the laser operation

The operation of any laser system requires an active region, positive feedback, and a pumping system. As discussed in Fig. 2.6, the pumping allows increasing the carrier density in the layers, whereas the active region confines the carriers leading to the amplification of light. The mirrors ensure the selection of the emission wavelengths. In the case of semiconductor lasers, two different approaches are used depending on their cavity's geometry. These two semiconductor lasers are the *Edge-Emitting Laser* (EEL) and *Vertical Cavity Surface-Emitting Laser* (VCSEL). The first semiconductor lasers proposed in 1963 was an edge-emitting laser [43–46]. Figure 2.7 shows a simplified example of an edge-emitting laser. The energy bandgap of an edge-emitting laser is linked to the double heterostructure shown in Fig. 2.6.

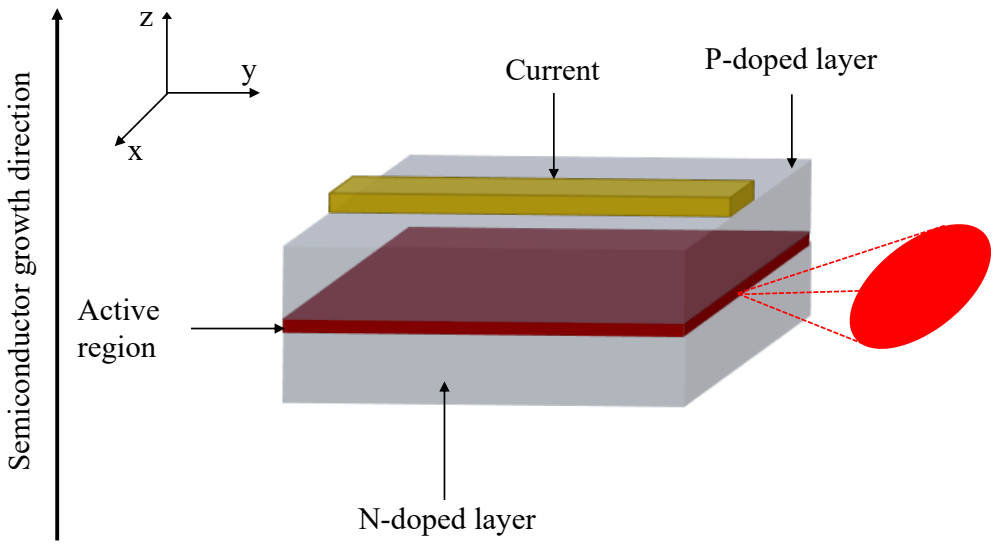

Figure 2.7: Simplified illustration of edge emitting laser.

In these lasers, the light propagates along the active region parallel to the wafer's surface. Consequently, the direction of emission (edge) is orthogonal to that of the semiconductor growth.

2.4.2 Mathematical Modelling of Edge-emitting semiconductor lasers

Modeling a semiconductor laser has to take into account the gain medium and the propagation conditions. Indeed, inside the laser cavity, we can consider two traveling

waves, the forward and backward propagation direction, as shown in Fig.2.8. The forward $E(z)^+$ and backward $E(z)^-$ fields are denoted as:

$$E(z)^+ = E(z)_{0f} exp(-i\frac{n\omega}{c}z - \frac{1}{2}\alpha_{abs}z) \tag{2.2}$$

$$E(z)^- = E(z)_{0b} exp(-i\frac{n\omega}{c}(L-z) - \frac{1}{2}\alpha_{abs}(L-z)) \tag{2.3}$$

where $E(z)_{0f}$ and $E(z)_{0b}$ are the amplitude of the forward and backward field, respectively, ω is the angular frequency, n is the refractive index of the active medium, and α_{abs} is the absorption loss that takes into account the material loss and the internal loss. As we stated in section 2.1, the gain must overcome the total optical losses to satisfy the lasing operation.

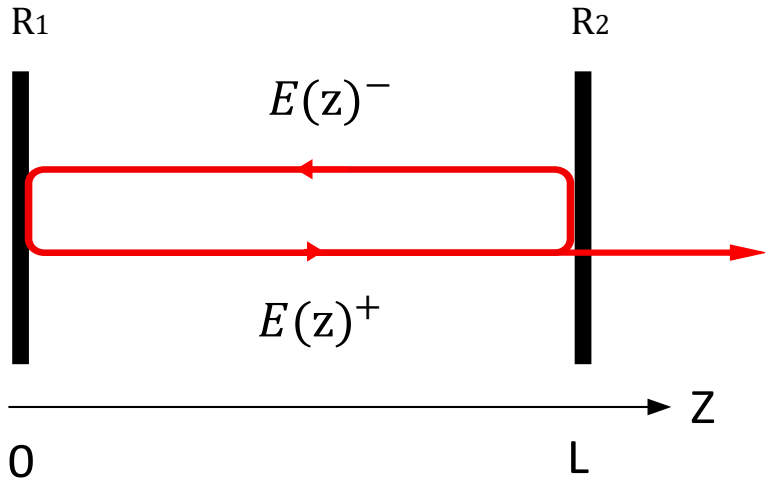

Figure 2.8: Fabry-Perot resonator consisting of a medium of length L confined between two mirrors with the reflection coefficient R_1 and R_2.

The condition that sustained the laser oscillation can be derived from the boundary conditions [47]:

$$\sqrt{R_1 R_2} exp(-2i\frac{n\omega}{c}L - \alpha_{abs}L) = 1 \tag{2.4}$$

with R_1, R_2 the edge facet reflectivities and L the cavity length. The threshold gain condition,i.e., the balance between the gain and the total losses is obtained from equ.(2.4):

$$G_{th} = \frac{1}{\Gamma}[\alpha_{abs} - \frac{ln(R_1 R_2)}{2L}] \tag{2.5}$$

with Γ the confinement factor. By introducing the slowly varying complex amplitude of the field according to [48] and following the same calculation as in [47], the rate equation of the laser output can be written as:

$$\frac{dE(t)}{dt} = [i\omega(N) + \frac{1}{2}(G(N) - \frac{1}{\tau_p})]E(t). \tag{2.6}$$

here, i is the imaginary number, N is the carrier density, $\omega(N)$ and G(N) are respectively, the angular optical frequency and the differential gain of the laser and τ_p is the photon lifetime. The photon lifetime relates to the photon losses in the cavity. Γ is hidden in $G(N)$.

The differential gain is a function of the carrier density and is governed by the following equation:

$$G(N) = G_N(N - N_0) \tag{2.7}$$

where G_N and $N_0 = N_{th} - \frac{1}{G_N \tau_p}$ are the differential gain and the carrier density at the transparency, respectively. N_{th} is the threshold carrier density. In free-running, the carrier density is very close to the threshold value, where,

$$G(N_{th}) = \frac{1}{\tau_p} \tag{2.8}$$

From Fig.2.6, it is clear that to model the rate equation of the carrier's density, we must consider the electron-holes recombination processes in the active region. According to [47], two distinct processes are involved in the carrier recombination mechanism. The first is the interband processes between the two bands in the active region and involves the radiative and non-radiative processes. The second corresponds to the intraband functions that occur within a band and consist of electron-electron and electron-photon scattering [49]. As demonstrated in [21, 47] by taking into account all the losses due to the spontaneous emission or non-radiative emission, the rate equation of the carrier density can be written as:

$$\frac{dN(t)}{dt} = R_p - \frac{N(t)}{\tau_s} - G(N)\left|E(t)\right|^2. \tag{2.9}$$

where, τ_s is the carrier lifetime and R_p is the pump rate. The pump rate of the laser in a free-running regime at threshold can be expressed as:

$$R_p = \frac{N_{th}}{\tau_s} \tag{2.10}$$

By introducing the equation 2.7-2.8 in 2.6 and 2.9, the rate equation of the laser can be rewritten as:

$$\frac{dE(t)}{dt} = [i\omega(N) + \frac{1}{2}(G_N(N - N_0) - \frac{1}{\tau_p})]E(t). \tag{2.11}$$

$$\frac{dN(t)}{dt} = R_p - \frac{N(t)}{\tau_s} - G_N(N(t) - N_{th})\left|E(t)\right|^2 - \frac{\left|E(t)\right|^2}{\tau_p}. \tag{2.12}$$

2.5 Vertical-Cavity Surface-Emitting Lasers (VCSEL)

The first semiconductor lasers developed were the edge emitters. Since then, a lot of work has been devoted to their improvement. These lasers emit light in the plane of the active region that is orthogonal to the semiconductor growth direction. In 1979, a new semiconductor laser design led to *Vertical Cavity Surface-Emitting Lasers* (VCSELs) [50]. This VCSEL was based on the material system InGaAsP/InP, and the operation wavelength was around 1.3 µm. Due to the cavity properties, the threshold current was very high (900 mA) at a low operation temperature (77 K). A new VCSEL device emitting at 874 nm at room temperature was proposed [51] in 1984. Still, the threshold current was considerable (i.e., 510 mA). Five years later, a new semiconductor material GaAlAs/GaAs, has been used to propose a new VCSEL with a threshold current of 6 mA [52]. Since these demonstrations, several research activities on the improvement of the VCSEL performance have been reported [53–57]. More specifically, the threshold current has been decreased significantly to reach 1-2 mA at room temperature. These advances have made VCSEL a powerful device for many applications [58].

2.5.1 Polarization properties of the VCSEL

Like the other types of semiconductor lasers, Vertical-Cavity Surface-Emitting Lasers (VCSELs) structure is based on the double heterostructure. Figure 2.9 shows the simplified representation of the VCSEL. The active region of the VCSEL is arranged between two Distributed Feedback Reflector (DBR) mirrors with reflectivities above 99%. The reflectivity of DBR on top is smaller than the one of the DBR on the bottom. The active region consists of one or more quantum well structures that improve the gain efficiency and lead to a low threshold current. The DBRs mirrors are formed by an alternating sequence of low and high refractive index layers with a thickness equal to a quarter of the wavelength of the material, leading to an index-modulation grating [59].

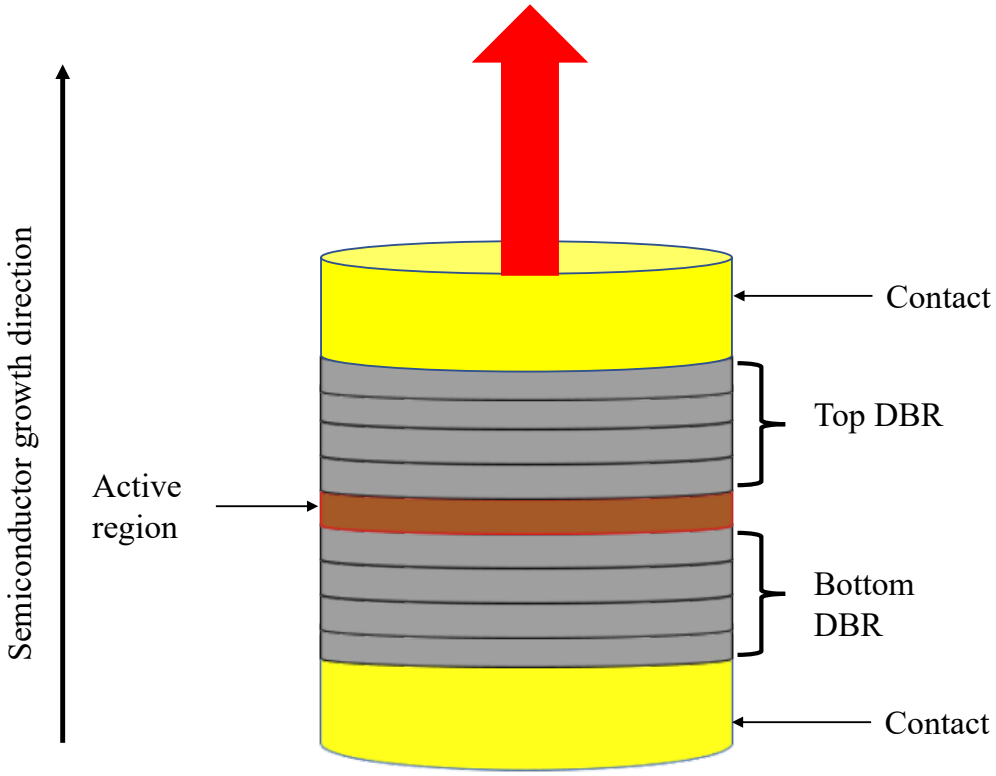

Figure 2.9: Simplified illustration of VCSEL.

The polarization properties of the VCSEL are linked to their cavity geometrical properties, the gain profile in the active region, and the bandwidth of the DBR. The gain profile of the material and the bandwidth of the DBR mirrors allow filtering and selecting the lasing wavelength. The thickness of the active region and the DBR mirrors act to determine the longitudinal modes and their corresponding mode spacing. The number of lasing modes

is linked to the balance between the gain in the active region and the losses. Unlike the EEL, where the asymmetry geometry favors a fixed linear polarization, the cylindrical geometry of the VCSEL cavity combined with the symmetry of the gain in the plane of the quantum wells leads to a weak polarization anisotropy giving rise to two linear orthogonal polarization directions. Usually, the VCSELs emit along with one of the two orthogonal directions. In addition, depending on the operation condition (bias current and operation temperature) higher-order transverse modes can be excited in the two linear orthogonal polarization modes of the VCSEL [60–64]. Moreover, polarization instability can be induced in the VCSEL when changing the injection current and the operating temperature. This instability includes the switching between the two orthogonal polarization modes [65]. The following subsection will be devoted to polarization switching and the related nonlinear dynamics.

2.5.2 Polarization switching

The polarization properties in VCSEL are beneficial for numerous applications that we will address later in this Chapter. The anisotropy in the VCSEL's structure plays a crucial role in the polarization properties [66, 67]. It has been demonstrated that although most VCSELs start lasing in one among two orthogonal polarization states, switching can be induced when varying the operation parameters (injection current and temperature).

Polarization switching and the related bistability have been extensively studied recently [68–70]. Several types of polarization switching (PS) occur when changing the operation parameters. The first type (Type I) of PS is shown in Fig. 2.10, where the injection current is varied for fixed temperature. Type I PS is from the high-frequency mode (ν_H) to the low-frequency mode (ν_L). As we can see, the type I PS refers to the situation where the polarization modes do not simultaneously switch on, and switching can occur abruptly between them by changing the injection current. A large region of stable operation on the two polarization modes leading to a hysteresis appears when varying the injection current.

The influence of the VCSEL substrate temperature have been reported in several works [55, 71, 72]. Fig. 2.11 depicts the polarization-resolved optical power evolution for different temperatures when varying the injection current [71]. Three typical different polarization switching scenarios were observed. Figures 2.11 (a), (b), and (c) were obtained for fixed substrate temperatures $T_{sub} = 10$ °C, $T_{sub} = 15$ °C, and $T_{sub} = 55$ °C, respectively. As we

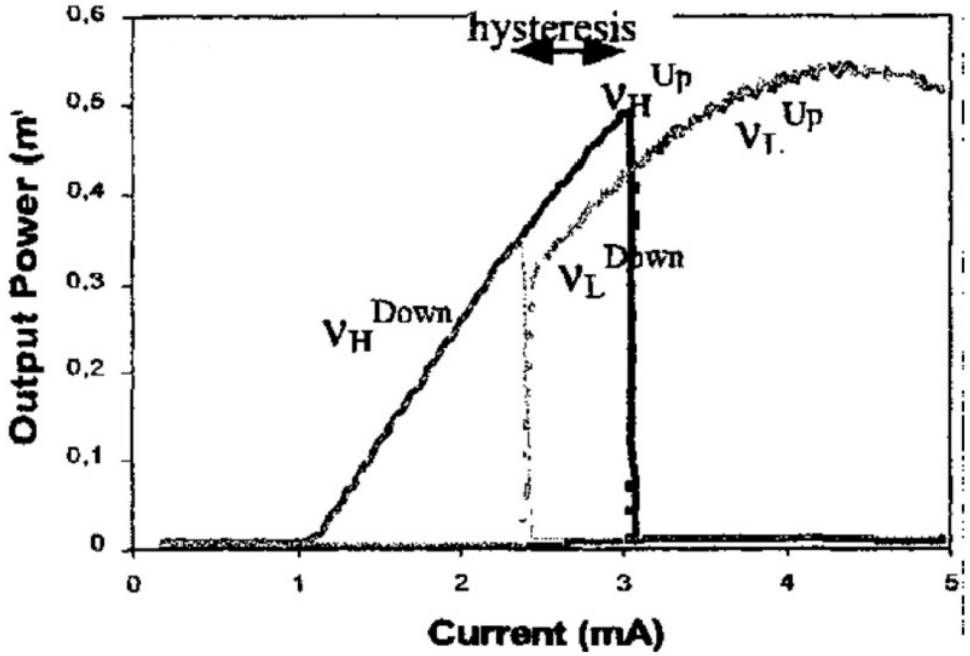

Figure 2.10: Polarization resolved power evolution when increasing (solid line) and decreasing (dashed line) the injection currents. Taken from [68].

can see in 2.11 (a), at low temperature, the polarization-resolved power leads to a type I PS. When the temperature is increased to $T_{sub} = 15$ °C, the type I PS takes place at a low injection current. Another polarization switching scenario referred to as PS II (type II PS) appears when the injection current keeps increasing. The type II PS is characterized by switching from the longer wavelength mode (ω_l) to the shorter longer-wavelength (ω_h) mode. When the substrate temperature range between $T_{sub} = 25 - 55$ °C, only the type II of PS was reported. Otherwise, the type I, II, and double PS have been extensively studied theoretically using classical numerical simulation and bifurcation analysis software [73, 74].

2.5.3 Modelling of VCSEL polarization dynamics

The classical model of semiconductor laser does not consider the anisotropy of the gain medium, which is a key parameter for the polarization properties in VCSEL. In 1995, San Miguel, Feng, and Moloney [75] established a model of the polarization dynamics in VCSEL. As we have shown in the previous section, the active region of the VCSEL is a quantum well structure in which light is emitted perpendicularly to the transverse plane

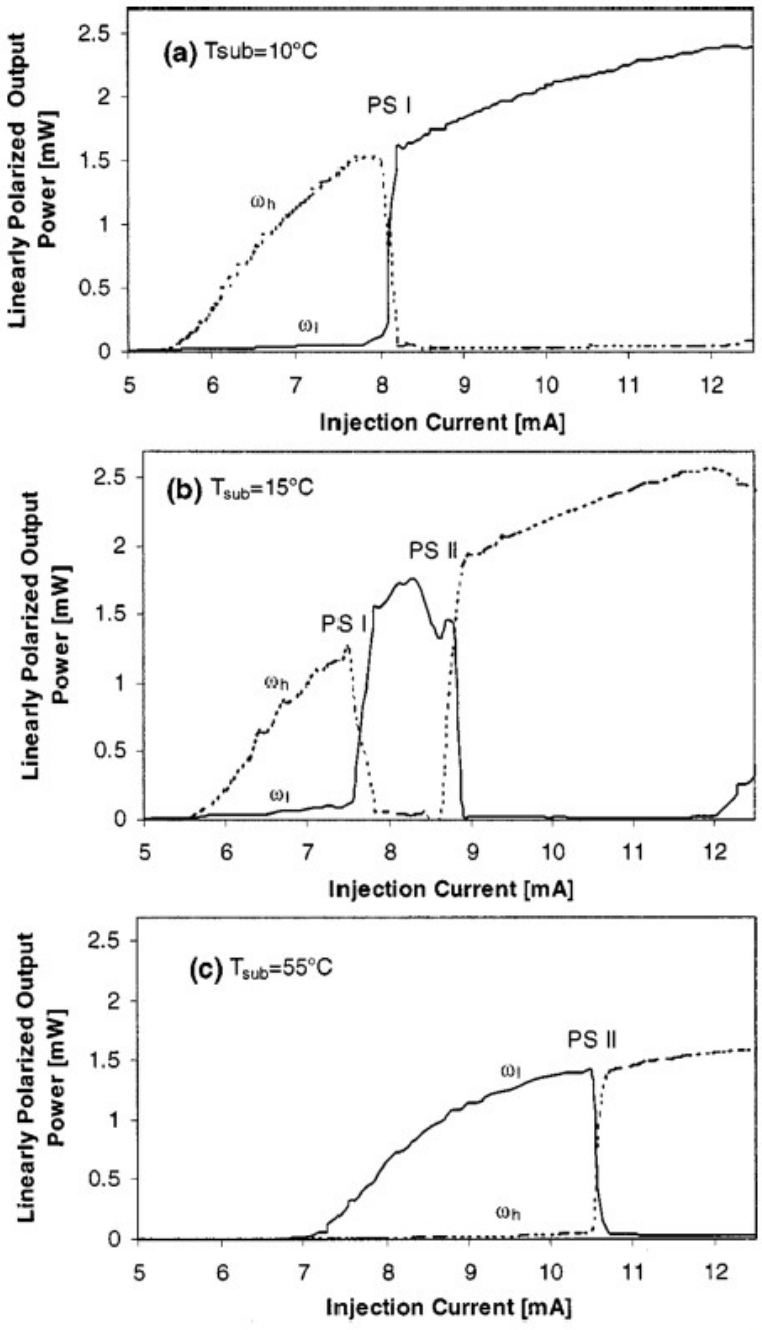

Figure 2.11: Polarization resolved power evolution when increasing (solid line) and decreasing (dashed line) the injection currents at different substrate temperatures. (a) $T_{sub} = 10$ °C, (b) $T_{sub} = 15$ °C, and (c) $T_{sub} = 55$ °C. The full and dashed curves correspond to the lower and higher energy mode. Taken from [71]

(along the z-direction) as shown in Fig 2.12. The two valence bands are heavy holes and light hole bands with high and low energies, respectively.

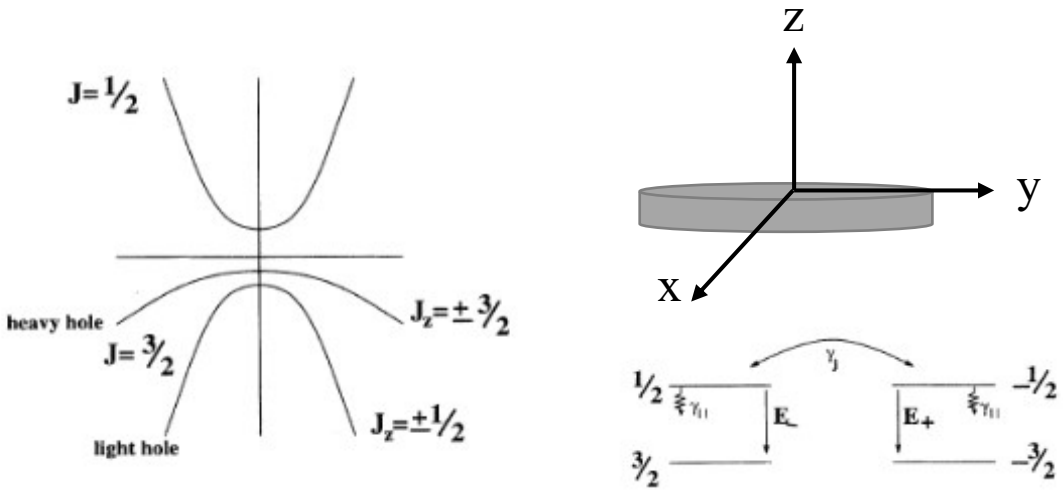

Figure 2.12: Band structure of a quantum well (left) and the four-level model energy transitions (right bottom). Taken from[75].

The two valence bands are not degenerate in the quantum well material due to the quantum confinement in the z-direction. Furthermore, the mixing between the valence band can be neglected [75]. The projection of the total angular momentum of the conduction and heavy hole band along the z-axis is $J_z = \pm\frac{1}{2}$ and $J_z = \pm\frac{3}{2}$, respectively. For the quantum well material, only the transitions for which the total angular quantum momentum in z-direction changes by $\Delta J_z = \pm 1$ are allowed. As a result, only two dipole transitions in the plane of the quantum well are allowed, i.e., those occurring within the subsystem as shown in Fig 2.12. The transition from $J_z = \frac{1}{2}$ to $J_z = \frac{3}{2}$ (spin-up) and $J_z = -\frac{1}{2}$ to $J_z = -\frac{3}{2}$ (spin-down) are associated with left and right-hand circularly polarized light of the electric field.

Using the four-level system, the simplified SFM model can be derived from the Maxwell-Bloch equation [72, 76]. The resulting rate equations that take into account the polarization modes can be written as:

$$\frac{dE_\pm}{dt} = -\kappa(1 + i\alpha)E_\pm + P_\pm. \tag{2.13}$$

$$\frac{dP_\pm}{dt} = -\gamma_{rp}(1 - i\alpha)P_\pm + \gamma_{rp}a(1 + \alpha^2)(N - N_t \pm M)E_\pm. \tag{2.14}$$

$$\frac{dN}{dt} = C - \gamma_e N - (E_+P_+^* + E_-P_-^* + cc) \tag{2.15}$$

$$\frac{dM}{dt} = -\gamma_s M - (E_+ P_+^* - E_- P_-^* + cc) \tag{2.16}$$

where $E_\pm$ and $P_\pm$ are the slowly varying amplitude of the circularly polarized (left (-) and right (+)) of the electrical field and the dipole polarization, respectively, N is the sum of the population inversion in the two radiation channels, and M is the population inversion of the channel with opposite spin. The carrier variable N and M can then be read [76, 77], :

$$N = N_+ + N_-, \tag{2.17}$$

$$M = N_+ - N_-, \tag{2.18}$$

with N_+ and N_- the carrier density associated to the transition $\Delta J_z = +1$ and $\Delta J_z = -1$, respectively. α represents the amplitude-phase coupling coefficient of the electrical field and the polarization. As for the EEL, α will be named linewidth enhancement in the following. a is the differential gain at the laser frequency as detailed in [76]. The relaxation rate of the amplitude of the electrical field and the polarization are taken into account by κ and γ_{rp}, respectively. γ_e and γ_s represent the relaxation rate of the N and M, respectively. Considering that γ_{rp} is much larger than the κ, γ_s and γ_e, the polarization can be adiabatically eliminated. By performing some variable change and taking into account the elimination of the polarization [77], the rate equation can be rewritten as:

$$\frac{dE_\pm}{dt} = \kappa(1 + i\alpha)(D \pm d - 1)E_\pm, \tag{2.19}$$

$$\frac{dD}{dt} = \gamma_e \mu - \gamma_e D(1 + |E_+|^2 + |E_-|^2) - \gamma_e d(|E_+|^2 - |E_-|^2) \tag{2.20}$$

$$\frac{dn}{dt} = \gamma_s d - \gamma_e d(|E_+|^2 + |E_-|^2) - \gamma_e D(|E_+|^2 - |E_-|^2) \tag{2.21}$$

D and n are the carrier density. $D = \frac{(N-N_t)}{N_{(th}-N_t)}$, where N, N_{th} and N_t are the carrier number and the carrier number at threshold and at transparency, respectively. n corresponds to the difference between the population inversions for the spin-up and spindown radiation channels. μ, is the normalized current injection defined as followed:

$$\mu = \frac{\tau_n}{\tau_e} \frac{\frac{I}{I_{th}} - 1}{1 - \frac{N_t}{N_{th}}} + 1 \tag{2.22}$$

In this equation, I, I_{th}, N_t and τ_n, correspond to the injection current, the threshold

current, the number of carriers at transparency, and the differential carrier lifetime at the threshold, respectively, τ_e and N_{th} represent the carrier lifetime and the number of carriers at the threshold.

It has been shown that the polarization switching mechanism is affected by the anisotropies of the quantum well structure [72]. By introducing the linear amplitude and phase anisotropies, the rate equation 2.19-2.21 can be rewritten as:

$$\frac{dE_{\pm}}{dt} = \kappa(1+i\alpha)(D \pm d - 1)E_{\pm} - (\gamma_a + i\gamma_p)E_{\pm} \tag{2.23}$$

$$\frac{dD}{dt} = \gamma_e\mu - \gamma_e D(1 + |E_+|^2 + |E_-|^2) - \gamma_e d(|E_+|^2 - |E_-|^2) \tag{2.24}$$

$$\frac{dn}{dt} = \gamma_s d - \gamma_e d(|E_+|^2 + |E_-|^2) - \gamma_e D(|E_+|^2 - |E_-|^2) \tag{2.25}$$

where γ_p and γ_a, are the linear phase and amplitude anisotropy, respectively. In the following, γ_p and γ_a will be named linear birefringence and linear dichroism.

To determine the rate equation for the linear polarization mode, we use the transformation between the linear and circular bases:

$$E_+ = \frac{E_x + iE_y}{\sqrt{2}} \tag{2.26}$$

$$E_- = \frac{E_x - iE_y}{\sqrt{2}} \tag{2.27}$$

The SFM model for the two linear polarization modes can then be expressed as follow:

$$\frac{dE_x}{dt} = -(\kappa + \gamma_a)E_x - i(\kappa\alpha + \gamma_p)E_x + \kappa(1+i\alpha)(DE_x + inE_y), \tag{2.28}$$

$$\frac{dE_y}{dt} = -(\kappa - \gamma_a)E_y - i(\kappa\alpha - \gamma_p)E_y + \kappa(1+i\alpha)(DE_y - inE_x), \tag{2.29}$$

$$\frac{dD}{dt} = -\gamma[D(1 + |E_x|^2 + |E_y|^2) - \mu + in(E_yE_x^* - E_xE_y^*)] \tag{2.30}$$

$$\frac{dn}{dt} = -\gamma_s n - \gamma[n(|E_x|^2 + |E_y|^2) + iD(E_yE_x^* - E_xE_y^*)] \tag{2.31}$$

The x-polarization mode (X-PM) and y-polarization mode (Y-PM) admit stationary solutions in the free-running. The stationary solution of X-PM is given by $E_y = 0$ and,

$$E_x = \sqrt{\frac{\mu}{\mu_x} - 1} e^{i\omega_x}, \tag{2.32}$$

$$\mu_x = 1 + \frac{\gamma_a}{\kappa}, \tag{2.33}$$

$$\omega_x = -\gamma_p + \alpha\gamma_a. \tag{2.34}$$

The stationary solution of Y-PM is given by $E_x = 0$,

$$E_y = \sqrt{\frac{\mu}{\mu_y} - 1} e^{i\omega_y}, \tag{2.35}$$

$$\mu_y = 1 - \frac{\gamma_a}{\kappa}, \tag{2.36}$$

$$\omega_y = \gamma_p - \alpha\gamma_a. \tag{2.37}$$

where μ_x and μ_y are the thresholds of the two polarization modes, X-PM and Y-PM, respectively. ω_x and ω_y are the angular frequencies of X-PM and Y-PM, respectively.

2.6 Nonlinear dynamics induced by external perturbation

Nonlinear lasers dynamics have attracted much attention since the works of Haken in 1975 [31], where he demonstrated a strong analogy between the laser equations and the Lorentz chaos equations. Due to their geometrical structure (Edge-Emitting Lasers, Vertical cavity Emitting lasers), the semiconductor lasers, therefore, also named *lasers diode*, are very sensitive to the external perturbations. It has been well established that several external perturbations such as direct modulation of the pumping current, optoelectronic feedback, optical feedback, and optical injection can induce a wide variety of nonlinear dynamics in the lasers. Figure 2.13 shows the different techniques of external perturbations techniques of the semiconductor lasers. Figure 2.13 (a) corresponds to the current modulation where the laser is driven with a time-varying modulation signal. External optical feedback [Fig. 2.13 (b)] occurs when a distant reflector partially returns the laser output in its cavity. Figure 2.13 (c) depicts the optoelectronic feedback. The external optical injection is shown in Fig. 2.13 (d): in that system, the light from a laser named *master laser* is injected into the cavity of a semiconductor laser named *slave laser*.

- **Semiconductor laser under external current modulation**

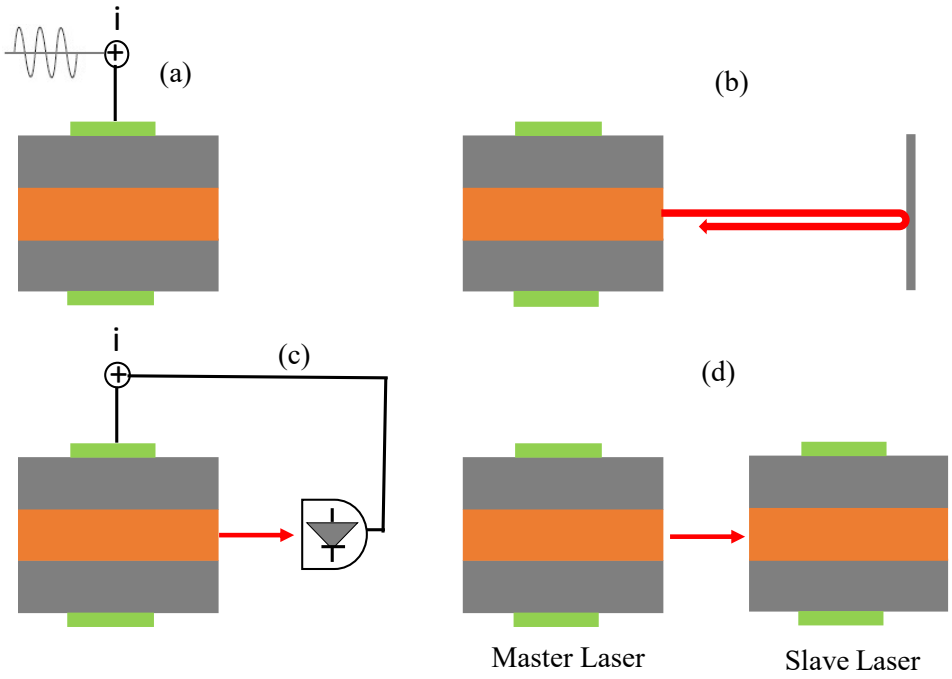

Figure 2.13: Semiconductor laser with external perturbation. (a) current modulation, (b) optical feedback, (c) optoelectronic feedback, and (d) optical injection.

The pump current modulation was one of the first techniques to destabilize a laser diode. A large variety of nonlinear dynamics are induced by direct modulation of the pump current in the semiconductor lasers theoretically and experimentally [78–81]. These nonlinear dynamics can include the distortion of harmonics, sub-harmonics pulsation, period-doubling bifurcation, and route to chaos for strong injection current modulation. It has been demonstrated that when the semiconductor laser is directly modulated close to the threshold current, the laser output can exhibit 40-70 ps optical pulses at a repetition rate of 200 MHz to 2.17 GHz [82]. It has also been theoretically reported that when the modulation frequency is close to the relaxation oscillation frequency, the semiconductor laser output can show period dynamics that lead to the chaos [83]. Experimental evidence has demonstrated the period-doubling leading to the chaos in a Distributed Feedback (DFB) laser under direct current modulation [81]. Most of the studies mentioned above relate to conventional EELs, but chaos due to the current modulation is not restricted to the EELs [76, 84–86].

VCSELs have also shown interesting nonlinear dynamics under direct current modulation due to their rich polarization properties. When the VCSELs are directly modulated, the transverse operation plays a crucial role in the resulting dynamics. Direct current

modulated multi-transverse VCSELs lead to rich polarization dynamics. More specifically, depending on the modulation parameters, the excitation of a higher-order transverse mode is found to induce a chaotic pulsation or generate time-periodic pulsing dynamics [84]. Polarization mode competition leads to a new chaotic behavior [86]. Besides the multi-transverse VCSELs, the nonlinear dynamics induced by direct current modulation in a single-transverse mode VCSEL has been studied [85]. The in-phase and anti-phase dynamics have been reported in the two linear polarization modes of the VCSEL [85]. Numerical simulations have demonstrated that polarization switching plays a crucial role in the appearance of complex dynamics in the two polarization modes [87].

- **Semiconductor laser subject to external feedback**

As shown in Fig. 2.13 (b), optical feedback consists in re-injecting a portion of the laser output from a distant reflector into the laser cavity. In 1980, Lang and Kobayashi published a paper on the effect of optical feedback in a Edge-emitting semiconductor lasers[88]. Since their work, semiconductor lasers with optical feedback have attracted much attention due to the fundamental and promising application interests [89–97]. A numerous of nonlinear dynamics including instability, bistability, self-pulsation, coherence collapse, and linewidth reduction have been observed in semiconductor laser [95, 98–104].

The semiconductor laser response to the optical feedback depends strongly on the delay induced by the round-trip of the light inside the external cavity ($\tau_{ext} = \frac{2L}{c}$), L is the length of the external cavity) and the feedback strength (the quantity of light from the reflector). Figure 2.14 shows one of the first reported mapping of the dynamical regime in the semiconductor lasers when varying the feedback ratio (feedback strength) and the length of the external cavity (delay) [105]. Similar mapping has been reported since then, although the results vary with the laser parameters. Several regimes of nonlinear dynamics are observed in the plane of the feedback parameters.

- **Regime I**: it appears at a relatively low feedback ratio and is characterized by spectrum narrowing or broadening depending on the feedback phase.

- **Regime II**: this regime is observed just after regime I when increasing the feedback ratio and is characterized by the unlocked dynamics. This regime appears for feedback level less than 0.01 % of the laser output.

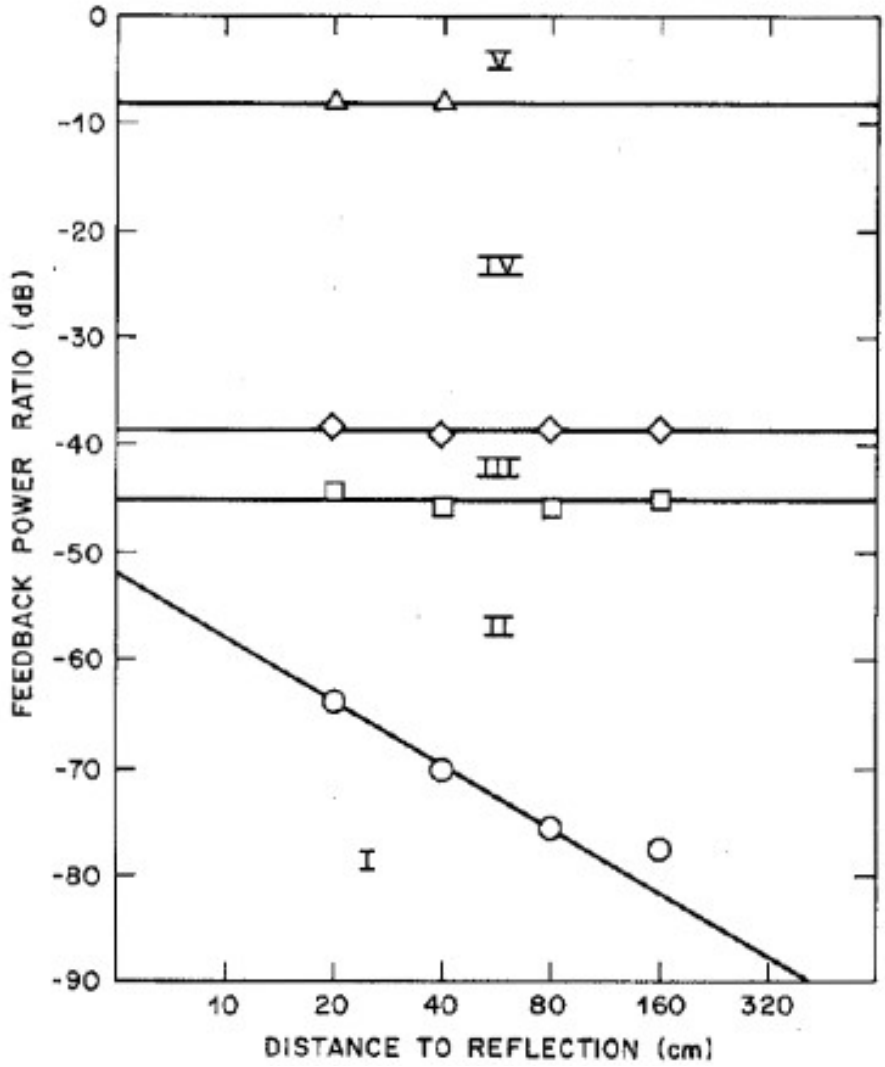

Figure 2.14: Dynamical regime of the laser response from optical feedback when varying the feedback ratio and the external cavity length. Taken from [105].

- **Regime III**: when the feedback level is close to 1 %, a narrow range of dynamics characterized by a narrow optical spectrum whatever the feedback phase takes place.

- **Regime IV**: it occurs for moderate feedback level (1 %). The laser output leads to the sidebands appearance on the optical spectrum that depend on the relaxation oscillation frequency. This behavior is known as coherence collapse.

- **Regime V**: this regime appears when the feedback ratio reaches (10 %), the laser output exhibits a single-mode operation, i.e., the laser dynamics is mainly dominated by narrow linewidth emission.

It is worth noticing that beyond the external cavity properties, the intracavity round-trip, the relaxation oscillation, and the phase-amplitude coupling (linewidth enhancement) play a key role in the dynamical properties of the laser [106].

For the optoelectronic feedback, the light emitted by the laser is detected by a photodiode and then injected again into the laser through the current injection [107]. Like optical feedback, optoelectronic feedback also induces a time delay. However, the optoelectronic and optical feedback differ because the optoelectronic feedback only influences the carrier population while optical feedback interferes with the complex electrical field.

In addition, experiments have highlighted interesting polarization dynamics in a single-mode VCSEL with optical feedback [108–110].Theoretical and numerical simulation have demonstrated two regimes of low frequency fluctuation in a VCSEL due to the competition between the two linear orthogonal polarization modes [111–114]. Experimental and theoretical analysis of the VCSEL response under weak optical feedback has been reported [115]. Random anticorrelated hopping between the polarization modes accompanied by rapid anticorrelated oscillations in the two orthogonal polarization modes intensities at the external-cavity frequency was reported [115], also leading to the first demonstration of the so-called coherence resonance due to the time-delayed feedback [116]

2.6.1 External optical injection in EEL

The entrainment between an external oscillator (master laser) and the intrinsic oscillator (slave laser) has attracted much attention due to its numerous applications. When the two oscillators are sufficiently close in frequency, i.e., the detuning frequency is small, the slave laser is entrained by the master laser leading to a well-known dynamics referred to as *optical injection locking*. In other words, optical injection locking is a technique where a slave laser is forced to adopt the frequency of a master laser by injecting the master laser output into the slave laser cavity. The optical injection locking has attracted much attention due to the improvement of the slave laser output properties through the transfer of coherence between the master and slave laser [21, 107]. Figure 2.15 maps the nonlinear dynamics of an EEL in the plane of the injection parameters (detuning and injection ratio) induced by single-mode optical injection. The optical injection locking is labeled as "s" and starts to appear at zero detunings in the mapping. The injection locking is observed for an extensive range of injection parameters.

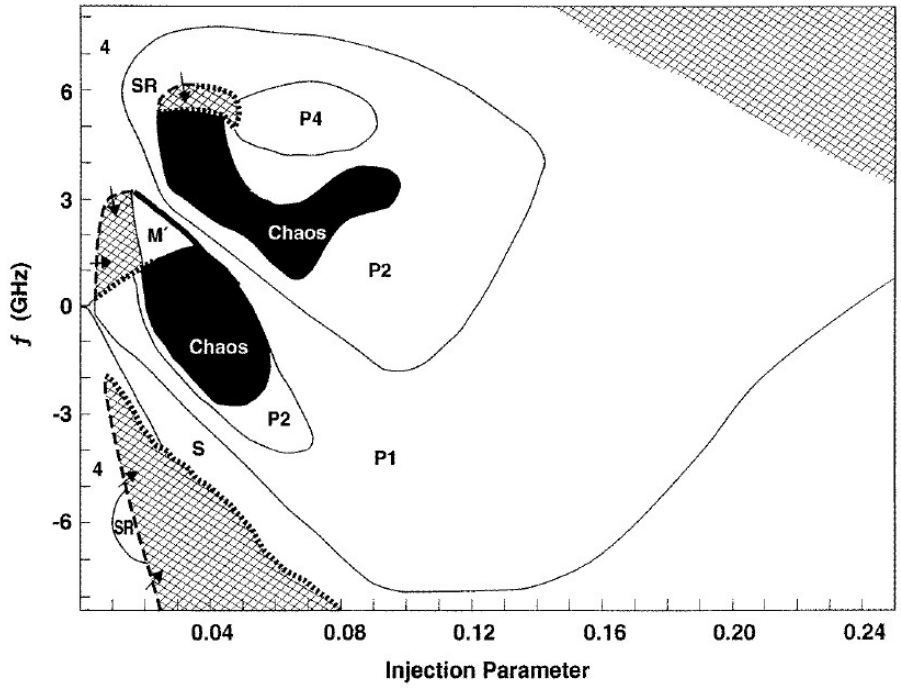

Figure 2.15: Mapping of nonlinear dynamics of EEL induced by single-mode optical injection. The laser output exhibits a variety of nonlinear dynamics, including optical injection locking, periodic dynamics, wave mixing, and chaotic dynamics. Taken from [117].

It can be seen that outside the injection parameters leading to the injection locking, no stationary dynamics is observed in the plane of the injection parameters. Depending on the injection parameters, the diode can bifurcate to four-wave mixing (4), subharmonic (SR) resonance, period one dynamics (P1), period-doubling (P2), period quadrupling (P4), multi-wave mixing (M), and chaos. Experimental, theoretical, and numerical simulations have shown excellent agreement for such nonlinear dynamics in a semiconductor laser with optical injection [118–122]. The bifurcations scenarios underlying the transition between the dynamical regions has been unveiled using numerical tools [123, 124]. The bifurcation analysis has shown that the transition between the injection locking and the subharmonic dynamic is due to the Saddle Node bifurcation. It was found that at a relatively high injection ratio, the Hopf bifurcation leads to the period one dynamics which is characterized by a regular pulsation at the relaxation oscillation frequency [123, 124]. The rich nonlinear dynamics induced by optical injection may bring new laser application in e.g., security, computing and sensing [107].

2.6.2 Polarization dynamics in VCSEL with optical injection

During the last decade, the nonlinear dynamics in VCSELs have attracted much attention due to the promising application that we will discuss in the next section[74, 125]. Due to their polarization properties, two types of linear optical injection can be realized in a VCSEL. Furthermore, as discussed early, the geometrical structure of the VCSEL leads to the emission along with two linear orthogonal directions. Most of the VCSELs are single-mode, i.e., emit typically along with one of the two linearly polarized orthogonal directions. As stated early, the polarization mode that contains the maximum gain is named dominant polarization mode, while the other one is named the depressed polarization mode. In the *parallel optical injection* the polarization of the injected light is parallel to that of the VCSEL (dominant polarization mode in free-running), whereas, in the *orthogonal optical injection* scheme, the polarization of the injected light is orthogonal to that of the VCSEL.

Beyond the nonlinear dynamics related to the EEL early discussed, orthogonal optical injection in a single mode VCSEL has induced additional polarization dynamics[73, 125–131]. The polarization dynamics in VCSEL have driven much attention since the observation of optical bistability in 1993 [132]. The operation conditions were chosen such that the VCSEL emits along with only one linear polarization mode in free-running. The authors have demonstrated optical switching and the corresponding bistability between the two polarization modes in a single-mode VCSEL under orthogonal optical injection [132]. Since then, the nonlinear dynamics and polarization properties are investigated through orthogonal optical injection.

Figure 2.16 shows the mapping of nonlinear dynamics in the plane of the injection parameters [77]. It is shown that the polarization switching is accompanied by the injection locking (IL) that extends mainly in the negative detuning. For positive detuning frequency, the polarization switching was accompanied by periodic dynamics (PD1). The squares in red indicate the switching points from the free-running polarization mode to the depressed polarization mode. In 2005, Sciamanna and Panajotov numerically unveiled new bifurcation sequences from the polarization switching [133]. It was found that depending on the injection parameters, a new solution called two polarization modes injection locking or elliptically polarized injection locking may appear before the polarization switching and destabilize to periodic or chaotic dynamics [133]. In addition, numerical simulations using

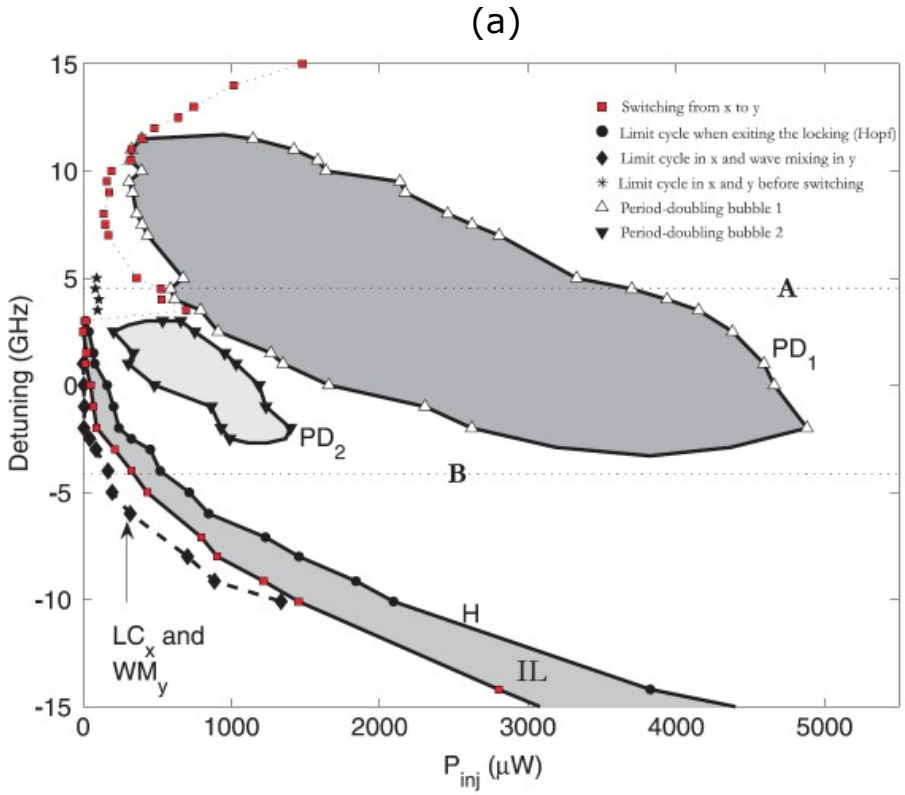

Figure 2.16: Mapping of nonlinear dynamics VCSEL induced by orthogonal optical injection. This mapping was obtained for fixed detuning frequency ($\Delta\nu = \nu_{ML} - \nu_{SL}$) when increasing the injected power. ν_{ML} and, ν_{SL} are the frequency of the master and slave laser respectively. Taken from [77].

bifurcation analysis software have been performed to reveal qualitatively different nonlinear dynamics, including wave mixing, limit cycle, subharmonic resonance and period-doubling route to chaos [74, 77].

Although parallel optical injection in VCSELs shows similarities to the optical injection in the conventional single-polarization EELs, some recent works have reported additional polarization dynamics [134]. Investigation of optical injection dynamics in a single-mode VCSEL subject to parallel optical injection has demonstrated various nonlinear dynamics [135, 136]. It was shown that for some injection parameters, the parallel injection might induce stable injection locking accompanied by the excitation of the normally depressed polarization mode [134–136]. It was also shown that by fine-tuning the injection parameters, the VCSEL might bifurcate to the periodic or chaotic dynamics generation in the two polarization modes. The bias current has been found to play a key role in these dynamics and their related bistability.

2.7 Applications of semiconductor laser nonlinear dynamics

The semiconductor lasers are now used in a wide range of applications ranging from optical communication to information security. Besides these applications, semiconductor lasers are very promising for many other applications.

2.7.1 Optical secure communication

As discussed in the introduction, semiconductor lasers are ubiquitous in the optical network telecommunication field due to the significant demand for large bandwidth. In addition to their use in communication systems, semiconductor lasers have been found to ensure information security through chaos synchronization. The chaos synchronization system is based on the optical injection scheme described in sections 2.6.1 and 2.6.2. Chaos synchronization uses two semiconductor lasers with similar structures. Chaotic operation is induced in the master laser through the optical feedback as described in section 2.6. The master laser output (chaotic field) is then re-injected in the slave laser cavity. When the two similar lasers are in the same condition (temperature, bias current), the slave laser output displays chaotic dynamics synchronized to that of the master laser. It is well established that the operation parameters and choice of laser system play a key role in ensuring the security in the encrypted message since only authorized users have knowledge of the parameters that enable synchronization[107, 137–139] .

2.7.2 Random number generation

The strong demand for security in data exchange and network communication has motivated the development of physical random number generation. High secure transmission requires a higher bit rate of random number generation that can not be achieved with conventional means. Such random numbers should not be reproducible, which is not guaranteed with pseudo-random algorithms. To this end, one of the recently suggested techniques of random number generation is based on the complexity of semiconductor lasers. Random bit generation from 1.7 to 140 Gb/s have been reported in semiconductor lasers thanks to the improvement of the chaos bandwidth [140–142]. Interestingly, in 2014, random number bit speed to 100 Gb/s was demonstrated using the polarization chaos of a free-running

VCSEL [143]. Very recently, spatio-temporal dynamics resulting from interference of many lasing modes have been applied to generate a random bit rate of 250 Tb/s [144].

2.8 Conclusion

This chapter has shown the fundamental physics of lasers and the mechanism underlying the lasing effect. More specifically, we have paid particular attention to two types of semiconductor lasers, i.e., EELs and VCSELs. We first provide an overview of the specific structures of the EELs and VCSELs, leading to their unique output properties. Section 2.4.2 and 2.5.3 show how the mathematical model results from the semiconductors laser structures. Due to their geometrical structure, VCSELs may exhibit multi-transverse mode operation linearly polarized along with two orthogonal directions in a wide range of operation conditions. At the same time, the EELs usually emit with a single polarization mode. We have discussed the different mechanisms of switching between the orthogonal polarization modes. Depending on the way the polarization switching (PS) is manifested, three types of PS are reported: type I PS, type II PS, and type I and II. These types of PS strongly depend on the operating conditions, such as bias current and temperature. We finally discussed the different techniques (external modulation feedback and external injection) to induced complex dynamics in the semiconductor lasers. Depending on the external perturbation condition, various nonlinear dynamics can be observed in the laser's output. The polarization dynamics of VCSELs not only add new scenarios for nonlinear laser dynamics but also induces dynamics that do not occur in otherwise single polarization mode lasers.

3

Optical frequency comb

Contents

3.1 Principle of optical frequency comb 44

3.2 Physical systems generating frequency comb 48

3.2.1 Electro-optics modulators 49

3.2.2 Microresonators 52

3.2.3 Semiconductor lasers-based frequency comb 55

3.2.4 Gain Switching lasers 56

3.3 Application of frequency combs 58

3.3.1 Distance measurements and laser ranging: LIDARs 58

3.3.2 Dual-comb spectroscopy 59

3.3.3 Optical frequency comb as communication sources 61

3.4 Conclusion 61

The optical frequency comb is a series of optical frequency lines with a fixed repetition rate and phase coherence between the comb lines. The optical frequency comb is becoming ubiquitous in modern technologies such as spectroscopy, microwave photonics, ranging or LIDAR, and optical communication. The discovery was rewarded by the Nobel prize to John L. Hall and Theodor W. Hansch in 2005.

This chapter reviews the principle of optical frequency comb generation and the key parameters such as carrier-envelope offset, comb spacing (repetition rate), and the linewidth of the comb lines. We also analyze some physical systems generating optical frequency combs. Most importantly, we highlight the main difference between the different systems and their promising applications. We finally describe the principle of optical frequency comb applications to LIDAR, dua-comb spectroscopy, and optical communication.

3.1 Principle of optical frequency comb

The generation of optical frequency comb originates from 1964 when Hargrove, Fork, and Pollack introduced the first mode-locked laser [145]. Since their works, many other mode-locked lasers system, including passively Q-switched mode-locked [i] [146], and continuous-wave (CW) mode-locked have been proposed [147]. The rapidly evolving developments of frequency combs during the past decade have revolutionized many technologies, as it can be seen in Fig.3.1 [148]. Fig.3.1 shows how fast the frequency comb technologies have grown. From the mode-locked femtosecond laser, many applications interconnected between them were launched. Section 3.3 of this chapter will be devoted to the development of some of these applications.

The term mode-locked is related to the phase relation between the comb lines. Indeed, unlike the classical multimode laser, where the phase and the amplitude of the individual mode fluctuate randomly, the mode-locked laser generating a frequency comb exhibits a coherent phase relationship between the comb lines.

As a result of phase-locking, the mode-locked laser output generates an ultra-short pulse repeating periodically in time. The envelope of the electrical field characterizes the pulse train and its corresponding carrier, as shown in Fig.3.2. When considering a single pulse

[i] The Q-switched mode-locking is the regime of passively mode-locked laser where the intracavity pulse energy oscillate due to the dynamic instability (also called Q-switching instability) related to the undamped relaxation oscillations

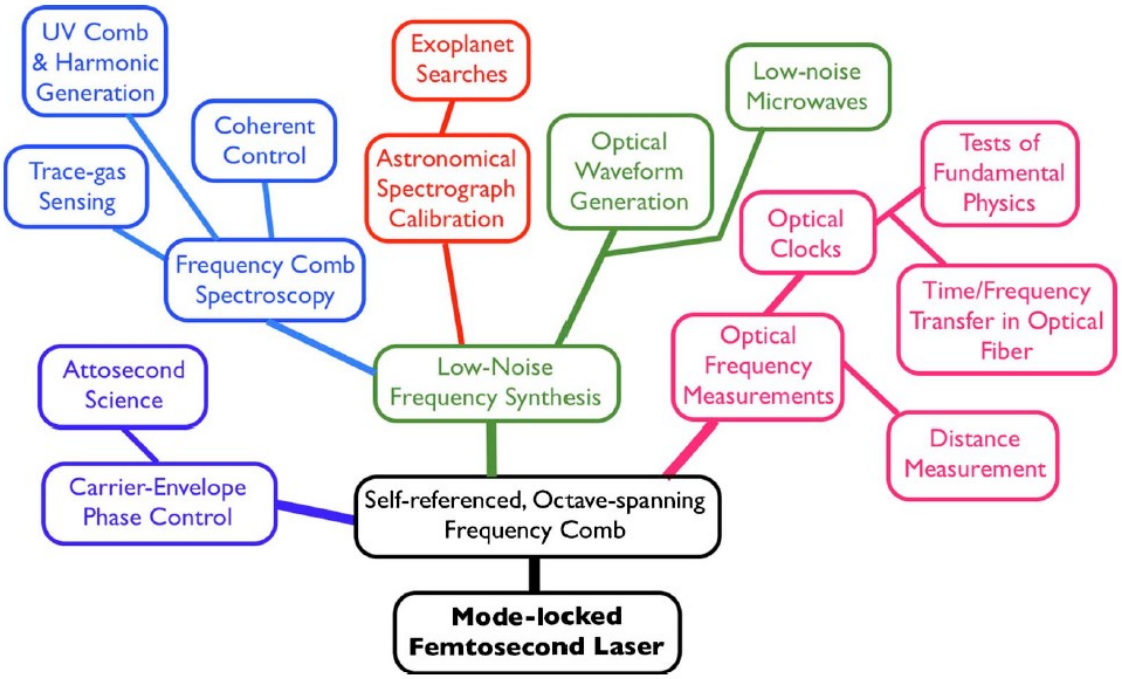

Figure 3.1: Frequency comb development from the femtosecond laser. Taken from [148].

as shown in Fig.3.3, the corresponding Fourier transformation is a continuous spectrum centered at the carrier's frequency, f_c. The temporal duration of the pulse at half maximum and the corresponding spectral width at half maximum are linked by the time-bandwidth product (TBP) through the following equation:

$$TBP = \Delta\tau_r \Delta\vartheta \tag{3.1}$$

where $\Delta\tau_r$ and $\Delta\vartheta$ are the temporal pulse duration at half maximum and the corresponding spectral width at half maximum, respectively. The time-bandwidth product allows determining the lowest pulse duration for a given optical spectrum. The lowest pulse duration corresponds to the minimum time-bandwidth product and is named *Fourier limit*. Low time-bandwidth product (often below 0.5) means high-quality pulses. The Fourier limit implies that the time-bandwidth product is at its minimum and there is no chirp. The minimum time-bandwidth product depends on the pulse shape, e.g., the Fourier limit of the sech^2-shaped pulses and Gaussian-shaped pulses are ≈ 0.315 and ≈ 0.44, respectively. The Fourier limit is particularly important in optical communication because the chromatic dispersion is then minimized and the distance of transmission in the fiber is maximized when the transmitter operates close to the Fourier limit.

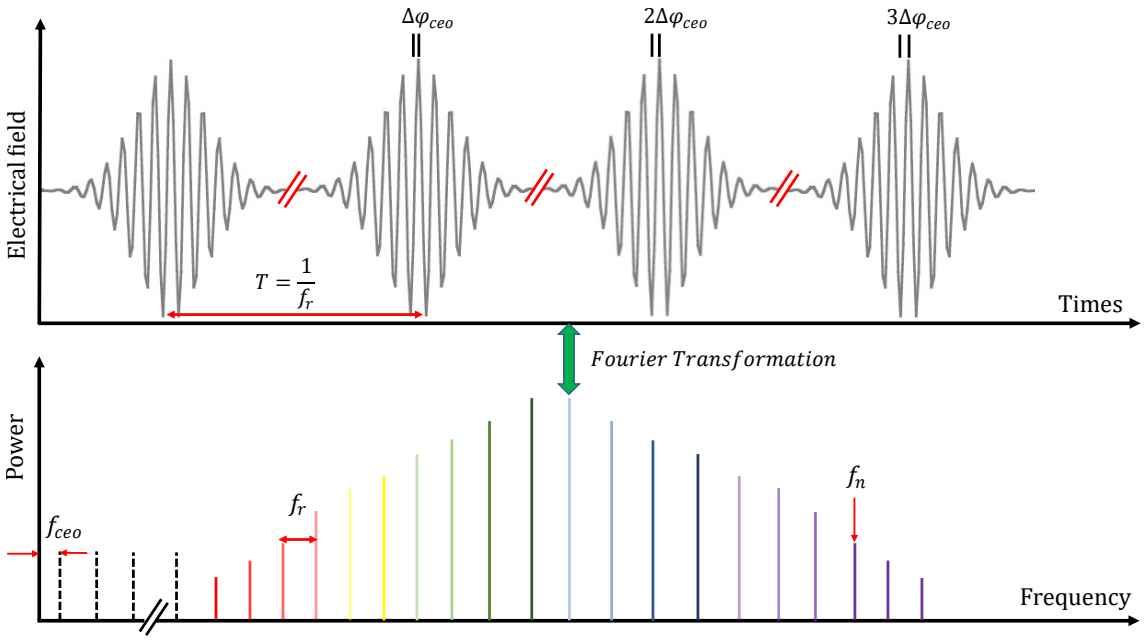

Figure 3.2: Principle of the optical frequency comb. The time-domain representation of the mode-locked laser output is ultra-short pulses with period T. The Fourier transformation in the frequency domain corresponds to a frequency comb with repetition rate $f_r = \frac{1}{T}$. A phase shift between the envelope of the electrical field and its corresponding carrier induces an offset in the frequency domain, $f_{ceo} = \frac{\Delta\phi_{ceo}}{2\pi} f_r$. This carried-envelope offset is a translation of all the comb lines from their harmonics frequencies nf_r.

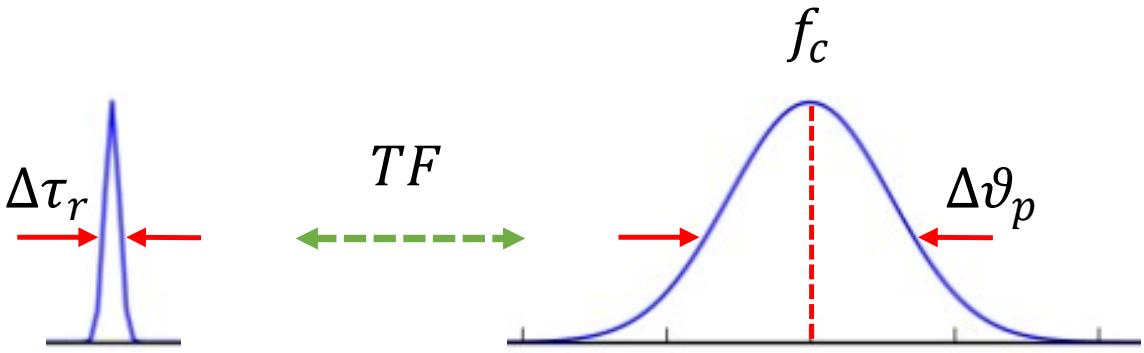

Figure 3.3: A single pulse in the time domain and the corresponding Fourier transformation in the frequency domain. The time-bandwidth product is computed using the pulse duration and the corresponding spectral width both at half maximum.

When considering a pulse train, i.e., the mode-locked laser emits a pulse periodically, as shown in Fig.3.2. The pulses train envelope's period, which corresponds to the round-trip time inside the laser cavity, can be expressed as:

$$T = \frac{L}{v_g} = \frac{1}{f_r} \tag{3.2}$$

where L and v_g are the cavity length and the group velocity, respectively. The dispersion inside the laser cavity induces a pulse-to-pulse phase shift between the envelope and the corresponding carrier. The phase shift can be written as:

$$\Delta\phi_{ceo}(t) = \phi_{ceo}(t) - \phi_{ceo}(t - T) \tag{3.3}$$

By doing the Fourier transform of the pulses train, the corresponding spectrum is composed by the multiple frequencies evenly spaced with a common phase relationship called *optical frequency comb*. The frequency separation between two consecutive comb lines is called *comb spacing* or *comb repetition rate*, f_r. The comb spacing is the inverse of the time-round trip inside the laser cavity, as it can be seen in equ.3.2. The regular change in the phase between the carrier and the envelope induces an offset in the optical spectrum called *carrier-envelope offset (CEO)* which can be expressed as:

$$f_{ceo} = \frac{\Delta\phi_{ceo}}{2\pi} f_r \tag{3.4}$$

In the frequency domain, the position of each comb line is described using the comb spacing (the repetition rate of the frequency comb) and the carried-envelope offset through the following equation:

$$f_n = f_{ceo} + n f_r \tag{3.5}$$

where n is a large integer. The carried-envelope offset can be suppressed ($f_{ceo} = 0$) when the phase shift is constant, ($\Delta\phi_{ceo} = 0$). The carried-envelope offset plays a key role in the stabilization of the comb lines.

- **Stability of the comb lines**

The variations in laser cavity properties, e.g., temperature, cavity length, and acoustic fluctuation, induce fluctuation in the comb spacing. The instability in the comb spacing has

embarrassed the growth of mode-locked laser technology and its use for several applications. High stable comb lines is one of the main requirements for a frequency comb to be used as a measurement tool. However, optical frequency comb-based mode-locked laser can be stabilized by locking the f_r to a high quality RF reference using a phase lock loop [149].

- **Range of comb spacing**

As presented early, the comb spacing of the mode-locked laser is linked to the cavity properties. The comb spacing is varied only using the cavity properties, i.e., the cavity length and the temperature inside the cavity. Usually, the comb spacing of a mode-locked laser is measured using a CW laser whose frequency (f_{cw}) is known. The resulting mixing between the output of the mode-locked laser and the CW is measured with a fast photodiode with bandwidth f_{bw}. The radio frequency signal spectrum is then composed by the harmonics of the comb spacing f_r and also by the optical beat-note between the reference signal (CW laser) and the comb lines frequency position given by the following relation [149]:

$$f_{bn} = |f_{cw} - f_{ceo} - nf_r| \tag{3.6}$$

The repetition rate of a mode-locked laser frequency comb is between tens of MHz to several GHz. The tunability of their comb spacing remains a crucial problem because it depends on the cavity length and the temperature of the gain medium.

3.2 Physical systems generating frequency comb

The limitations of the mode-locked laser frequency combs, such as difficulty controlling the comb spacing, generation of pulses with unstable energy, the timing jitter (random fluctuations in pulse positions), uneven comb spacing, and the carrier-envelope offset, have limited their use in several applications. Extensive theoretical and experimental studies have focused on developing a new optical frequency comb solution to overcome the limitation of the mode-locked lasers. This section will provide an overview of the most common technique of frequency comb generation.

3.2.1 Electro-optics modulators

The optical frequency comb generation based on the electro-optic modulators has been adopted as an alternative to the limitation of the mode-locked lasers frequency combs. This technique is relatively simple because the frequency comb is generated by directly modulating a high-quality single frequency CW laser. The optical frequency comb generation process is linked to the electro-optic effect.

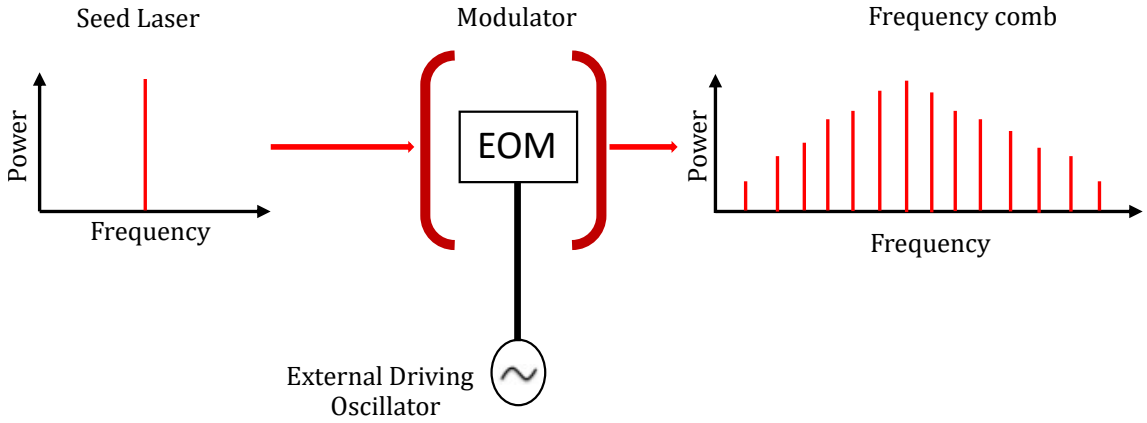

Figure 3.4: Basic experimental setup for optical frequency comb generation with an Electro-optic modulator. The output of a high quality cw laser is injected into the modulator driven with an external RF signal.

The electro-optic effect is related the change of the refractive index when a nonlinear material is submitted to a strong electrical field. The electro-optics effect includes several phenomena, such as the Pockels effect (linear electro-optic effect) and the Kerr effect. The Pockels effect modifies the refractive index of the material with the applied electrical field. In contrast, the Kerr effect shows a change in the refractive index proportionally to the square of the electrical field. The transparent materials displaying the Pokels effect are the perfect candidate for building a modulator. The output power of a high-quality CW laser is injected into the electro-optic modulator (EOM), as shown in Fig.3.4. An RF signal is then applied to drive externally the modulator, which modulates the material's refractive index.

An optical frequency comb can be generated using a phase modulator or amplitude modulator (Match-Zehnder Modulator). Frequency comb generation with an electro-optic modulator is based on the phase modulation of the input of a CW laser. An RF signal generator drives the modulator. At the output of the modulator, the CW laser output acquires a new phase and field whose Fourier transform leads to an optical frequency comb.

Due to the sinusoidal form of the applied voltage, the frequency combs based on phase modulation present two regions of comb lines with maximum amplitude at the wings of the spectrum [150] making the resulting comb very asymmetric. A fine-tune in the voltage of the modulator permits controlling the position of these maxima. Furthermore, the number of resulting comb lines can be tailored with the modulation index and the voltage, but the asymmetric of the comb remains [150]. The frequency comb-based phase modulator bandwidth is very narrow and decreases when the modulation frequency (comb spacing) decreases. However, the modulator can acquire other functionality by adding interferometer, polarizers, and quarter-wave plates [150]. A polarization modulator can be obtained by adding one or two polarizers to the phase modulator. To obtain an intensity modulator, a quarter-wave plate is added after the polarization modulator and then the set is placed between two crossed polarizers. Finally, the Mach–Zehnder modulator can be created by introducing an electro-optic material within an interferometer, usually a Mach–Zehnder interferometer. An interference effect takes place and then leads to a low driving voltage.

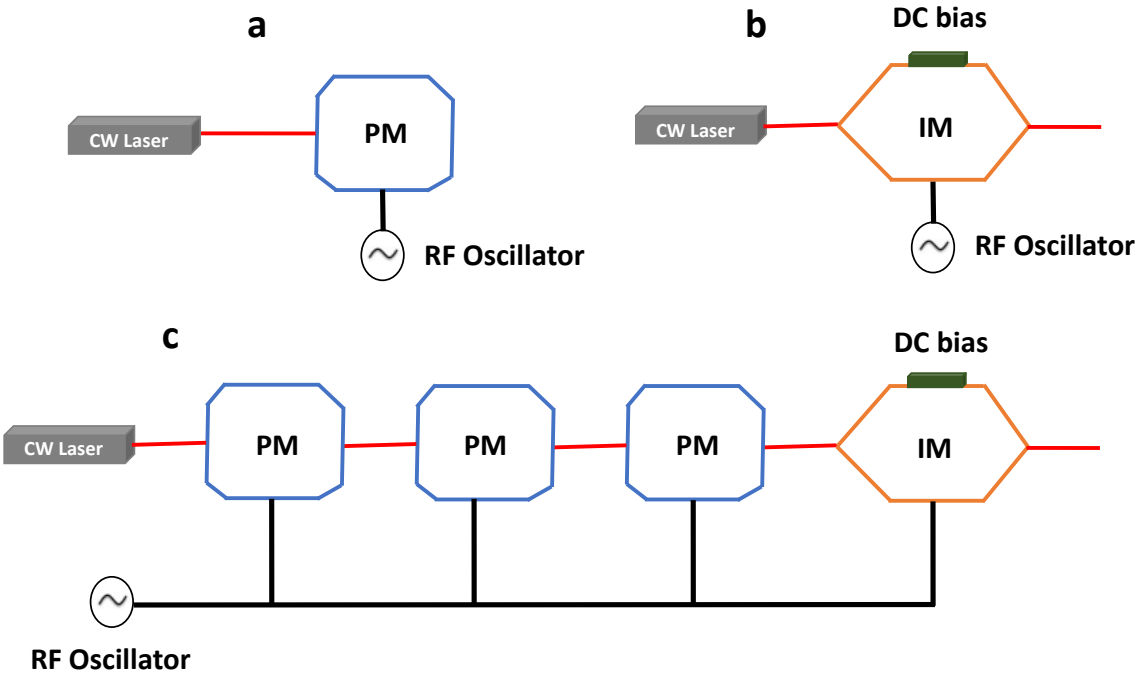

Figure 3.5: Schematic of the different experimental setup for optical frequency comb generation based on Electro-Optic Modulator. (a) Phase modulator (PM), (b) Intensity modulator (IM), and (c) Association of several phase modulators with an intensity modulator.

Match-Zehnder Modulator has two arms in which a voltage is applied [Fig.3.5 (b)]. Compared to the phase modulator [Fig.3.5 (a)], the voltage is an additional degree of

freedom for the Match-Zehnder Modulator, which can be used to control the flatness of the comb.

- **Electro-optic modulator inside an optical resonator**

Frequency comb generation using an electro-optic modulator is quite limited in bandwidth. One way to overcome this limitation consists in placing the modulator inside an optical resonator as shown in 3.4. The round-trip of the comb lines inside the resonator through the modulator creates a cascade effect increasing the number of comb lines. Frequency comb with a total bandwidth of several THz has been demonstrated by placing a phase modulator inside an optical resonator [151, 152]. Although a broadband optical frequency comb can be obtained, the lack of flatness remains a crucial obstacle that has to be solved.

- **Association of phase modulators with an intensity modulator**

The experimental setup using only one modulator is inefficient when a flat and high repetition rate frequency comb is required. One of the comb-based modulator's main limitations is the fluctuation in the comb lines, i.e., some comb lines can have very low intensity. Moreover, the association between a phase modulator and an intensity modulator improves the comb flatness and increases the comb spacing. The modulators (phase and intensity modulators) are driven with the same RF signal. Recent work has demonstrated flat optical frequency comb using such configuration [153, 154]. Associating only one phase modulator and an intensity modulator is insufficient to generate a wide frequency comb with a high repetition rate. As seen in 3.5 (c), cascade phase modulators with an intensity modulator can be used to achieve large comb spacing while remaining wide bandwidth. The phase modulator is used to increase the number of comb lines by a factor proportional to the number of modulators through successive injection of the generated comb. In general, the number of phase modulators is between two and four. The intensity modulator is added to improve the flatness of the frequency comb at the output of the last phase modulator. The phase shift between the electro-optic modulator has to be taken into account. Broad optical frequency comb with a bandwidth of 380 GHz at a wide repetition rate of 10 GHz within 1 dB from the maximum amplitude has been proposed in the recent work [155, 156]

Despite these limitations, the electro-optic modulator provides several advantages compared to the classical comb source, e.g., mode-locked lasers. The first advantage is the tunability

of the comb. Indeed, the resulting comb from the modulator is tunable because the electro-optics modulator generally has a large bandwidth of operation. Moreover, the comb repetition rate can be easily tuned directly from the RF signal generator. Of particular interest is the very low linewidth of the electro-optic modulator frequency comb. As an RF signal generator is used to drive the modulator, comb lines linewidth less than 1 Hz can be demonstrated.

3.2.2 Microresonators

Optical frequency comb generation using the mode-locked laser and electro-optic modulator is limited in repetition rate. As stated above, the repetition rate of an optical frequency comb-based electro-optic modulator is limited by its bandwidth which is less than typically 100 GHz. Large comb spacing is needed for applications that require access to the individual comb lines, such as optical waveform synthesis [157], high-capacity telecommunications or astrophysical spectrometer calibration [158].

- **Principle of micro-comb generation**

In 2007, a new physical system generating a high repetition rate frequency comb using a microresonator has been demonstrated [159]. The combination between the parametric conversion process and four-wave mixing leads to a broad optical frequency comb with a repetition rate equal to the free spectral range of the cavity [160, 161]. Optical frequency comb generation using a microresonator requires the following conditions:

- Cavity medium that exhibits third-order nonlinearity,
- High quality-factor (Q) cavity,
- Low dispersion in the cavity.

Figure 3.6 shows the principle of optical frequency comb generation using high-quality factor (Q) microresonators. The microresonator is pumped with the output of a tunable CW laser after amplification through Erbium-Doped Fiber Amplifier (EDFA) as shown in Fig.3.6 (a). When a resonant mode of the microresonator matches with the CW laser frequency, the parametric frequency conversion annihilates two pump photons (from the CW laser whit angular frequency ω_p) and generates a new pair of photons called signal at frequency upshifted ω_s and idler at frequency downshifted ω_i. It is worth noticing that

in the frequency comb generation using a microresonator, the CW pump laser is part of the resulting comb. The conservation of energy implies that the frequency difference between the two generated photons and the pump is the same as shown in Fig.3.6 (b). Interestingly, the parametric conversion process is strongly enhanced, giving rise to an efficient sideband generation when the frequencies corresponding to the signal and idler match a mode of the microresonator. A cascade four-wave mixing (FWM) occurs where the two generated photons (signal and idler at different frequencies) served as the pump to produce higher order of sidebands through a further parametric conversion process. This process is known as non-degenerate FWM as shown in Fig.3.6 (b).

When the two generated photons and the pump have a comparable power level inside the resonator, the cascade FWM becomes dominant and then leads to further sidebands generation. Interestingly, the signal and idler have a fixed relation phase with respect to the pump source. The cascade FWM process, together with the fixed relation phase, the comb lines, and equal separation between the frequency lines, combine to generate an optical frequency comb.

- **Comb bandwidth and repetition rate**

The bandwidth and repetition rate are critical parameters characterizing an optical frequency comb. The dispersion inside the cavity limits the bandwidth of a microresonator-based optical comb. The variation in the free spectral range of the cavity is indeed due to the dispersion which decreases the efficiency of the parametric conversion process. In the presence of dispersion and acoustics fluctuation, the degenerate and non-degenerate FWM is less efficient because the comb modes are not fixed with respect to the cavity modes. Interestingly, besides the dispersion limiting the comb generation process, another physical phenomenon allows overcoming that limit. Effectively, when the injection in the microresonator is of a higher power, the Kerr nonlinearity takes place. The Kerr nonlinearity then leads to a frequency pulling that extends the comb bandwidth beyond the dispersion limit leading to octave-spanning bandwidths [160].

The basic principle of microresonator frequency comb generation leads to a large comb spacing compared to electro-optic modulators. Indeed, frequency comb with a total bandwidth of hundred of THz and repetition rate close to 1 THz has been demonstrated [159–161]. Although wide comb spacing is useful for several applications, as we mentioned above, a tunable repetition rate is also needed for many applications such as dual-comb

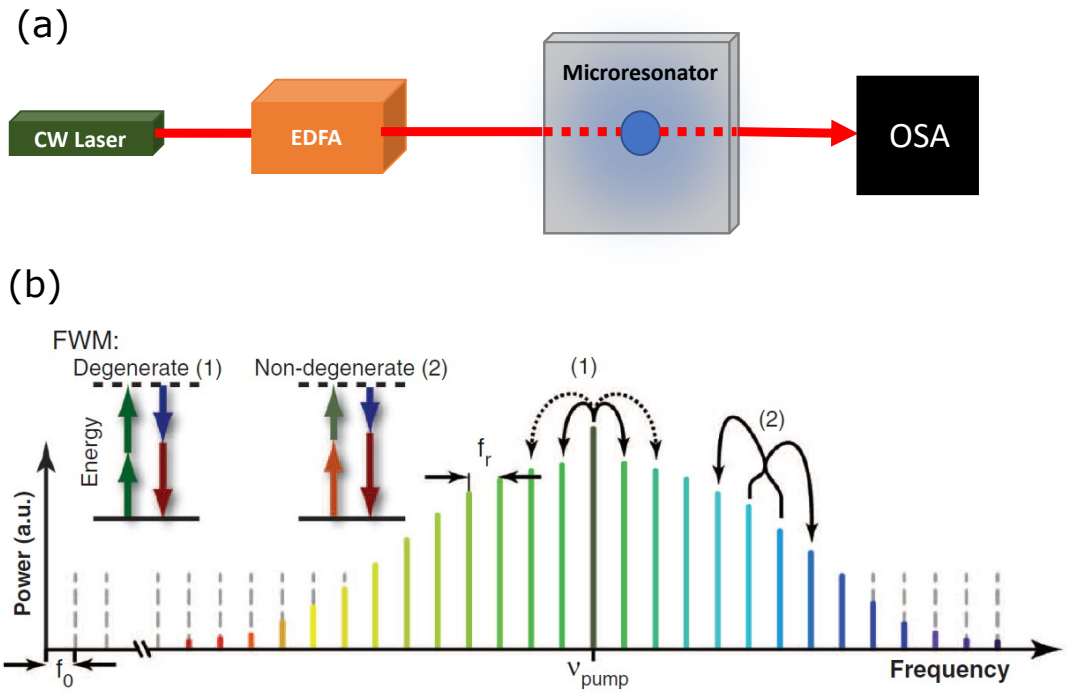

Figure 3.6: Principle of optical frequency comb generation using a microresonator. (a) high quality-factor (Q) microresonator is injected with a CW tunable laser. High power injection and the coupling of the pump laser with a resonant mode of microresonator mode allow producing the parametric conversion process. The parametric conversion process occurs through the degenerate and non-degenerate Four-Wave Mixing. (b) Optical frequency comb characterized by the repetition rate f_r (free spectral range of the microresonator) and the carrier-envelope offset (f_0) (see section 3.1), taken from [161]. The comb is generated by combining degenerate and non-degenerate four-wave mixing processes. The degenerate FWM refers to a situation where two photons from the pump source at the same frequency are converted into a pair of photons equally spaced with respect to the pump sources. In contrast, in the non-degenerate FWM, all the photons have different frequencies. The cascade FWM leads to strong sideband generation at the phase relation phase between them.

spectroscopy and optical communication. The comb spacing of the microresonator-based frequency comb is fixed by the free spectral range of their cavity, but some techniques have been recently employed to control it. Different microresonator geometries and materials have led to comb spacing ranging from 13 GHz (microresonator radius of 4.85 mm) [162] up to 850 GHz (microresonator radius of 40 µm) [160]. For many applications, the stability of the comb spacing is also crucial. The stabilization of the frequency comb from the microresonator is more complex than the optical frequency comb generated from the

electro-optic modulator. One of the main drawbacks of the microresonator comb is its large linewidth (several kHz to MHz) compared to the electro-optic modulator comb (linewidth can be lower than 1 Hz).

3.2.3 Semiconductor lasers-based frequency comb

The past decade has seen the development of several approaches for generating frequency combs. These comb generation processes involve much-complicated setup and engineering to control the comb stability, comb spacing, and bandwidth leading to a significant increase in power consumption and fabrication cost. Semiconductor lasers provides advantage of small size and low power consumption. This subsection reviews some semiconductor lasers generating optical frequency comb.

- **Quantum cascade lasers**

Very recently, optical frequency comb generation using semiconductor lasers has been investigated. One of the first semiconductor lasers studied was the quantum cascade laser. In 2012, it was demonstrated that the broadband quantum cascade laser modes in free-running can be phase-locked giving rise to an optical frequency comb operation [163]. Like the case of microresonators, the physical mechanism underlying the frequency comb generation in quantum cascade lasers is attributed to a strong third-order nonlinearity (Kerr effect) in the gain medium. In fact, the Kerr effect leads to a phase-locking mechanism through a cascade four-wave mixing process. Since the first demonstration, phase-locking in quantum cascade lasers has attracted much attention leading to the soliton observation [164] and the extension of the comb bandwidth from Mid-IR to THz frequency range. Interestingly, a theoretical study has used Maxwell-Bloch equations to provide a further understanding of the quantum cascade lasers frequency comb generation process [165]. Unfortunately, unlike the electro-optic modulators, the comb spacing of the quantum cascade lasers comb is determined by the cavity length and the group refractive index. Comb spacing (e.g., 6-mm-long devices, corresponding to comb spacing of $\approx$ 7.5 GHz [166]) can be decreased when increasing the cavity length. Another drawback is the large comb linewidth, typically from several kHz to MHz.

- **Quantum dot lasers**

The nonlinear dynamics in quantum dot lasers has driven a lot of attention due to their compactness, low cost, and energy-efficiency, which make them the perfect laser candidate for many applications [167–175]. Mode locking have been demonstrated using two-section lasers with an integrated intracavity quantum dot saturable absorber. Most importantly, several recent studies have reported very wide optical frequency comb dynamics using quantum dot lasers [176–178]. Frequency combs with bandwidth covering the band C and L are indeed demonstrated [176, 179]. Like for quantum cascade laser, the comb spacing of the quantum dot lasers frequency comb (tens of GHz) is fixed by the cavity properties. Optical injection into a quantum dot laser has been recently used to improve their comb flatness and bandwidth [180]. As we will see in the next section, an important parameter for optical communication is the coherence of the comb lines. Compared to the electro-optic modulator where the linewidth RF beat note can be less than 1 Hz, the one of the quantum dot lasers has been found to range from several kHz to MHz [181].

Besides the quantum dot and quantum cascade lasers, frequency comb dynamics have been observed in various semiconductor laser systems, including mode-locked integrated external-cavity surface-emitting lasers (MIXSELs) and quantum dash lasers. Unfortunately, for most of these semiconductor lasers, the comb spacing is very hard to tune without changing the cavity properties. Recent activities have paid a lot attention to a new optical frequency comb generation process based on externally driven semiconductor lasers since it provides an easy solution to harness the comb properties.

3.2.4 Gain Switching lasers

The gain switching technique was initially used to generate a short optical pulse in a laser by modulating its gain. The gain switching technique involves driving the laser diode through a modulated pump current. Figure 3.7 shows the principle of gain switching of a laser diode leading to an optical frequency comb. The first observation of optical frequency comb using gain switching technique was performed in Discrete Mode lasers (DMLs) in 2009 [182]. Since then, the optical comb generation by gain switching of edge-emitting lasers (EEL) has been studied extensively [183–185]. More specifically, some contributions have analyzed the phase noise, linewidth, the jitter and the bandwidth, which are part of the key parameters for many applications, including dual-comb spectroscopy and optical data communication [186–188].

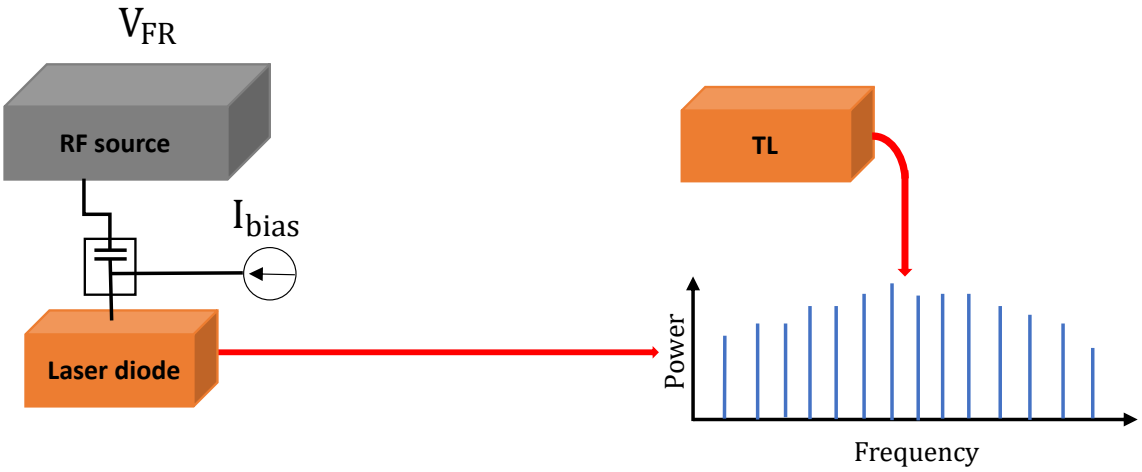

Figure 3.7: Principle of gain switching of semiconductor lasers. A single-mode laser diode's output is externally driven with an RF source to generate short pulses corresponding to an in the frequency domain. The generated comb can be further controlled by injecting optical field from a tunable laser (TL).

Recently, optical injection using a single-mode laser in the frequency comb generated by gain switching has improved the properties of a very noisy optical comb. The phase noise, time jitter, frequency chirp, and relative intensity noise (RIN) are indeed reduced by optical injection [189, 190]. Beyond the comb spectral quality, the optical injection has influenced the nonlinear dynamics in the gain-switched-based frequency comb. Furthermore, harmonics comb leading to the decrease in the initial comb spacing, and complex dynamics are observed in a large area in the plane of the injection parameters (injected power and detuning frequency) [190].

Of particular interest is the generation of two polarization frequency comb in a vertical-cavity surface-emitting laser (VCSEL) using the gain switching technique [191–193]. The optical injection has been found to induce rich nonlinear polarization dynamics contributing to increase the polarization comb bandwidth [191–193]. Experimental and theoretical investigation have used the polarization of the injected light to control the comb properties such as comb bandwidth, amplitude comb lines and harmonics comb dynamics [192]. Unfortunately, the performance of the comb generation depends strongly on the modulation parameters [194]. Especially for the VCSEL, the birefringence must be a rational fraction of the modulation frequency to avoid the unlocking between the polarization combs [193].

3.3 Application of frequency combs

Optical frequency combs have revolutionized several scientific fields, including optical data communication, dual-comb spectroscopy, optical metrology, astronomical spectrograph calibration, microwave waveform synthesis, and optical clocks. Optical comb technologies are becoming mature, and in the meantime, the number of promising applications is increasing. The frequency combs are the perfect candidate for all the above applications due to their large number of lines, stable comb spacing, narrow linewidth, and common phase relationship between the comb lines. Each optical frequency comb application required specifics properties that cannot be satisfied by only one comb generation technique.

3.3.1 Distance measurements and laser ranging: LIDARs

LIDAR stands for light detection and ranging. LIDAR is a technique of distance measurement based on light properties analysis. The first demonstration of LIDAR technology using an optical frequency comb was in 2000 [195]. Since then, the optical comb is becoming crucial in LIDAR development. In the conventional LiDAR technology, a series of pulses train encounters an obstacle, and then a part of the light is reflected to the emitter (laser). The distance is then deduced by measuring the delay between the emission and the detection time through signal processing. Two techniques can be used to extract the distance information: direct time-of-flight measurement and linear optical sampling (LOS) measurement. In the time-of-flight, the distance measurement employs a single comb split in two parts. The distance is determined by measuring the delay between the reflected beam (green) and the reference beam (red). In the direct time-of-flight measurement, the maximum distance resolution is limited by the resolution bandwidth of the photodiode. However, the dual-comb LIDAR allows overcoming this limitation through linear optical down-sampling. In dual-comb LIDAR, an interference between two optical frequency combs named comb 1 (green part) and comb 2 (blue) at slightly repetition rate f_r and $f_r + \Delta f$, respectively, allows extracting the information from an obstacle as shown in Fig. 3.8. The time corresponding to the repetition rate of comb 1 and comb 2 is T_r and $T_r + \Delta T$, respectively. As seen in Fig. 3.8, in the distance measurement, comb 1 (signal pulses train) is separated into two parts.

One part encounters the obstacle and is reflected in the emitter, while the second part

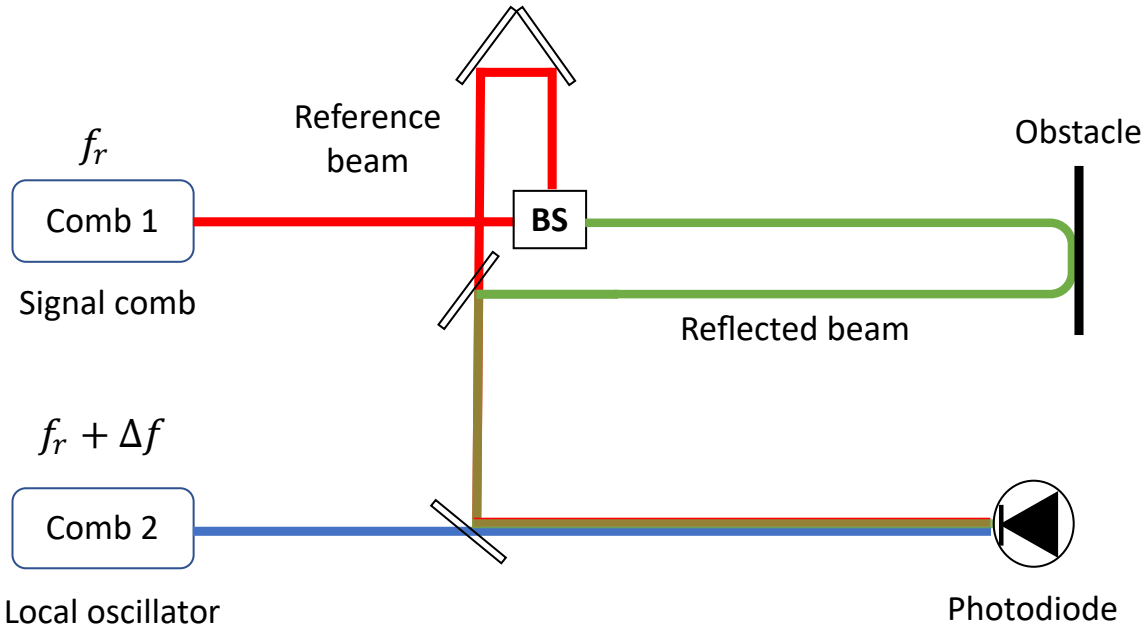

Figure 3.8: Principle of LIDAR-based dual-comb. Two phase-locked comb (Comb 1 and comb 2) at slightly repetition rate (f_r and $f_r + \Delta f$) are used to measure a distance of an obstacle with a photodiode. Comb 1 is used to interact with the obstacle, while comb 2 acts as a local oscillator. A beam splitter allows separating the signal comb (comb 1) in two-part, red and green.

acts as reference pulses. The time delay (Δt) between the reflected and the reference pulses is measured by mixing them. The optical cross-correlation between the reflected pulses (green) and the local oscillator (blue) allows extracting the distance information.

LIDAR technology is used in various fields such as measurement of the speed and direction of the wind as a function of the altitude, the detection of threats in the military context, speed measurement by the police officers, localization of obstacles for the future autonomous cars, drone, robots, etc.

3.3.2 Dual-comb spectroscopy

Dual-comb spectroscopy is one of the main applications of optical frequency comb that has driven significant attention last decade. Compared to the conventional spectroscopy techniques, dual-comb spectroscopy provides a high signal-to-noise ratio (SNR) overbroad optical bandwidths. Figure 3.9 shows the principle of the dual-comb spectroscopy. The dual-comb spectroscopy is based on multi-heterodyne beating of two frequency combs at a slight different comb spacing f_r and $f_r + \Delta f$ for comb 1 and comb 2, respectively,

where Δf is the difference between the comb spacing of the two combs. In most of the dual-comb spectroscopy measurements, one comb acts as a local oscillator, and the other is used to interrogate the sample as shown in Fig. 3.9. The two combs can also be used to interrogate the sample [196]. Before interrogating the sample, comb 1 and comb 2 are mixed to create a power spectrum evenly separated by the frequency offset (Δf) between the two combs. This power spectrum serves as a reference (reference signal in Fig. 3.9). After interrogating the sample with comb 2, each line of comb 1 beats with all the lines in comb 2 (sample signal in Fig. 3.9). The multi-heterodyne beat allows retrieving the information regarding the sample absorption.

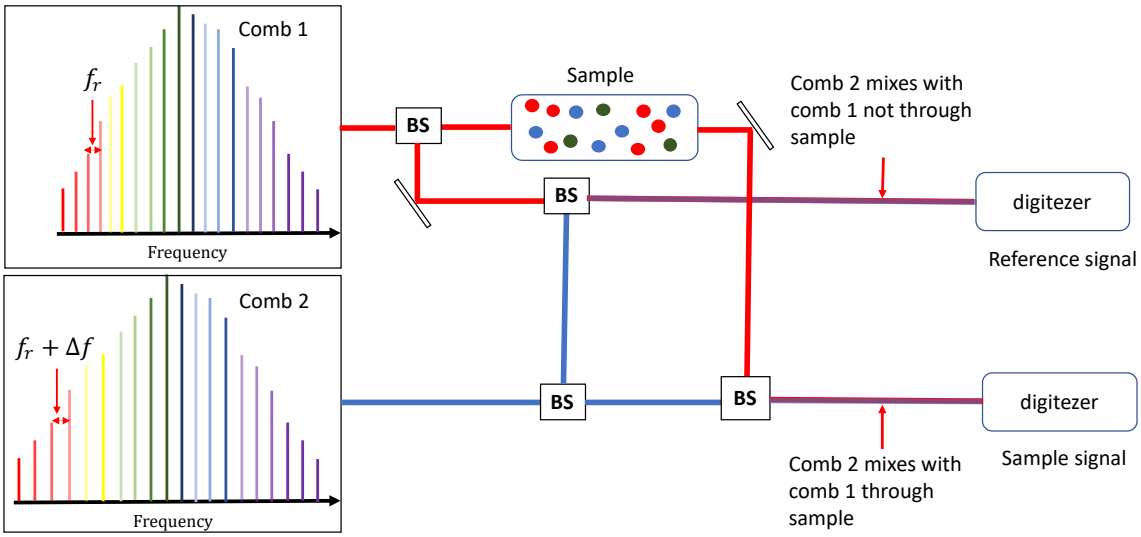

Figure 3.9: Principle of dual-comb spectroscopy measurement. Comb 1 interrogates the sample while comb 2 is used as a local oscillator. The sample information (the absorption and dispersion) is then measured.

Several optical frequency comb generation configurations have been used to perform dual-comb spectroscopy measurements. The measurement requirement varies from a sample to another one. The absorption measurement of the sample is performed at a frequency corresponding to the comb spacing. For dual-comb spectroscopy measurement of a liquid of large organic molecules, the resolution (comb spacing) required is several GHz. Microresonator, quantum dot lasers, quantum cascade lasers, and mode-locked lasers frequency comb have been recently used to perform such measurement, but they are limited when low resolution is required. However, the gas spectroscopy requires a very low resolution, i.e., f_r should be approximately a few hundred of MHz and Δf range between 10 and 100 kHz. Such spectroscopy measurements have been performed with electro-optic modulators-based comb [197] and gain-switching technique [198]. Compared

to many applications of the frequency comb, dual-comb spectroscopy does not require large bandwidth. The absorption information has been extracted recently with a total bandwidth of approximately 35 GHz [197], which is lower than the comb spacing of most microresonator frequency comb generator systems.

3.3.3 Optical frequency comb as communication sources

As stated in the introduction, the optical frequency comb is becoming ubiquitous in the high-capacity optical communication systems due to their fixed and stable comb spacing and the coherence between the phase of the comb lines [6]. The optical comb is used to replace the hundreds of individual lasers in the conventional WDM communication system with the aim to decrease the energy consumption and the size of the optical fiber communication systems. The modern WDM communication system requires strict optical frequency comb properties such as low linewidth, tunable comb spacing, and high power per comb line. Recent experiments have demonstrated an aggregate 5.376 Tbit/s PAM-4 data transmission capacity over 25-km of standard single-mode fiber using a frequency comb from a passively mode-locked quantum dash laser with a channel spacing of 34.224 GHz [199]. Unfortunately, the limitation of mode-locked lasers for high-capacity communication is their large linewidth (several MHz). Very recently, microresonator-based soliton was used to transmit data stream of more than 50 Tbit/s on 179 individual optical carriers that span the entire telecommunication C, and L bands [200]. The weaknesses of the microresonator-based optical comb are the fluctuation in the phase of the comb lines and uneven comb spacing due to the cavity properties, as we discuss in section 3.2.2. Compared to the mode-locked laser and microresonator, the combs generated by the electro-optic modulator provide very low linewidth (1 Hz), stable comb spacing, and high phase coherence between the comb lines, making them excellent candidates for the modern high-capacity optical communication system.

3.4 Conclusion

In this chapter, we have reviewed the optical frequency comb generation principle based on the mode-locked lasers. We have also provided a wide view of some different physical systems generating optical frequency comb and some promising applications depending on their comb properties. Interestingly, the microresonators, mode-locked lasers, quantum

cascade laser, and quantum dot lasers can generate very wide comb, but their comb spacing is imposed by their cavity properties, i.e., gain medium length, dispersion, and temperature. The electro-optic modulator generates a tunable comb by their comb spacing is limited by the bandwidth of the modulator. Finally, we have shown the principle of some optical frequency comb applications, including spectroscopy, LIDAR and optical communication. That overview shows room for investigating alternative approaches to control the comb properties, ideally using conventional semiconductor lasers that are widely available commercially and at low fabrication costs.

4

Theoretical analysis of optical injection dynamics of frequency combs

Contents

4.1 Tailoring the frequency comb dynamics 64

4.2 Modelling of the EEL with frequency comb injection 66

4.3 Numerical mapping of nonlinear dynamics 70

4.3.1 Three comb lines injection 70

4.3.2 Seven comb lines injection 72

4.4 Bifurcation analysis 74

4.4.1 Bifurcations diagram 74

4.4.2 Nonlinear wave mixing 76

4.4.3 Injection locking with selective amplification 76

4.4.4 Chaos bandwidth analysis 77

4.4.5 Broadened comb dynamics 79

4.5 Tailoring of the comb properties 83

4.5.1 Pulse width and time bandwidth product 83

4.5.2 Number of resulting comb lines 84

4.6 Phase of comb lines analysis 85

4.7 Conclusion 86

In this chapter, we theoretically investigate the nonlinear dynamics of a single-mode diode laser optically injected with a frequency comb. More specifically, we vary the injection parameters (injection ratio and detuning frequency) and the injected comb properties (number of injected lines and comb spacing) to map the nonlinear dynamics of the laser diode numerically. A sequence of bifurcations is found to lead to specific nonlinear dynamics, which significantly differ from those observed in the case of single-frequency optical injection. We first observe what is called the selective amplification of the less detuned comb line corresponding to the so-called *optical injection locking*. The optical injection locking range is bounded by a nonlinear modulation as a result of nonlinear wave mixing depending on both the detuning frequency and the injected comb spacing. Of particular interest is the case of a large injection ratio. The laser diode bifurcates from the injection locking to an unlocked time-periodic dynamics corresponding to a new frequency comb that significantly extends the number of injection comb lines to a much broader optical spectrum. The resulting comb is controlled by the injection parameters, the injected comb properties, and the laser parameters. We also report on several other dynamics, including chaotic dynamics and harmonic frequency comb generation. A close inspection of the chaos demonstrates an improvement of its bandwidth with the number of injected comb lines. The main part of the results in this chapter are based on our publications [22, 24].

4.1 Tailoring the frequency comb dynamics

We have seen in Chapter 2 that under external perturbation (optical feedback, optical modulation, and optical injection), a semiconductor laser can exhibit a wide variety of nonlinear dynamics [107]. The optical injection has been used to control the coherence properties of a semiconductor laser through the optical injection locking technique [21, 201]. Bifurcation to nonlinear dynamics have been much demonstrated, including optical chaos [123, 124, 202], nonlinear wave mixing [21, 203], periodic-self pulsation [169], dissipative solitons in large-aperture laser diodes [204, 205] and multistability dynamics [124, 206]. Experimental and theoretical mappings, which provide an overall picture of the nonlinear dynamics in the plane of the injection parameters, have been reported [124, 203]. A bifurcation analysis, i.e., analysis of qualitative changes in the nonlinear dynamics, have been achieved using standard numerical integration of the rate equations [123]. Very recently, continuation techniques allowed to analyze supercritical and subcritical

bifurcations and to unveil a global understanding of the bifurcation scenarios, including the mechanism of period-doubling and multipulse excitability [124].

Since nonlinear dynamics from external perturbation can generate time-periodic dynamics, optical combs can be achieved from diode lasers. For example, a Radio-frequency (RF) signal modulation of a single-mode semiconductor laser, i.e., gain switching, can produce an optical frequency comb [183, 207]. Gain switching was initially used for very short optical pulse generation and then has been recently used to demonstrate the comb generation in the Discrete Mode lasers (DMLs) and Distributed Feedback (DFB) laser [182]. Most importantly, it has been demonstrated that optical injection into the noisy optical spectra generated by gain-switching of a diode laser can be transformed into high-quality optical frequency combs [208]. Recent research has reported interesting nonlinear dynamics of optical frequency comb generated by gain-switching of a laser diode subject to an optical injection [190, 198]. These nonlinear dynamics include harmonic frequency comb dynamics and chaotic dynamics. Yet to date, the opposite situation in which an optical frequency comb is injected into the cavity of a single-mode semiconductor laser is much less studied and deserved significant attention.

Optical injection with a frequency comb into a single-mode laser diode has driven recent interest [11, 13, 14, 16, 17, 209–211]. The first studies have focused on the ability of the laser diode to achieve the optical injection locking to the desired comb line.

The optical injection locking solution of a laser diode subject to an optical frequency comb has been extensively investigated in [17]. The injection locking region for 3-comb lines injection is shown in Fig. 4.1. The injected comb line are separated by $\Omega = 1.2$ GHz. The region referred to as IL and NI correspond to injection locking and no injection locking, respectively. The optical injection locking to a frequency comb is characterized by the selective and the amplification of the comb lines that show the smallest detuning from the frequency position of the injected laser [9]. The unlocked comb lines are suppressed. In Fig. 4.1, the authors observed as many locking regions as the number of injected comb lines. This property is also reported in several other studies [16, 212]. These locking regions appear close to the frequency position of the injected comb lines, i.e., they are separated by the injected comb spacing. Interestingly, the locking regions are always smaller than the injected comb spacing. The authors determine the minimum injected comb spacing to achieve stable injection locking to be 0.16 GHz. Beyond the injection locking, several recent studies have been devoted to the optimization of the suppression ratio of the unlock

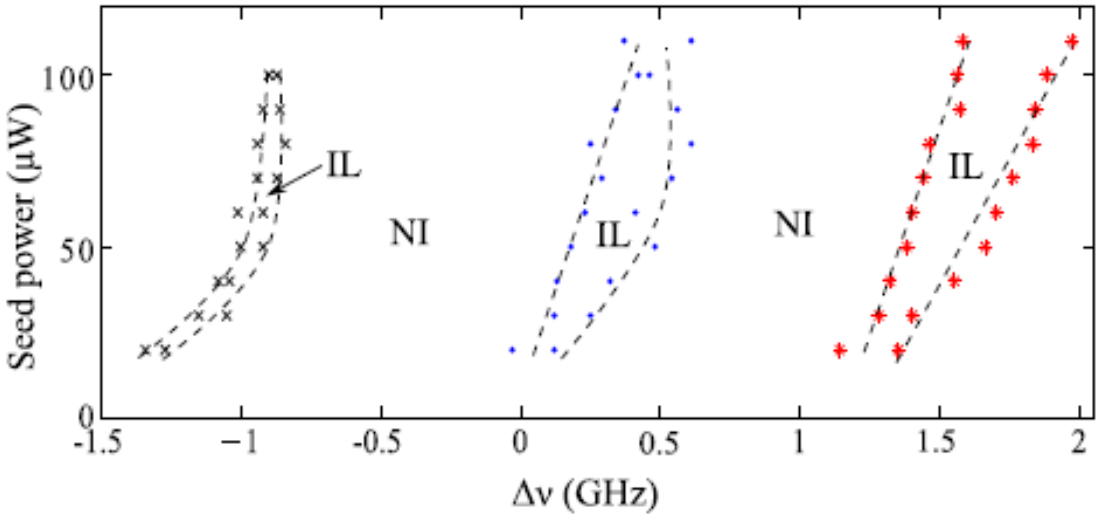

Figure 4.1: Mapping of optical injection locking with selective amplification of a semiconductor laser subject to optical frequency comb injection. IL correspond to the injection locking and NI to non injection locking. The injected comb had three lines separated by 1.2 GHz. Taken from [17]

comb line as a function of the injection parameters and the injected comb properties [10, 12, 13]. In the literature, only a few recent research works are reported on the optical injection dynamics of frequency combs [18–20]. They have focused on, e.g., harmonic comb dynamics and devil's staircases near Hopf bifurcations.

In this chapter, the nonlinear laser dynamics induced by an optical frequency comb injection are first theoretically investigated. This is carried out for large detuning frequency and high injection ratio hence going beyond the existing knowledge. The injected comb properties (number of lines and comb spacing) are varied to reveal locked and unlocked time-periodic dynamics in the plane of the injection parameters. The optical injection parameters, the injected comb properties, and the bias current of the injected laser are then used to tailor the comb dynamics.

4.2 Modelling of the EEL with frequency comb injection

Here, we describe the mathematical model of an edge-emitting laser (EEL) subject to an optical injection from a frequency comb. This is carried out by modifying the rate equation of the laser system in free-running (see chapter 2, equation 2.11 and 2.12) with

the complex electrical field of the injected comb. The rate equation model for the injected laser is found in chapter 2, equation (2.11):

$$\frac{dE_S(t)}{dt} = [i\omega(N) + \frac{1}{2}(G(N) - \frac{1}{\tau_p})]E_S(t) + E_M(t). \tag{4.1}$$

where $E_S(t)$ and $E_M(t)$ are the injected laser and the injected comb complex electrical fields, respectively. The complex electrical field of the injected laser output is expressed as:

$$E_S(t) = E(t)e^{i(2\pi\nu_0 t+\phi(t))}, \tag{4.2}$$

with $E(t)$, ν_0, and $\phi(t)$ are the amplitude, the free-running frequency and the phase of the injected laser, respectively.

As we introduced in [13], we will model the complex electrical field of the injected comb as the sum of several frequencies component:

$$E_M(t) = \sum_j E_j(t)e^{i(2\pi\nu_j t+\varphi)}, \tag{4.3}$$

where $E_j(t)$ is the amplitude of the j-th comb-line, ν_j is the frequency of the j-th comb-line, φ is the initial phase of each comb-line. To simplify the calculation, we set the initial phase of each comb-line to 0 and we suppose that the comb lines have the same constant amplitudes, E_{inj}.

In general, as the variation of the carrier density N due to external injection is very small, the angular frequency as a function of carrier density can be expressed as:

$$\omega(N) = \omega_0 + \frac{1}{2}\alpha G_N \Delta N \tag{4.4}$$

where G_N, is the differential gain, $\Delta N = N - N_{th}$, $\omega_0 = \omega(N_{th})$ and the parameter α describes the coupling between the amplitude and the phase of the electrical field as introduced in chapter 2.

By introducing the equation (4.2) to (4.3) in equation (4.1), the amplitude-phase equations of the injected laser can be written as:

$$\dot{E}(t) = \frac{1}{2}G_N(N(t)-N_{th})E(t)+E_{inj}\sum_j \cos(2\pi\Delta\nu_j t-\phi(t)), \tag{4.5}$$

$$\dot{\phi}(t) = \frac{1}{2}\alpha G_N(N(t)-N_{th})+\frac{E_{inj}}{E(t)}\sum_j \sin(2\pi\Delta\nu_j t-\phi(t)), \tag{4.6}$$

$$\dot{N}(t) = R_p - \frac{N(t)}{\tau_s} - G_N(N(t)-N_{th})E(t)^2 - \frac{E(t)^2}{\tau_p}. \tag{4.7}$$

In these equations, $\Delta\nu_j = \nu_j - \nu_0$ is the detuning between the injected comb lines at ν_j and the injected laser emitting at ν_0, N_{th} is the threshold carrier density, R_p is the pump rate and τ_s is the carrier lifetime, respectively.

The stationary solution of the injected laser without optical injection is characterized by $\dot{E}(t) = 0$, $\dot{\phi}(t) = 0$ and $\dot{N}(t) = 0$. After the calculation, we obtain :

$$E_0^2 = \tau_p(R_p - \frac{N_{th}}{\tau_s}) \tag{4.8}$$

In the following, the initial value of the amplitude and carrier density of the field of the injected laser will be equal to the stationary solution E_0 and the carrier density at threshold N_{th}, respectively. We shall use κ for the injection ratio with $\kappa = \frac{E_{inj}}{E_0}$.

Table 4.1: Semiconductor laser parameters used for numerical simulations.

G_N	$7.9 \times 10^{-13}\ m^3s^{-1}$	Differential gain
N_{th}	$2.91924 \times 10^{24}m^{-3}$	Carrier density at threshold
α	5	Linewidth enhancement factor
τ_s	$2 \times 10^{-9}s$	Carrier lifetime
τ_p	$2 \times 10^{-12}s$	Photon lifetime

In the following, we will use the rate equations (4.5)-(4.7) to explore the nonlinear dynamics of a single-mode laser diode. The rate equations are integrated using a fourth-order Runge-Kutta method with a time step equal to 1.2 ps. Numerical simulations are typically performed for 80 ns. The detuning frequency value is defined from the central injected comb line and is referred to as $\Delta\nu$. The laser parameters and their numerical value are summarized in Table 4.1.

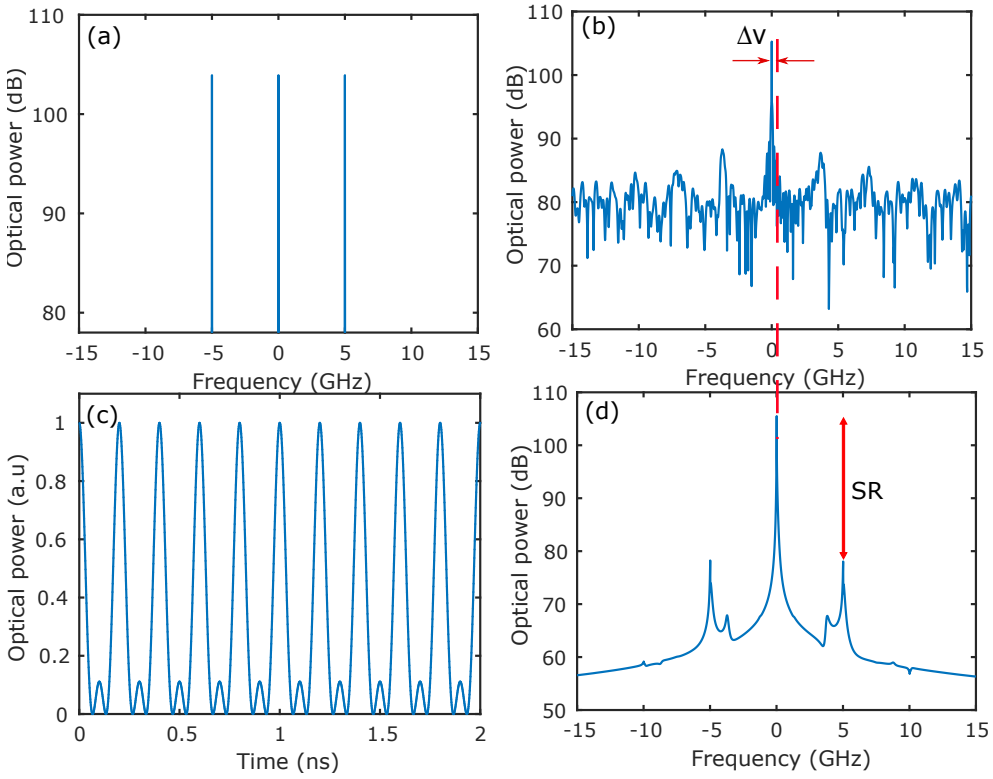

Figure 4.2: Optical spectra shown (a) and (c) correspond to the injected comb for three comb lines and the corresponding time series, respectively, (b) shows the free running output of the injected laser, and (d) the injected laser under injection locking condition. $\Omega = 5$ GHz is the comb spacing and $\Delta\nu = 10$ MHz is the detuning.

We first highlight Fig. 4.2, the fundamental difference between the single-mode and frequency comb optical injection dynamics, especially regarding the injection locking solution. Figure 4.2 (a) and (c) show the optical spectrum of the injected comb and the corresponding time series, respectively. The injected comb has three frequency lines with a constant phase between them and is separated in frequency by $\Omega = \nu_{j+1} - \nu_j = 5$ GHz. Figure 4.2 (b) corresponds to the optical spectrum of the injected laser in a free-running regime. The time series corresponding to this optical spectrum is time stationary. It is well known in the literature that entrainment between an external oscillator and the intrinsic oscillator of the injected laser can lead to the so-called optical injection locking when the difference between the frequency of the oscillators is sufficiently small [21, 74, 123, 124]. When the external oscillator is a single frequency laser, the optical injection locking state in the injected laser is characterized by the concentration of all the emitted power at the frequency of the external oscillator leading to stable and time stationary dynamics. Therefore, when the external oscillator is a frequency comb, the output of the injected

laser is time modulated. The optical spectrum corresponding to the optical injection locking state, as shown in Fig. 4.2 (d), is not time stationary, but the power is distributed between the injected comb lines. Figure 4.2 (d) is obtained for detuning $\Delta\nu = 10$ MHz from the central injected comb line. The comb line that is the less tuned from the injected laser is selected and amplified with a suppression ratio (SR) of the unlocked comb lines around 27 dB. Such a selective amplification through injection locking has been observed experimentally [10, 13].

4.3 Numerical mapping of nonlinear dynamics

This section maps the nonlinear dynamics of a single-mode laser diode under the injection of an optical frequency comb. When varying the injection ratio and the detuning frequency, besides the injection locking, we observe unlocked time-periodic dynamics corresponding to a broad optical frequency comb. We also report the impact of the number of injected comb lines on the injected laser dynamics.

4.3.1 Three comb lines injection

The optical injection into a single-mode laser diode cavity leads to a rich variety of nonlinear dynamics. According to the single-frequency optical injection, no stable dynamics can exist outside the injection locking area. Here, we carefully analyze the nonlinear dynamics of a single-mode laser diode induced by an optical frequency comb injection. We observe that the injection locking can bifurcate to peculiar dynamics corresponding to a significantly broadened comb when varying the injection ratio and the detuning.

To further understand these nonlinear dynamics, we categorized in the mapping of Fig. 4.3 the output of the laser under 3-comb lines injection. The numerical mappings are obtained for a fixed detuning frequency $\Delta\nu$ and varying the injection ratio κ from 0 to 0.8. The detuning is increased to achieve several times the injected comb spacing. We plot these mappings by following the consecutive maxima in the times series, and we compare them to the largest value of maximum. When this difference is less than 0-2% of the largest maximum, we conclude that the times series is time-periodic. To confirm this observation, we also follow the frequency lines in the power spectra. When the injected comb spacing regularly separates them, we conclude that the dynamic is time-periodic. The region

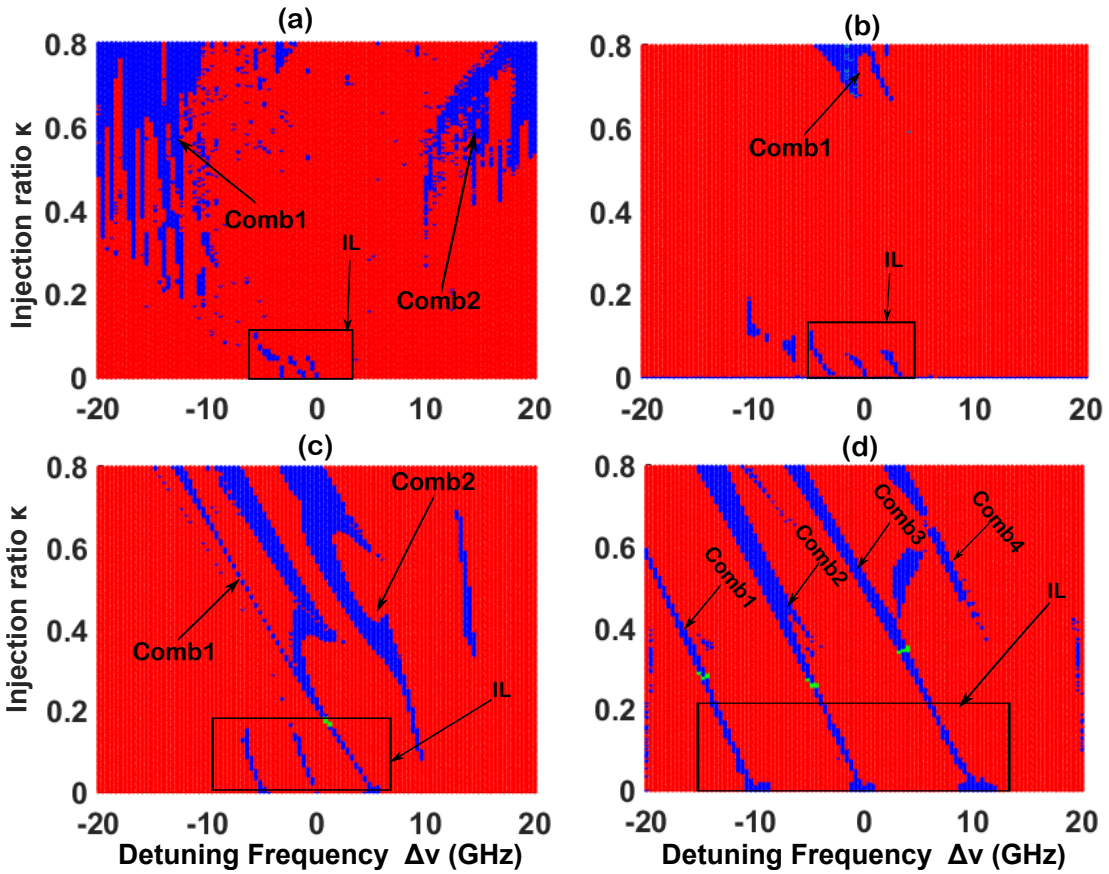

Figure 4.3: Numerical mapping of the semiconductor laser dynamics when subject to optical injection with frequency combs is shown by varying κ as a function of detuning frequency for comb spacing of 1, 3, 5 and 10 GHz respectively for (a)-(d) 3 comb lines injection. Different regions are observed: Injection locking (IL), unlocked time-periodic dynamics (Comb1, Comb2, Comb3, and Comb4). The green color corresponds to the limit of the injection locking region.

shaded in blue corresponds to the time-periodic dynamics at the periodicity of the comb spacing, which can be either the result of injection locking or new frequency comb solutions. The shaded areas in red correspond to any other dynamics that we will call complex dynamics. These dynamics include harmonic combs, period one, period two, higher period dynamics, quasi-periodicity, and chaotic dynamics. Figure 4.3 (a), (b), (c) and (d) are obtained for fixed injected comb spacing of $\Omega = 1, 3, 5$ and 10 GHz, respectively. The relaxation oscillation frequency (ROF) is around $ROF = 3.6$ GHz. The region labeled as IL corresponds to the injection locking with selective amplification. The ones referred to as Comb1, Comb2, Comb3, and Comb4 correspond to the new frequency comb dynamics. As mentioned earlier, IL is a time-periodic solution at the comb spacing frequency in which selective amplification occurs at the frequency corresponding to the less detuned

comb line. We limit the IL region as the one where the suppression ratio between the less detuned comb line from the injected comb and the next strongest comb line is larger than 10 dB. The green points in the mapping indicate the limit of the IL regions. These mapping show as many IL regions as the injected number of comb lines as already observed experimentally in [17]. We observe from these mappings that the laser diode output shows new frequency comb dynamics, whatever is the injected comb spacing. The comb regions are more structured when the injected comb spacing increases. Figure 4.3 (a) for 1 GHz injected comb spacing shows two comb regions. The isolated regions in blue are comb regions but separated by a wide variety of harmonic comb dynamics shaded in red. The harmonic combs are new frequency combs but with smaller comb spacing compared to the injected one. Figure 4.3 (b) shows the mapping for 3 GHz comb injection, where only one comb region is observed at a very large injection ratio. The 5 GHz comb injection [Fig. 4.3 (c)] shows two wide comb regions referred to as Comb1 and Comb2 appearing at detuning close to -5 GHz and 10 GHz. Comb1 is connected to the IL region of the injected comb line at +5 GHz. The transition between the IL dynamics and the new comb dynamics is characterized by the progressive increase in power of the unlocked comb lines and the appearance of new frequency lines. Another narrow comb region is observed around the detuning of 15 GHz. For 10 GHz comb injection [Fig. 4.3 (d)], all the IL regions are connected to a comb region. The distinct comb regions are typically separated by $\Delta\nu \sim$ multiple of comb spacing Ω. Compared to single-mode injection, we conclude that injection of comb dynamics leads to new IL solutions and new time-periodic dynamics corresponding to the generation of new comb solutions, which we shall analyze in detail later.

4.3.2 Seven comb lines injection

In this subsection, we analyze the effect of an increase in the number of the injected line on the comb dynamics. To this end, we map in detail in Figure 4.4 the nonlinear dynamics of the injected laser under 7-comb lines injection. Figure 4.4 (a), (b), (c) and (d) are obtained for fixed injected comb spacing of $\Omega = 1, 3, 5$, and 10 GHz, respectively. We observe as many IL regions as the number of injected comb lines which correspond to the regions around zero κ and start appearing at the injected comb lines frequency position.

In agreement with the 3-comb lines injection case, the new comb regions become more structured with the injected comb spacing. The case of $\Omega = 1$ GHz comb injection shows

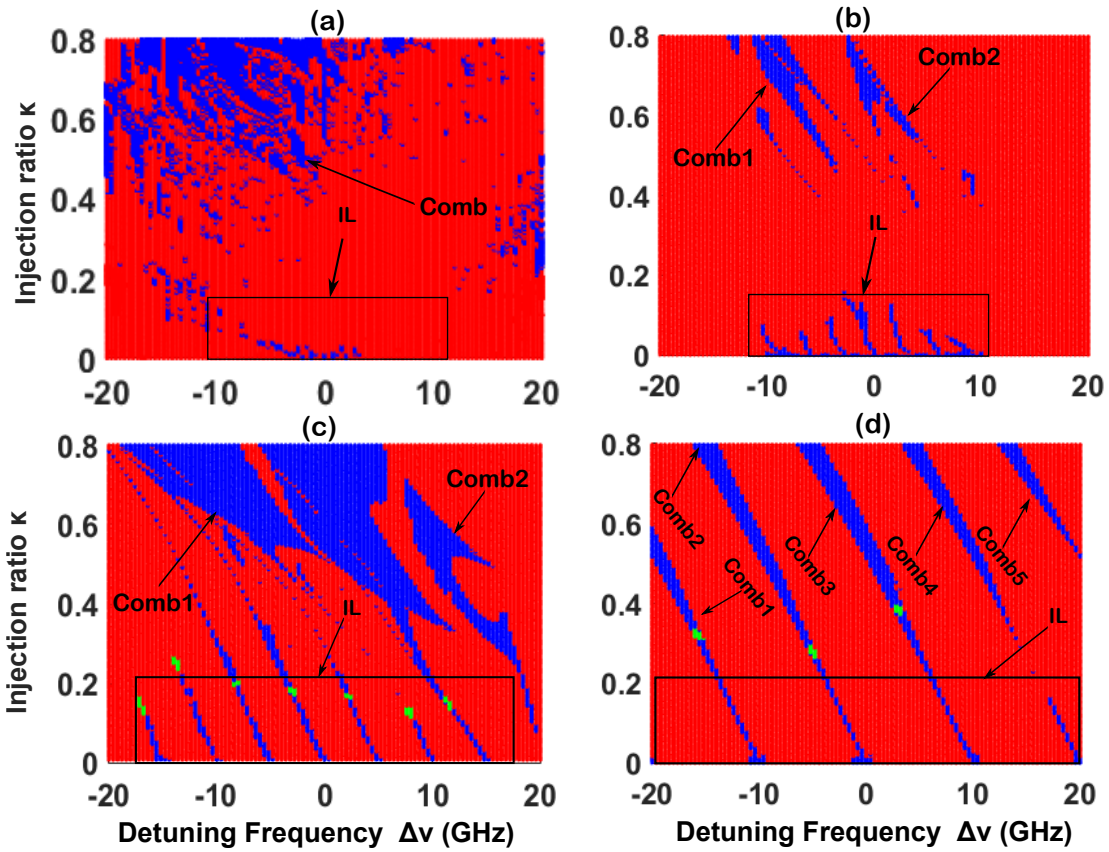

Figure 4.4: Numerical mapping of the semiconductor laser dynamics when subject to optical injection with frequency combs is shown by varying κ as a function of detuning frequency for comb spacing of 1, 3, 5 and 10 GHz respectively for (a)-(d) 7 comb lines injection. Different regions are observed: Injection locking (IL), unlocked time-periodic dynamics (Comb1, Comb2, Comb3, Comb4 and Comb5). The green color corresponds to the limit of the injection locking region.

several isolated regions of comb dynamics, which start to be structured when increasing the injection ratio. When the comb spacing is increased to $\Omega = 3$ GHz, two new comb regions are observed. Like for 3-comb lines injection, the comb dynamics related to $\Omega = 1$ GHz and $\Omega = 3$ GHz comb injection are observed at a high injection ratio. When comparing Fig. 4.4 to Fig. 4.3, we observe that the comb regions extend both in size and in numbers with the number of the injected comb lines. The area corresponding to the new comb dynamics extends with the increase of injection ratio κ but more significantly towards the negative detuning values. For Ω smaller than ROF, no injection locking region is found to bifurcate to the new comb dynamics, while for Ω larger than ROF, at least one IL region is connected to the new comb [Fig. 4.4 (a) and (b)]. We can conclude that increasing the number of comb lines in the injection field impacts the injected laser

dynamics and additional new comb solutions can be observed in the same range of injection parameters.

4.4 Bifurcation analysis

We perform a bifurcation analysis of the laser diode dynamics induced by a frequency comb injection. To this end, we use the model of the injected laser with frequency comb in section 4.2 (equation 4.5-4.7). Several bifurcations scenarios leading to the comb dynamics will be analyzed in the plane of the injection parameters as a function of the frequency position of the injected comb lines. We will carefully address the dynamics that emerge from the injection locking to the new frequency comb dynamics.

4.4.1 Bifurcations diagram

We have discussed in the previous section the appearance of the unlocked time-periodic dynamics corresponding to a new frequency comb. Here, we will describe the different scenarios leading to the new comb dynamics. To this end, we provide in Fig. 4.5 various bifurcation diagrams which are obtained for fixed injected comb spacing $\Omega = 5$ GHz. These diagrams are obtained by scanning the injection ratio κ for a fixed detuning frequency. The maxima and minima of the intensities $I_{out} = |E|^2$ corresponding to each injection ratio are plotted.

The bifurcations diagram on the left and right panels correspond to 3 and 7-comb lines injection, respectively. Figures 4.5 (a_1) and (b_1) are obtained for $\Delta\nu = -5$ GHz i.e., the less detuned comb line is the left comb line at -5 GHz. Figures 4.5 (a_2) and (b_2) depict the bifurcation diagram for $\Delta\nu = 0$ GHz. Figures 4.5 (a_3) and (b_3) plot the bifurcation diagram for $\Delta\nu = 5$ GHz i.e., the less detuned comb line is the right comb line at +5 GHz. The red arrows in the bifurcations diagrams indicate the unlocked time-periodic dynamics. The bifurcation diagrams show a narrow region of injection locking at a small injection ratio. When the injection ratio is increased, the Hopf bifurcations lead to the excitation of the relaxation oscillation frequency, which is well known as period-one dynamics [123, 124, 203]. In comb injection, the period-one dynamics are characterized by a wave mixing between the relaxation oscillation frequency and a new frequency that depends on the injected comb spacing. When the injection ratio increases further, the injected laser shows

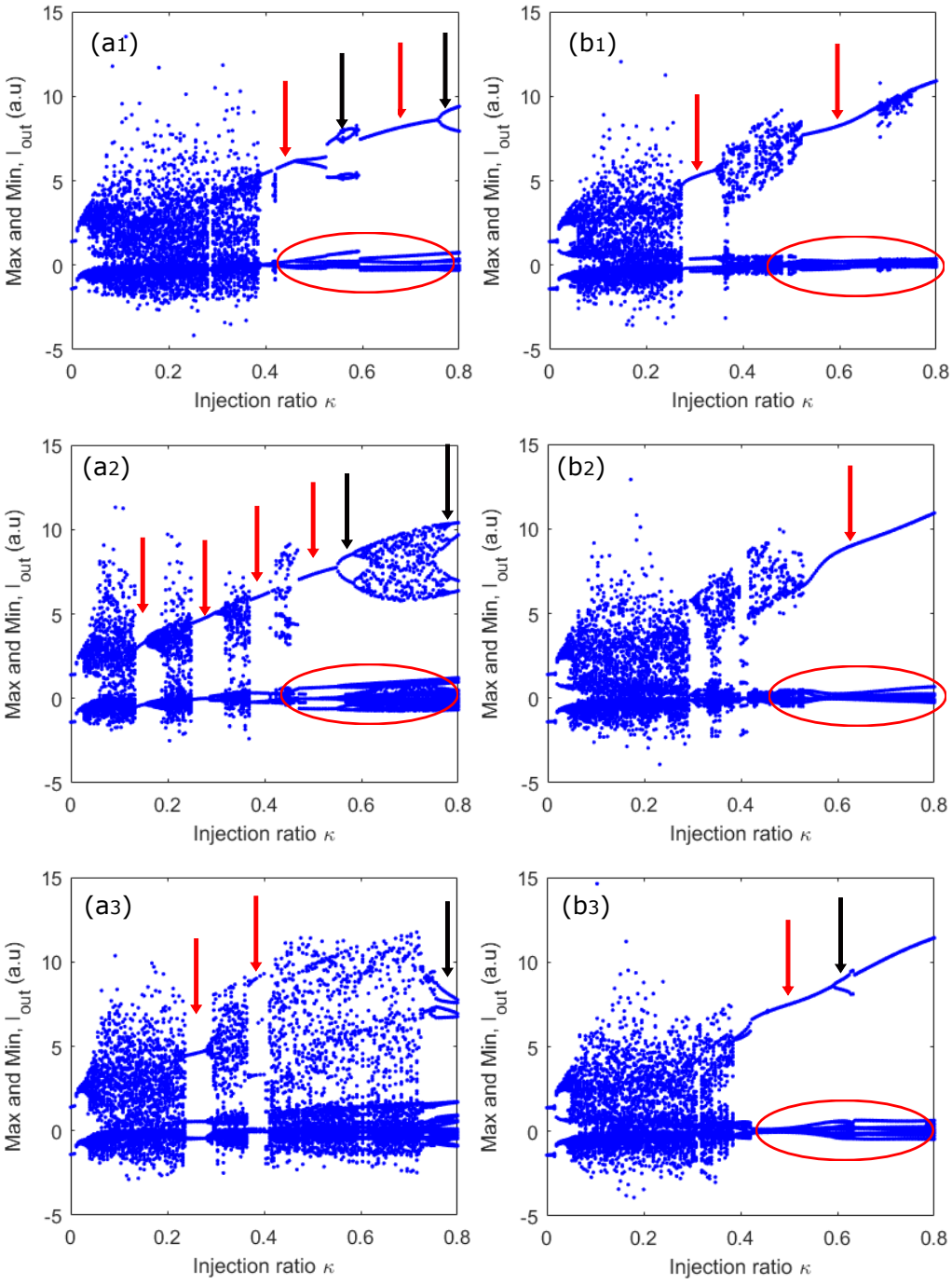

Figure 4.5: Bifurcation diagram of the injected laser output when varying the injection ratio and detuning. These diagrams are obtained for fixed injected comb spacing $\Omega = 5$ GHz. The left and the right panels correspond to 3 and 7 comb lines injection respectively. (a_1, b_1), (a_2, b_2) and (a_3, b_3) are obtained for detuning $\Delta\nu = -5$ GHz, $\Delta\nu = 0$ GHz, and $\Delta\nu = 5$ GHz, respectively. The surround area in the bifurcations diagrams corresponding to the complex pulse generation at very low intensity.

more complex dynamics and then bifurcates to another unlocked time-periodic dynamics corresponding to a new frequency comb. The red arrows indicate the comb regions in the bifurcation diagrams. Section 4.4.5 will provide an in-depth analysis of these comb dynamics and the related bifurcations. Figures 4.5 (a_1) and (a_2) show that the new comb or complex dynamics can bifurcate to harmonics frequency comb corresponding to a new frequency comb with a comb spacing smaller than the initially injected comb spacing 5 GHz. The black arrows indicate the harmonic comb regions in the bifurcation diagrams. The 3-comb lines injection is richer in harmonics frequency comb dynamics than the case of the 7-comb lines injection case. It is worth noticing that at a large injection ratio, the minimum of the pulse deteriorates, leading to new pulse generation at a very low intensity, as indicated by the encircled area in the bifurcations diagrams. The minima and maxima of these new low-intensity pulses are well discriminated in the bifurcation diagram. More detail will be provided on the new pulses in the following.

4.4.2 Nonlinear wave mixing

We analyze in more detail the nonlinear wave mixing that occurs at a low injection ratio. We fix the detuning frequency $\Delta\nu = 0.2$ GHz and the comb spacing $\Omega = 5$ GHz. The bifurcation diagrams for $\Delta\nu = 0.2$ GHz are quite similar to the one of $\Delta\nu = 0$ GHz [Figs. 4.5 (a_2) and (b_2)]. Figure 4.6 (a) and (b) show the optical spectra and the corresponding times series for 3 and 7-comb lines injection, respectively, for $\kappa = 0.006$. More specifically, Fig 4.6 (a) and (b) show a wave mixing, i.e., the injected laser output is intensity-modulated as a result of nonlinear wave mixing between the detuning frequency and a new frequency that depends on the injected comb spacing. In the mapping of Fig. 4.3 and Fig. 4.4, these wave mixings are obtained at the boundary of the injection locking region. By varying the detuning around the IL region of the mapping, the nonlinear wave mixing can bifurcate to harmonics locking as previously observed in [16, 18, 20]. These harmonics locking dynamics are observed when the detuning is close to a fractional integer of the injected comb spacing. The nonlinear wave mixing observation is not restricted to the zero detuning case but also occurs at the boundaries of the other IL regions.

4.4.3 Injection locking with selective amplification

We then keep the detuning fixed to $\Delta\nu = 0.2$ GHz and increase the injection ratio to a larger than the one of Fig. 4.6 (wave-mixing). The number of frequencies involved in the

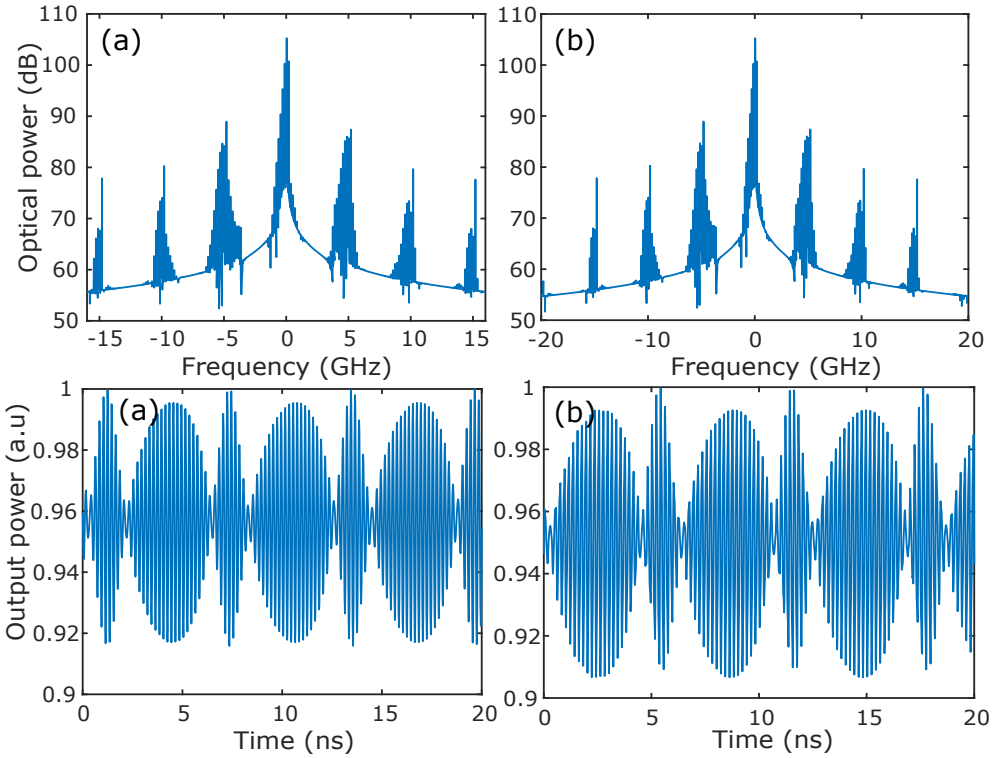

Figure 4.6: Optical spectra of nonlinear wave mixing between the detuning frequency and the injected comb spacing and their corresponding times series. (a) and (b) correspond to the three and seven comb lines injected and are obtained for $\Delta\nu = 0.2$ GHz $\kappa = 0.006$, and $\Omega = 5$ GHz.

nonlinear wave mixing decreases to give rise to a time-periodic dynamics that corresponds to the injection locking with selective amplification of the central injected comb line as shown in Fig. 4.7 (a) and (b). In both cases, the suppression ratio of the unlocked comb lines is the same (equal to 14 dB). Optimization of the suppression ratio can be controlled with the injection parameters (Injection ratio and detuning) and with the comb properties, as also confirmed experimentally [10, 12, 17, 209]. The suppression ratio is maximum at detuning close to zero. The appearance of additional comb lines beyond the injected comb lines is due to the nonlinear dynamics in the injected laser, i.e., the modulation of the carrier density at the injected comb spacing.

4.4.4 Chaos bandwidth analysis

We next analyze the chaotic dynamics occurring from IL. Figure 4.8 shows an example of chaotic dynamics. The top and bottom correspond to 3 and 7-comb lines injection, respectively. These figures are obtained for the same detuning and comb properties as

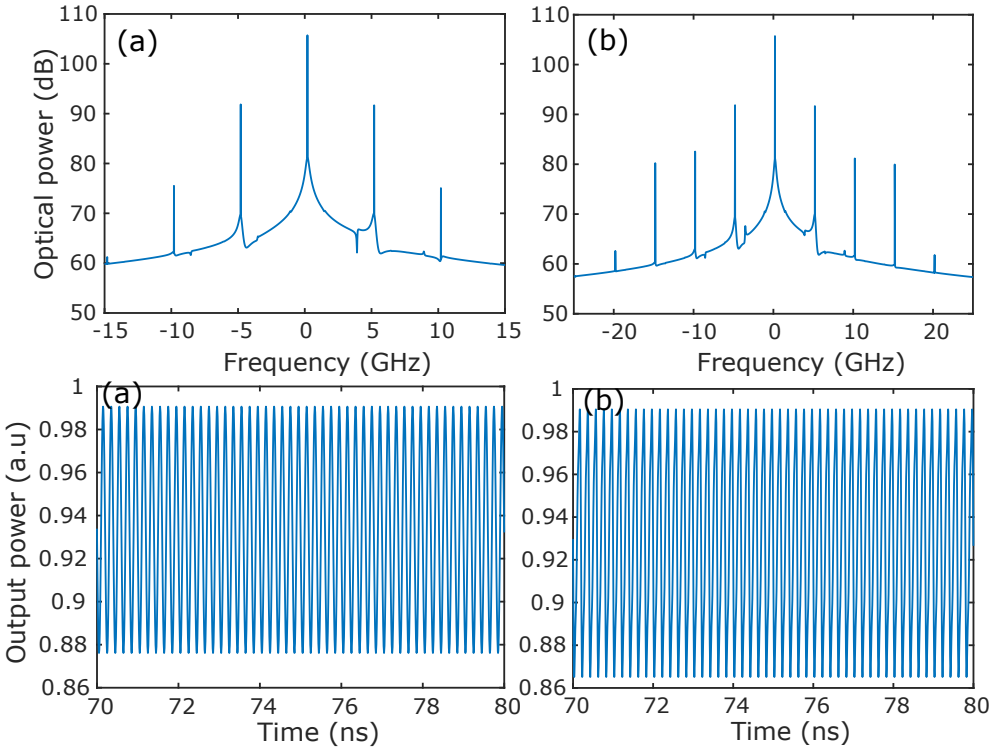

Figure 4.7: Optical spectra of injection locking with selective amplification and their corresponding times series. (a) and (b) correspond to the three and seven comb lines injected and are obtained for, $\Delta\nu = 0.2$ GHz $\kappa = 0.012$, and $\Omega = 5$ GHz.

in Fig. 4.7 when increasing the injection ratio from $\kappa = 0.012$ to $\kappa = 0.1$. $((a_1), (b_1))$, $((a_2), (b_2))$, and $((a_3), (b_3))$, correspond to the optical spectra, the times series and the power spectra, respectively. To evaluate the impact of the increase in the number of injected comb lines on the injected's laser chaos, a close inspection of the power spectra is made. Chaos bandwidth is defined in the literature as the upper frequency of the power spectrum that contains 80% of the signal linear energy [213, 214] as indicated on the power spectra of Fig. 4.8 $((a_3), (b_3))$. The power spectra show that the chaos bandwidth for the 3-comb lines injection case is 9.92 GHz, which is several times higher than the free-running relaxation oscillation frequency (3.6 GHz).

When the number of injected comb lines increases to 7, the chaos bandwidth is slightly larger (10.57 GHz) than for the 3-comb lines injection case (9.92 GHz), suggesting that a wideband chaotic signal can be generated when increasing the number of injected comb lines significantly. The question of how to increase chaos bandwidth has received significant attention recently in the context of chaos-based applications [214–218]. Optical injection of comb instead of single frequency is therefore a way to further boost the chaos bandwidth.

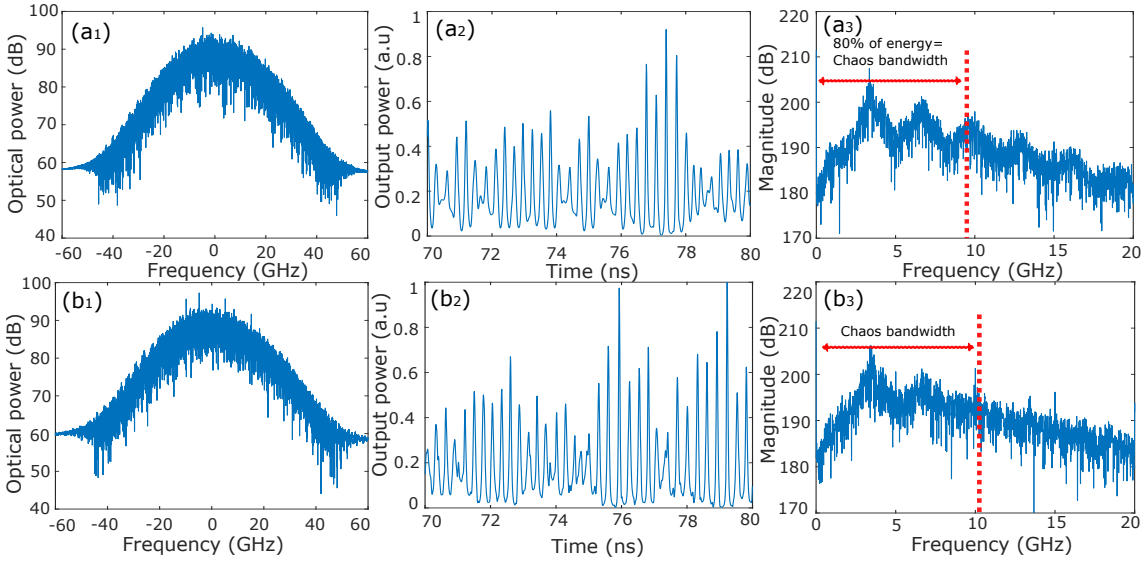

Figure 4.8: (a_1, b_1), (a_2, b_2), and (a_3, b_3), corresponds to the optical spectra, the times series and the power spectra of a chaotic dynamics, respectively. The top and bottom correspond to the three and seven comb lines injection and are obtained for $\Delta\nu = 0.2$ GHz, $\kappa = 0.1$ and $\Omega = 5$ GHz.

4.4.5 Broadened comb dynamics

The chaotic dynamics presented in subsection 4.4.4 bifurcates to an unlocked time-periodic dynamics corresponding to an optical frequency comb sharing some properties with the injected comb. For the same detuning as in Fig. 4.8, when increasing the injection ratio, the injected laser output shows in Fig. 4.9 a new comb dynamics. The bifurcation between this comb dynamics and the chaotic dynamics shown in Fig. 4.8 is abrupt. The top and bottom panels analyze 3 and 7-comb lines injection, respectively. Figure 4.9 (a_1) and (b_1) correspond to the optical spectra of the unlocked time-periodic dynamics. The red dashed lines in each optical spectrum indicate the position of the central injected comb lines. We consider a frequency line to be a comb line when its amplitude is more than -30 dB from the maximum comb amplitude. The number of resulting comb lines increases with the number of injected comb lines. We observe that 7-comb lines injection leads to a wider comb with 29 lines involved rather than 17 lines for 3-comb lines injection. A close inspection of the times series in Fig. 4.9 (a_2) and (b_2) shows a periodic signal at 0.2 ns (5 GHz) that corresponds to the frequency spacing of the frequencies lines in the optical spectra and to the injected comb spacing.

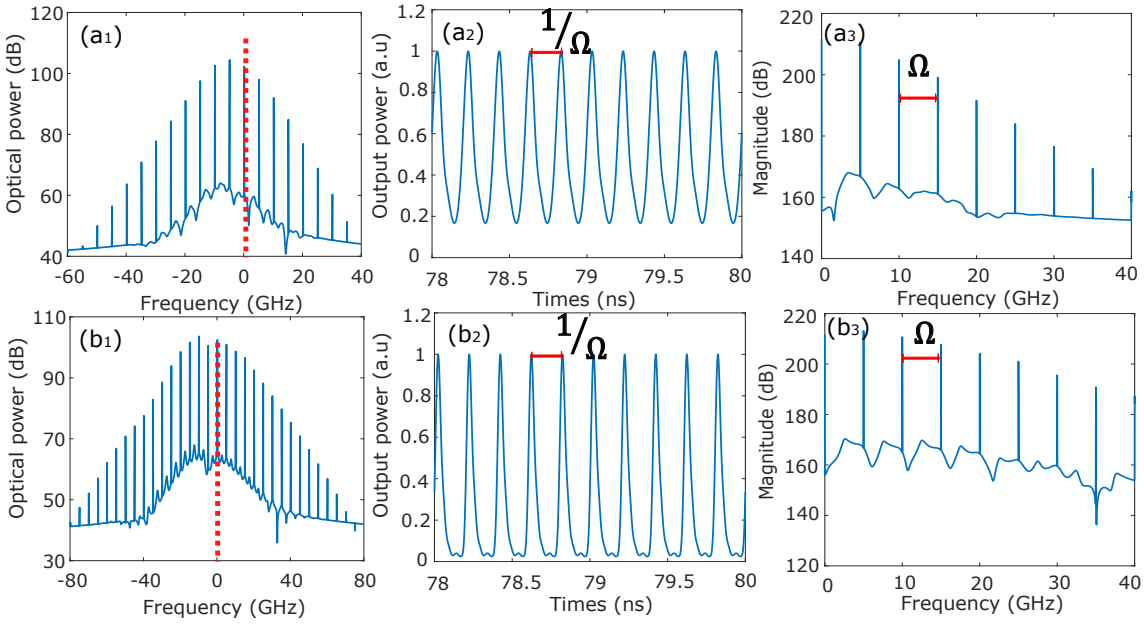

Figure 4.9: (Unlocked times-periodic dynamics induced by optical comb injection in the comb 1 region [Fig. 4.3 (c) and Fig. 4.4] (c)]. (a_1, b_1), (a_2, b_2), and (a_3, b_3), correspond to the optical spectra, the times series and the power spectra, respectively. The top and bottom correspond to the three and seven comb lines injection, respectively and are obtained for $\Delta\nu = 0.2$ GHz and $\Omega = 5$ GHz. The top and bottom cases are obtained for $\kappa = 0.202$ and $\kappa = 0.284$, respectively.

Some injection parameters can lead to comb dynamics with very complex pulse shaping, especially when the injected comb spacing is decreased. An analysis of the power spectra shows that the frequency lines are regularly separated the 5 GHz. When further increasing the injection ratio, another new comb dynamics is observed, as shown in Fig. 4.10. This second comb dynamics appears in the comb region referred to as "comb 2 " in the mapping of Fig. 4.3 (c) and Fig. 4.4 (c). The optical spectra (a_1, b_1), the times series (a_2, b_2) and the power spectra (a_3, b_3) confirm that the output comb spacing matches the injected comb spacing in both cases. It is worth noticing that the unlocked comb is frequency shifted from the injection-locked selective amplification solution. The frequency-shifted is also observed in Fig. 4.7 and increases with the injection ratio κ. The increase of κ leads to a decrease of the average carrier density, giving more power in the injected laser and shifting the instantaneous frequency towards the red through the equation (4.7). This explains the redshift of the main comb line (less detuned comb line) by increasing κ. A comparison between the region labeled "comb 1" and "comb 2" through the optical spectra shows that "comb 2" is broader than "comb 1," i.e., shows more comb lines. The comb extension is increased within the same comb region with both the injection ratio and the

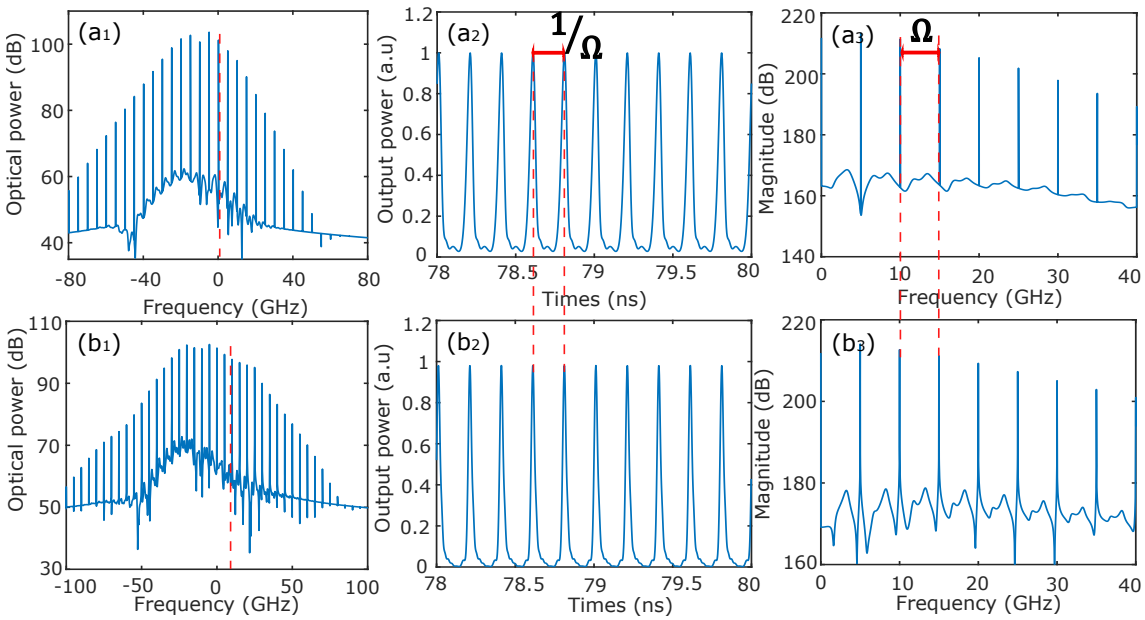

Figure 4.10: (a_1, b_1), (a_2, b_2), and (a_3, b_3), corresponds to the optical spectra, the times series and the power spectra, respectively, in the comb 2 region [Fig. 4.3 (c) and Fig. 4.4] (c)]. The top and bottom correspond to the three and seven comb lines injection and are obtained for $\Delta\nu = 0.2$ GHz and $\Delta\nu = 10$ GHz, respectively. They are obtained for $\kappa = 0.6$, and $\Omega = 5$ GHz.

detuning frequency, as we will address in the next section.

Further insight on the bifurcations sequences across the regions of 3-comb lines injection is depicted in Fig. 4.11.

These optical spectra analyze the transition between the "comb 1" and "comb 2" regions of the mapping of Fig. 4.3 (c) for fixed injection ratio $\kappa = 0.5$ when varying the detuning frequency $\Delta\nu$. When the detuning is close to the regions of comb dynamics, the chaotic dynamics start to be regular with the appearance of remarkable frequencies leading to unlocked time-periodic dynamics. We first observe the harmonic comb. The spacing of the harmonic frequency lines decreases with the detuning frequency. Figure 4.11 (a) shows the harmonics comb with repetition rate at half (2.5 GHz) of the injected comb spacing. From Fig. 4.11 (a), harmonics comb with very low comb spacing can be observed when varying the detuning towards negative value. When the detuning is sufficiently close to the "comb 1", region the harmonics at 2.5 GHz disappear smoothly to give rise to a new comb with a repetition rate corresponding to the injected comb spacing as shown in Fig. 4.11 (b). The new comb dynamics bifurcates when changing the detuning with the

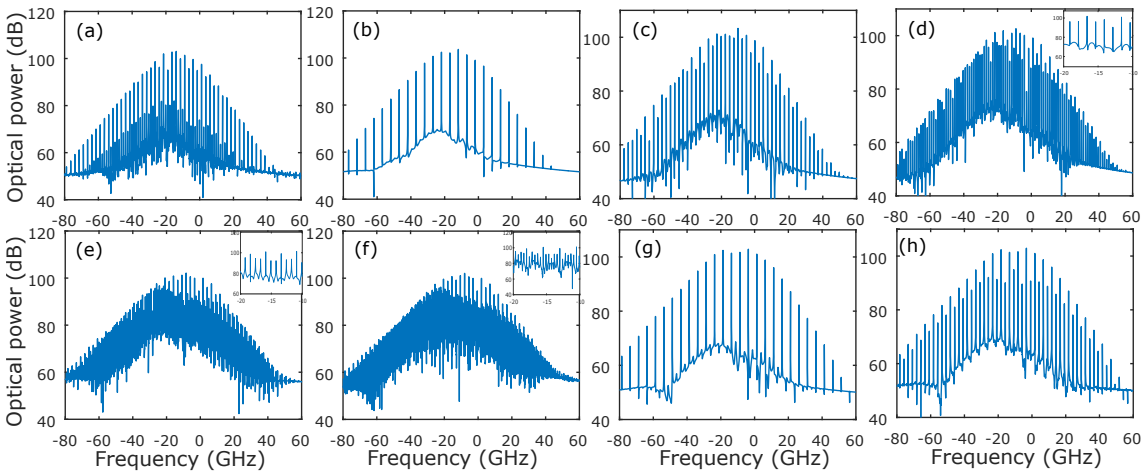

Figure 4.11: Bifurcation sequences leading to unlocked time-periodic dynamics for 3-comb lines injection. (a), (c), (d), (e), (f) and (h),harmonics comb dynamics corresponding to a new frequency comb with comb spacing a fractional integer of the injected one. (b) and (g) corresponds to the new comb dynamics in the region of "comb 1" and "comb 2", respectively. These optical spectra are obtained for fixed injection ratio $\kappa = 0.5$, and injected comb spacing $\Omega = 5$ GHz. (a), (b), (c), (d), (e), (f) (g) and (h) are recorded for $\Delta\nu = -8.8$ GHz, $\Delta\nu = -6.8$ GHz, $\Delta\nu = -5.1$ GHz, $\Delta\nu = -4$ GHz, $\Delta\nu = -3.3$ GHz, $\Delta\nu = -2.9$ GHz, $\Delta\nu = 1.4$ GHz, and $\Delta\nu = 1.8$ GHz.

appearance of harmonics lines at half of the injected comb spacing to another harmonic comb with a repetition rate of 2.5 GHz, as shown in Fig. 4.11 (c). When we keep varying the detuning towards positive value, a succession of harmonics combs dynamics takes place at the quarter, at sixth, and a twelfth of the injected comb spacing as shown in Fig. 4.11 (d), (e), and (f), respectively. The decrease in the harmonics combs spacing leads to complex dynamics, which bifurcate again to a new harmonics comb dynamics giving rise to the "comb 2" region in Fig. 4.11 (g). Like for "comb 1", Fig. 4.11 (g) bifurcates again to harmonics comb dynamics. Each comb region is bounded by complex harmonics comb dynamics. The injection ratio can also be fine-tuned to reveal several harmonics dynamics around the new comb regions. This harmonics scenario leading to new comb dynamics with both the detuning and injection ratio is not restricted to a specific injected comb spacing and number of injected lines. Harmonic combs with very low comb spacing can also be observed when injecting a comb with a smaller comb spacing e.g., with $\Omega = 1$ GHz.

4.5 Tailoring of the comb properties

This section analyzes the comb properties as a function of the injection parameters and shows how one can tailor the resulting comb dynamics. We first provide an analysis the pulse width and the corresponding time-bandwidth product when varying the injection ratio. We also compare the properties of the comb in the different comb regions for fixed injected comb properties. The injected comb is used to control the resulting output comb lines of the injected laser. Finally, we analyze the phases of the comb lines for 3 and 7-comb lines injection.

4.5.1 Pulse width and time bandwidth product

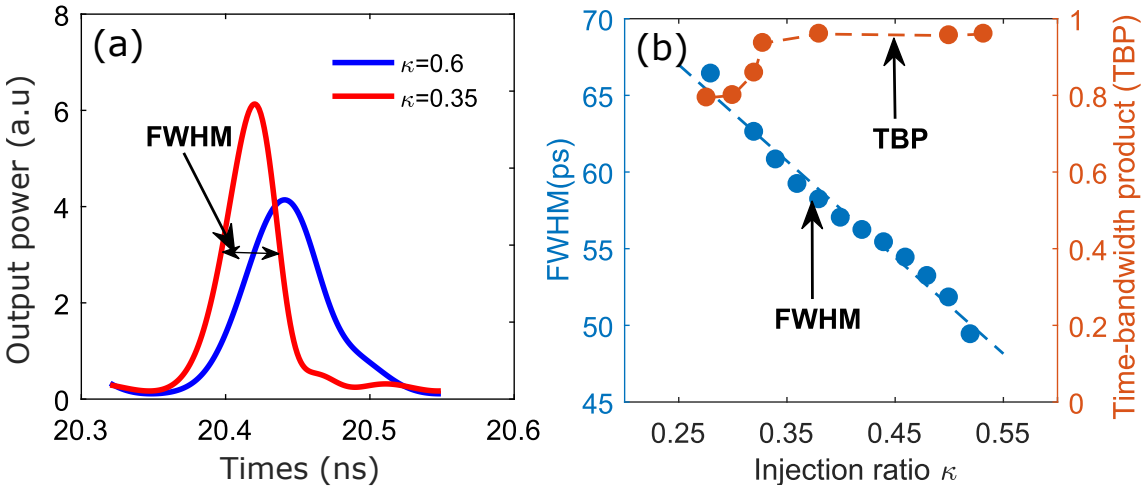

Figure 4.12: Optimization of the new comb dynamics for $\Omega = 5$ GHz for 3-comb lines injection. (a) pulse width in comb 1 and comb 2 for $\Delta\nu = 0.2$ GHz, $\kappa = 0.35$ (red), and $\kappa = 0.6$ (blue), respectively. (b) Full width at half maximum (FWHM) of the comb1 on the left vertical axis and time-bandwidth product (TBP) on the right vertical axis when increasing the injection ratio κ.

The pulse width is analyzed for fixed detuning frequency $\Delta\nu = 0.2$ GHz for the case of 3-comb line injection. Figure 4.12 (a) shows the pulse width in the comb 1 (red) and comb 2 (blue) regions. Figure 4.12 (b) depicts the full width at half maximum (FWHM) of the pulse on the left vertical axis and the time-bandwidth product on the right vertical axis in comb 1 for $\Omega = 5$ GHz, $\Delta\nu = 0.2$ GHz, and for 3-comb lines injection. The time-bandwidth product shown in Fig. 4.12 is computed from the product between the

FWHM and the spectral width at the half maximum that is calculated from the simulated optical spectra. The pulse width decreases when the injection ratio increases, but the corresponding time-bandwidth product increases. The time-bandwidth product achieves a maximum of 0.96, which is about twice the Fourier limit ~ 0.44 for a Gaussian shape pulse.

4.5.2 Number of resulting comb lines

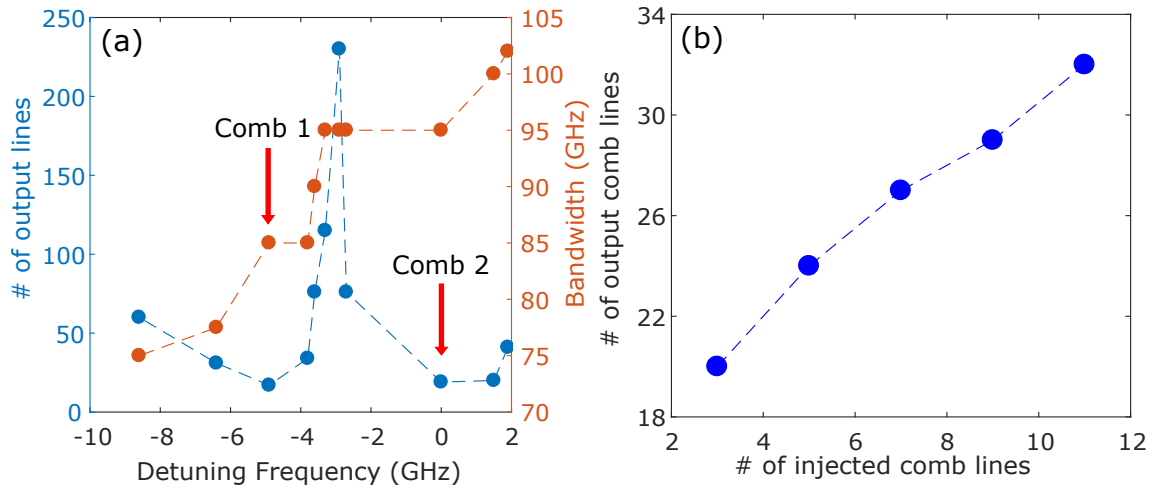

Figure 4.13: Number of comb lines and comb bandwidth analysis for $\Omega = 5$ for 3- comb lines injection. (a) number of comb lines on the left vertical axis and comb bandwidth on the right vertical axis when scanning the detuning frequency $\Delta\nu$ across the comb regions for fixed injection ratio $\kappa = 0.5$. (b) number of output comb lines in the injected laser as a function of the number of lines of the injected comb for $\Delta\nu = 0$ GHz and $\kappa = 0.8$.

Further analysis of the number of output comb lines of the injected laser is given in Fig. 4.13 for $\Omega = 5$ GHz and 3-comb lines injection. Fig. 4.13 (a) corresponds to the number of output comb lines (left vertical axis(blue)) and to the corresponding bandwidth (right vertical axis (red)) for fixed injection ratio $\kappa = 0.5$ when varying the detuning frequency. Like in section 4.4.5, the comb lines are analyzed at -30 dB from the maximum amplitude. The comb bandwidth increases linearly with detuning making the comb 2 wider (19 lines) than comb 1 (17 lines). The maximum number of comb lines (230 lines) is found between comb 1 and comb 2. That is explained by the appearance of harmonics comb with very small comb spacing described in Fig. 4.11. Figure 4.13 (b) plots the number of output lines as a function of the number of injected comb lines for fixed injection parameters. We observe that the new comb becomes wider by comparison to the injected

comb. It is worth noting that the new comb extends more when increasing the injection current of the injected laser. For example, when we increase the drive current of the injected laser by 15%, the number of comb lines goes from 21 to 27. An in-depth analysis of the effect of the injection current will be given in the next chapter.

4.6 Phase of comb lines analysis

This section analyzes the evolution of the phases of the comb lines for the case of 3 and 7-injected comb lines and for fixed injection parameters. We restrict the analysis to the comb lines at -30 dB from the maximum amplitude.

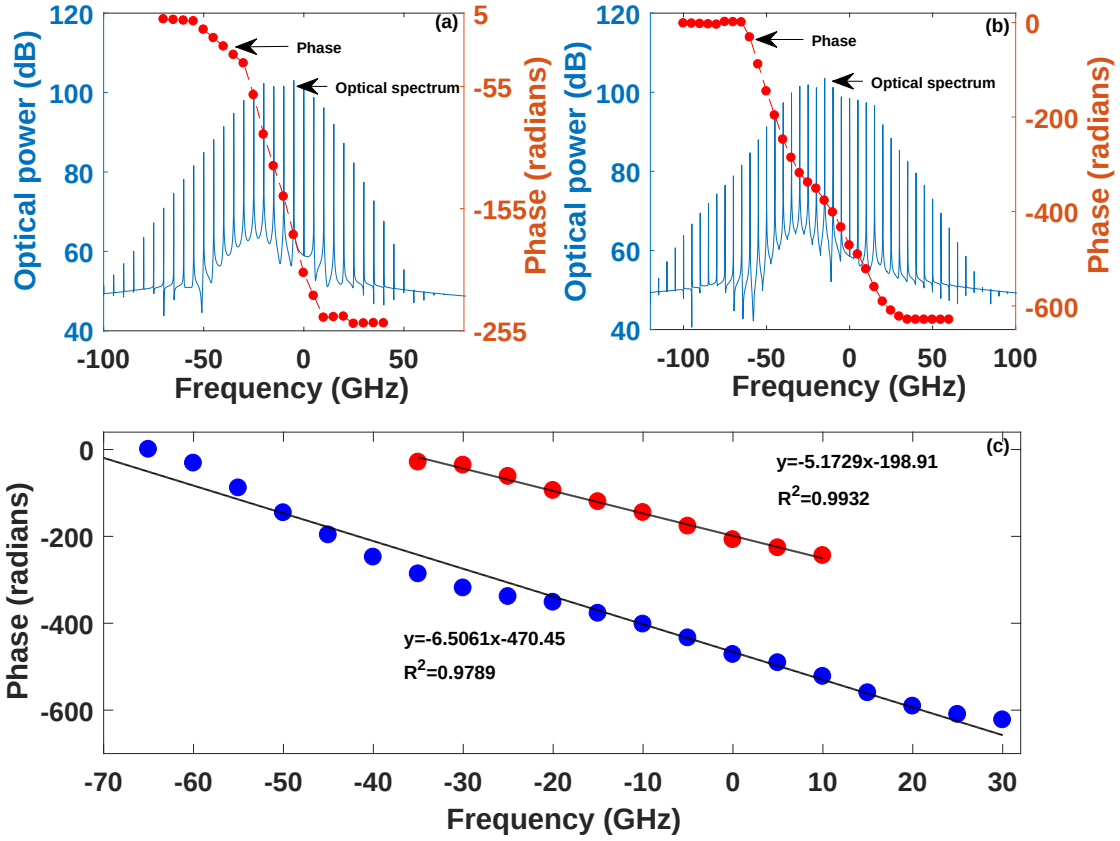

Figure 4.14: Optical spectra and phase for each comb line for $\Delta\nu = 0$ GHz, $\kappa = 0.8$ and $\Omega = 5$ GHz. (a) and (b), optical spectra (left vertical axis), phase (right vertical axis) for 3 and 7 comb line, respectively. (c) fitting of the linear part of the phase dependence for 3 comb lines (red) and 7 comb lines (blue).

The phase relation between the comb lines can be seen in Fig. 4.14, where the injected

comb spacing is $\Omega = 5$ GHz. We made a fast Fourier transform (FFT) of the optical field to plot in (a) and (b) the optical spectra on the left vertical axis and the corresponding phase information on the right vertical axis for 3 and 7-comb lines injection, respectively. For fixed injection parameters, we observe that the comb lines have constant phase differences in both cases. We analyze in (c) the linear fit of the phase spectra for 3-comb lines (red) and 7-comb lines (blue) injection. The phase-locking gets slightly worst when increasing the number of injected comb lines.

4.7 Conclusion

In summary, we show that a semiconductor laser can generate a broadened frequency comb from the injection locking solution. We demonstrate this technique by submitting a single-mode laser diode under an optical frequency comb injection. When increasing the injection ratio, the laser diode first shows a nonlinear wave mixing between the detuning frequency and a new frequency that depends on the comb spacing. The injected laser achieves the injection locking solution with selective amplification of the closest comb line in detuning. More complex dynamics, including period one, periodic, quasi-periodicity, and chaotic dynamics, are observed when varying the injection parameters. Most importantly, for some detuning frequency, the injected laser bifurcates to new comb solutions when the injection ratio is increased. The bifurcation analysis allows unveiling several harmonics combs leading to a new comb with significantly increased injected comb lines. The number of resulting lines involved in the new comb solution, and therefore, the pulse width can be controlled by the injection parameters and by the number of injected lines. In particular, theoretically, a multiplication of the number of comb lines by a factor as high as 100 is shown. Our result answers the requirement of comb application in Chapter 3, section 3.3, because of the stable comb repetition rate, which is very useful for frequency comb spectroscopy, optical communication, and LIDAR. Most importantly, the combs proposed in this section are a powerful tool for frequency comb spectroscopy due to the tunability of their repetition rate. Besides its interest for nonlinear dynamics, injection of a comb is therefore shown to be a technique to generate a significantly broadened comb from a diode laser with controllable properties. These theoretical predictions will be confirmed experimentally in the next chapter.

5

Experimental optical nonlinear dynamics of diode laser frequency combs

Contents

5.1 Experimental setup 88

5.2 Mapping of nonlinear dynamics 91

5.2.1 Injected comb spacing>ROF 92

5.2.2 Injected comb spacing<ROF 94

5.3 Comparison between theory and experiments 95

5.3.1 Asymmetric comb injection 95

5.3.2 Symmetric comb injection 97

5.4 Nonlinear wave mixing leading to comb dynamics 99

5.4.1 Unlocked time-periodic dynamics for increasing injection strength 99

5.4.2 Unlocked time-periodic dynamics when varying the detuning . . . 100

5.5 Comb performance analysis 104

5.5.1 Number of lines versus the injection parameters 105

5.5.2 Time bandwidth product and phase dynamics 106

5.5.3 Impact of the bias current on the comb dynamics 106

5.5.4 Tailoring the comb dynamics 107

5.6 Conclusion 109

In chapter 4, we have made an in-depth theoretical analysis of a single-mode laser diode submitted to injection of comb. Here, we experimentally map the nonlinear dynamics of a Distributed Feedback (DFB) laser subject to an optical injection from a frequency comb as a function of injection strength and the detuning frequency between the injected comb and the injected laser. We plot the mapping for injected comb spacing both below and above the relaxation oscillation frequency and for strong injection strength and large detuning. Interestingly, we identify several regions of the injection parameters (detuning and injection strength) where the injected laser output shows either a time-periodic dynamics corresponding to an injection locking with selective amplification, or even a new frequency comb with the same comb spacing as the injected one, or harmonic combs with comb spacing being harmonic of the one of the injected comb. We furthermore show that these dynamics are organized around the detuning frequency close to the multiple of the injected comb spacing. We also report on the impact of the amplitude of injected comb lines on the laser diode dynamics. The asymmetry of the injected comb is shown to modify the size of the injection locking region in the parameters space. Numerical simulations are then performed to emphasize the impact of the asymmetry in the optical comb injection. An excellent agreement between theory and experiment is found. Besides these unlocked time-periodic dynamics, we also reveal a wide variety of nonlinear dynamics, including nonlinear wave mixing, harmonics frequency comb, and complex dynamics. The performance of the resulting new frequency comb is found to be controlled with the injection parameters and with the injection current of the injected laser. The main results of this chapter are summarized in our recent publication [23].

5.1 Experimental setup

The experimental setup used to analyze the optical injection dynamics from a frequency comb is shown in Fig. 5.1. The output of a continuous-wave (CW) tunable laser (Yenista Tunics T100S) is first amplified by an Erbium-Doped Fiber Amplifier (EDFA). The linewidth of the tunable laser is measured to be approximately 30 MHz. Electric signal modulation is generated by an Arbitrary Waveform Generator (AWG) (Tektronix AWG 700002A) and sent to the RF port of a Mach-Zehnder (MZ) Modulator. The first polarization controller (P.C) is used to align the laser polarisation with the input of the MZ modulator. The MZ modulator uses is based on a $LiNbO_3$ with a 12.5 GHz

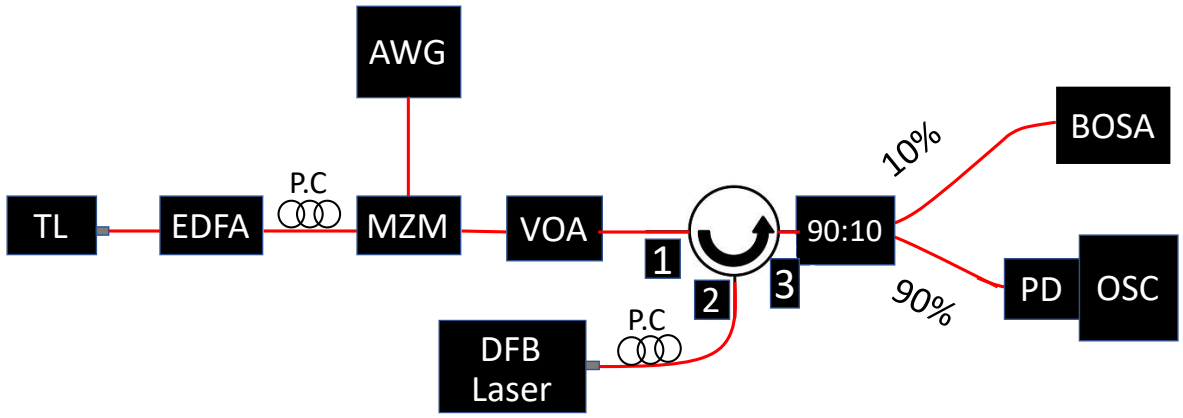

Figure 5.1: (a) Experimental setup for frequency comb injection. TL: Tunable Laser, EDFA: Amplifier, P.C: Polarization Controller, AWG: Arbitrary Waveform Generator, MZM: Mach-Zehnder Modulator, VOA: Variable Optical Attenuator, BOSA: Brillouin Optical Spectrum Analyser, PD: photodiode, OSC: Oscilloscope.

bandwidth. An optical comb with 3 optical frequency lines is generated in the output of the MZ modulator. The generated comb spacing can be changed from the AWG. The comb's optical power is controlled using a variable optical attenuator (VOA). The fiber circulator is arranged to provide isolation for the injected laser. The injected laser dynamics is analyzed with a high-resolution optical spectrum analyzer BOSA 400, which allows monitoring optical spectra with a resolution of about a minimum 0.1 pm or 12 MHz at the operating wavelength of 1550 nm. The second polarization controller (PC) allows controlling the polarization of the injected light. The temporal output is measured with a real-time digital oscilloscope (OSC) with a sampling rate of 50 GSamples/s and a bandwidth of 16 GHz. A photodiode (PD) (Newport 1544-B) 12 GHz bandwidth is placed at the input of the oscilloscope to convert the optical signal to an electrical signal.

- **Laser diode**

In this study, we use an edge-emitting laser, particularly a distributed feedback (DFB) laser emitting $\sim$ 1549.7 nm as an injected laser. The temperature of operation was maintained at 20° C. The light-current characteristic of the injected laser is shown in Fig. 5.2, where we plot the evolution of the emitted power as a function of the injection current. A linear fit determines the threshold current of the injected laser: $I_{th} = 6.9$ mA. We will typically operate at injection current at about 1.5 times the threshold current. In Fig. 5.2, the laser diode always operates at free-running. This chapter will use a modulated signal to destabilize the laser diode and investigate its nonlinear dynamics.

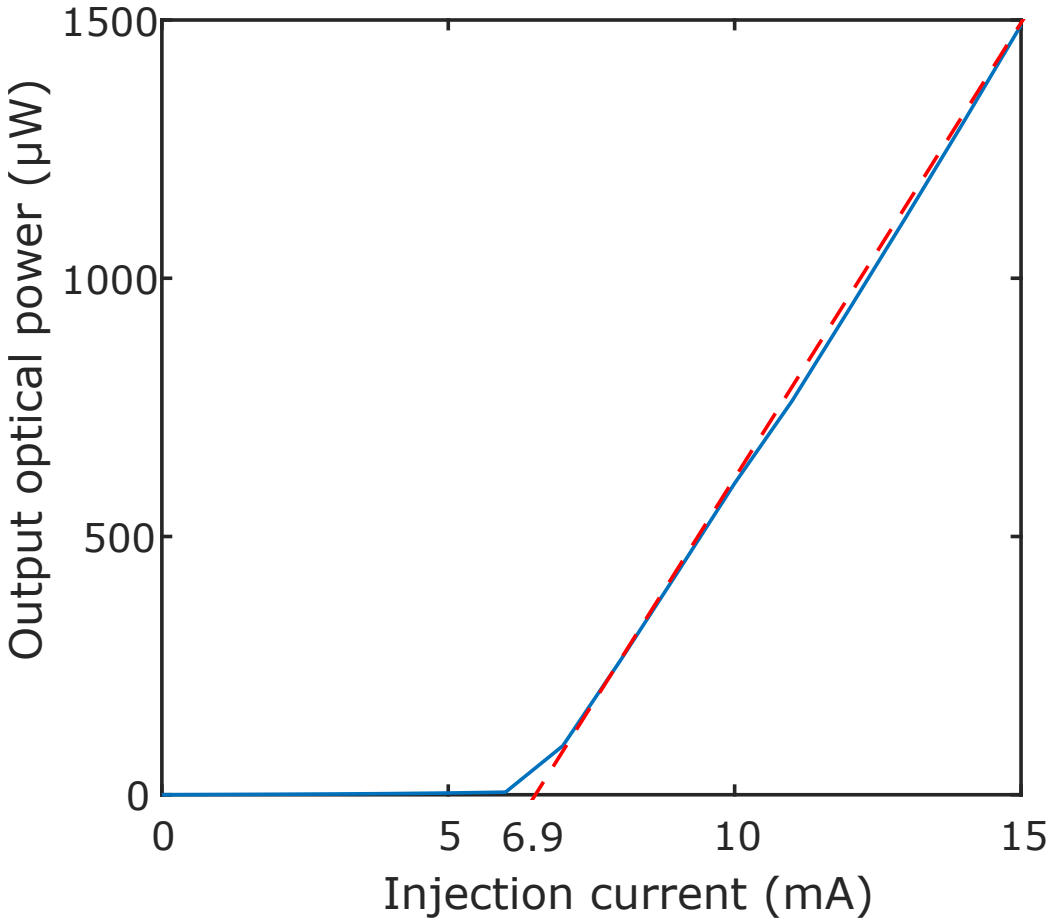

Figure 5.2: Evolution of the emitted power by the injected laser as a function of the injection current. We use a linear fit to determine the threshold current: $I_{th} = 6.9$ mA.

- **Laser diode output and injected comb**

Figure 5.3 (a) shows the optical spectrum of the injected laser in free-running at a bias current of 12 mA.

Figure 5.3 (b) shows the output of the tunable laser after modulation with the MZ modulator. This figure is obtained for a fixed comb spacing $\Omega = 5$ GHz. The experimental configuration leads to an asymmetric injected comb generation,i.e., the injected comb lines do not have the same amplitude. The amplitude of the comb lines can be equalized by fine-tuning the voltage of the modulator, but in that case, the total output power of the modulator strongly decreases due to the relation between the voltage and the modulator transmission function. As we discussed in chapter 4, strong injected power is required

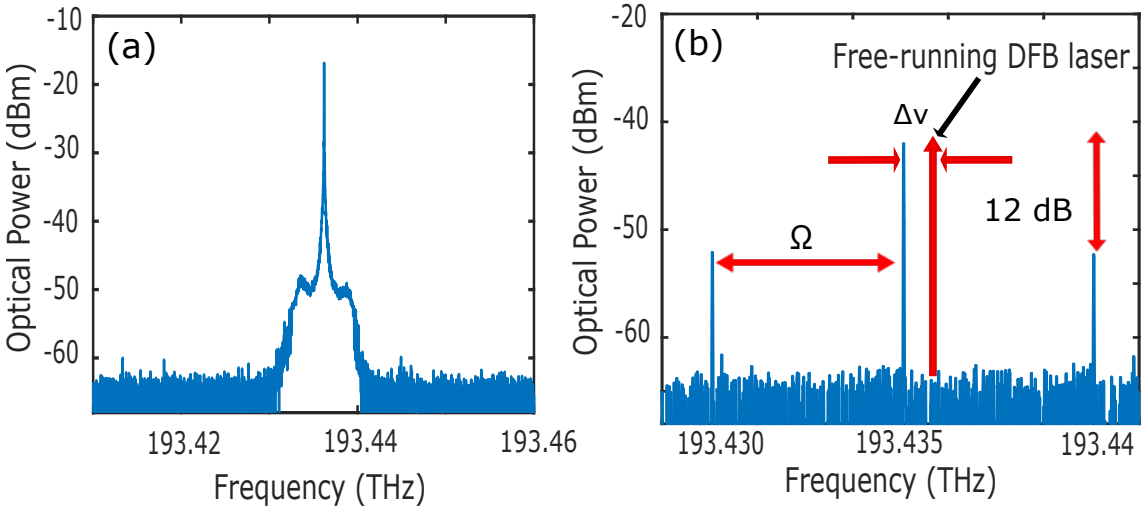

Figure 5.3: (a) Optical spectrum of the injected laser in free-running and, (b) optical spectrum of the injected comb for fixed comb spacing $\Omega = 5$ GHz.

in our experiment. The comb spacing is varied by changing the period of the sinusoidal function from the AWG. The difference between the power of the central comb line and the sides comb lines is around 12 dB. The difference between the red arrow and the central injected comb line represents the detuning frequency $\Delta\nu$. The detuning frequency can be defined for any injected comb lines. According to Chapter 4, we will call the main comb line the comb line that has the smallest detuning from the injected laser in this experiment. In the following text, the detuning frequency is defined with respect to the frequency of the central comb line, i.e., $\Delta\nu = \nu - \nu_0$, where ν and ν_0 are the frequencies of the central injected comb line and the injected laser, respectively. The injection strength is calculated by estimating the fiber loss between the modulator and the input of the injected laser. The power displayed by the modulator is always multiplied by the loss ratio to determine the power received by the injected laser. We define $\kappa = \frac{P_m * \gamma}{P_{SL}}$, where γ is the fiber loss ratio, P_m and P_{SL} are the power of the modulator output and injected laser output without injection, respectively.

5.2 Mapping of nonlinear dynamics

In this section, the injected laser diode nonlinear dynamics are categorized in a map in the plane of the injection parameters for injected comb spacing below and above the Relaxation Oscillation Frequency (ROF). We show that whatever is the injected comb

spacing, an unlocked time-periodic dynamics corresponding to a new frequency comb can be demonstrated. We also report that the value of the injected comb spacing plays a crucial role in the appearance of these new frequency combs.

5.2.1 Injected comb spacing>ROF

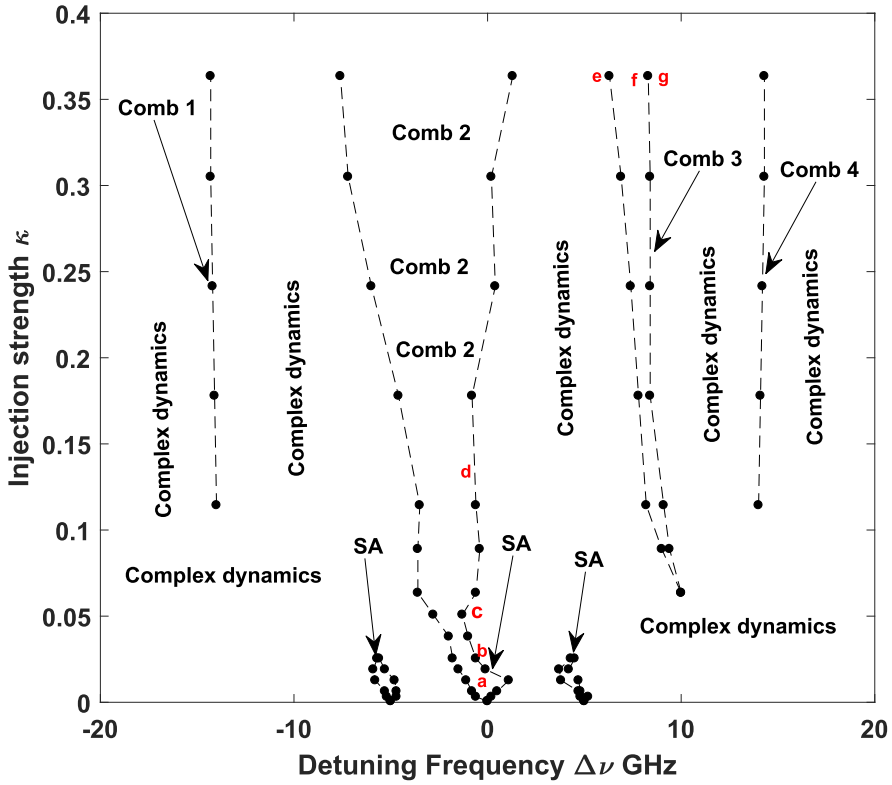

Figure 5.4: Experimental dynamical mapping of single frequency laser subject to an optical injection from a frequency comb for $\Omega = 5$ GHz. Several regions are observed: SA: Selective amplification, Unlocked time periodic dynamics (Comb 1, Comb 2, Comb 3 and Comb 4) and complex dynamics.

Figure 5.4 summarizes the different nonlinear dynamics of the injected laser subject to a modulated signal with comb spacing of $\Omega = 5$ GHz. The operation current, i.e., bias current, is fixed to 1.74 times the threshold current, which corresponds to 12 mA. For this injection current, the relaxation oscillation frequency is $ROF = 4.8$ GHz. As we emphasized in chapter 4, the comb injection is a modulation of power, i.e., under optical injection locking conditions, the whole power is not concentrated in a single frequency line but shows three optical lines. The central comb line is the less detuned from the frequency

position of the main comb lines in the injected laser. The two sides comb lines are strongly suppressed, leading to the selective amplification (SA) of the central comb line. When the detuning is set around each of the comb lines in the injection laser, we observe a SA region. The size of the SA region of the central injected comb lines is larger than the ones of the side comb lines, which is a consequence of the asymmetry in the amplitude of the injected comb lines. Recent study has concluded that when the injected comb lines have the same amplitude, their individual SA region has comparable sizes [17]. For injection strength beyond $\kappa > 0.02542$, the injected laser does not show a SA region for the side injected comb lines. By contrast, the injected laser output shows the SA on the central injected comb line until $\kappa = 0.1144$ and then bifurcates to an unlocked time-periodic dynamics region corresponding to a new frequency comb region called "comb 2" in the mapping. The bifurcation from the SA to the "comb 2" is characterized by the appearance of new frequency lines followed by an increase of power in each individual comb line. Close to the bifurcation point, the injected comb line that contains the maximum power changes position from the comb line that is closest in detuning from the injected laser frequency to another. When we increase the detuning, another comb region far from the SA region and different from comb 2 region appear, referred to as "comb 3" in Fig. 5.4. The "comb 3" region appears when the detuning is close to a multiple of the injected comb spacing. The minimum injection strength required to observe the "comb 3" region is found to be $\kappa = 0.06355$. This new frequency comb region extends with the injection strength and extends more toward negative values of the detuning. When we further increase the detuning towards positive and negative values, other comb regions called "comb 1" and "comb 4" start to appear when the detuning is close to $\Delta\nu = -14$ GHz and $\Delta\nu = 14$ GHz, respectively. The size of these comb regions is smaller than the one of "comb 2" and "comb 3". A fine-tuning of the injection parameters around these comb regions was not possible due to the limited resolution of the tunable laser. We observe the harmonics comb dynamics between these new frequency comb regions, i.e., new frequency comb lines start to appear with a comb spacing that is multiple integrals of the injected line spacing. The injected laser can show several irregular dynamics depending on the injection parameters, including period one, period two, higher other periods, and quasi-periodicity. All these dynamics are identified to be complex dynamics in the mapping of Fig. 5.4.

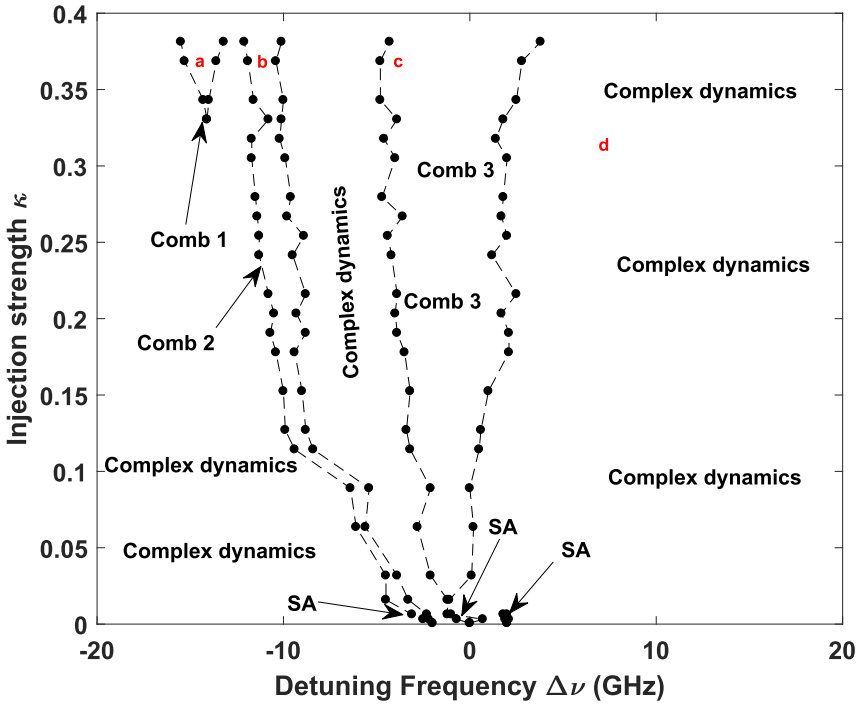

Figure 5.5: Nonlinear dynamics mapping of single frequency laser subject to a frequency comb injection for $\Omega = 2$ GHz. We observe Several regions: SA, Unlocked time periodic dynamics (Comb 1, Comb 2 and Comb 3) and complex dynamics.

5.2.2 Injected comb spacing<ROF

We next analyze how the injected comb spacing can influence the nonlinear dynamics of the injected laser. We have studied in Fig. 5.4 the nonlinear dynamics of the injected laser being injected with a comb spacing ($\Omega = 5$ GHz) close to the relaxation oscillation frequency ($ROF = 4.8$ GHz). Figure 5.5 shows the mapping of nonlinear dynamics when the injected comb spacing is smaller than the relaxation oscillation frequency, i.e., $\Omega = 2$ GHz. In Fig. 5.5, we observe several new frequency comb regions labeled as "comb 1", "comb 2", and "comb 3". We also observe other dynamics like harmonics frequency comb and irregular dynamics that we identify as complex dynamics in the mapping. Unlike to $\Omega = 5$ GHz comb injection where only the SA region of the central injected comb line is connected to a comb region, Fig. 5.5 shows that two SA regions can be connected to the new frequency comb regions when changing the comb spacing. We have checked that despite the appearance of a frequency comb dynamic around the comb line at -2 GHz, its SA region remains very narrow, i.e., the transition between the SA region and the new

comb region appears at low injection strength and detuning. The bifurcation scenario from the SA to the new frequency comb is qualitatively the same as for the $\Omega = 5$ GHz comb injection case. It is essential to mention that besides the comb region labeled as "comb 1", "comb 2", and "comb 3", several isolated comb regions (not shown, but well predicted in the numerical mapping of next section) with very narrow sizes are observed. These narrow comb regions are very unstable (noisy) and bifurcate easily toward more complex dynamics. Together with the irregular dynamics, these unstable comb dynamics are categorized as complex dynamics in the mapping of Fig. 5.5. Similar to $\Omega = 5$ GHz comb injection case, the new frequency comb dynamics start to appear always when the detuning frequency is close to a multiple of the injected comb spacing. For both $\Omega = 5$ GHz and $\Omega = 2$ GHz comb injection cases, the new comb dynamics differ from a region to another.

5.3 Comparison between theory and experiments

The experimental configuration leads to an asymmetric frequency comb injection which was not accounted for in the numerical simulation of chapter 4. In this section, we therefore, theoretically analyze the laser diode dynamics by adapting the mathematical model detailed in Chapter 4 to the realistic experimental configuration. We examine the influence of the injected comb line's amplitudes on the nonlinear dynamics of the laser diode.

5.3.1 Asymmetric comb injection

As already introduced in chapter 4, we have performed our numerical simulations using the following rate equations (see chapter 4 section 4.2):

$$\dot{E}(t) = \frac{1}{2} G_N \Delta N(t) E(t) + \sum_j E_j \cos(2\pi \Delta\nu_j t - \phi(t)), \tag{5.1}$$

$$\dot{\phi}(t) = \frac{1}{2} \alpha G_N \Delta N(t) + \sum_j \frac{E_j}{E(t)} \sin(2\pi \Delta\nu_j t - \phi(t)), \tag{5.2}$$

$$\dot{N}(t) = R_p - \frac{N(t)}{\tau_s} - G_N \Delta N(t) E(t)^2 - \frac{E(t)^2}{\tau_p}. \tag{5.3}$$

The semiconductor laser parameters are the same as in chapter 4 excepted α=3, the linewidth enhancement, and $R_p = 1.5R_{th}$, the pump rate.

Figure 5.6 (a) and (b) plot the numerical mapping of nonlinear dynamics of a single-mode laser diode under a modulated signal in the plane of the injection parameters. The modulated signal is here an asymmetric frequency comb, i.e., the injected comb lines do not have the same amplitude. The injected comb has three frequency lines. Figure 5.6 (a) and (b) have to be compared with the Fig. 5.4 and Fig. 5.5, respectively. The bias current of the injected laser is fixed to 1.5 times the threshold current. We plot these mapping by following the maxima and their frequency position in the radio frequency spectra. We select the successive maxima and then calculate the difference between their frequencies. The new frequency comb dynamics are characterized by the fact that this difference is always equal to the injected comb spacing. To model the experimental configuration, we consider that the side comb lines have 12 dB amplitude less than the amplitude of the central line. Our numerical mapping reproduces qualitatively and quantitatively the experimental findings. In Fig. 5.6, we observe several nonlinear dynamics, including time-periodic dynamics, chaotic dynamics, period one, and quasi-periodicity. We summarize in blue the time-periodic dynamics, i.e., the SA or new frequency comb region. The other dynamics are shaded in grey and are referred to as complex dynamics. Figure 5.6 (a) and (b) show the theoretical mapping of nonlinear dynamics for fixed comb spacing to $\Omega = 5$ GHz and $\Omega = 2$ GHz, respectively. Here, the injection locking is defined as SA on the mappings. We consider injection locking when the ratio between the main comb line and the next strongest comb lines is more than 10 dB. The asymmetry of the injected comb is found to impact the size of the three SA regions.

The lower is the amplitude of the injected comb line, the smaller is its SA region. We observe in the map of Fig. 5.6 (a), four regions of the new frequency comb region labeled "comb 1", "comb 2" , "comb 3" and "comb 4". The regions "comb 1" and "comb 2" appear when the detuning is close to $\Delta\nu = -14.6$ GHz and $\Delta\nu = 14.6$ GHz, which is in excellent agreement with the experiment. Figure 5.6 (b), shows three new frequency comb regions called "comb 1", "comb 2" and "comb 3". As we discuss for $\Omega = 5$ GHz, we observe as many SA regions as the number of the injected comb lines. In agreement with experimental findings, Fig. 5.6 (b) shows two SA regions connected to the new comb dynamics regions. A fine-tuning in injection parameters allow us to unveil some isolated comb dynamics regions (for example, see Fig. 5.6 (a) detuning -10 GHz) as we discussed in the experimental

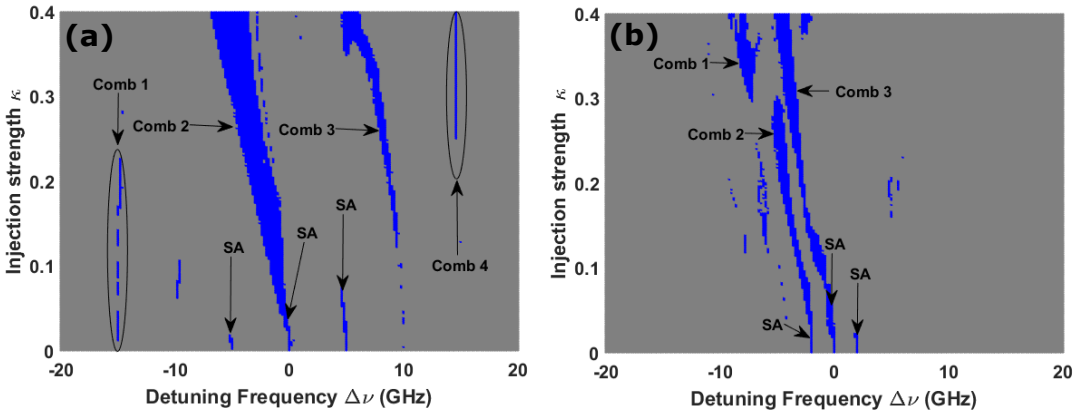

Figure 5.6: Numerical mapping of a semiconductor laser subject to optical frequency comb injection. (a) and (b) correspond to an asymmetric comb injection similar to the experimental conditions for $\Omega = 5$ GHz and $\Omega = 2$ GHz, respectively. The blue and gray part correspond to the time periodic dynamics and unlocked chaotic dynamics, respectively. Different regions observed: SA, Comb 1, comb 2, comb 3, comb 4 and comb 5 unlocked time periodic dynamics.

mapping of Fig. 5.5. These new frequency comb dynamics regions extend with the injection strength and extend more towards negative values of detuning. The size of the SA regions varies depending on which comb line in the injected laser is the less detuned, which is the consequence of the asymmetry of the injected comb line. The impact of the asymmetry of the injected comb lines on the SA regions increases when the injected comb spacing decreases. The shift of the "comb 2" and "comb 3" regions towards negative detuning values is linked to the linewidth enhancement factor α. Indeed, for $\alpha \to 0$, these comb regions become more symmetric and would even move towards positive detuning if α would be negative.

5.3.2 Symmetric comb injection

To analyze how the nonlinear dynamics of the injected laser are impacted by the asymmetry of the injected comb lines, we show in Fig. 5.7 (a) and (b) the numerical mapping of nonlinear dynamics under symmetric comb injection. The injected frequency comb lines have the same amplitude, the other parameters of the injected laser are kept fixed. Figure 5.7 (a) and (b) are obtained for injected comb spacing of $\Omega = 5$ GHz and $\Omega = 2$ GHz, respectively. Unlike Fig. 5.6, the SA region corresponding to each injected comb lines have almost a comparable size. For $\Omega = 5$ GHz comb injection, the comb 1 region in

Fig. 5.6 (a) is suppressed. The comb 2 region of Fig. 5.6 (a) always remains, but becomes narrower at large injection strength and corresponds now to the comb 1 region of Fig. 5.7 (a). Like for $\Omega = 2$ GHz in Fig. 5.6 (b), two SA regions are now connected to new frequency comb regions. When sweeping the detuning across the frequencies of the injected comb lines, several large comb regions called "Comb 3", "Comb 4" and "Comb 5" are observed. They appear when the detuning is close to 10, 15, and 20 GHz, which corresponds to multiples of the injected comb spacing. It is worth mentioning that the "Comb 3" and "Comb 4" regions are observed in the same area of the injection parameters as in Fig. 5.6 (a), but with a significant increase of their size. In contrast to the asymmetry case for $\Omega = 2$ GHz, where two SA regions are connected to the new comb regions, Fig. 5.7 (b) shows that only the SA region of the comb line at -2 GHz is connected to a comb region (comb 3 in the mapping). The new comb dynamics called "Comb 2" appears when the detuning is close to -4 GHz, which is equal to twice the injected comb spacing. This new comb region extends with the injection parameters. For detuning close to 4 times the injected comb spacing, i.e., -8 GHz, another frequency comb region labeled as "comb 1" is observed. As shown in Section 4.4 through bifurcation diagrams, the pulse shape varies

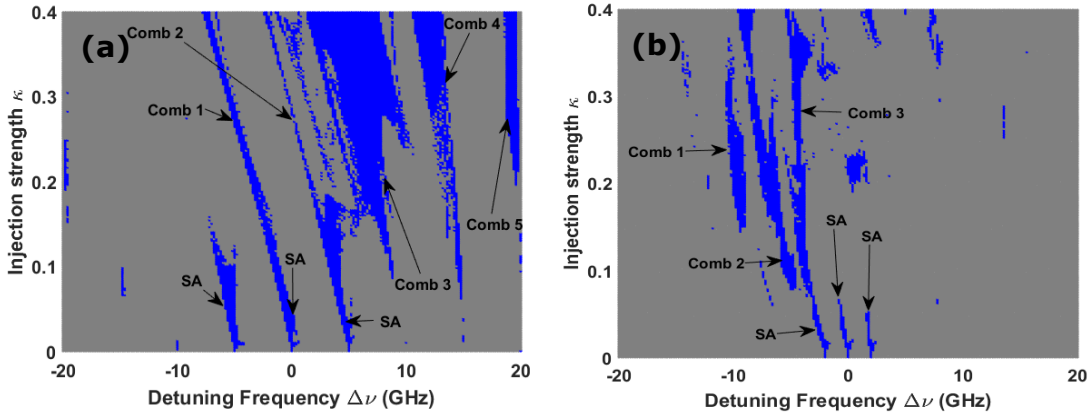

Figure 5.7: Numerical mapping of nonlinear dynamics of a semiconductor laser subject to a flat optical frequency comb injection. (a) and (b), should be compared to Fig. 5.6 (a) and (b) when all injected comb lines have now the same amplitude. The blue and gray part correspond to the time periodic dynamics and unlocked chaotic dynamics, respectively. Different regions observed: SA, Comb 1, comb 2, comb 3, comb 4 and comb 5 unlocked time periodic dynamics.

from one comb region to another.

5.4 Nonlinear wave mixing leading to comb dynamics

In this section, we experimentally vary the injection parameters and the comb properties to unveil several nonlinear dynamics of the laser diode with injection from a frequency comb. We show that the unlocked time-periodic dynamics can bifurcate smoothly from injection locking with selective amplification, nonlinear wave mixing, and complex dynamics.

5.4.1 Unlocked time-periodic dynamics for increasing injection strength

We provide more details on the dynamics leading to the unlocked time-periodic dynamics. Figure 5.8 shows the evolution of the output of the injected laser corresponding to the letters a, b, c, and d on the mapping of Fig. 5.4, i.e., injected comb spacing $\Omega = 5$ GHz.

The red arrow in the optical spectra of (a) and (d) indicates the position of the central injected comb line. For fixed detuning frequency $\Delta\nu = -0.5$ GHz, when varying the injection strength, the laser diode output shows the injection locking with selective amplification of the main comb lines in Fig. 5.8 (a). These dynamics are labeled as "SA" in the mapping of Fig. 5.4. The suppression ratio of the side injected comb lines is around 20 dB. From Fig. 5.8 (a), when increasing the injection strength, the injected laser output shows a modulated power as a result of a nonlinear wave mixing involving the detuning and a new frequency that depends on the injected comb. Wave mixing is always observed when the injection parameters are close to the limit of the SA region. In the region of wave mixing, the injected laser output can bifurcate to fractional injection locking leading to the harmonics frequency comb generation, as observed in [16, 18]. When we keep increasing the injection strength, the laser output becomes more complex as shown in Fig. 5.8 (c). We will not discuss the chaos and the complex dynamics properties here. When we further increase the injection strength, the laser output displays an unlocked time-periodic dynamics corresponding to a new frequency comb in Fig. 5.8 (d). This new comb is found in the "comb 2" region. Unlike Fig. 5.8 (a), we observe the appearance of new frequency comb lines accompanied by the increase of the power in the side comb lines. We also observe an offset of the main comb lines with respect to the frequency of the central comb line of the injection laser.

Figure 5.9 (a), (b), (c), and (d) analyze the times series corresponding to the optical spectra in Fig. 5.8 (a), (b), (c), and (d), respectively. Fig. 5.9 (a) and (d) correspond to the

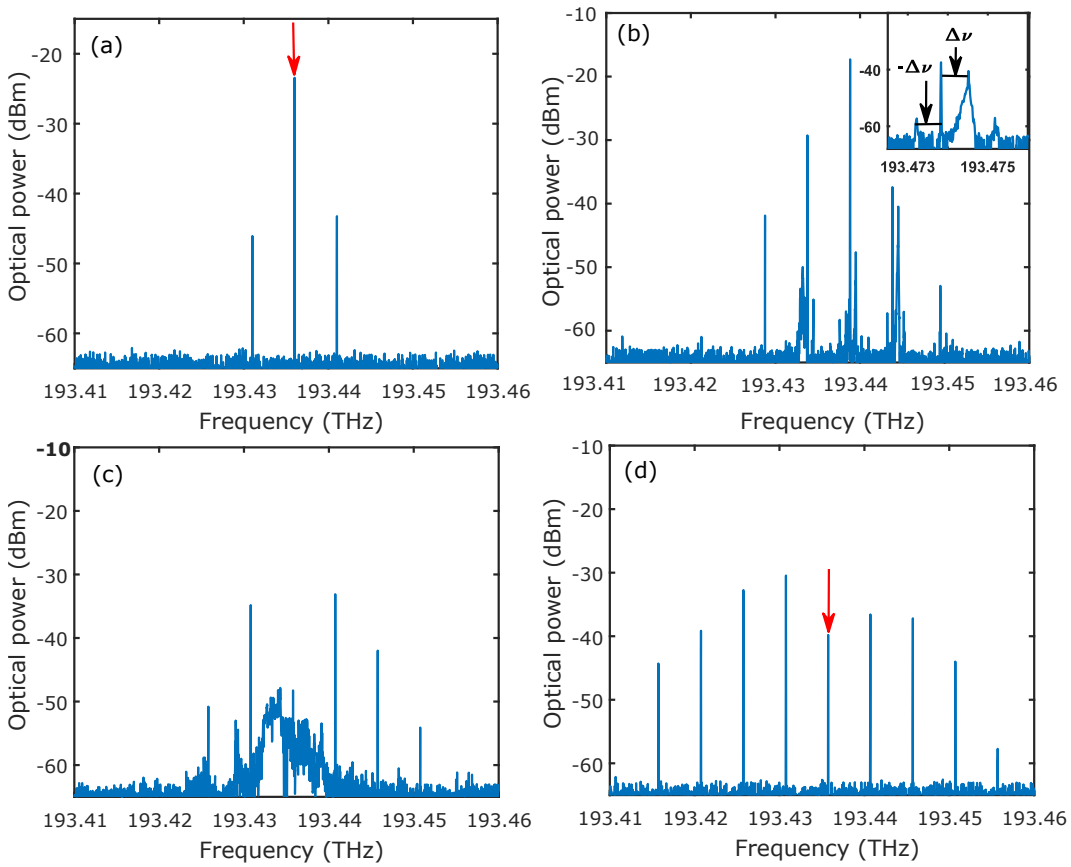

Figure 5.8: Optical spectra when varying the injection strength κ for fixed comb spacing $\Omega = 5$ GHz and detuning $\Delta\nu = -0.5$ GHz. The injected laser output shows the following dynamics: (a) Injection locking at $\kappa = 0.0045$, (b) Wave mixing at $\kappa = 0.025$, (c) complex dynamics at $\kappa = 0.061$ and (d) frequency comb at $\kappa = 0.15$. The red arrow in each optical spectra indicated the position of the central injected comb line.

times series of the injection locking with selective amplification and unlocked time-periodic dynamics (new frequency comb), respectively. In Fig. 5.9 (a) and (d), we observe a sinusoidal signal with a repetition rate corresponding to the injected comb spacing. These times series are very much close to the one of the injected field. Figure 5.9 (b) and (c) correspond to the times series of the wave mixing and complex dynamics, respectively. We observe in Fig. 5.9 (b) a modulation with two incommensurable frequencies, i.e., detuning frequency and the injected comb spacing.

5.4.2 Unlocked time-periodic dynamics when varying the detuning

Further insight into unlocked time-periodic dynamics is given in Fig. 5.10, where the optical spectra are analyzed for a fixed injection strength $\kappa = 0.36$ and detuning frequency

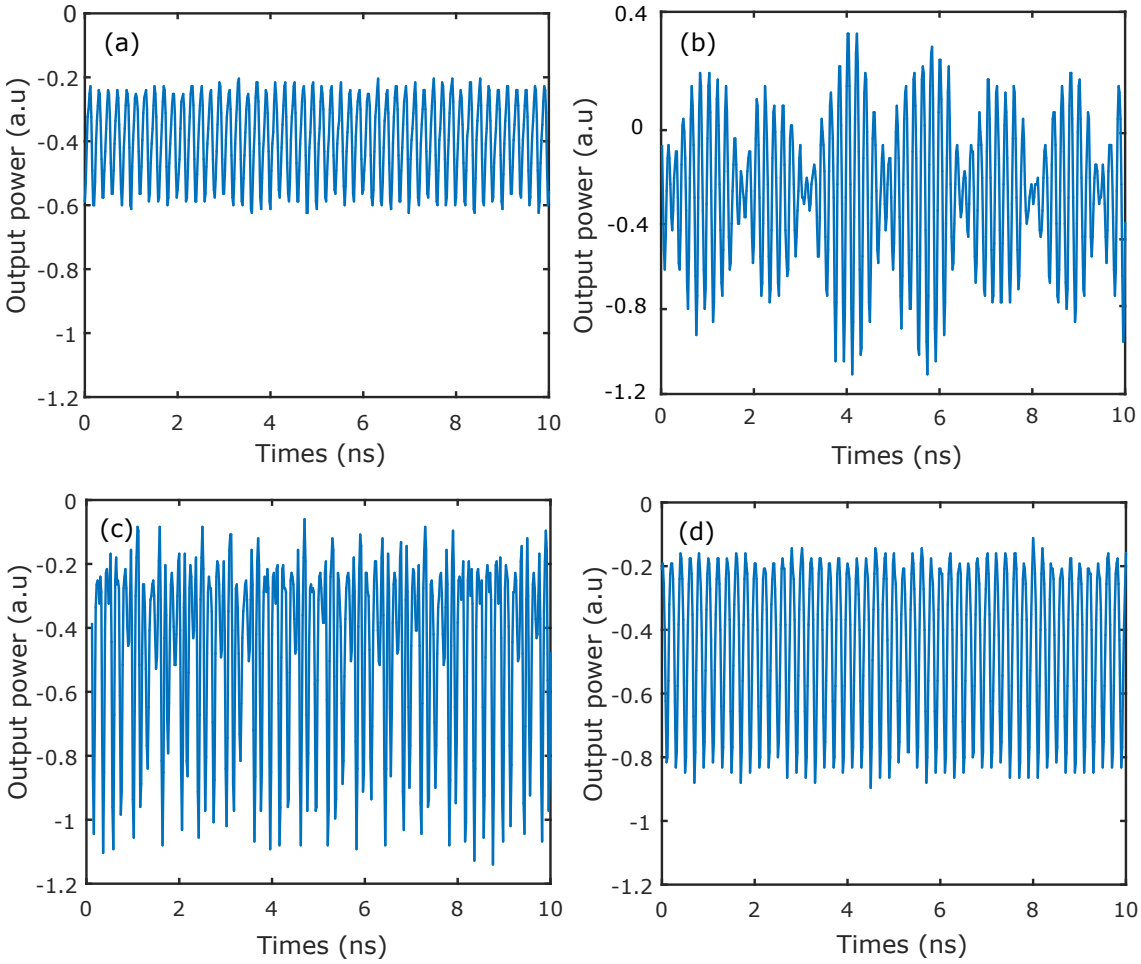

Figure 5.9: (a), (b), (c) and (d) times series corresponding to the optical spectra (a), (b), (c) and (d) of Fig. 5.8, respectively.

$\Delta\nu$ being swept around the "comb3" region in the mapping of Fig. 5.4. When varying the detuning close to the new frequency comb region, we observe the appearance of additional peaks in between the comb lines as shown in Fig. 5.10 (e) and (g). The additional comb lines gradually disappear to give rise to a new frequency comb dynamics as shown in Fig. 5.10 (f). Interestingly, when the detuning is sufficiently close to a fractional value of the injected line spacing, harmonics frequency comb, i.e., frequency comb with harmonics comb spacing compared to the injected comb is observed. The times series corresponding to optical spectra in Fig. 5.8 (d) and Fig. 5.10 (f) differ, but we always observe a repetition rate at the injected comb spacing. The times series here differ from the one observed in Fig. 5.9 (d).

In Fig. 5.11 we analyze the optical spectra corresponding to the letters identified in the mapping of Fig. 5.5 by a, b, c, and d. Here, the injected comb spacing is below the

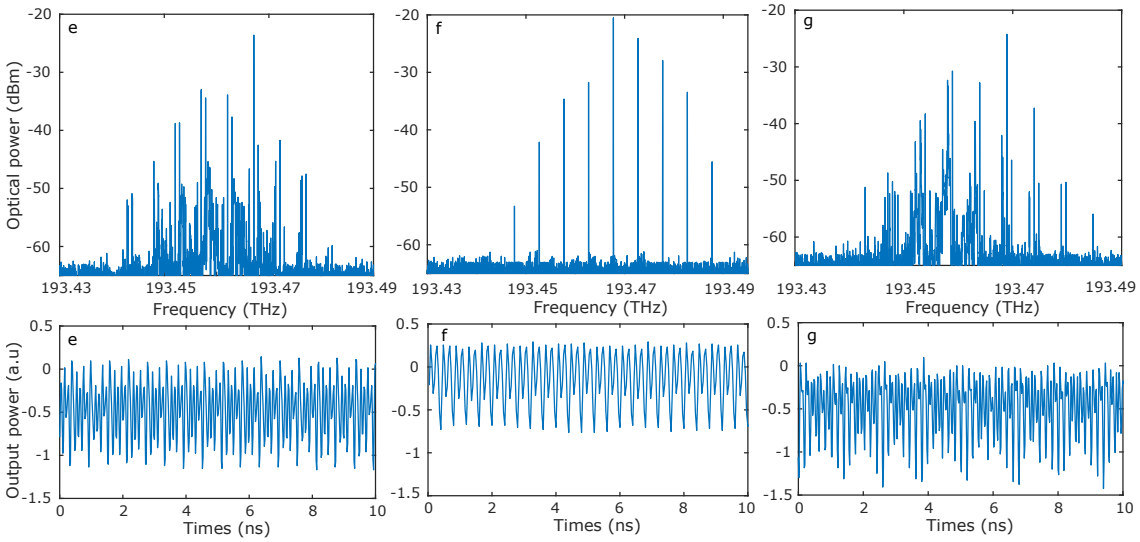

Figure 5.10: Optical spectra and corresponding times series when varying the detuning $\Delta\nu$ for fixed comb spacing $\Omega = 5$ GHz and injection strength $\kappa = 0.36$ GHz. We observe: (e) and (g) Wave mixing at $\Delta\nu = 5.4$ GHz and $\Delta\nu = 9.1$ GHz, respectively, (f) new frequency comb at $\Delta\nu = 8$ GHz. The letters (e), (f) and (g) are indicated on the map of Fig. 5.4

relaxation oscillation frequency (4.8 GHz), i.e., $\Omega = 2$ GHz. These optical spectra have been recorded for fixed injection strength $\kappa = 0.3686$, but varying the detuning. To better visualize the detuning, we show in the optical spectra of Fig. 5.11 (a), (b), and (c) red and black arrow to indicate the frequency position of the central injected comb line and injected laser free-running frequency, respectively. Figures 5.11 (a)-(c) correspond to frequency combs dynamics in the regions "comb 1", "comb 2", and "comb 3", respectively.

The comparison between Fig. 5.11 (a), (b), and (c) shows that the detuning frequency can be used to precisely control the comb properties, i.e., number of total lines, the flatness of the comb lines, and power distribution among comb lines. It is also important to highlight that the combs in Fig. 5.11 (a) and (b) are obtained for detuning values more than 7 and 5 times the injected comb spacing, respectively. When the laser diode is injected with a single frequency laser, the stable dynamics is a stationary dynamics whose stability is bounded by the injection locking region [124]. That injection locking range is typically of maximum few GHz wide although its frequency span can be extended in specific laser systems that incorporate quantum dots [219, 220] as a result of the improved relaxation oscillation damping in these lasers. In the comb injection, by contrast, stable dynamics are frequency combs with the same repetition rate as the injected comb spacing and are

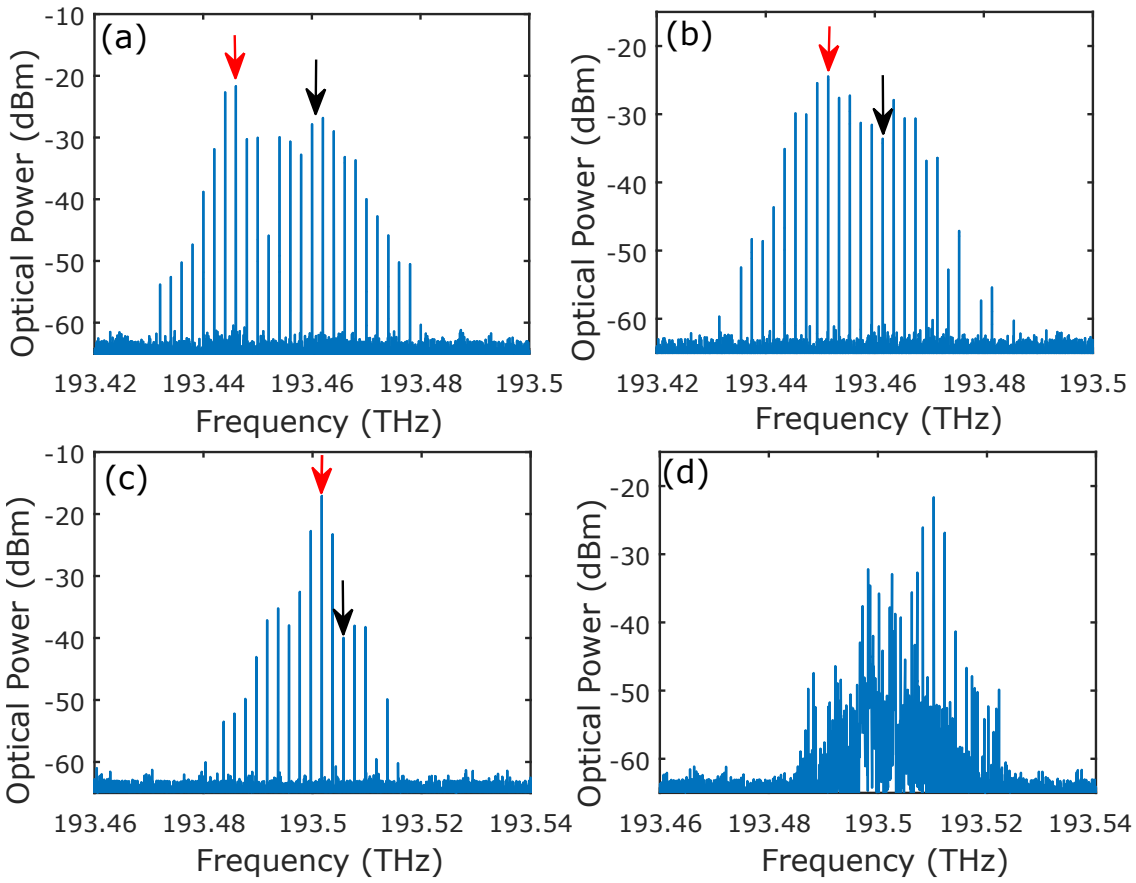

Figure 5.11: Optical spectra for fixed comb spacing to $\Omega = 2$ GHz: (a) Unlocked time periodic dynamics in "comb 1" region at $\kappa = 0.3686$ and $\Delta\nu = -15$ GHz, (b) Unlocked time periodic dynamics in "comb 2" region at $\kappa = 0.3686$ and $\Delta\nu = -10.2$ GHz, (c) Unlocked time periodic dynamics in "comb 3" region at $\kappa = 0.3686$ and $\Delta\nu = -3.8$ GHz and (d) complex dynamics at $\kappa = 0.3177$ and $\Delta\nu = 5.7$ GHz.

observed in several regions in the plane of the injection parameters extending over several tens of GHz of detuning and significantly beyond the SA region. Figure 5.12 (a), (b), (c) and (d) correspond to the times series of the optical spectra in Fig. 5.11 (a), (b), (c) and (d), respectively. Unlike the times series corresponding to the comb dynamics in Fig. 5.8 (d), the times series in Fig. 5.12 (a)-(c) are not sinusoidal, but we checked that the repetition rate is always equal to the injected comb spacing. As shown in Fig. 5.12 (a)-(c), we observe that the comb dynamics change with the appearance of the new pulse at a low intensity from a region to another, as discussed in the bifurcation diagrams in chapter 4 (section 4.4). The injection parameters can be used to control the new comb properties inside or between comb regions.

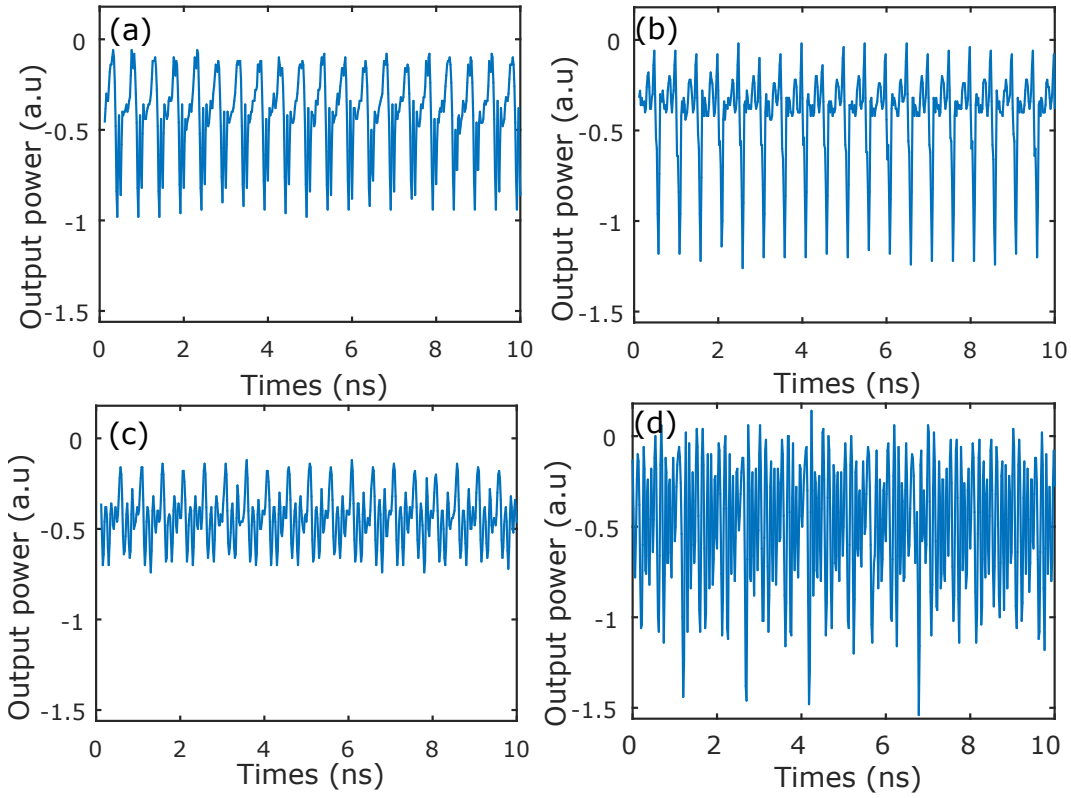

Figure 5.12: (a), (b), (c) and (d) times series corresponding to the optical spectra (a), (b), (c) and (d) of Fig. 5.11, respectively.

5.5 Comb performance analysis

This section analyzes the properties of the new frequency comb. We carefully tune the injection parameters and the injected comb properties to show how far the total number of output comb lines and the Carrier to Noise Ratio (CNR) can be increased. Besides the comb properties, we provide an in-depth analysis of the time-bandwidth product and the relative phase between comb lines. We also analyze the resulting output comb lines when varying the injection current in the injected laser.

The properties of a frequency comb depend on the expected applications. Most of the frequency comb applications require a large number of lines and higher power in the individual comb lines. In the following, we will characterize the resulting comb properties by the number of resulting comb lines and the Carrier to Noise Ratio (CNR). Figure 5.13 (a) shows the optical spectrum from which we analyze the frequency comb properties. The pulse width in the corresponding time-series is shown in Fig. 5.13 (b). The vertical

double arrow in the optical spectrum of Fig. 5.13 (a) indicates the CNR, i.e., the difference, in dB, between the maximum amplitude in the optical spectrum and the noise level. We analyze the resulting output comb lines by considering the comb lines whose amplitude lies above 30 dB from the maximum amplitude. The time-bandwidth product is measured by estimating the product of the optical spectrum width at half maximum and the corresponding pulse width.

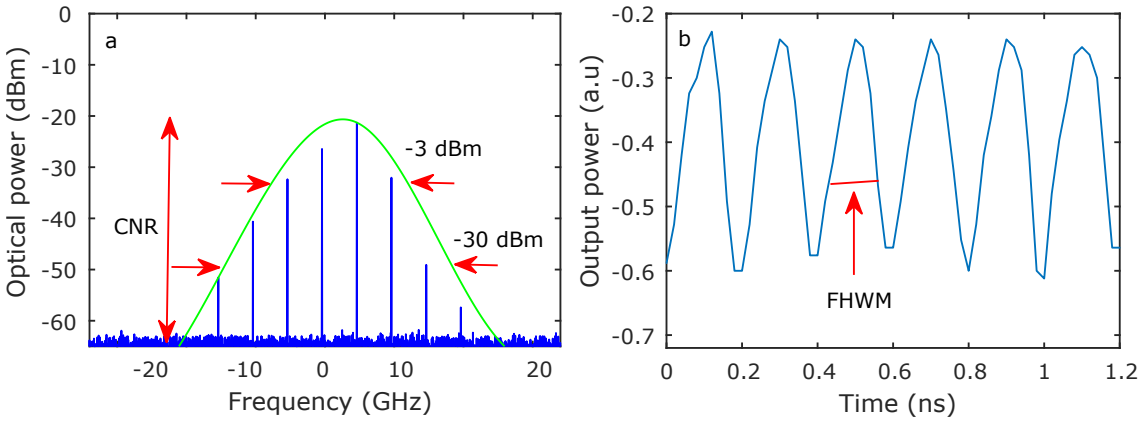

Figure 5.13: Analysis method of the output comb properties. (a) and (b) optical spectrum in comb 2 region in the map of Fig. 5.4 at $\kappa = 0.1398$ and the corresponding time series of the output power.

5.5.1 Number of lines versus the injection parameters

In Fig. 5.14 (a), for $\Omega = 5$ GHz and $\Delta\nu = -3$ GHz, we show the pulse width and the corresponding number of output comb lines of the injected laser as a function of the injection strength (κ) within the parameter range corresponding to the new frequency comb region (comb2) in Fig. 5.4. The pulse width decreases with the injection strength while the corresponding number of output comb lines in the injected laser increases, which is in excellent agreement with our previous theoretical prediction in chapter 4. Figure 5.14 (b) analyzes the number of output lines on the left vertical axis and the Carrier to Noise ratio (CNR) on the right vertical axis, respectively, for fixed comb spacing $\Omega = 2$ GHz and injection strength $\kappa = 0.46$. The total number of lines and the CNR both increase when the detuning frequency varies toward negative values. Optimization of the output number of lines up to 7 times the number of injected lines and a maximum CNR of 50 dB are achieved in our experiment.

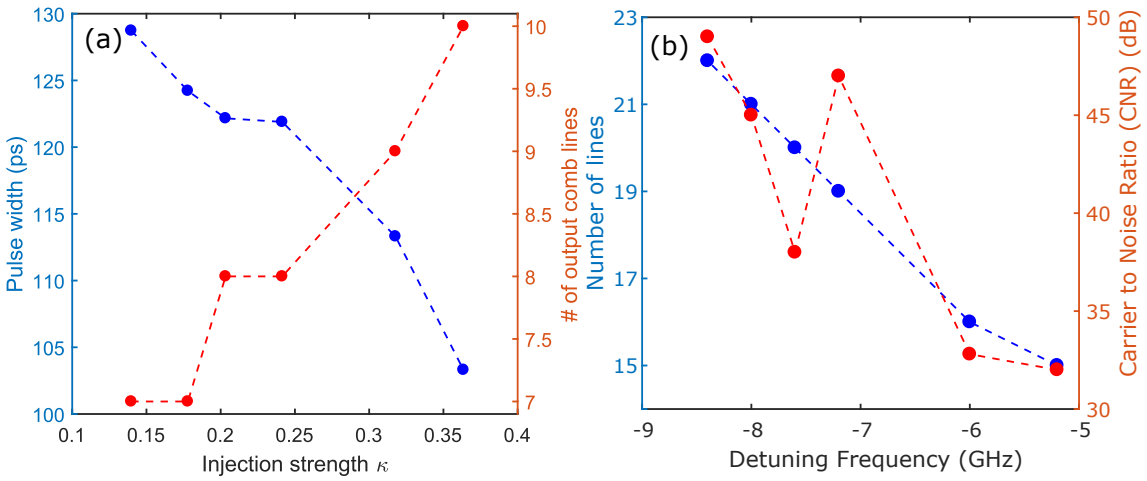

Figure 5.14: Control of the number of total comb lines with the injection parameters. (a) pulse width at half maximum (left vertical axis) and number of output comb lines of the injected laser (right vertical axis) for fixed $\Omega = 5$ GHz and detuning $\Delta\nu = -3$ GHz when varying the injection strength and (b) number of output lines and Carrier to Noise ratio (CNR) on the left and right vertical axis, respectively for fixed comb spacing $\Omega = 2$ GHz and injection strength $\kappa = 0.46$.

5.5.2 Time bandwidth product and phase dynamics

Figure 5.15 plots the time-bandwidth product, i.e., the product between the pulse width at half-maximum and the spectral width at half-maximum computed as shown in Fig. 5.13.

The time-bandwidth product is measured for fixed detuning frequency $\Delta\nu = -3$ GHz and varying the injection strength in the "comb 2" region in Fig. 5.4. When varying the injection strength, we observe that the time-bandwidth product increases from 0.93 at $\kappa = 0.1398$ to 1.14 at $\kappa = 0.3635$, which is much close to 3 times the Fourier limit ~ 0.44 for a Gaussian pulse shape. This is in very good agreement with our theoretical findings in [22]. Interestingly, the time-bandwidth product saturates at high injection strength. This can be explained by a proportionality between the increase in the number of output comb lines and the decrease in the pulse width when we increase the injection strength as shown in Fig. 5.14.

5.5.3 Impact of the bias current on the comb dynamics

Figure 5.16 shows the impact of the injection current on the comb dynamics for fixed comb spacing $\Omega = 2$ GHz. For fixed injection parameters detuning $\Delta\nu = 0$ GHz and $\kappa = 0.22$,

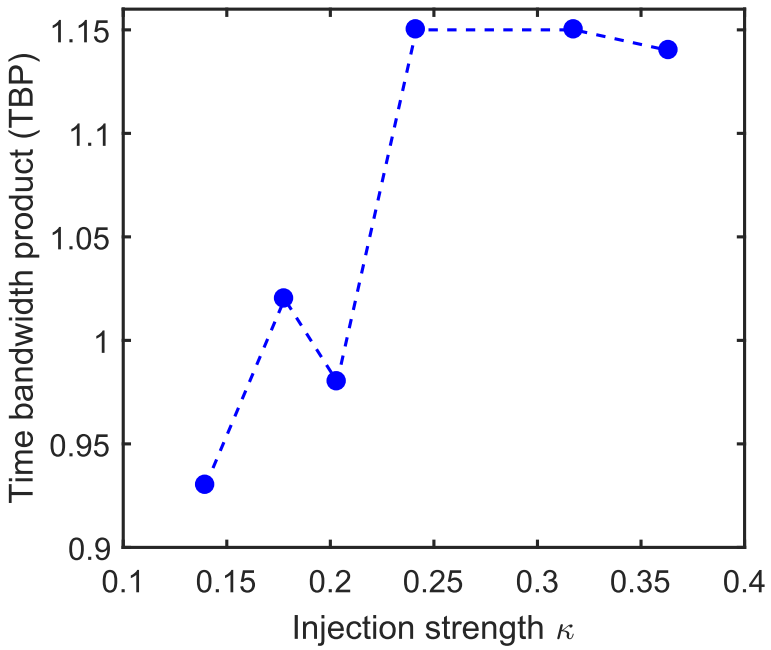

Figure 5.15: Tailoring of the frequency comb properties through injection parameters. Time-bandwidth product for fixed comb spacing $\Omega = 5$ GHZ detuning $\Delta\nu = -3$ GHz.

when varying the injection current from 14 mA to 16 mA, we observe an increase of 60 % of the number of output lines from Fig. 5.16 (a) to (b). We summarize in Fig. 5.16 (c) the evolution of the comb properties, i.e., the number of lines on the left vertical axis and the CNR on the right vertical axis. The number of output lines increases with the injection current to achieved 26 lines at $I_{th} = 18$ mA while the CNR decreases at the same time. The decrease in the CNR is due to the dynamical instability leading to the increase of the noise pedestal. To provide further inside of the injection current on the comb properties, we plot in Fig. 5.16 (d) the number of comb lines for fixed comb spacing $\Omega = 2$ GHz and detuning $\Delta\nu = -9.4$ GHz for two distinct injection currents, i.e., $I_{th} = 12$ mA in red and $I_{th} = 15$ mA in blue. The number of lines increases in both cases with the injection strength. For the same region in the plane of the injection parameters, the number of resulting output lines is larger for $I_{th} = 15$ mA than for $I_{th} = 12$ mA.

5.5.4 Tailoring the comb dynamics

To analyze how to control the comb dynamics, we calculate the number of total output comb lines in regions labeled comb1, comb2, comb3 of Fig. 5.5. In Fig. 5.9, we plot the number of output lines when varying $\Delta\nu$. For fixed κ, the number of output comb lines

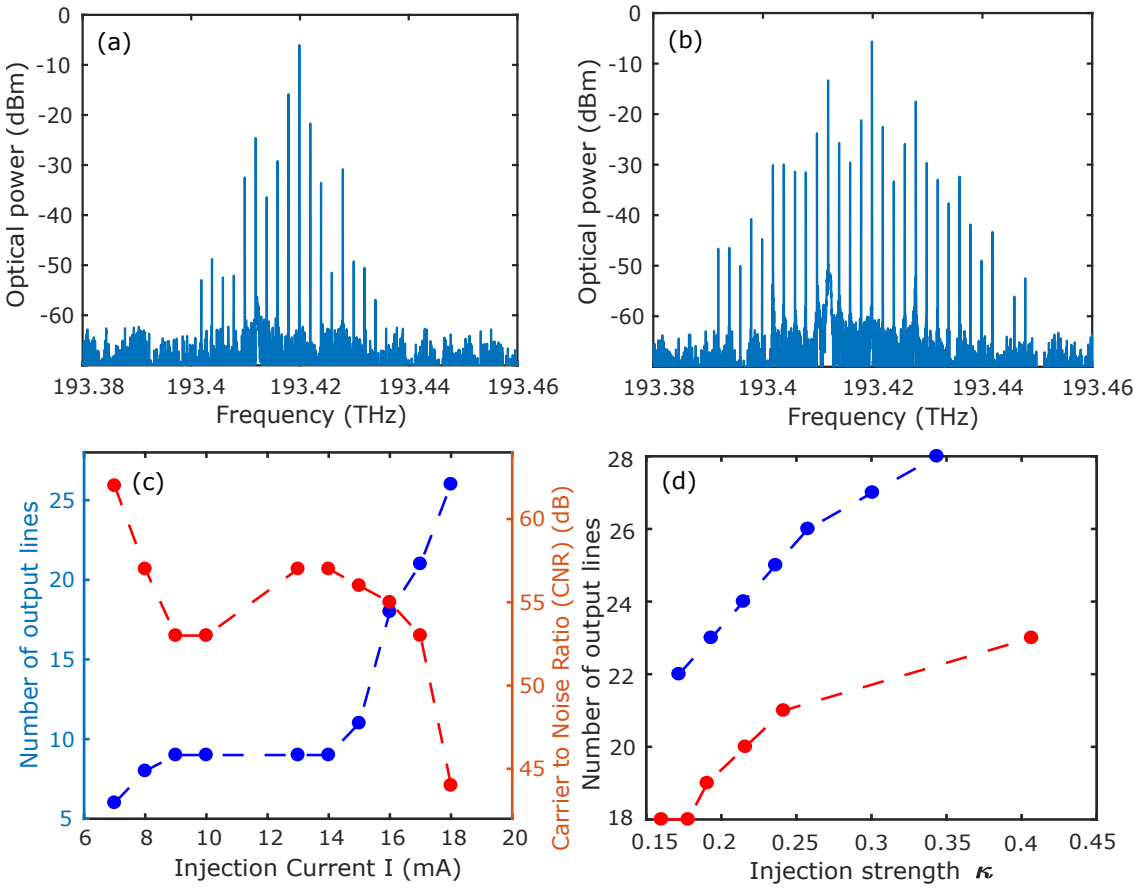

Figure 5.16: Control of the number of resulting comb lines with the injection current. These figures are obtained for fixed injected comb spacing $\Omega = 2$ GHz. (a) and (b) optical spectra for $\Delta\nu = 0$ GHz and $\kappa = 0.22$ when varying the injection current from $I_{th} = 14$ mA to $I_{th} = 16$ mA. (c) evolution of the number of total line on the left vertical axis and the CNR on the right vertical axis for $\Delta\nu = 0$ GHz and $\kappa = 0.22$ when varying the injection current. (d) number of output lines as a function of the injection strength for $\Delta\nu = -9.4$ GHz. The red and blue curves are obtained for $I_{th} = 12$ mA and $I_{th} = 15$ mA, respectively.

increases with the detuning. The larger is the detuning value, the larger is the number of output lines in the injected laser. The minimum value of the number of lines is always found in the comb region connected to the SA region of the central injected comb line. In the "comb3" region, for fixed κ, when we change the detuning from negative to positive values, we observe an abrupt increase of the number of lines in the optical spectrum. This result confirms our numerical analysis in [22]. The injection experiment, therefore, provides a very fine-tuning of the comb properties in the injected laser.

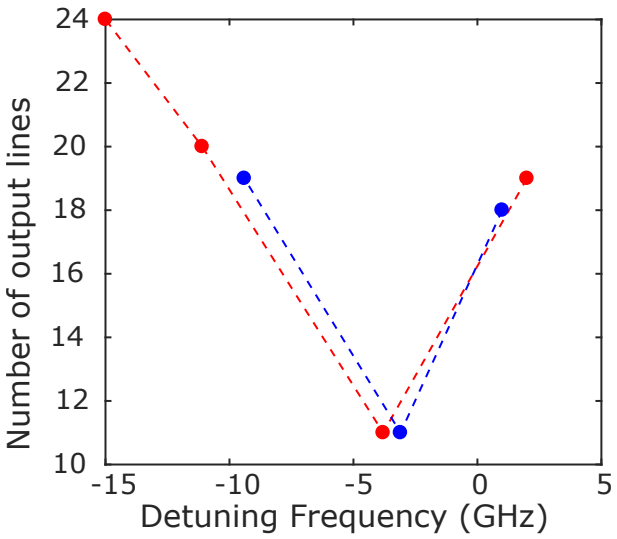

Figure 5.17: Number of output comb lines in different comb regions as a function of detuning frequency for fixed $\Omega = 2$ GHz. The blue and red curves are obtained for $\kappa = 0.2542$ and $\kappa = 0.3813$, respectively.

5.6 Conclusion

In conclusion, we have demonstrated experimentally and numerically the nonlinear dynamics of a single-mode laser subject to the optical injection from a modulated signal. By varying either the injection parameters (injection strength, detuning frequency) or the comb properties (amplitude of the injected lines, comb spacing), we identify a rich variety of nonlinear dynamics, including selective amplification of the main comb line, wave mixing between comb lines spacing and frequencies at detuning values, comb dynamics and complex dynamics. Most importantly, the comb dynamics are observed even for very large detuning values, being several times the injection comb spacing. The injection parameters can be tuned to carefully extend the resulting number of total comb lines and the relative amplitudes of comb lines. We have increased the number of lines in the comb by a factor as high as 10 times and the bandwidth from 4 GHz to 40 GHz for the case of 2 GHz comb injection. The CNR is as high as 62 dB. The injection current in the injected laser is also another parameter to control the number of total comb line for fixed injection parameters. In comparison to other approaches, the proposed solution is interesting because of the large number of parameters and tunability in the control of the comb properties. Finally, the experiment and theory unveil the importance of the asymmetry of the injected comb in the comb dynamics. This experiment and the excellent agreement

with numerical simulations motivate further analysis of more complex features such as injection of a frequency comb into a Vertical-Cavity Surface-Emitting Laser (VCSEL) to exploit the polarization dynamics for applications like dual-comb spectroscopy and polarization division multiplexing in optical data communications.

6

Tailoring the frequency comb properties through VCSEL polarization dynamics

Contents

6.1 Motivations 112

6.2 Setup for VCSEL injection 113

6.3 Polarization switching and bistability 116

6.4 Bifurcation scenarios leading to polarized harmonics comb . . . 118

6.4.1 Detuning induced harmonics comb 118

6.4.2 Injected power induced harmonics comb 119

6.4.3 Polarization resolved optical spectra 125

6.5 Bifurcation scenarios leading to two polarization comb 126

6.5.1 Detuning close to zero 126

6.5.2 Detuning close to the birefringence 128

6.5.3 Polarization resolved analysis of two polarization comb dynamics . 128

6.5.4 Coherence of the two polarization comb lines 129

6.6 Tailoring the polarization frequency comb 130

6.6.1 General case 130

6.6.2 Central comb line close to Y-PM 131

6.6.3 Central comb line close to X-PM 132

6.7 Conclusion 133

Optical frequency combs have found applications in optical communication and dual-comb spectroscopy. To increase the network connectivity speed debit and optical transmission bandwidth through optical fiber, the optical injection of a frequency comb into a DFB laser has attracted much attention. We have shown in chapter 4 and 5 that a single-mode diode laser can show interesting locked and unlocked time-periodic dynamics when subject to an optical frequency comb injection. Compared to the EEL, VCSEL provides notable improvement due to their design. Opposite to the EEL, where the light is emitted parallel to the surface, the VCSEL emits perpendicularly to the surface. The emission properties of the VCSEL lead to a high-quality output beam compared to the EELs. Here, we analyze the nonlinear dynamics and polarization properties of a VCSEL with a comb injection. When the polarization of injection is tuned to be orthogonal to that of the VCSEL, polarization switching leads to a significantly extended output comb in the depressed polarization mode. Most importantly, for some injection parameters, polarization mode competition can induce two combs with orthogonal polarizations. The comb spacing of the two polarization combs is controlled by the injection parameters through the mechanism of harmonic comb generation. Harmonic frequency combs with the repetition rate of hundreds of MHz are demonstrated. Such combs have been recently used for dual-comb spectroscopy [196–198]. We also report on the tailoring of the resulting comb properties, i.e., the power of the individual output comb lines above the noise pedestal (Carrier to Noise Ratio (CNR) and the number of lines (bandwidth) with the injection parameters. CNR and the number of output lines up to 60 dB and 15 times the number of injected lines are demonstrated. Finally, we unveil several interesting nonlinear polarization dynamics of VCSEL when varying both the injection parameters and the comb properties, which extend our work beyond the particular applicability of the reported frequency combs. We observe that the power required to switch increases with the injected comb spacing and there is no linear dependency between the comb spacing and the switching threshold.

6.1 Motivations

VCSEL is a single longitudinal mode device due to its cavity properties. Multi-transverse mode operation can be induced in the VCSEL in free-running when varying the drive current and the temperature [221]. The design of the VCSEL leads to the possibility of emission with polarization with orthogonal direction. Switching between the two linear

polarization modes can be induced with the drive current and the operation conditions [69, 72]. For instance, it has been experimentally and theoretically shown that with a field polarized perpendicularly to that of the free-running VCSEL can induce several bifurcation sequences leading to PS. Experimental and theoretical investigation have provide a wide view on the scenarios leading to the polarization switching (PS) in VCSEL [73, 125–127, 129, 130, 222]. Standard numerical method and numerical tool have used the rate equation of the VCSEL to provide an in-depth analysis of the bifurcation scenarios around the PS points [73].

As introduced in the chapter 2, beyond the PS, orthogonal optical injection in VCSEL can promote interesting polarization dynamics including, nonlinear wave mixing, periodic dynamics, polarization mode hopping and chaotic dynamics [84, 115, 223–226]. Very recently, VCSEL have even shown complex polarization dynamics without any external perturbation [227]. Besides the injection parameters (injected power and detuning frequency), the polarization of injection provides an additional possibility to induce and control PS and its corresponding bistability [74, 130, 134–136, 223, 224].

The possibility of the VCSEL to select, amplify, and transmit the desired frequency line when injected with an optical frequency comb has been recently reported [228]. More specifically, the authors evaluate the performance of filtering and amplification effect in a single-mode VCSEL with a frequency comb injection. Yet to date, the nonlinear polarization dynamics of the VCSEL under optical frequency comb injection have not been addressed so far and deserve significant attention.

In chapters 4 and 5, we have experimentally and theoretically demonstrated that a single-mode edge-emitting laser can show injection locking with selective amplification, nonlinear wave mixing and unlocked time-periodic dynamics under narrow optical frequency comb injection. Here, we address the polarization dynamics of VCSEL subject to a modulated signal optical injection such as the one from a frequency comb.

6.2 Setup for VCSEL injection

In Fig. 6.1 (a), we show the experimental setup for the optical injection of a frequency comb in a VCSEL. A continuous-wave (CW) tunable laser (Yenista Tunics T100S) is amplified by an Erbium-Doped Fiber Amplifier (EDFA) and sent to a $LiNbO_3$ Mach-Zehnder (MZ)

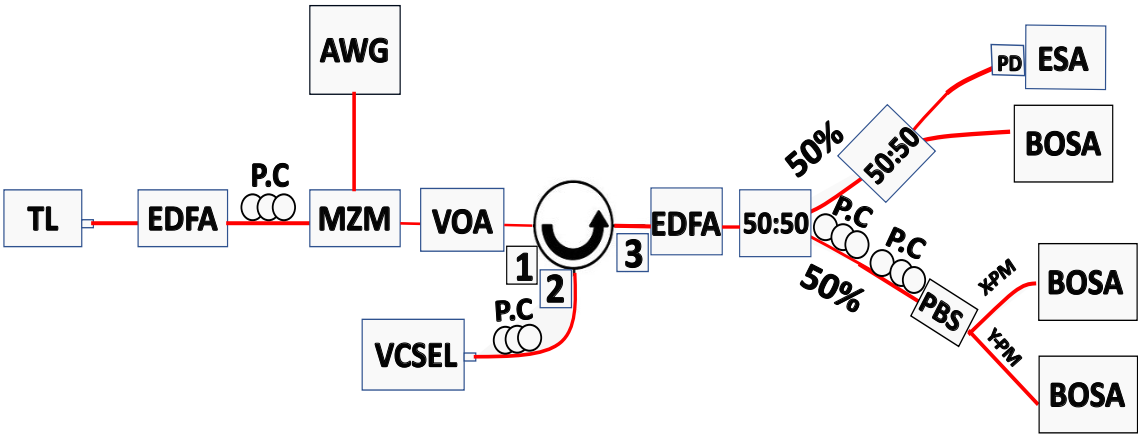

Figure 6.1: Set up for frequency comb injection into a VCSEL. TL: Tunable Laser, EDFA: amplifier, P.C: Polarization Controller, AWG: Arbitrary Waveform Generator, MZM: Mach-Zehnder Modulator, VOA: Variable Optical Attenuator, BOSA: Brillouin Optical Spectrum Analyser, PD: photodiode.

Modulator with a 12.5 GHz bandwidth. The linewidth of the tunable laser is around 30 MHz. The polarization controller P.C at the input of the (MZ) Modulator allows aligning its input with the polarization of the tunable laser. Electric signal modulation is generated by an Arbitrary Waveform Generator (AWG) (Tektronix AWG 700002A) and sent to the RF port of the (MZ) Modulator. At the output of the (MZ) modulator, an optical frequency comb with lines of different power levels is generated. The total optical power of the comb lines is controlled with a Variable Optical Attenuator (VOA). The injected laser is a single-mode VCSEL which is biased at a current of I=6 mA corresponding to 2 times the threshold current. At this current, the total output power has been measured to be $P_{VCSEL} = 330$ µW. The dominant Polarization Mode (X-PM) emits at $\sim$ 1553.8 nm. A fiber circulator is arranged to provide isolation for the VCSEL injection. The polarization controller at the input of the VCSEL allows controlling the polarization of the injected light. An amplifier (EDFA) is used to amplify the VCSEL output. An optical coupler is used to split the light in two paths with equal power. The first path is used to analyze the nonlinear dynamics of the total output power of the VCSEL with a high-resolution optical spectrum analyzer BOSA 400, which allows monitoring optical spectra with a resolution of about a minimum of 0.1 pm or 12 MHz at the operating wavelength of 1550 nm. In the second path, two consecutive polarization controllers are used to provide maximum alignment between the linear polarization modes of the VCSEL and the axes of the polarized beam splitter (PBS) to discriminate the linear polarization modes and observe them in separate optical spectra on the BOSA.

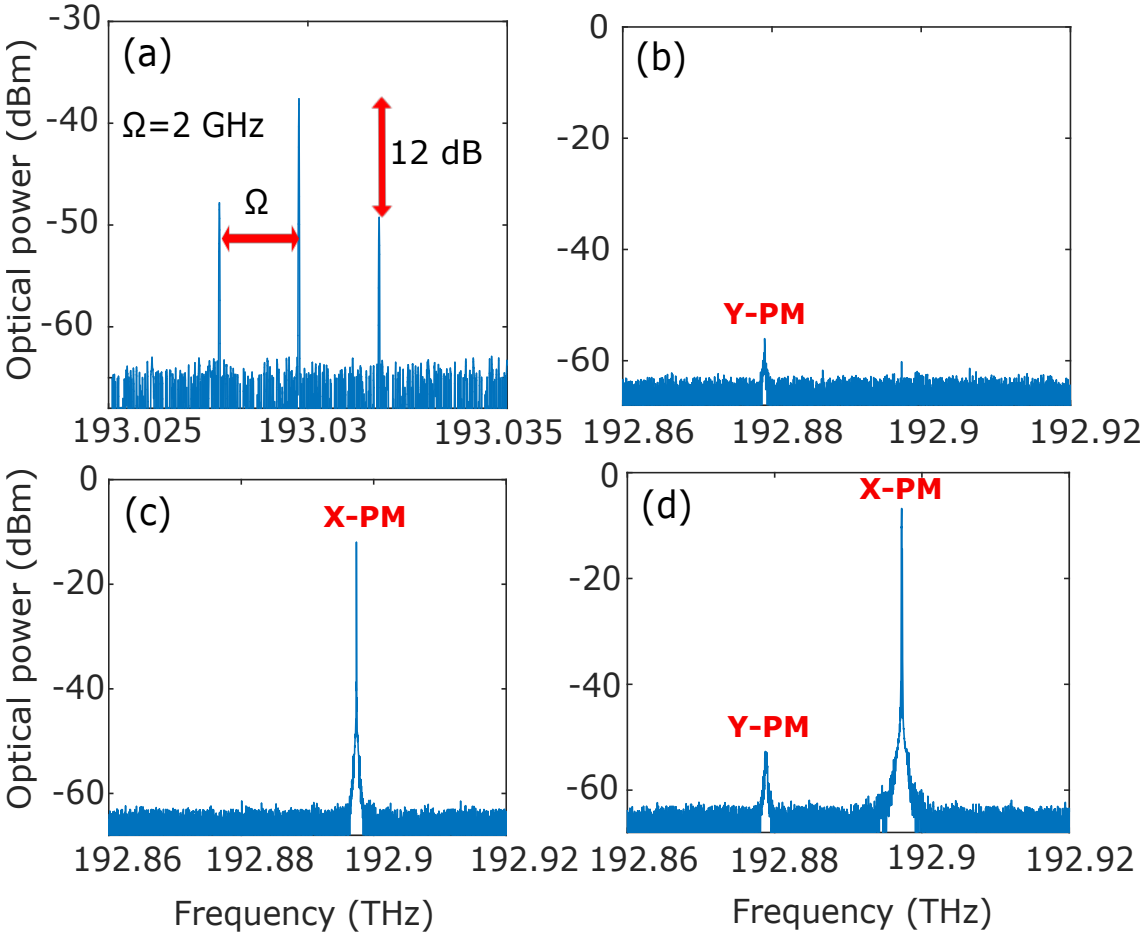

Figure 6.2: (a) Optical spectra of the injected comb with a comb spacing of $\Omega = 2$ GHz. (b), (c) and (d) correspond to the polarization resolved optical spectra of Y-PM, X-PM and the total output, respectively.

Figure 6.2 (a) shows the optical spectrum of the injected comb for a fixed comb spacing $\Omega = 2$ GHz. The difference between the power of the central comb line and the side comb lines is around 12 dB. Figure 6.2 (b) shows the optical spectrum of the depressed polarization optical power (Y-PM) of the VCSEL in the free-running regime. The maximum power of this polarization mode is around -53 dBm. Figure 6.2 (c) shows the optical spectrum of the dominant polarization (X-PM) of the VCSEL in the free-running regime. This polarization mode emits with a maximum power of around -10 dBm. Figure 6.2 (d) presents the optical spectrum of the total output power of the VCSEL in free running. The difference between the frequencies of the linear polarization modes, which results from the VCSEL birefringence, is around 17.71 GHz at 23°C. In the following, the frequency detuning $\Delta\nu$ is defined from the frequency of the central comb line to the frequency of

VCSEL X-PM i.e., $\Delta\nu = \nu_0 - \nu_X$, where ν_0 and ν_X are the frequencies of the central injected comb line and the X-polarization mode of VCSEL (X-PM), respectively. To make sure that the polarization of the injection matches with the Y-polarization mode of the VCSEL, we analyze the output dynamics of the VCSEL. It is well known that when the polarization of the injection matches with that of the VCSEL, the smallest injected power is required to switches the VCSEL. We set the detuning to zero from Y-PM and adjust the polarization such that the polarization switching accompanied by injection locking is achieved for minimum injected power.

6.3 Polarization switching and bistability

In this section, we will analyze the polarization dynamics of the VCSEL with optical frequency comb injection. More specifically, we map in the plane of the injection parameters the polarization switching and the corresponding bistability when varying the injected comb spacing.

We analyze in Fig. 6.3, the polarization switching (PS) curve in the plane of the injection parameters. We fixed the detuning frequency, $\Delta\nu = \nu_0 - \nu_x$ and then we increase and decrease the injected power to find the PS power and the corresponding bistability. We consider PS is achieved when the difference between the power of the normally depressed polarization mode (Y-PM) and X-PM is larger than 30 dB. The main goal is to evaluate the impact of the injected comb spacing on the evolution of the switching power and the corresponding bistability. To this end, we compare in the plane of the injection parameters, the PS on-power and off-power for single-frequency injection and for different injected comb spacing. Figure 6.3 maps the comparison of the PS curve between single-mode injection and comb injection when increasing the injected power and injected comb spacing. Figure 6.3 (a) shows the mapping for single-mode and comb with comb spacing $\Omega = 500$ MHz, (b) $\Omega = 500$ MHz comb and $\Omega = 2$ GHz comb injection, and (c) $\Omega = 2$ GHz comb and $\Omega = 4$ GHz comb injection.

The central injected comb line matches X-PM and Y-PM's frequency position when the detuning frequency is $\Delta\nu = 0$ GHz and $\Delta\nu = -17.7$ GHz, respectively. We observe that the PS curves and the corresponding bistability are impacted by frequency comb injection. For negative detuning from Y-PM, i.e., detuning smaller than $\Delta\nu = -17.7$ GHz, the width of the bistability area is larger than for positive detuning both for single-mode and

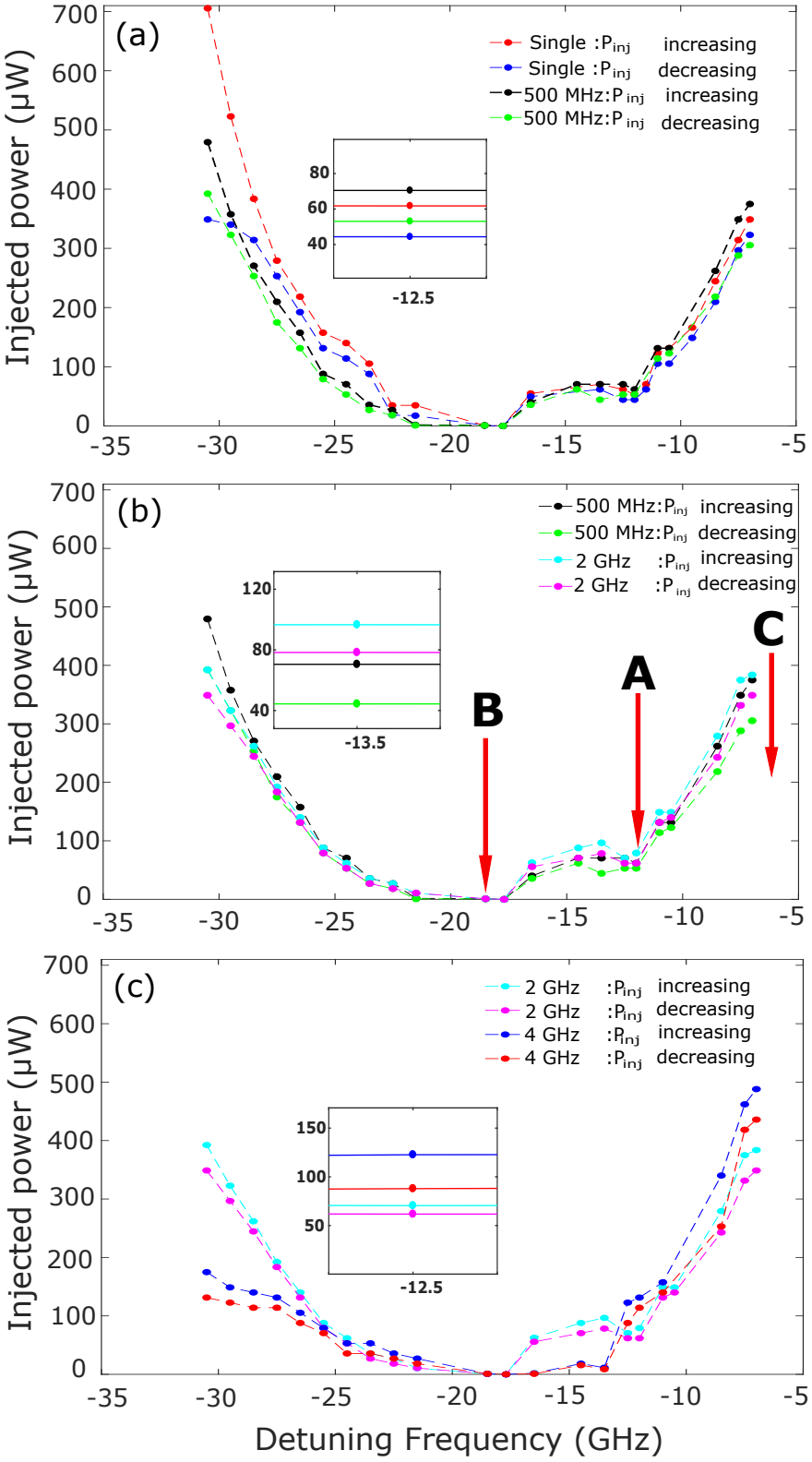

Figure 6.3: Mapping of polarization switching bistability in the plane of injection parameters for single and frequency comb injection. In the map, we analyse the switching curves when increasing the injected comb spacing. (a) single-mode and 500 MHz comb injection , (b) 500 MHz and 2 GHz comb injection, and (c) 2 GHz and 4 GHz comb injection.

comb injection. This is in agreement with the observation made for orthogonal injection with single frequency injection [130]. The injected power required to switch is larger for single-mode injection than for comb injection when the detuning is negative, i.e., $\Delta\nu < -17.7$ GHz. Most importantly, in the range of detuning $\Delta\nu < -17.7$ GHz, the switching power decreases when the injected comb spacing is increased. For detuning frequency positive, i.e., $\Delta\nu > -17.7$ GHz, the power required to switch is smaller for single-frequency injection than for comb injection and increases with injected comb spacing. Figures 6.3 (b) ($\Omega = 500$ MHz and $\Omega = 2$ GHz comb spacing) and (c) ($\Omega = 2$ GHz and $\Omega = 4$ GHz comb spacing) show that there is no simple linear dependence between the increase of the PS power and the increase of the injected comb spacing. Depending on the injection parameters, PS can lead to different polarization dynamics. The red arrows in the mapping of Fig. 6.3 (b) indicate the detuning for which we will provide an in-depth bifurcations analysis in the following.

6.4 Bifurcation scenarios leading to polarized harmonics comb

In this section, we will analyze the different bifurcation scenarios leading to polarized optical frequency comb dynamics. The effect of the detuning frequency and the injected power on the new comb dynamics and the related harmonics comb lines are also highlighted. The polarization-resolved properties of the comb dynamics will be studied. Finally, we will report on the phase relationship between the polarized comb lines.

6.4.1 Detuning induced harmonics comb

We first analyze the VCSEL output for fixed injected power when doing a sweep of the detuning between the two polarization modes (X-PM and Y-PM). Figure 6.4 shows a bifurcation scenario for a fixed injected comb spacing of $\Omega = 2$ GHz and fixed injected power of $P_{inj} = 150$ µW. In Fig. 6.4, the top and bottom show the optical spectra and the corresponding zoom. When varying the detuning frequency from X-PM to Y-PM, the VCSEL first bifurcates successively to complex dynamics and unstable comb (noisy comb) in Y-PM (not shown) with the presence of frequency lines around the main comb lines. These frequency lines disappear gradually to give rise to a stable comb as shown in Fig. 6.4 (a_1). When we keep varying the detuning frequency, the new comb solution remains stable over a wide range of parameters. It then bifurcates to an unstable comb

accompanied by new frequency lines around the main comb lines. The frequency position of these new frequency lines changes with the detuning to give rise to complex harmonics comb dynamics in Fig. 6.4 (a_2). The corresponding zoom shows that these dynamics correspond to harmonics comb at a quarter of comb spacing of Fig. 6.4 (a_1). Careful tuning of the detuning frequency may lead to harmonics comb at a quarter of the injected comb spacing creating a new comb with a repetition rate of $\Omega = 500$ MHz. Such a small comb spacing is very useful for dual-comb spectroscopy [229] because the gas spectroscopy requires typically very low resolution. The VCSEL then shows in Fig. 6.4 (a_3) a stable harmonics comb at half of the comb spacing of Fig. 6.4 (a_1). When further varying the detuning, complex dynamics take place in the VCSEL output and then bifurcate to a new harmonic comb dynamics creating new combs with comb spacing of $\Omega = 670$ MHz as shown in Fig. 6.4 (a_4).

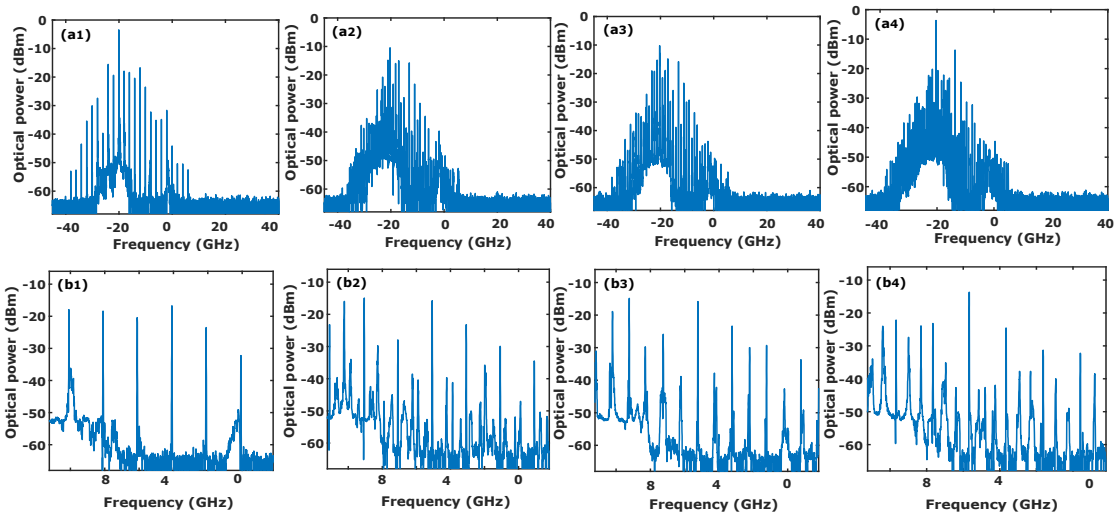

Figure 6.4: Nonlinear dynamics when varying the detuning frequency for fixed comb spacing $\Omega = 2$ GHz and injected power $P_{inj} = 150$ µW. The VCSEL output shows: (a_1) new frequency comb at $\Delta\nu = -9.8$ GHz, (a_2) complex dynamics at $\Delta\nu = -10.8$ GHz,(a_3) harmonic comb at half of the injected comb spacing at $\Delta\nu = -11$ GHz, (a_4) harmonic comb at third of the injected comb spacing at $\Delta\nu = -11.4$ GHz. The optical spectra in (b_1), (b_2), (b_3), and (b_4) correspond to the zoom in of the spectra in (a_1), (a_2), (a_3), and (a_4), respectively

.

6.4.2 Injected power induced harmonics comb

In this subsection, we describe the bifurcations scenarios A and B indicated in the mapping of Fig. 6.3.

6.4.2.1 Bifurcation scenario A

The cascade of bifurcations leading to the comb shown in Fig. 6.4 will be analyzed now. We first analyze the polarization dynamics of the VCSEL in the plane of the injection parameters for the bifurcation scenario indicated by the red arrow with the letter A in Fig. 6.3 (b).

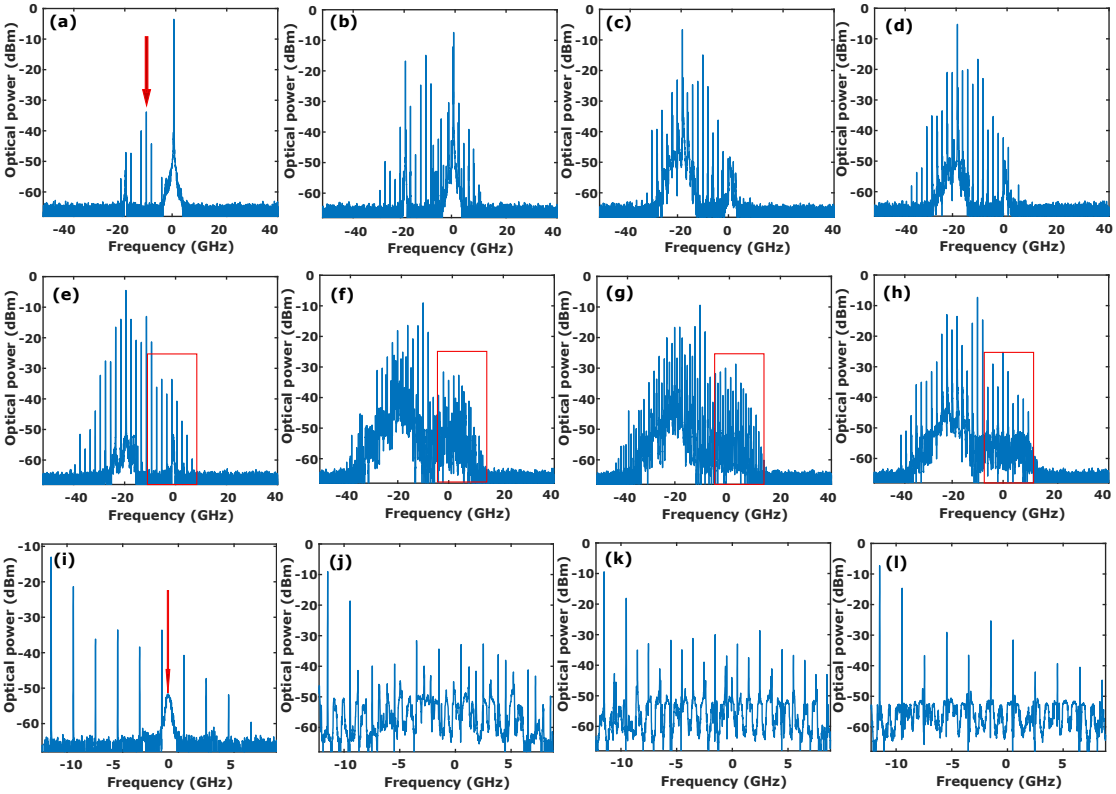

Figure 6.5: Scenario A: Optical spectra for fixed comb spacing $\Omega = 2$ GHz and detuning $\Delta\nu = -10.78$ GHz when varying the injected power P_{inj}. (a), (b) unlocked dynamics at $P_{inj} = 0.3$ µW, $P_{inj} = 64$ µW, respectively, (c) PS with complex dynamics at $P_{inj} = 95.7$ µW , (d) and (e) Unlocked time-periodic dynamics corresponding to a frequency comb at $P_{inj} = 100.5$ µW and $P_{inj} = 113.1$ µW, respectively, (f) and (g) harmonics at third and half of the comb spacing in both polarization modes at $P_{inj} = 352$ µW, and $P_{inj} = 440$ µW, and (h) Unlocked time-periodic dynamics in both polarization modes corresponding to a frequency comb at $P_{inj} = 688$ µW. The optical spectra in (i), (j), (k), and (l) represent zooms of the optical spectra in (e), (f), (g), and (h), respectively. The red arrows in the optical spectrum of (a) and (i) indicate the position of the central injected comb line and the residue of X-polarization mode after PS due to the spontaneous emission noise.

Figures 6.5 (a)-(h) show the route to the polarization switching accompanied by a broad

comb generation in Y-polarization mode. The detuning frequency and the injected comb spacing are fixed, $\Delta\nu = -10.78$ GHz and $\Omega = 2$ GHz, respectively. At low injected power, $P_{inj} = 0.3$ µW, the VCSEL is still emitting like in free-running as shown in Fig. 6.5 (a). The red arrow in the optical spectrum indicates the frequency position of the injected central comb line. When the injected power is increased, the polarization modes of the VCSEL start to be excited as shown in Fig. 6.5 (b). The level of power in the normally depressed polarization mode (Y-PM) is increased, but X-PM remains the polarization mode that shows the maximum power. An increase in the injected power switches the maximum power to the normally depressed polarization mode (Y-PM) accompanied by complex dynamics as shown in Fig. 6.5 (c). The strongest peak around -20 GHz in the optical spectrum appears at the free-running frequency position of Y-PM. The suppression ratio of the dominant polarization mode in free-running (X-PM) is around -50 dB. The residue of power in the X-PM frequency position is due to the spontaneous emission noise. When the injected power is increased, the VCSEL bifurcates progressively to an unlocked time-periodic dynamics corresponding to an extended frequency comb with the same comb spacing as the injected one (see Fig. 6.5 (d)). The bifurcation is characterized by the appearance of new frequency lines at the injected comb spacing and the decrease in the noise pedestal. The number of new comb lines increases while the noise pedestal decreases to give rise to a very stable comb in Fig. 6.5 (e). The strongest comb lines in the optical spectra in Fig. 6.5 (d) and (e)) appear at the frequency position of Y-PM of the VCSEL in free-running. The window box in the optical spectrum of Fig. 6.5 (e) is well visible in Fig. 6.5 (i). We observe that the comb lines are regularly separated by the injected comb spacing. The red arrow indicates the residue of X-PM due to the spontaneous emission noise. When the injected power is increased from Fig. 6.5 (e), the VCSEL bifurcates to the excitation of both polarization modes with chaotic dynamics generation in the two polarization modes (not shown). When increasing the injected power again, harmonics comb that extends on both polarization modes are unveiled as shown in Fig. 6.5 (f) and (g). The red window box in Fig. 6.5 (f) and (g) is well seen in Fig. 6.5 (j) and (k), respectively. We observe that the optical spectra in Fig. 6.5 (f) and (g), are indeed harmonic combs at third and half of the comb spacing of Fig. 6.5 (e), respectively. Harmonic comb dynamics has previously been analyzed in [18, 20] for edge-emitting laser (EEL), but for injected comb spacing several times the relaxation oscillation frequency of the DFB laser in free-running. It is interesting to notice that chaotic dynamics in both polarization mode is observed between Fig. 6.5 (f) and Fig. 6.5

(g). A fine-tune in the injected power leads the VCSEL output to dynamics quite close to harmonic comb at a quarter of the injected comb spacing. When further increasing the injected power, the VCSEL bifurcates to complex dynamics in both polarization mode. These complex polarization dynamics disappear progressively to give rise to the frequency comb encompassing the two orthogonal polarizations, as shown in Fig. 6.5 (h) and in the corresponding zoom in (l). Optical injection has induced either a single polarization comb (e) or a broad optical comb encompassing the two polarization modes (h) in a single mode VCSEL injected with a narrow comb in single polarization (a).

6.4.2.2 Linewidth and coherence of the polarized comb lines

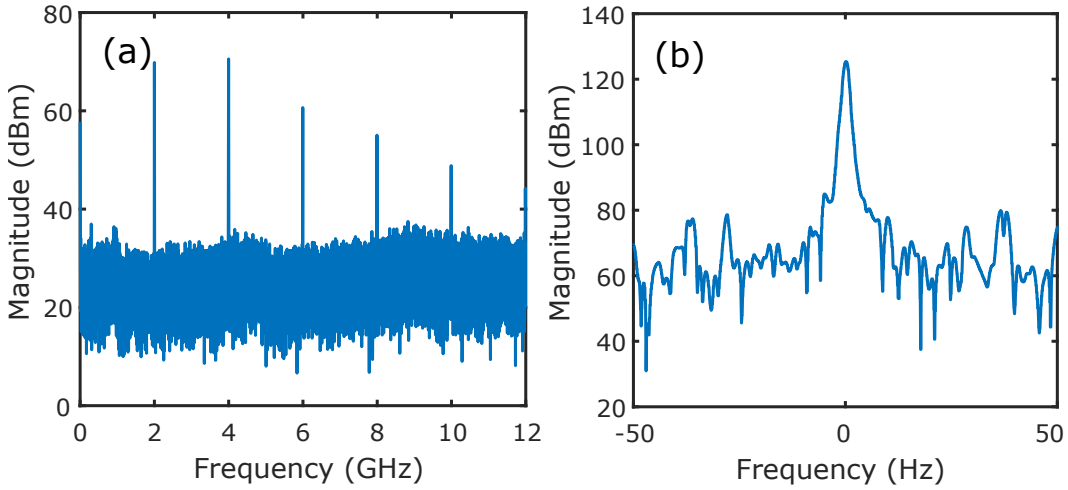

Figure 6.6: (a) the power spectrum of the comb shown in Fig. 6.5 (e) and the corresponding zoom in (b).

To address the coherence between the new comb lines, we plot in Fig. 6.6 (a) the power spectra corresponding to the comb observed for $P_{inj} = 113.1$ µW (Fig. 6.5 (e)). We place a high-speed photodiode at the input of an electrical spectrum analyzer (ESA) with the resolution set to 1Hz and examine the linewidth of the power spectrum. Figure 6.6 (a) shows that the frequency lines in the power spectrum are regularly spaced by 2 GHz corresponding to the repetition rate of the polarized comb in Fig. 6.5 (e). We next select the frequency line at -2 GHz on the ESA with the maximum resolution as shown in Fig. 6.6 (b). Like in [230–232], the linewidth at -3 dB is approximatively 1.1 Hz, which is several times narrower than the linewidth of the optical spectrum (25.2 MHz). As discussed in Chapter 3, the linewidth of the beat note in the power spectrum is several times lower than the linewidth of the comb lines in the optical spectrum, which suggests that the comb lines in the optical spectrum are coherent.

6.4.2.3 Bifurcation scenario B

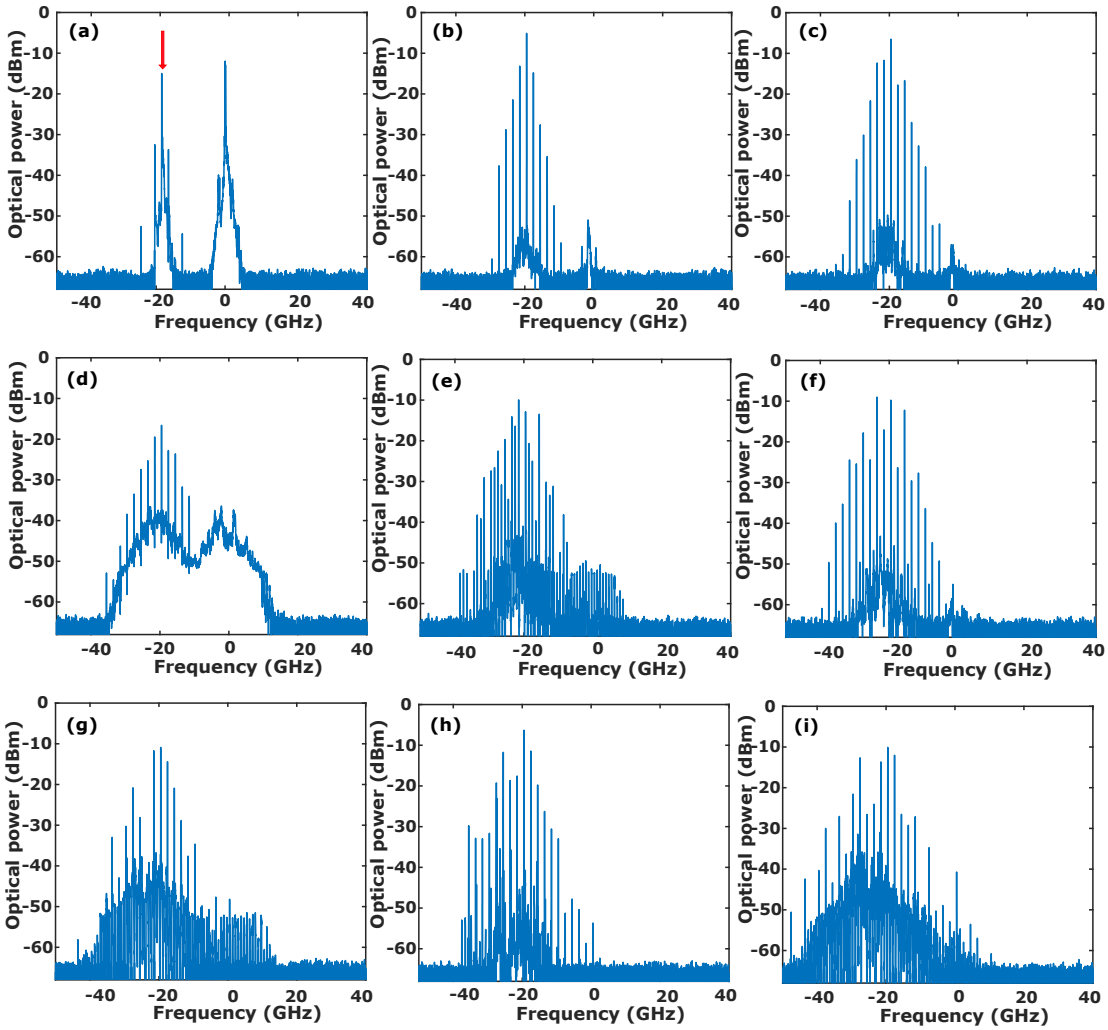

Figure 6.7: Scenario B: Route to polarization switching with harmonics frequency comb generation for detuning close to the birefringence, i.e, frequency position of Y-PM, $\Delta\nu = -17.7$ GHz and for fixed $\Omega = 2$ GHz. When increasing the injected power, the VCSEL output shows the following dynamics: (a) Unlocked dynamics at $P_{inj} = 0.3$ µW, (b) and (c) PS with new frequency lines generations at $P_{inj} = 16$ µW and $P_{inj} = 32$ µW, respectively, (d) complex dynamics in both polarization modes at $P_{inj} = 40$ µW, (e) and (f) Unlocked time-periodic corresponding to a harmonics comb and comb at repetition of $\Omega = 2$ GHz in Y-PM at $P_{inj} = 56$ µW, and $P_{inj} = 64$ µW, respectively, (g) complex dynamics at $P_{inj} = 376$ µW, (h) frequency comb at $P_{inj} = 400$ µW, and (i) complex dynamics with comb lines at $P_{inj} = 696$ µW. The red arrow in optical spectrum of (a) indicated the position of the central injected comb line.

We next analyzed the sequence of bifurcation indicated by the red arrow B in the mapping

of Fig. 6.3 (b). The arrow B corresponds to the ideal position for which the power required to switch polarization is the smallest. Figure 6.7 shows the VCSEL output for a fixed injected comb spacing $\Omega = 2$ GHz and a detuning frequency $\Delta\nu = -17.7$ GHz. The frequency position of the injected comb spacing matches with the one of the normally depressed polarization mode (Y-PM). For low injected power, on the contrary to Fig. 6.5 (a), the VCSEL exhibit an unlocked dynamics weak excitation of both polarization mode as shown in Fig. 6.7 (a). The red arrow in the optical spectrum indicates the frequency position of the central injected comb line. A small increase in the injected power is sufficient to switch from the dominant polarization mode (X-PM) to the depressed polarization mode (Y-PM) as shown in Fig. 6.7 (b). The polarization mode that contains the maximum gain is now the Y-PM. The polarization switching is accompanied by unlocked time-periodic dynamics with a repetition rate corresponding to the injected comb spacing in Y-PM. When we increase the injected power from Fig. 6.7 (b), the VCSEL remains stable on the comb dynamics with the appearance of new frequency lines until reaching about 3 times the number of injected comb lines [Fig. 6.7 (c)]. When we keep increasing the injected power, the VCSEL bifurcates abruptly to the excitation of the two polarization modes accompanied with complex dynamics generation as shown in Fig. 6.7 (d). The dominant polarization (X-PM) is again gradually eliminated to give rise to a polarized (Y-PM) unlocked time-periodic dynamics when increasing the injected power [Fig. 6.7 (d)]. This time-periodic dynamics is harmonics comb with a repetition rate at half of the injected comb spacing. This harmonics comb becomes more stable with a decrease of the noise pedestal and the suppression of the small quantity of X-PM power when the injected power is increased. The harmonics frequency lines then disappear smoothly to give rise to a stable comb with the same comb spacing as the injected one as shown in Fig. 6.7 (f). This comb has a larger bandwidth than the one shown in Fig. 6.7 (c). From Fig. 6.7 (f), the comb starts to deteriorate and complex dynamics take place in Y-PM [Fig. 6.7 (g)]. When further increasing the injected power, the VCSEL output becomes a stable comb again with a significant noise pedestal. A fine-tuning of the injected allows to achieve the minimum noise pedestal and then the VCSEL to emits a complex comb dynamics as shown in Fig. 6.7 (i). As previously demonstrated in [74] for the single-frequency injection in VCSEL, the comparison between Fig. 6.3 and Fig. 6.7 show that the switching and the related dynamics depend on the injected power and on the detuning.

6.4.3 Polarization resolved optical spectra

In the previous sections, we have shown that a single mode VCSEL can exhibit a single polarization comb (Fig. 6.5 (e)) or a broad comb spanning on the two polarization modes (Fig. 6.5 (h)). We present in Fig. 6.8 the polarization resolved optical spectra of the comb shown in Fig. 6.5 (e) and (h). In Fig. 6.8, the top and bottom panels correspond to the polarization-resolved optical spectra of an example of comb in Fig. 6.5 (e) and (h), respectively. These optical spectra are obtained by using two polarization controllers and a polarized beam splitter (PBS). Figure 6.8 (a), (b) and (c) are obtained for a fixed injected power $P_{inj} = 183.3$ µW and detuning $\Delta\nu = -10.53$ GHz. Figure 6.8 (a), (b) and (c) shows the optical spectra of X-PM, Y-PM and the total output power of the VCSEL, respectively. We observe that only the Y-PM [Fig. 6.8 (b)] and the total output power [Fig. 6.8 (c)] show a frequency comb. The red arrow in the box of Fig. 6.8 (a) indicates the residue of the X-PM due to the spontaneous emission noise.

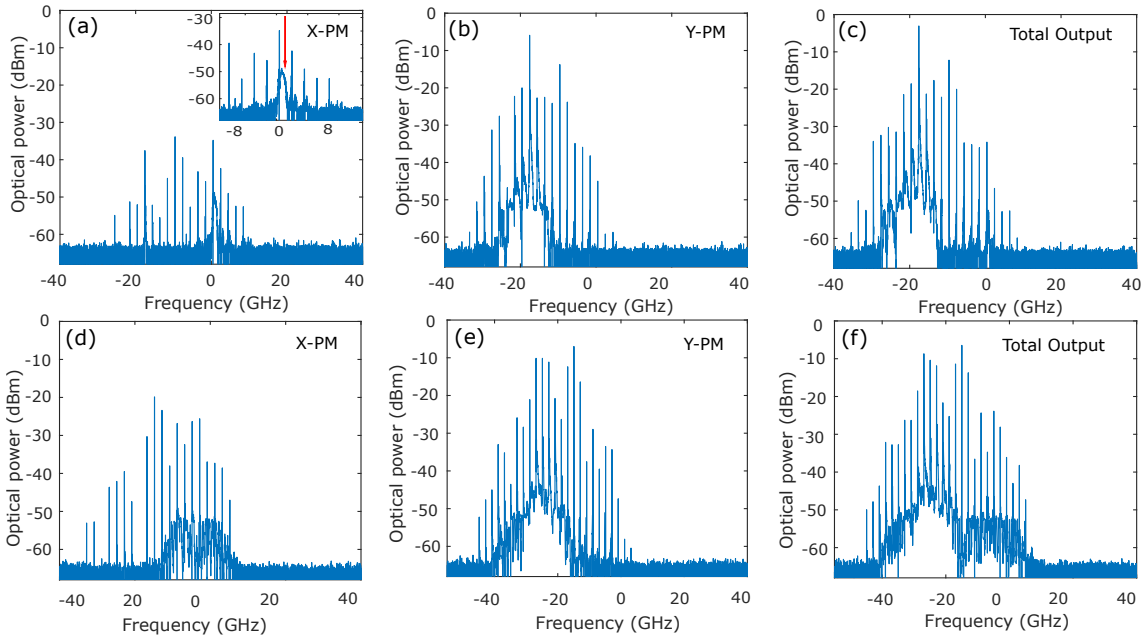

Figure 6.8: Optical spectra for each polarization and total output power of the VCSEL showing the sequence of bifurcation leading to a broad frequency comb generation for fixed $\Omega = 2$ GHz and detuning $\Delta\nu = -10.53$ GHz. (a), (b) and (c) polarization resolved comb for X-PM, Y-PM, and the total output, respectively at $P_{inj} = 183.3$ µW. (d), (e) and (f) polarization resolved optical spectra of X-PM, Y-PM, and the total output, respectively at $P_{inj} = 680$ µW.

Figure 6.8 (d), (e) and (f) shows the optical spectra of X-PM, Y-PM and the total output

power of the VCSEL, respectively, for a fixed injected power $P_{inj} = 680$ µW and detuning $\Delta\nu = -10.78$ GHz. We observe a frequency comb in both polarization modes, which combine to give rise to a frequency comb in the total power. The amplitudes of the comb lines in X-PM are controllable with the detuning and the injected power. We have shown that injection of a frequency comb can induce either a single or a two polarization comb in a single-mode VCSEL injected with a single polarization comb.

6.5 Bifurcation scenarios leading to two polarization comb

We show in the previous section that the VCSEL can bifurcate to polarized comb dynamics. Here, we will exploit the competition between the polarization modes to induce in a single longitudinal mode VCSEL two combs with orthogonal polarizations. The locking and the coherence between these polarized comb lines are also analyzed.

6.5.1 Detuning close to zero

The previous section has analyzed the bifurcation series when varying the detuning close to the birefringence $\Delta\nu = -17.7$ GHz. Here, we show how to exploit the polarization dynamics in order to extend to a much broader optical spectrum involving new frequency comb dynamics. Figure 6.9 depicts the bifurcation scenario leading to broad frequency comb generation in the two polarization modes. This scenario is indicated by the red arrow C in the mapping of Fig. 6.3 (b). Optical spectra are recorded for a fixed detuning $\Delta\nu = -6.5$ GHz and an injected comb spacing $\Omega = 2$ GHz when varying the injected power P_{inj}.

For a low injected power, the VCSEL remains stable on the dominant polarization mode X-PM as shown in Fig. 6.9 (a). The red arrow indicates the frequency position of the central injected comb line. Figures 6.9 (b) and (c) show that the VCSEL output is an unlocked dynamics but is still emitting on X-PM despite a significant increase in the injected power. The normally depressed polarization mode starts to be excited in Fig. 6.9 (c). When we increase the injected power, the VCSEL bifurcates to a two polarization mode solution as shown in Fig. 6.9 (d). The polarization mode that contains the maximum gain has switched from X-PM to Y-PM, but not with a complete polarization switching. The bifurcation leading to the excitation of the two polarization modes is characterized by

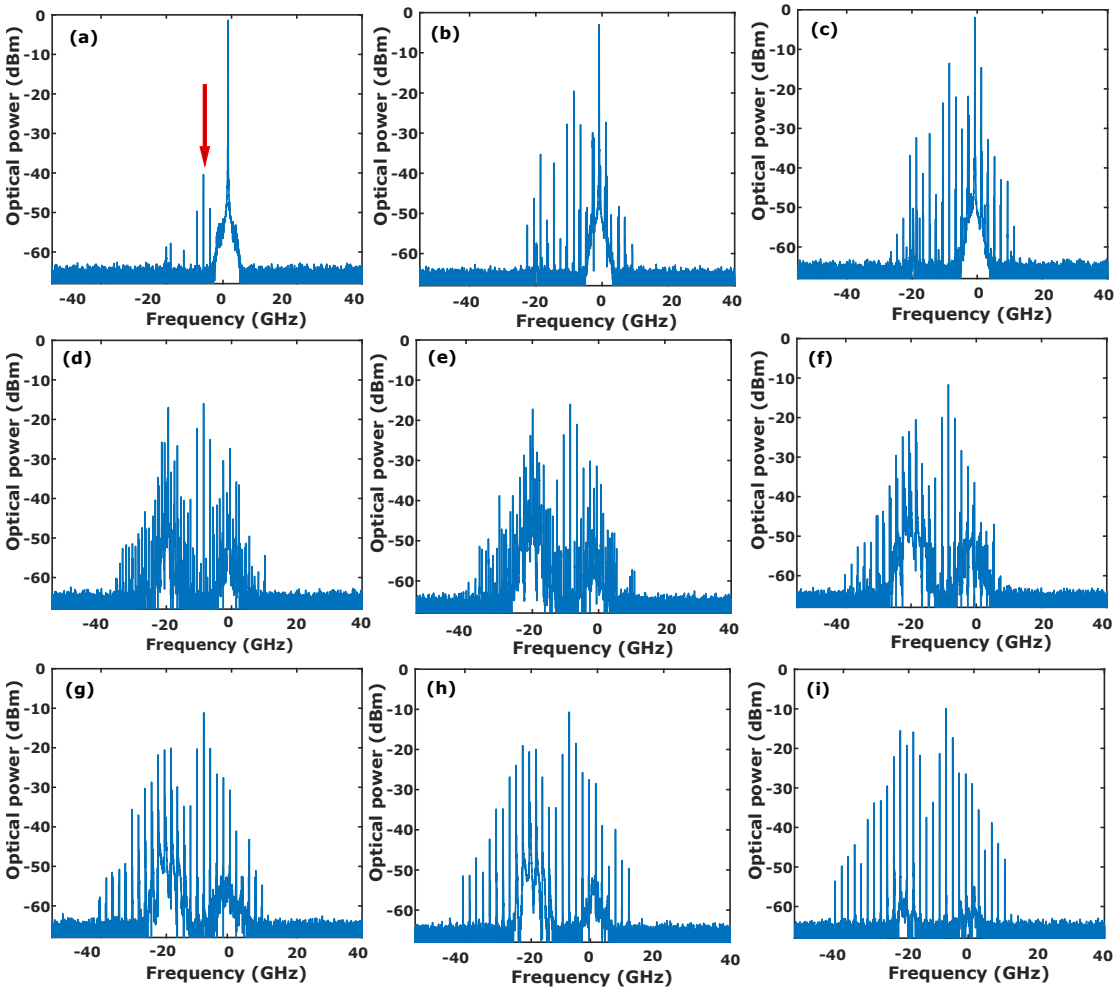

Figure 6.9: Scenario C: Optical spectra of two polarization frequency comb dynamics for fixed comb spacing to $\Omega = 2$ GHz, and detuning $\Delta\nu = -6.5$ GHz. (a), (b) and (c), unlocked dynamics at $P_{inj} = 0.3$ µW, $P_{inj} = 80$ µw and $P_{inj} = 216$ µw, respectively, (d) incomplete PS at $P_{inj} = 224$ µW, (e) complex harmonic comb in both polarization modes at $P_{inj} = 408$ µW, (f) and (g) complex comb in both polarization modes at $P_{inj} = 520$ µW and $P_{inj} = 576$ µW, respectively, (h) and (i) comb in both polarization modes $P_{inj} = 600$ µW and $P_{inj} = 640$ µW, respectively. The red arrow in optical spectrum of (a) indicated the position of the central injected comb line.

the appearance of new frequency lines in both polarizations creating a harmonics comb. A succession of complex dynamics and harmonics frequency comb takes place in the VCSEL output when increasing the injected power as shown in Fig. 6.9 (e) and (f). Figure 6.9 (g) shows that when we keep increasing the injected power, new frequency lines at the injected comb spacing start to appear in both polarization modes creating unstable comb dynamics in the two polarizations. The instability and the noise pedestal decrease with

the injected power to give rise to a very stable comb formed by two combs with orthogonal polarizations in Fig. 6.9 (h) and (i). The number of resulting comb lines increases with the increase of the injected power.

6.5.2 Detuning close to the birefringence

As we have seen in the previous cases, the PS threshold and the injection parameters can be used to induce in a single device a single polarization comb (Fig. 6.5 (e)) or a two polarization comb (Fig. 6.5 (h) and Fig. 6.9 (i)). The power in X-PM and Y-PM are controllable by the polarization mode competition, and the number of resulting comb lines can be extended thanks to the nonlinear dynamics. Figure. 6.10 (a), (b) and (c) show the two polarization comb for injected comb spacing $\Omega = 500$ MHz, $\Omega = 2$ GHz, and $\Omega = 4$ GHz, respectively. We observe that the two polarization combs dynamics is not restrictive to a specific injected comb spacing.

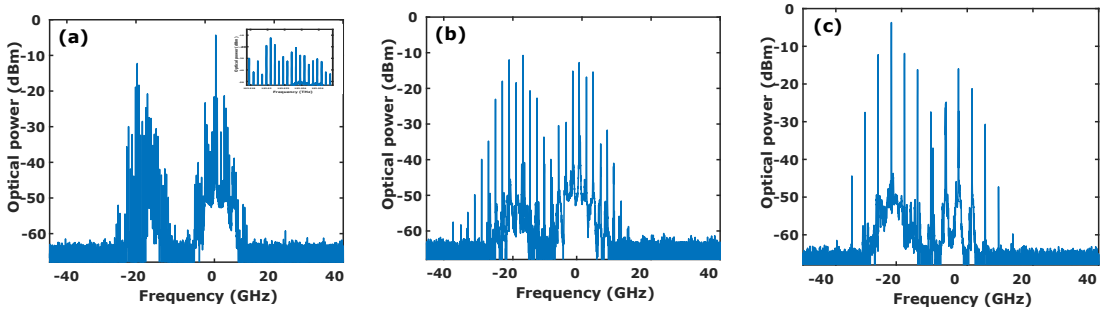

Figure 6.10: Optical spectra revealing the nonlinear dynamics of two polarization frequency comb when varying both the comb properties and the injection parameters. (a), (b), ad (c) are obtained for $\Omega = 500$ MHz, $\Omega = 2$ GHz, and $\Omega = 4$ GHz. The injected light parameters are (a) $\Delta\nu = -23.2$ GHz and $P_{inj} = 54$ µW, (b) $\Delta\nu = -15.7$ GHz and $P_{inj} = 72$ µW, and (c) $\Delta\nu = -16.9$ GHz and $P_{inj} = 96$ µW.

6.5.3 Polarization resolved analysis of two polarization comb dynamics

Figure 6.11 depicts the polarization-resolved optical spectra corresponding to Fig. 6.9 (i). Figure. 6.11 (a), (b), and (c) show the optical spectra of X-PM, Y-PM, and the total output power, respectively. We observe that the total output power is formed by two combs (X-PM and Y-PM) with orthogonal polarizations. The carrier to noise ratio

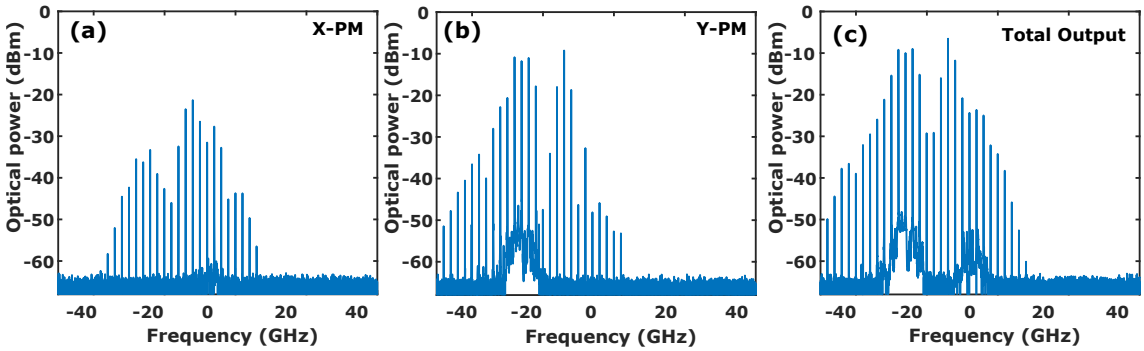

Figure 6.11: Polarization resolved spectra corresponding to the comb evolution in scenarios C. (a), (b), (c), optical spectra of X-PM, Y-PM and total output power, respectively for fixed $P_{inj} = 552.8$ µW and $\Delta\nu = -6.8$ GHz.

(CNR) of the comb in X-PM is around 40 dB which is close to the maximum found in the frequency comb obtained by gain switching VCSEL [233].

6.5.4 Coherence of the two polarization comb lines

Some applications (optical communication and gas spectroscopy) of optical frequency comb require a high degree of coherence between the comb lines, i.e., very narrow linewidth in the order of Hz. Figure 6.12 (a) analyzes the power spectrum corresponding to the two polarization comb of Fig. 6.11 (c). A polarization controller (P.C) at 45° between X-PM and Y-PM was placed at the input of the high-speed photodiode. The resolution of the electrical spectrum analyzer is fixed at 1 Hz. Figure 6.12 (a) shows that the power spectrum is composed by frequency lines separated by the repetition rate of the comb in Fig. 6.11 (c) (2 GHz). The power spectrum did not show any additional beat note, suggesting that the X-PM comb lines are locked to those in Y-PM. In other words, there is no shift between the comb lines in X-PM and the ones in Y-PM. By varying the detuning, a frequency shift can be induced between X-PM and Y-PM combs, therefore unlocking the polarization combs and observing a beat note at the frequency shift between the X-PM and Y-PM comb. A beat note is then observed in the power spectrum at the frequency shift between the X-PM and Y-PM comb. Like in Fig. 6.6 (a), we select the frequency line at 2 GHz and we show the corresponding zoom in Fig. 6.12 (b). The linewidth is approximately 1Hz at -3 dB. The linewidth of the beat field (power spectrum) is much narrower than the one of the comb lines in the optical spectrum, which demonstrates that the comb lines are coherent. The linewidth measurement was limited by the resolution

bandwidth of the ESA.

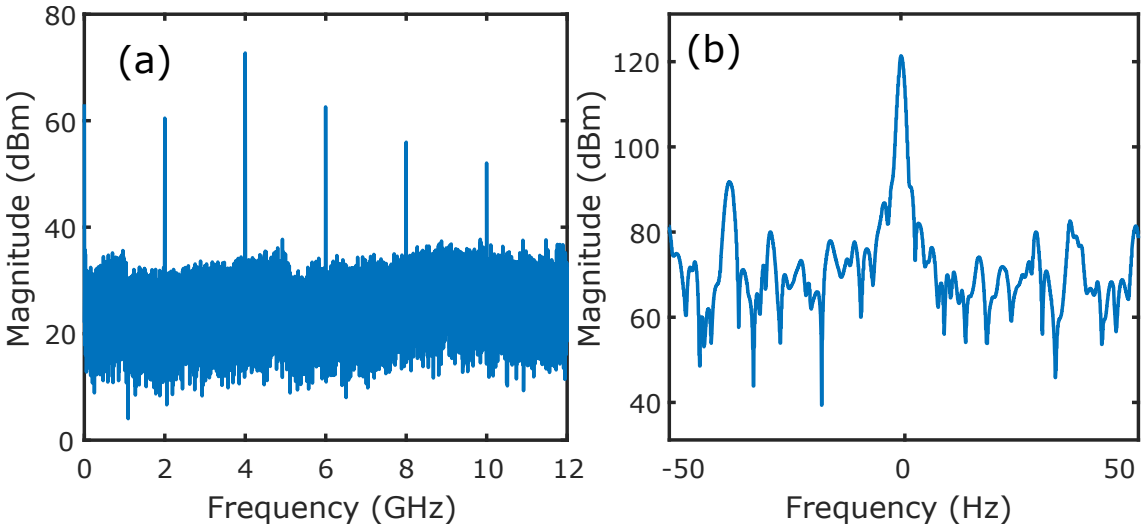

Figure 6.12: (a) the power spectrum of the comb in Fig. 6.11 (c) and the corresponding zoom in (b).

6.6 Tailoring the polarization frequency comb

The previous section showed the possibility of generating either a single polarization or two polarization comb by fine-tuning the injection parameters. Here, we will use the polarization switching and the injection parameters to optimize the new comb properties. Most specifically, we will report on the resulting comb bandwidth (number of comb lines) and the Carrier to Noise Ratio (CNR) for the bifurcation sequences indicated by the letters A, B, and C in the mapping of Fig. 6.3 (b).

6.6.1 General case

A high-quality optical frequency comb is needed for several applications. One of the main weaknesses of the optical frequency comb is the lack of power in the individual comb lines, which makes their use as an independent light source difficult. Figure 6.13 analyzes the performance of the combs corresponding to the bifurcation sequence A in Figure. 6.3. The blue and red in each map show the bandwidth on the left vertical axis and the CNR on the right vertical axis, respectively. Figure 6.13 (a) is obtained for fixed detuning $\Delta\nu = -11.2$ GHz when varying the injected power. We observe that the bandwidth increases when

increasing the injected power, which is in agreement with our conclusions in chapters 4 and 5.

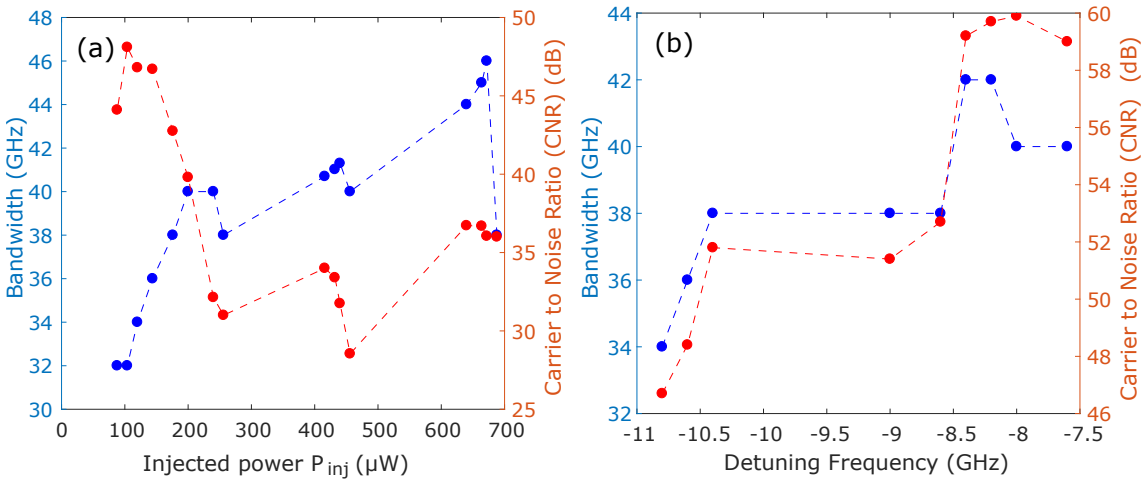

Figure 6.13: Control of frequency comb properties with the injection parameters for a fixed comb spacing of $\Omega = 2$ GHz . The curves in blue and red in each map correspond to the bandwidth on the left vertical axis and the CNR on the right vertical axis, respectively. (a) is obtained for fixed detuning $\Delta\nu = -11.2$ GHz when varying the injected power. (b) is obtained for fixed injected power $P_{inj} = 608$ µW when varying the detuning frequency.

When varying the injected power for fixed detuning, several distinct comb regions can be observed as shown in Fig. 6.5. The comb bandwidth deteriorates at the bifurcations point between these comb regions, which explains the discontinuities in the evolution of the bandwidth in Fig. 6.13 (a). At the transition point of each comb region, the bandwidth and the CNR get down and then increase again with the injected power. The best value of CNR is found close to the PS point while the bandwidth is low. Figure 6.13 (b) shows the evolution of the bandwidth and the CNR when scanning the detuning between X-PM and Y-PM frequency position for fixed injected power $P_{inj} = 608$ µW. We observe that the CNR and the bandwidth increase with the detuning toward zero detuning value, i.e., the region where polarization switching is not possible as described for the bifurcation scenario C in Fig. 6.10.

6.6.2 Central comb line close to Y-PM

We provide an analysis of the comb dynamics and harmonic comb when the detuning is close to the birefringence. Figure 6.14 shows the comb bandwidth on the left vertical

axis and the CNR on the right vertical axis corresponding to the bifurcation scenario B (in Figure. 6.3). Figure 6.14 (a) is obtained for fixed detuning $\Delta\nu = -18.8$ GHz, when varying the injected power.

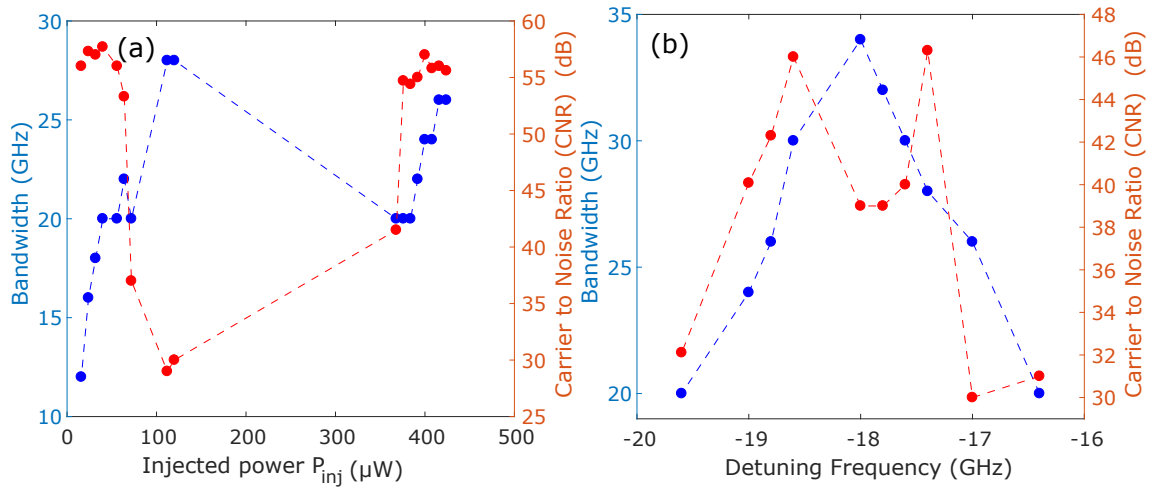

Figure 6.14: Comb performance with the injection parameters for a fixed comb spacing of $\Omega = 2$ GHz . The curves in blue and red in each map correspond to the bandwidth on the left vertical axis and the CNR on the right vertical axis, respectively. (a) is obtained for fixed detuning $\Delta\nu = -18.8$ GHz when varying the injected power. (b) is obtained for fixed injected power $P_{inj} = 120$ µW.

Like in Fig. 6.13 (a), the best value of the CNR (Fig. 6.14 (a)) is found at low injected power, i.e., close to the PS point. The CNR of Fig. 6.7 (b), (c), and (f) are estimated to be 54.48 dB, 53.36 dB, and 49.26 dB, respectively, which explain that the decrease of the CNR is due to the increase in the noise pedestal. Figure 6.14 (b) analyzed the comb properties for fixed injected power when varying the detuning across the comb region, such that the frequency of the injected main comb line is close to the frequency position of the normally depressed polarization mode Y-PM. We observe that the CNR and the comb bandwidth start to get maximum when the detuning is close to $\Delta\nu = -17.7$ GHz, i.e., when the central injected comb line is close to the frequency position of Y-PM.

6.6.3 Central comb line close to X-PM

Figure 6.15 analyzes the performance of the combs of the injection parameters indicated by the letter C (in Figure 6.3). Figure 6.15 (a) is obtained for $\Delta\nu = -6.5$ GHz when varying the injected power. Figure 6.15 (b) is obtained for fixed injected power $P_{inj} = 640$ µW when varying the detuning frequency. Figure 6.15 (a) and (b) show that the bandwidth

and the CNR both increase with the injected power and the detuning frequency, which was not the case when the detuning is close to Y-PM or the general case.

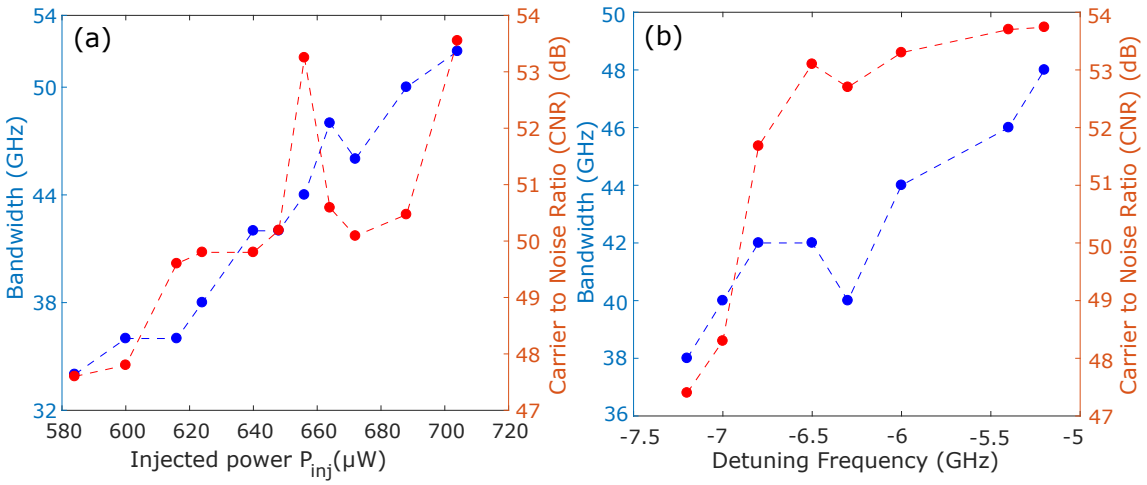

Figure 6.15: Tailoring the comb properties for a fixed injected comb spacing of $\Omega = 2$ GHz . The blue and red in each map correspond to the bandwidth on the left vertical axis and the CNR on the right vertical axis, respectively. (a) is obtained for fixed detuning $\Delta\nu = -6.5$ GHz when varying the injected power. (b) is obtained for fixed injected power $P_{inj} = 640$ μW.

6.7 Conclusion

In conclusion, we have experimentally analyzed the nonlinear polarization dynamics of a VCSEL subject to optical frequency comb injection. By tuning both the polarization and the injection parameters, we have enabled an optical control of the comb spacing, the Carrier to Noise Ratio (CNR), and the polarization of the optical frequency comb of the VCSEL output light. Similar to optical injection of a single-frequency, we observe that polarization switching (PS) plays a crucial role in the dynamics. The best value of the CNR is found to be close to the PS point. A sweep of the detuning of the injected light shows a significant increase of both the CNR and the comb bandwidth for a detuning of $\Delta\nu = -17.7$ GHz, i.e., when the injection central comb line has a frequency close to that of the normally depressed VCSEL polarization mode. The best comb performance is observed when the nonlinear dynamics induced comb extension combines with the excitation of the two polarization modes in the VCSEL since it is a way to improve the comb bandwidth further. Our results show the possibility of controlling the comb properties to adapt it to several applications. The generation of the two polarization comb and the tailoring of the

comb properties are the first steps towards dual-polarization comb generation and related application in dual-comb spectroscopy.

7

Contrasting the case of parallel and orthogonal injection in VCSEL frequency comb

Contents

7.1 Modelling the VCSEL with parallel comb injection 136

7.2 Theoretical results: Bifurcation diagrams analysis 139

7.2.1 Parallel optical injection 140

7.2.2 Orthogonal optical injection 144

7.3 Experimental results: VCSEL with parallel injection 146

7.3.1 Bias current close to the threshold 147

7.3.2 Bias current far from the threshold 149

7.3.3 Comb performance analysis 151

7.4 Conclusion 153

The nonlinear dynamics of a VCSEL with the polarization of the injected light parallel to that of the free-running VCSEL is less studied than the case of orthogonal optical injection. The parallel optical injection has been used to induce single-mode operation in multi-transverse modes VCSEL [234]. This is achieved when the detuning frequency is close to one of the transverse modes. Moreover, recent works have analyzed several bifurcation scenarios in the case of parallel optical injection that differs from the case of orthogonal optical injection. Theoretical and experimental studies have reported that parallel optical injection can induce injection locking accompanied with the excitation of the normally depressed polarization mode [134–136]. The mapping in the plane of the injection parameters has demonstrated several dynamics such as injection locking in the dominant polarization mode of the VCSEL coexisting with periodic dynamics in the normally depressed polarization mode, and also chaos in both polarization modes [206, 235].

Chapter 6 has discussed polarization switching and the related dynamics in a single-longitudinal mode VCSEL subject to optical injection of a comb with orthogonal polarization. More specifically, we have injected a frequency comb in the non-lasing polarization mode of the VCSEL to unveil either a single or two polarization combs. Here, we describe experimentally and theoretically the bifurcation scenario of the VCSEL with parallel comb injection. We also provide a comparison between parallel and orthogonal optical injection in the VCSEL when varying the linear dichroism. Finally, we analyze the impact of the injection current on the nonlinear dynamics of the VCSEL subject to parallel optical injection.

7.1 Modelling the VCSEL with parallel comb injection

This section introduces the mathematical model used to analyze the polarization dynamics in VCSEL with optical frequency comb injection. The parallel optical injection is modeled in the framework of the Spin-Flip Model (SFM). To this end, we modify the rate equation presented in chapter 2 by considering the external injection with a frequency comb.

A semiconductor laser with optical injection has been widely modeled by analogy with a Fabry-Perot cavity [47, 77]. The optical injection is taking into account by using the traveling wave approach to model the semiconductor laser. Modeling the Spin-Flip Model(SFM) [72] with optical injection is quite similar to the edge-emitting lasers. The

SFM parameters will be chosen such that the dominant polarization mode of the VCSEL in free-running emits along the x-axis. The SFM model rate equation found in chapter 2, (equations 2.28-2.31) can be modified with the injected field as follows:

$$\frac{dE_x}{dt} = -(\kappa + \gamma_a)E_x - i(\kappa\alpha + \gamma_p)E_x + \kappa(1 + i\alpha)(DE_x + inE_y) + E_M, \tag{7.1}$$

$$\frac{dE_y}{dt} = -(\kappa - \gamma_a)E_y - i(\kappa\alpha - \gamma_p)E_y + \kappa(1 + i\alpha)(DE_y - inE_x), \tag{7.2}$$

$$\frac{dD}{dt} = -\gamma[D(1 + |E_x|^2 + |E_y|^2) - \mu + in(E_yE_x^* - E_xE_y^*)], \tag{7.3}$$

$$\frac{dn}{dt} = -\gamma_s n - \gamma[n(|E_x|^2 + |E_y|^2) + iD(E_yE_x^* - E_xE_y^*)]. \tag{7.4}$$

Where E_x and E_y are the linearly polarized complex fields in the x and y directions respectively, D and n are the carrier density, γ_p and γ_a, are linear birefringence and linear dichroism respectively, γ_s is the spin-flip relaxation rate, γ is the decay rate of D, κ is the field decay rate, α is the linewidth enhancement factor and μ is the normalized bias current. The injected field is the same as the one introduced in chapter 4 (equ. 4.3)

$$E_M = \kappa_{inj} \sum_j E_j(t) e^{i(2\pi\nu_j t + \varphi_j(t))} \tag{7.5}$$

with angular frequency ω_j and amplitude E_j corresponding to the j_{th} comb lines, and coupling coefficient κ_{inj}. To simplify the calculation, we suppose the phase of the individual injected comb lines to be $\varphi_j = 0$. We consider a narrow comb with three frequency lines.

To define the detuning frequency between the SFM model and the injected comb lines, we show in Fig. 7.1 the diagram of the different involved frequencies. The detuning frequency $\Delta\nu_j$ is the difference between ω_j and $\frac{\omega_x+\omega_y}{2}$, with $\omega_x = \alpha\gamma_a - \gamma_p$ and $\omega_y = \gamma_p - \alpha\gamma_a$, the frequency corresponding to the linear polarization mode X and Y, respectively. We consider that zero detuning value matches the central injected comb line (j=2). Using the scheme of Fig. 7.1, the angular detuning frequency corresponding to each injected comb line can be written as:

$$\Delta\omega_1 = \Omega - \Delta\omega; \tag{7.6}$$

$$\Delta\omega_2 = \Delta\omega; \tag{7.7}$$

$$\Delta\omega_3 = \Delta\omega + \Omega. \tag{7.8}$$

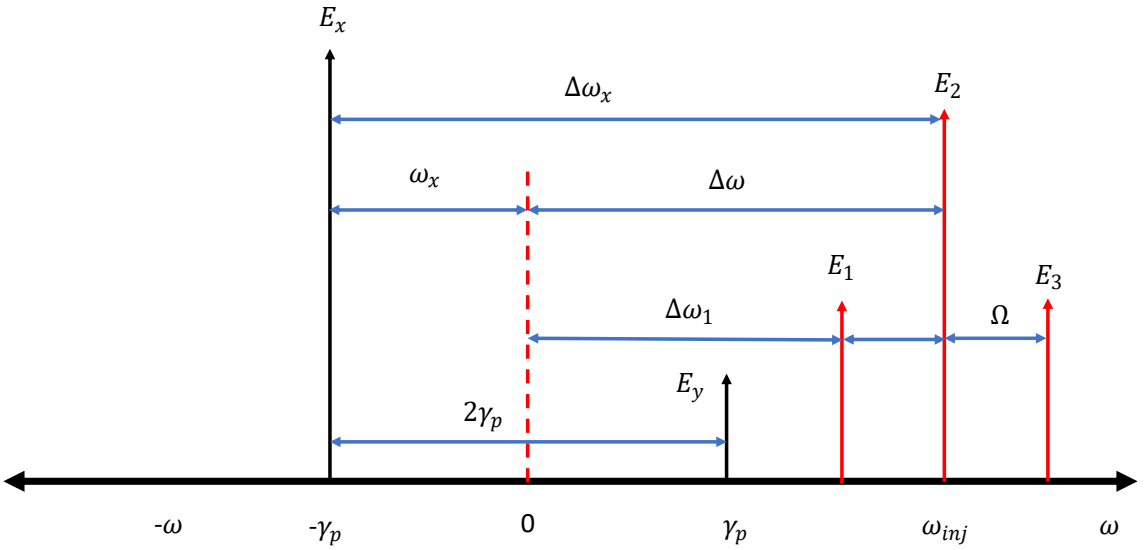

Figure 7.1: Diagram of detuning frequency for SFM. γ_p, the birefringence, ω_x, the angular frequency of the X-PM, $\Delta\omega_x$, the detuning angular frequency between the X-PM and the central injected comb lines and $\Delta\omega_x$, the detuning angular frequency between $\frac{\omega_x+\omega_y}{2}$ and the central injected comb line.

To take into account the frequency comb injection with angular detuning $\Delta\omega$ from the central injected comb line, the injected comb and the field of the polarization modes can be rewritten as:

$$E_M = \kappa_{inj}(E_1(t)e^{i(\Delta\omega_1 t)} + E_2(t)e^{i(\Delta\omega_2 t)} + E_3(t)e^{i(\Delta\omega_3 t)}) \tag{7.9}$$

$$E_x(t) = A_x(t)e^{i((\omega_x+\Delta\omega)t-\phi_x)} \tag{7.10}$$

$$E_y(t) = A_y(t)e^{i((\omega_y+\Delta\omega)t-\phi_y)} \tag{7.11}$$

with A_x and A_y the amplitude of the fields of the X-polarization and Y-polarization modes, respectively. For simplicity, we keep the same variable notation as equ.(7.1)-(7.4). By Substituting the equ.(7.9)-(7.11) into (7.1) and (7.2), the SFM model can now be written as:

$$\frac{dE_x}{dt} = \kappa(1+i\alpha)(DE_x + inE_y - E_x) - i(\gamma_p + \Delta\omega)E_x - \gamma_a E_x + \kappa_{inj}(E_1 e^{-i\Omega} + E_2 + E_3 e^{i\Omega}) \tag{7.12}$$

$$\frac{dE_y}{dt} = \kappa(1+i\alpha)(DE_y - inE_x - E_y) + i(\gamma_p - \Delta\omega)E_x + \gamma_a E_x \tag{7.13}$$

$$\frac{dD}{dt} = -\gamma[D(1 + |E_x|^2 + |E_y|^2) - \mu + in(E_y E_x^* - E_x E_y^*)], \tag{7.14}$$

$$\frac{dn}{dt} = -\gamma_s n - \gamma[n(|E_x|^2 + |E_y|^2) + iD(E_y E_x^* - E_x E_y^*)]. \tag{7.15}$$

We consider an optimal coupling between injected comb and the VCSEL, corresponding to the case $\kappa_{inj} = \kappa$. In the following, we will consider κ_{inj} as the injection strength, with $\kappa_{inj} = \frac{E_{inj}}{E_0}$, where E_{inj} and E_0 are the total amplitude of the injected field and the total amplitude of the VCSEL in free-running, respectively.

We first plot the VCSEL output in free-running in Fig. 7.2. Then, numerical simulation has been performed using the following SFM parameters in table 7.1:

κ	33 ns^{-1}	The field decay rate
γ_a	-0.1 ns^{-1}	The linear dichroism
α	2.8	Linewidth enhancement factor
μ	2.29	The normalized bias current
γ_p	9 GHz	The linear birefringence
γ	2.08 ns^{-1}	The decay rate of D
γ_s	2100 ns^{-1}	The spin-flip relaxation rate

Table 7.1: The semiconductor laser parameters and their numerical value. Taken from [134].

The normalized bias current μ used in our simulation is approximately two times the threshold current. The numerical simulations have been done with a long time series of 200 ns and a time step of 1.2 ps. As shown in Fig. 7.2, the VCSEL in free-running emits of the linear X-polarized mode (X-PM) (a), and the linear Y-polarized mode (Y-PM) (b) shows a very low power due to the spontaneous noise emission.

7.2 Theoretical results: Bifurcation diagrams analysis

This section will theoretically analyze the nonlinear dynamics of a single-mode VCSEL optically injected with a frequency comb. We inject 3-comb lines in either the dominant or in the normally depressed polarization mode of the VCSEL. We observe that the VCSEL can bifurcate to comb dynamics with extended bandwidth and possibly involving the two polarization modes. For the same detuning frequency, the bifurcation scenario differs between the parallel and the orthogonal optical injection. The two polarization combs can

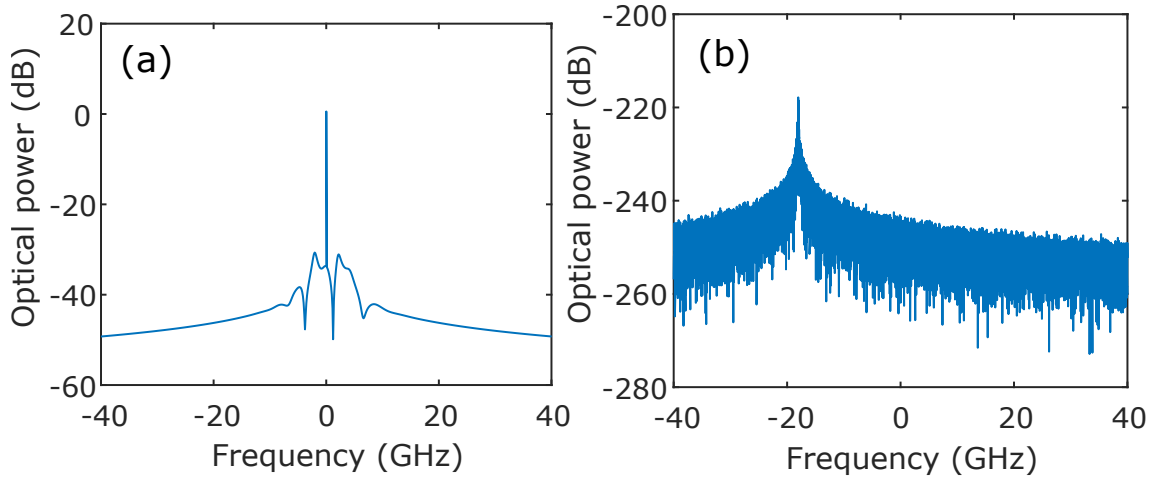

Figure 7.2: Polarization resolved optical spectra of the VCSEL in free-running. (a) and (b) correspond to the X-polarization mode (X-PM) and Y-polarization mode (Y-PM). These optical spectra are obtained using the SFM parameters of table 7.1.

be suppressed with the linear dichroism (γ_a) in the case of parallel injection and becomes a single polarization comb. At the same time, no significant effect on the comb dynamics is observed for orthogonal injection. We use the SFM parameters to induce harmonics comb giving rise to a new comb with smaller comb spacing.

7.2.1 Parallel optical injection

We numerically analyze the bifurcation diagrams of the VCSEL with optical comb injection in Fig. 7.3 for fixed injected comb spacing $\Omega = 2$ GHz and detuning frequency $\Delta\nu_x = -9$ GHz when increasing the injection strength. The polarization of the injected comb is parallel to that of the VCSEL. These diagrams are plotted using the rate equation (7.12)-(7.15). The numerical simulations have been performed with the SFM parameters in table 7.1 and the same simulation conditions as in Fig. 7.3. These bifurcation diagrams are obtained by selecting the minima and the maxima of the polarization-resolved intensities, $I_{x,y} = |E_{x,y}|^2$ for each injection strength. The simulation length was 200 ns with a time step of 1.2 ps. In Fig. 7.3, the left and right panels correspond to the bifurcation diagrams of X-PM and Y-PM, respectively. Figure 7.3 (a_1) and (b_1) correspond to the fixed linear dichroism $\gamma_a = -0.1\ ns^{-1}$.

When increasing the injection strength, the VCSEL first shows unlocked dynamics and then bifurcates to complex dynamics in X-PM. When we keep increasing the injection

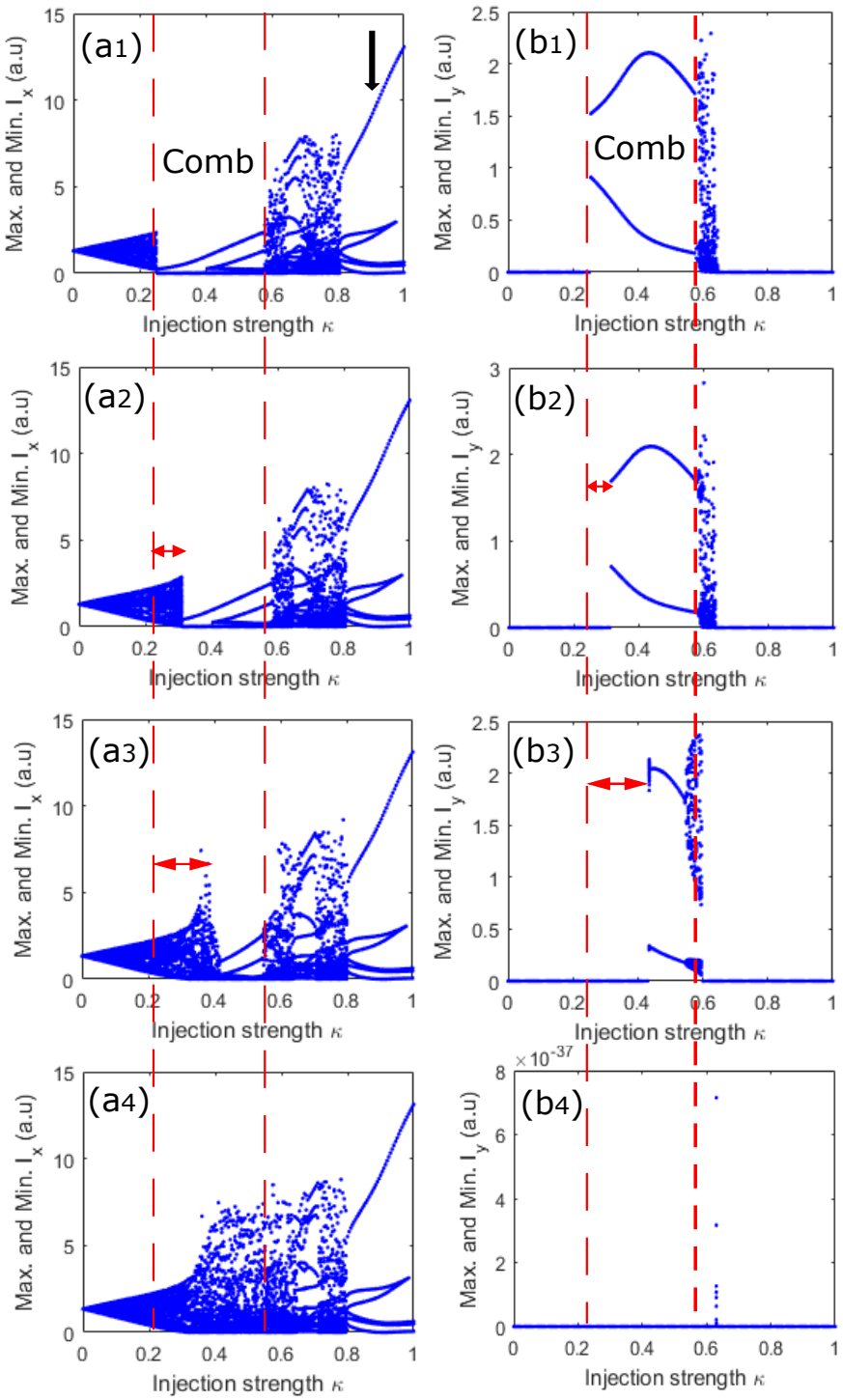

Figure 7.3: Bifurcation diagrams for fixed injected comb spacing $\Omega = 2$ GHz and detuning $\Delta\nu_x = -9$ GHz. The left and right panels correspond to X-polarization mode (X-PM) and Y-polarization mode (Y-PM). (a_1, b_1), (a_2, b_2), (a_3, b_3) and (a_4, b_4), are obtained for $\gamma_a = -0.1\ ns^{-1}$, $\gamma_a = -0.2\ ns^{-1}$, $\gamma_a = -0.6\ ns^{-1}$, and $\gamma_a = -0.8\ ns^{-1}$

strength, the VCSEL bifurcates abruptly to the excitation of the depressed polarization accompanied by comb generation at the same repetition rate as the injected one. The two dashed lines show the limits of the comb region in each polarization mode. The comb region is referred to as "comb" in the bifurcation diagrams (a_1) and (b_1). The comb in X-PM has more lines than the one in Y-PM. The number of resulting comb lines in Y-PM can be controlled with the injection parameters (detuning and injection strength). When we increase the injection strength again, complex dynamics take place in the two polarization modes. We check that the VCSEL can bifurcate from the two polarization comb dynamics for some injection parameters to harmonics polarization comb in X-PM and Y-PM. A further increase in the injection strength leads to abrupt suppression of the power in the Y-PM and the appearance of harmonics comb in X-PM. These harmonics comb dynamics become complex and give rise to a polarized comb in X-PM indicated by the black arrow in Fig. 7.3 (a_1). This X-PM comb has the same repetition rate as the injected one. We next decrease the linear dichroism γ_a to highlight its effect on the two polarization comb dynamics. Figure 7.3 (a_2), (a_3), (b_2), and (b_3) show that when decreasing γ_a, the size of the two polarization comb region decreases. The double horizontal arrows in the bifurcation diagrams indicate how much the comb regions decrease. The bifurcation sequences are similar to the case of $\gamma_a = -0.1\ ns^{-1}$. When the linear dichroism reaches $\gamma_a = -0.8,\ ns^{-1}$ the two polarization comb dynamics disappear and all the power in Y-PM is suppressed as shown in Fig. 7.3 (a_4) and (b_4). Therefore, excepted for the disappearance of the comb region in Y-PM, the bifurcation scenario in X-PM remains similar when varying γ_a.

Figure 7.4 shows an example comb and complex dynamics in the two polarization modes. Fig. 7.4 (a_1) and (b_1) show the optical spectra of comb dynamics in X-PM and Y-PM, respectively. It is well visible that the bandwidth of the frequency comb in the injected polarization mode (X-PM) is larger than the comb in the Y-PM. An example of complex dynamics is shown in Fig. 7.4 (a_2) and (b_2). As discussed above, depending on the injection parameters and injected comb properties, these complex dynamics can simultaneously bifurcate to a two polarization harmonic comb or single-polarization comb.

For fixed normalized bias current $\mu = 2.29$ and $\gamma_a = -0.8\ ns^{-1}$, there is no possibility to observe the two polarization comb in the plane of the injection parameters. To overcome this limitation, we keep all the parameters used to obtained Figure 7.3 (a_4), (b_4), and then we increase the normalized bias current.

When the normalized bias current is approximately 2.9 times the threshold current, $\mu = 4.2$,

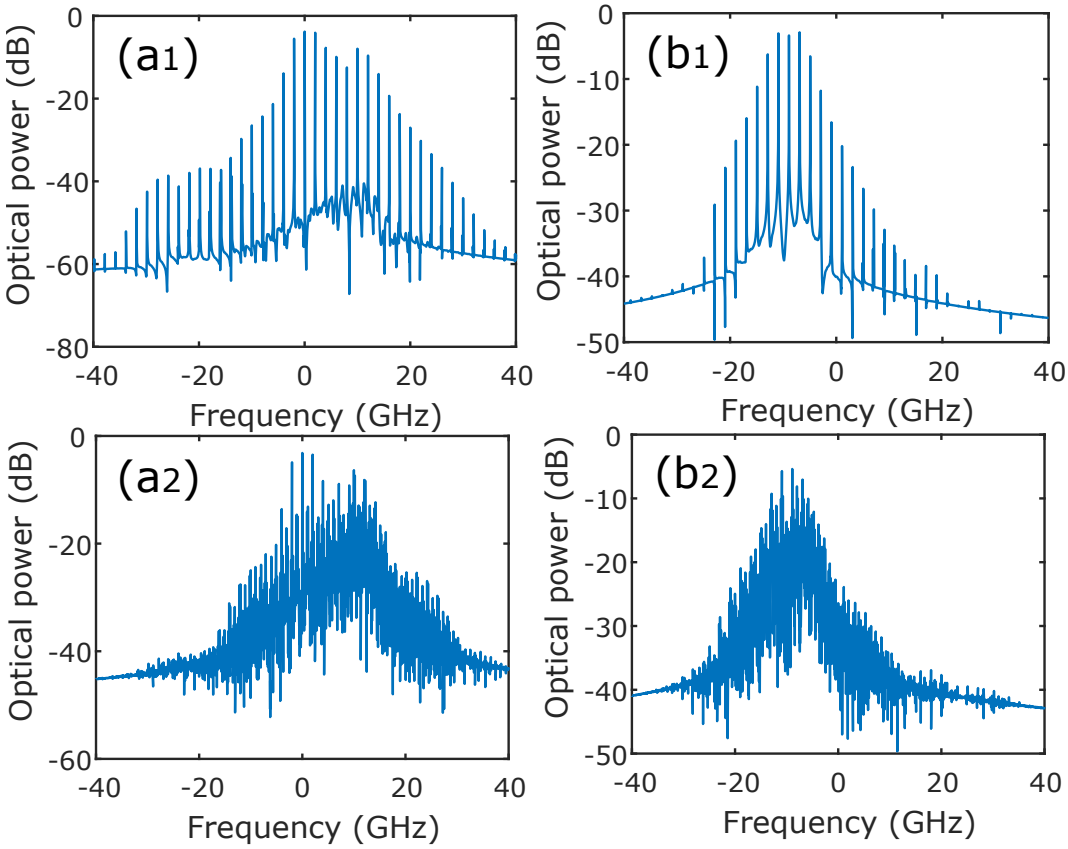

Figure 7.4: Optical spectra for fixed $\Omega = 2$ GHz, $\Delta\nu_x = -9$ GHz, and $\gamma_a = -0.6\ ns^{-1}$. The left and right panels correspond to X-PM and Y-PM, respectively. (a) and (b) correspond to the two polarization comb dynamics and are obtained for $\kappa = 0.525$. (a) and (b) correspond to the complex polarization dynamics obtained for $\kappa = 0.6$.

the two polarization comb dynamics start to appear again, as shown in Fig. 7.5. The left and right panels correspond to X-PM and Y-PM, respectively. In each bifurcation diagram, the two dashed line regions correspond to the two polarization comb regions. The bifurcation sequences leading to the polarization combs remain similar to those observed for $\mu = 2.29$. The modification of the comb dynamic with the bias current is explained in Chapters 4 and 5, where theoretical and experimental results have shown a significant improvement in the comb properties with the injection current. Figure 7.5 (c) and (d) show the bifurcation diagrams for $\mu = 5.29$, i.e., the bias current is approximately 3.5 times the threshold current. Unlike Fig. 7.5 (b) where the Y-PM comb disappears abruptly, in Fig. 7.5 (c) and (d) the VCSEL output shows a bifurcation to harmonics dynamics in both polarization modes before the polarized comb generation in X-PM.

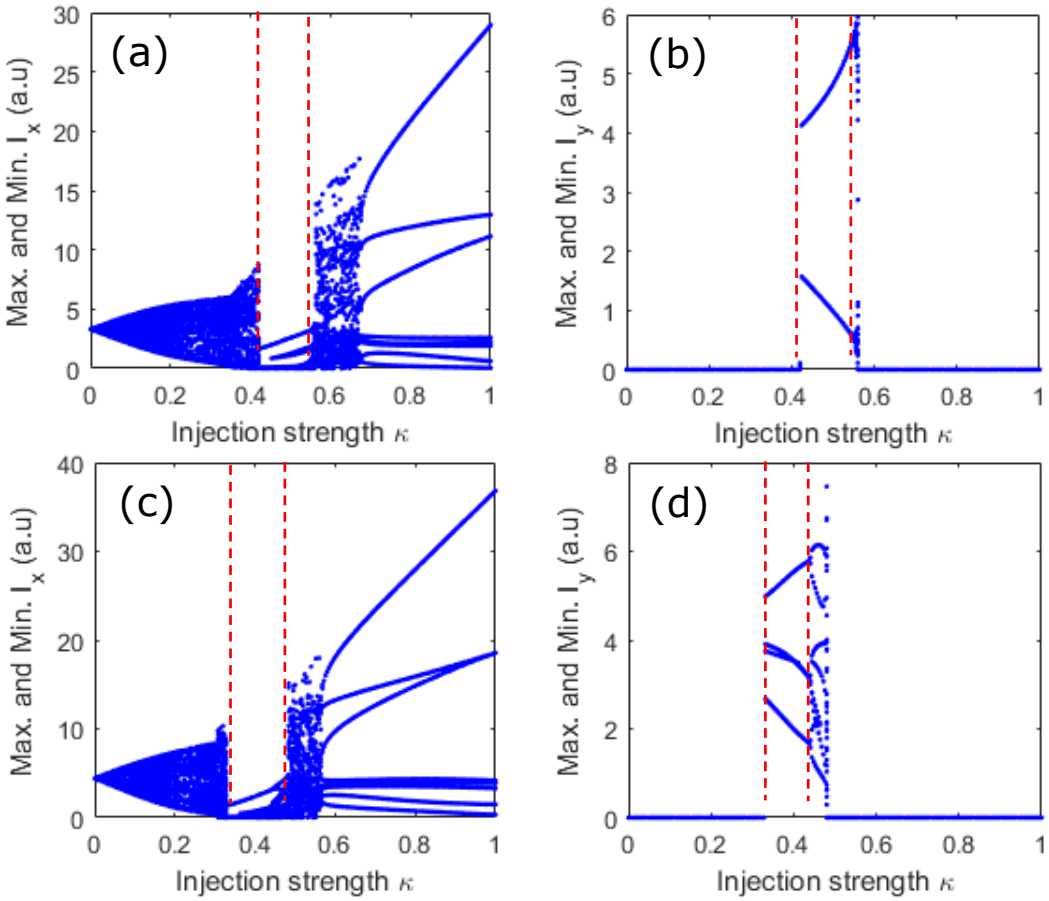

Figure 7.5: Bifurcation diagrams for fixed injected comb spacing $\Omega = 2$ GHz and $\gamma_a = -0.8\ ns^{-1}$. The left and right panels correspond to X-PM and Y-PM, respectively. (a) and (b) are obtained for $\mu = 4.2$ and (c) and (d) for $\mu = 5.29$.

7.2.2 Orthogonal optical injection

Here, we analyze the polarization dynamics numerically when the injected comb's polarization is orthogonal to that of the VCSEL. To this end, we modify the laser system equation (7.12)-(7.15) by inserting the injected comb in the nonlasing polarization mode equation (Y-PM).

The rate equation of the SFM becomes:

$$\frac{dE_x}{dt} = \kappa(1 + i\alpha)(DE_x + inE_y - E_x) - i(\gamma_p + \Delta\omega)E_x - \gamma_a E_x \tag{7.16}$$

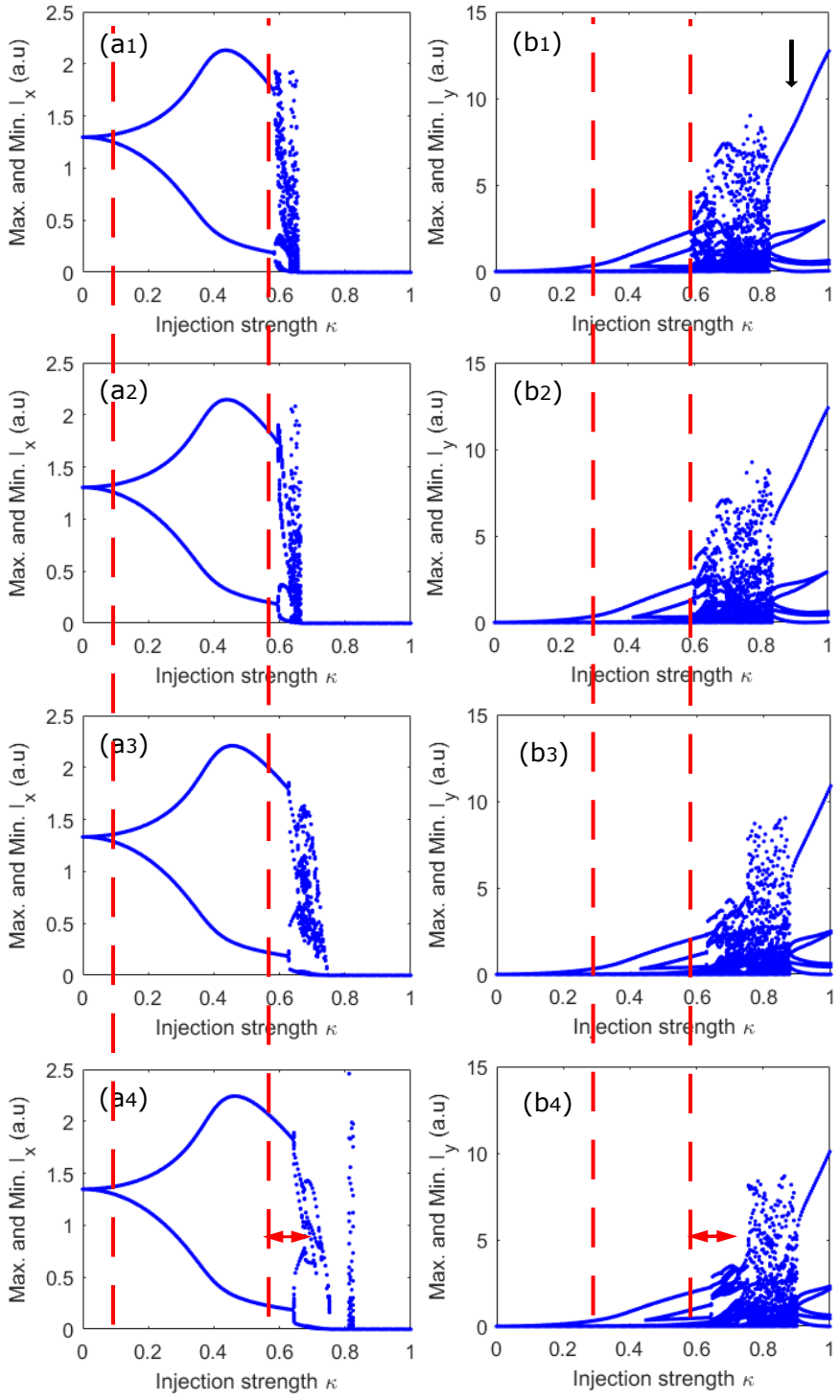

Figure 7.6: Bifurcation diagram for fixed injected comb spacing $\Omega = 2$ GHz and detuning $\Delta\nu_y = -9$ GHz for orthogonal optical injection. The left and right panels correspond to X-polarization mode (X-PM) and Y-polarization mode (Y-PM). (a_1, b_1), (a_2, b_2), (a_3, b_3) and (a_4, b_4), are obtained for $\gamma_a = -0.1\ ns^{-1}$, $\gamma_a = -0.2\ ns^{-1}$, $\gamma_a = -0.6\ ns^{-1}$, and $\gamma_a = -0.8\ ns^{-1}$

$$\frac{dE_y}{dt} = \kappa(1+i\alpha)(DE_y - inE_x - E_y) + i(\gamma_p - \Delta\omega)E_x + \gamma_a E_x + \kappa_{inj}(E_1 e^{-i\Omega} + E_2 + E_3 e^{i\Omega}) \quad (7.17)$$

$$\frac{dD}{dt} = -\gamma[D(1 + |E_x|^2 + |E_y|^2) - \mu + in(E_y E_x^* - E_x E_y^*)], \quad (7.18)$$

$$\frac{dn}{dt} = -\gamma_s n - \gamma[n(|E_x|^2 + |E_y|^2) + iD(E_y E_x^* - E_x E_y^*)]. \quad (7.19)$$

Further insight of the influence of γ_a on the two polarization comb dynamics is given in Fig. 7.6, where the bifurcation diagrams for various value of γ_a are plotted. These bifurcation diagrams are obtained for the same SFM parameters and injected comb spacing ($\Omega = 2$ GHz) as in Fig. 7.3 (case of parallel optical injection). The detuning frequency from Y-PM is $\Delta\nu_y = -9$ GHz. The left and right panels correspond to X-PM and Y-PM, respectively. The region between the two red dashed lines correspond to the comb area. Contrasting to parallel optical injection where the two polarization comb is induced abruptly when increasing the injection strength, X-PM starts to be excited with the appearance of new frequency lines at a frequency given by the injected comb spacing. Figure 7.6 shows that whatever is γ_a, the two polarization comb is observed. Interestingly, the size of the two polarization combs area increases slightly when γ_a decreases. It is worth noticing that the bifurcation scenario remains the same. This increase is indicated by double arrow in the bifurcation diagram of Fig. 7.6 (a_4) and (b_4). The complete polarization switching occurs when the injection strength is around $\kappa = 0.652$. The switching is accompanied by complex dynamics in Y-PM that leads to a polarized comb indicated by the black arrow in the bifurcation diagram of Fig. 7.6 (b_1). Unlike the parallel injection, where the number of lines in Y-PM is much smaller than for the X-PM, we checked that the Y-PM comb is much broader, i.e., the number of lines is larger than for the X-PM comb.

7.3 Experimental results: VCSEL with parallel injection

This section will analyze the nonlinear dynamics of a single-mode VCSEL subject to parallel optical injection experimentally. First, we report on the bifurcations scenarios leading to the excitation of the depressed polarization mode (Y-PM) accompanied by two polarization comb generations. We also provide a close inspection of the comb dynamics as a function of the injected comb spacing. When the bias current is close to the threshold, the performance of frequency comb dynamics decreases with the injected comb spacing.

To overcome this limitation, we increase the injected comb spacing and the bias current simultaneously.

The experimental results in this section have been obtained with the setup shown in Fig. 6.1. First, the polarization controller at the input of the VCSEL was fine-tuned to align the polarization of the injected comb with that of the VCSEL.

7.3.1 Bias current close to the threshold

Here, we discuss the limitations of the two polarization comb dynamics as a function of the injected comb spacing and how to overcome them.

7.3.1.1 Comb spacing $\Omega = 1$ GHz

We first describe the bifurcation sequences of the VCSEL output under the same operating condition as the case of orthogonal injection (Chapter 6), i.e., the bias current is $I = 6$ mA. Figure 7.7 shows the VCSEL output for fixed injected comb spacing $\Omega = 1$ GHz, and detuning frequency $\Delta\nu = 1.6$ GHz. Figure 7.7 (a) and (b) show that when increasing the injected power, the dominant polarization mode (X-PM) of the VCSEL is destabilized, accompanied by nonlinear wave mixing. This nonlinear wave mixing is similar to that described in Chapter 5 in Fig. 5.8 (b). When we increase the injected power from Fig. 7.7 (b) to (c), the VCSEL output is still showing a wave mixing, but the number of frequency lines involved is decreasing, giving rise to the appearance of the comb in the X-PM. The depressed polarization mode (Y-PM) starts to be excited. An increase in the injected power is sufficient to excite a frequency comb in the two polarization modes, as shown in Fig. 7.7 (d). These frequency combs have the same repetition rate as the injected ones. The most significant comb line in the Y-PM appears at its free-running frequency position. These two polarization combs have comparable power with 9 frequency lines in the X-PM comb and 8 in the Y-PM comb at -30 dB from the maximum. When we keep increasing the injected power, the Y-PM comb quality deteriorates while the number of lines in X-comb increases, as shown in Fig. 7.7 (e). A fine-tuning of the injected power allows unveiling harmonics frequency between the main comb lines as shown in Fig. 7.7 (f), creating a new frequency comb with a repetition rate of $\Omega = 500$ MHz. These harmonics comb take place in the two linear polarization modes. When we increase the injected power from Fig. 7.7 (g), the VCSEL bifurcates to the complex dynamics generation in each polarization mode. As a result, a comb takes place in X-PM accompanied by the

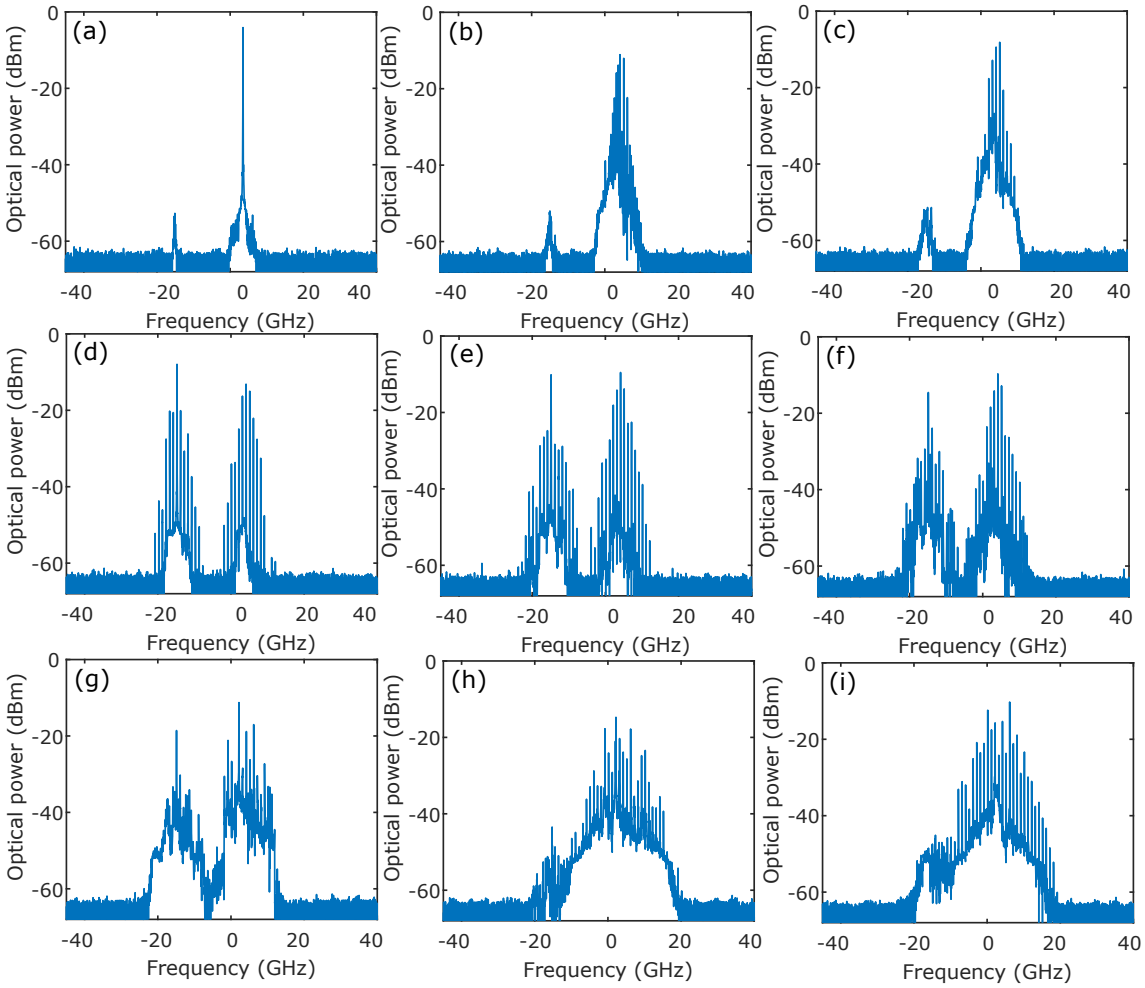

Figure 7.7: Bifurcation scenarios leading to the excitation of the depressed polarization mode. These optical spectra are obtained for detuning $\Delta\nu = 1.6$ GHz and injected comb spacing $\Omega = 1$ GHz. (a) stable output at $P_{inj} = 3$ µW, (b) and (c) wave mixing at $P_{inj} = 16$ µW and $P_{inj} = 32$ µW, respectively, (d) two polarization comb at $P_{inj} = 48$ µW, (e) and (f) two polarization harmonics comb, at $P_{inj} = 80$ µW and $P_{inj} = 96$ µW,respectively, (g) two polarization complex dynamics at $P_{inj} = 128$ µW, and (h) and (i) X-polarization comb at $P_{inj} = 144$ µW, and $P_{inj} = 240$ µW, respectively.

suppression of the power in Y-PM as shown in Fig. 7.7 (h). A further increase in the injected power leads to a single polarization comb in X-PM with the same repetition rate as the injected comb. This X-PM is broader than the X-PM comb of Fig. 7.7 (d), and (e), but the noise pedestal is significantly increased. The experimental bifurcation scenario described here is in excellent agreement with the theoretical bifurcation analysis of Fig. 7.3.

7.3.1.2 Comb spacing $\Omega = 2$ GHz

To evaluate the impact of the injected comb spacing on the two polarization comb dynamics, we increase it to $\Omega = 2$ GHz. The detuning frequency is the same as Fig. 7.7, i.e., $\Delta\nu = 1.6$ GHz. For low injected power, Fig. 7.8 (a) and (b) shows that the VCSEL output is stable like in free-running and then bifurcates to the nonlinear wave mixing between the detuning and new lines that depend on the injected comb spacing as already shown Fig. 7.7 (b) and (c). When increasing the injected power, the VCSEL output shows two polarization combs in Fig. 7.8 (c) and (d). Compared to Fig. 7.7 (b) and (c), we observe a significant decrease in the number of resulting comb lines in each polarization mode. Each polarization mode has only 3-lines at -30 dB from the maximum. Like in Fig. 7.7, further, an increase in the injected power leads to the complex dynamics that bifurcates to polarized comb in X-PM as shown in Fig. 7.8 (e) and (f). This polarized comb has an important noise pedestal. When we increase the injected comb spacing to $\Omega = 4$ GHz, the Y-PM is excited but without comb generation. We checked that the two polarization comb is not observed in the plane of the injection parameters. The bifurcation leads to a polarized comb or a related harmonic comb. Under parallel optical injection, when the bias current is below $I = 6mA$, the two polarization combs are not observed, whatever is the injection parameters and the injected comb spacing. In contrast, when the polarization of the injected comb is orthogonal to that of the VCSEL, excitation of the two polarization modes with comb generation is always observed, whatever is the bias current.

7.3.2 Bias current far from the threshold

We now increase the bias current to $I = 8$ mA, which is 2.67 times the threshold current. Here, we increase the injected comb spacing to $\Omega = 4$ GHz.

Figure 7.9 is recorded for fixed detuning frequency $\Delta\nu = -0.9$ GHz when increasing the injected power P_{inj}. Like Fig. 7.7 (c) and (b), we observe a modulation of the VCSEL output at low injected power (see Fig. 7.9 (a) and (b)). Unlike Fig. 7.7 and Fig. 7.8 where the nonlinear wave mixing in X-PM is accompanied with two polarization comb, the VCSEL bifurcates to the selective amplification of the central injected comb line in X-PM as shown in Fig. 7.9 (c). The number of comb lines increases with the injected power due to the modulation of the carrier density, as we can see in Fig. 7.9 (d). When we keep increasing P_{inj}, the VCSEL output bifurcates to a comb that extends in both polarization modes as shown in Fig. 7.9 (e). We checked through the polarization-resolved

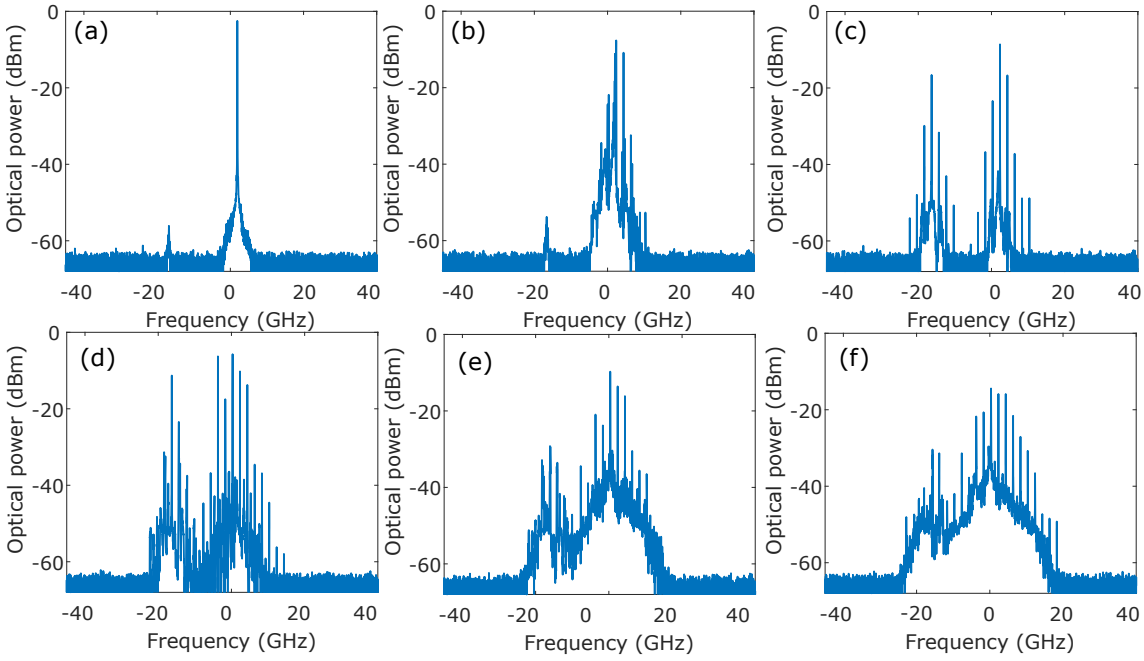

Figure 7.8: Bifurcation scenarios leading to the excitation of the depressed polarization mode. These optical spectra are obtained for detuning $\Delta\nu = 1.6$ GHz and injected comb spacing $\Omega = 2$ GHz. (a) stable output at $P_{inj} = 3$ µW, (b) wave mixing at $P_{inj} = 16$ µW, (c) two polarizations comb at $P_{inj} = 48$ µW, (d) two polarization harmonics comb at $P_{inj} = 112$ µW, (e) two polarization complex dynamics at $P_{inj} = 208$ µW, and (f) X-polarization comb at $P_{inj} = 240$ µW.

optical spectra that two combs with orthogonal polarization form this overall comb. The two combs have the same repetition rates as the injected comb. An increase in the injected power P_{inj} leads to a harmonic comb with new comb lines appearing between the main comb lines creating a new comb with a repetition rate of $\Omega = 2$ GHz (Fig. 7.9 (f)). The injection parameters can be used to increase the power in the harmonic comb lines. Some injection parameters lead to harmonics frequency comb with repetition at a quarter of the injected one (not shown). The harmonics comb bifurcates to the complex polarization dynamics when increasing the injected power as shown in (Fig. 7.9 (g)). A further increase in the injected power gives rise to a wide, stable comb in Fig. 7.9 (h). Like in Fig. 7.9 (e), this comb appears in the two polarization modes with comparable power. Compared to Fig. 7.9 (e) and (f), the noise pedestal is much decreased, which increases the amplitude of the comb lines from the noise level (CNR), hence improving the applicability of such a comb as the light source. When increasing P_{inj} further, the comb is destabilized through a significant increase in the noise pedestal ((Fig. 7.9 (i)), but the comb lines are still observed. We have shown that the performance (Bandwidth) of the two polarization

combs based on parallel optical injection is limited by the increase of the injected comb spacing for fixed bias current. However, the increase of the bias current allows improving the polarization combs bandwidth.

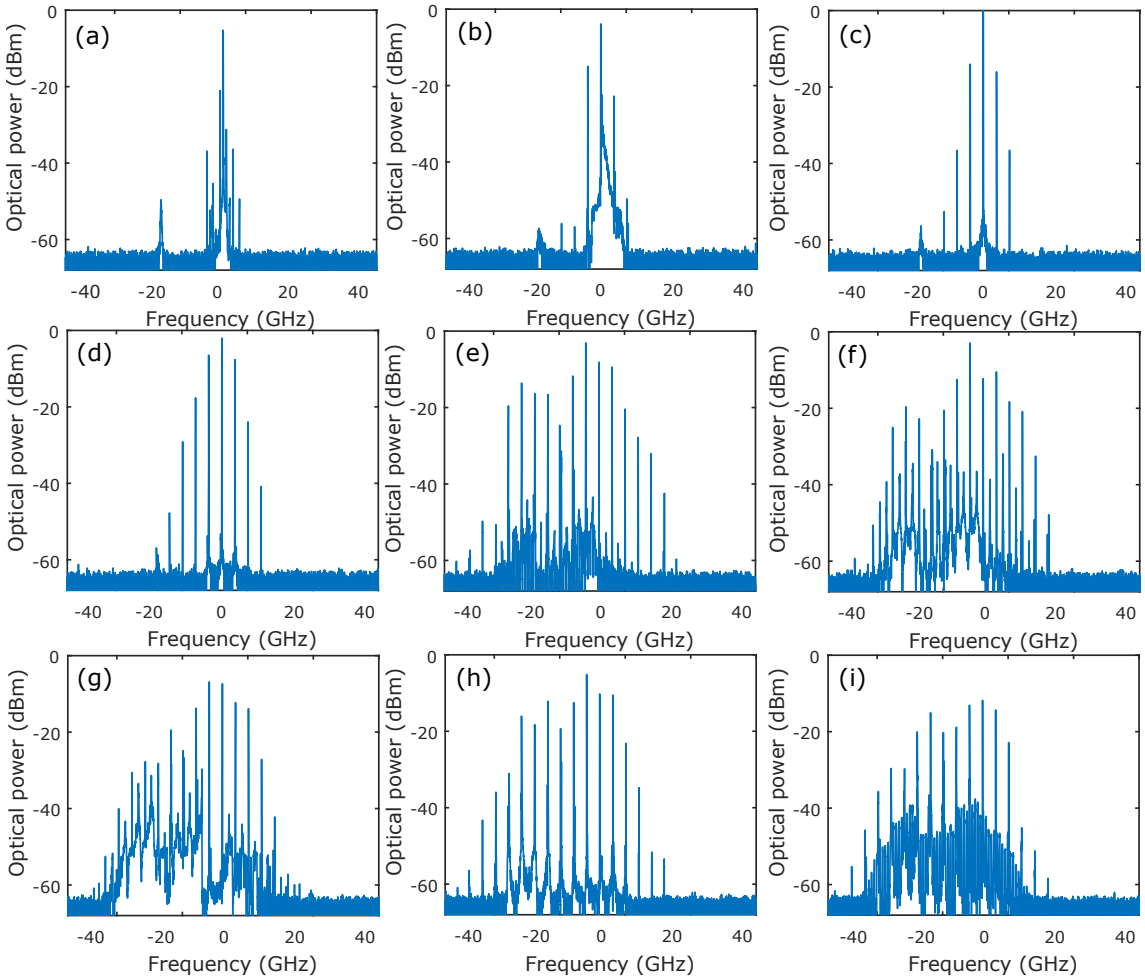

Figure 7.9: Bifurcation scenarios leading to the excitation of the depressed polarization mode. These optical spectra are obtained for detuning $\Delta\nu = -0.9$ GHz and injected comb spacing $\Omega = 4$ GHz. (a) and (b) wave mixing at $P_{inj} = 3$ µW, and $P_{inj} = 32$ µW, respectively, (c) and (d) single polarization comb at $P_{inj} = 48$ µW and $P_{inj} = 228$ µW, respectively, (e), (h) and (i) two polarizations comb at $P_{inj} = 304$ µW, $P_{inj} = 560$ µW and $P_{inj} = 704$ µW, respectively, (f) two polarization harmonics comb at $P_{inj} = 376$ µW, (g) two polarization complex dynamics at $P_{inj} = 448$ µW.

7.3.3 Comb performance analysis

To define the injection parameters that lead to the best comb dynamics, we plot in Fig. 7.10 the comb performance.

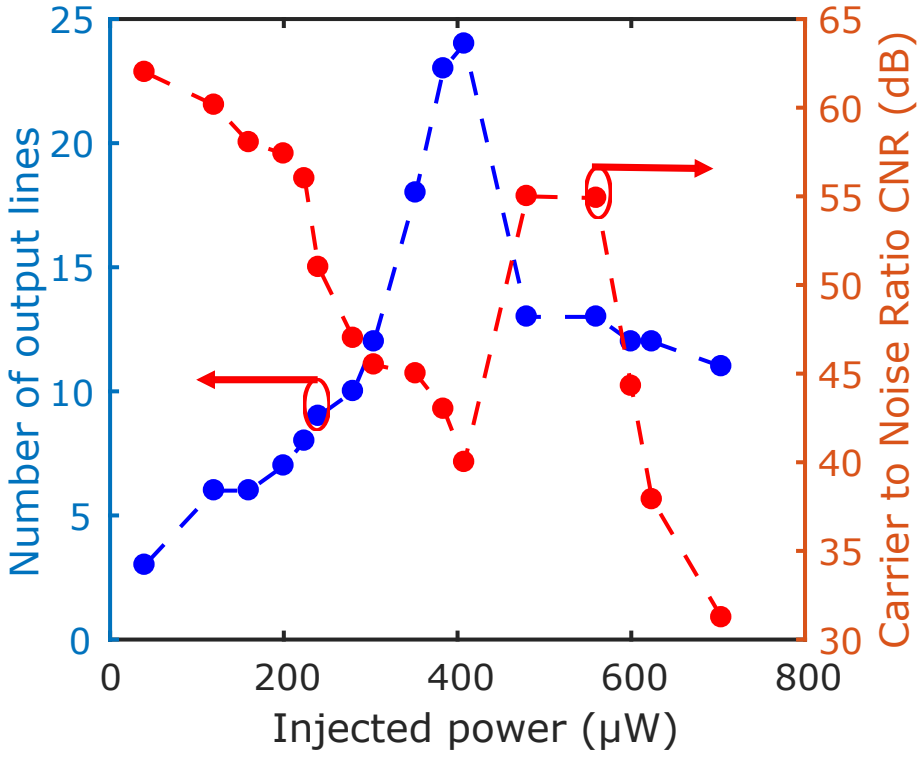

Figure 7.10: Comb performance for fixed bias current $I = 8$ mA, injected comb spacing $\Omega = 4$ GHz and detuning frequency $\Delta\nu = -0.9$ GHz. The left and right vertical axis show the number of resulting comb line (bandwidth) and the Carrier to Noise Ratio, respectively.

These comb properties are analyzed for a fixed bias current $I = 8$ mA, an injected comb spacing $\Omega = 4$ GHz, and a detuning frequency of $\Delta\nu = -0.9$ GHz. The left and right vertical axis show the resulting comb line (bandwidth) and the Carrier to Noise Ratio (CNR). The CNR and the number of comb lines (bandwidth) are calculated using the definition of Fig. 5.13. Figure 7.10 shows that for low injected power, the CNR is the largest and then decreases with the injected power to reach a minimum at $P_{inj} = 400$ μW. On the other hand, the number of comb lines increases with the injected power to reach a maximum at $P_{inj} = 400$ μW. The maximum number of lines and the minimum of the CNR are obtained at the same injected power. This is due to the appearance of harmonic comb lines, which increase the number of comb lines, but the noise pedestal increases as shown in Fig. 7.9 (f). The destabilization of the comb explains the decrease in the CNR and the number of lines at high injected power, as we can see in Fig. 7.9 (i).

7.4 Conclusion

We have demonstrated experimentally and theoretically that VCSEL can bifurcate to interesting polarization dynamics even under parallel optical frequency comb injection. These polarization dynamics include two polarization comb with orthogonal polarizations. We have numerically analyzed the influence of linear dichroism on the two polarization comb dynamics. Interestingly, when the VCSEL is subjected to parallel optical injection, the two polarization comb area becomes narrower when the linear dichroism decreases until it disappears at $\gamma_a = -0.8\ ns^{-1}$. On the other hand, when the polarization of the injected comb is orthogonal to that of the VCSEL, the two comb regions become much broader when decreasing γ_a. We have also reported that, under parallel injection, the comb dynamics performance decreases with the injected comb spacing and can be increased with the bias current. Finally, we have found that the CNR is the best at low injected power. The single or two polarization combs induced by parallel optical injection is not efficient in term of the number of lines at low bias current. Also, two polarization comb is observed only is if the bias current significantly large, at least twice the threshold current for the VCSEL considered here. In contrast, the single and two polarization combs have comparable properties in terms of CNR and bandwidth, whatever is the bias current.

8

Conclusions and perspectives

Contents

8.1 Summary of the dissertation 156

8.2 Perspective for future work 159

Throughout this thesis, we have discussed the nonlinear dynamics of semiconductor lasers optically injected with optical frequency combs. This study has been realized theoretically and experimentally. More specifically, we first studied the optical injection locking and selective amplification and the related bifurcations to nonlinear dynamics in edge-emitting lasers (EEL). We finalized our study by the nonlinear dynamics and polarization properties in VCSELs subjected to parallel or orthogonal optical injection of frequency combs. In this chapter, we summarize the thesis work and, most importantly, highlight the main achievements. We will then propose some perspectives for future work.

8.1 Summary of the dissertation

In chapter 2, we have investigated the fundamental physics of semiconductor lasers. We have first presented the three-ingredient essential for the laser operation: (1) a gain medium to provide amplification to the light, (2) a cavity to confine and then select the wavelength, and (3) a pump system to provide more electrons in the excited state to compensate the loss due to the absorption and the photons released by the cavity. We have also presented the physical mechanism underlying the operation of edge (EEL) and surface-emitting (VCSEL) laser operation. Semiconductor lasers can exhibit a wide variety of nonlinear when subjected to external perturbations (external modulation, feedback, and optical injection). These nonlinear dynamics include optical injection locking, periodic dynamics, chaotic dynamics, and complex dynamics. We have finally shown that these nonlinear dynamics can be used for several applications.

In chapter 3, we have presented the basic knowledge of the optical frequency comb. In a general way, we have first described the principle of optical frequency comb generation in a mode-locked laser using the time domain and frequency domain representation. Optical frequency comb can be generated by numerous physical systems such as electro-optic modulators, microresonators, semiconductors lasers, and gain-switching lasers. The physics underlying the optical frequency comb generation differs from a system to another. We have also emphasized the advantages and weaknesses of each physical system generating optical frequency comb. The mode-locked lasers, microresonators, quantum cascade lasers, and quantum dot lasers can generate broadband comb (spanning octave) with a repetition rate of 10-1000 GHz. The stability and tunability of their comb repetition rate depend

on their cavity properties. However, the electro-optic modulator can generate a broad comb, but their repetition rate is limited by the bandwidth of the modulator (a few tens of GHz). We finally described the principle of some modern technology using an optical frequency comb.

Chapter 4 has provided an in-depth numerical analysis of nonlinear dynamics in a laser diode with optical injection from frequency combs. We first mapped the nonlinear laser dynamics in the plane of the injection parameters. We have observed time-periodic dynamics corresponding to the injection locking with selective amplification at a low injection ratio at detuning frequency close to each injected comb line's frequency position. A saddle-node bifurcation leads to a modulation of laser output corresponding to a nonlinear wave mixing involving the detuning frequency and a new frequency depending on the injected comb spacing. The injection locking then bifurcates to an unlocked time-periodic dynamics corresponding to a broad optical spectrum with the same repetition rate as the injected one. Interestingly, the unlocked time-periodic dynamics are also observed at a large injection ratio and for large detuning, contrasting with the single-mode optical injection where no stationary dynamics can be obtained outside the injected locking region. The analysis of the pulse shape, the phase of the comb lines and the time-bandwidth product confirms that the time-periodic dynamics are optical frequency comb (new comb) sharing some properties in common with the injected comb. The comb dynamics show a cascade of bifurcations to harmonics frequency combs, increasing the number of output comb lines and decreasing the comb spacing. When the comb becomes chaotic, the chaos bandwidth is found to increase with the number of injected comb lines.

Chapter 5 has analyzed experimentally and numerically the nonlinear dynamics of comb injection. Additional numerical simulations are performed to account the asymmetry of the comb line amplitudes. When varying the injection strength and detuning frequency, we have revealed several dynamics, including injection locking with selective amplification of the main comb lines, nonlinear wave mixing, and unlocked time-periodic dynamics corresponding to an optical frequency comb (new comb). A comparison between theory and experiments allows concluding a strong agreement in the new comb appearance in the plane of the injection parameters. It is worth noticing that the size of the injection locking region of each injected comb line depends strongly on its amplitude. The phase analysis allows observing phase coherence between the comb lines. We have finally used the injection parameters and the bias current of the injected laser to control the comb

properties.

We have analyzed in Chapter 6 the polarization dynamics in a single-mode VCSEL subject to orthogonal optical frequency comb injection. We have shown that the power required to switch the VCSEL is smaller for comb injection than for single-mode injection when $\Delta\nu < -17.7$ GHz, while the switching power is larger for comb injection for single-mode injection when $\Delta\nu > -17.7$ GHz. Most importantly, there is no simple linear dependence between the increase in the injected comb spacing and the polarization switching (off and on) threshold. Similar to single-mode injection, we have found that polarization switching (PS) plays a crucial role in the laser dynamics. We have shown that the VCSEL can bifurcate to a single or two polarizations comb with the same comb spacing when varying the injection parameters. The PS and the injection parameters can be used to control the bandwidth, the repetition rate, and the carrier to noise ratio (CNR) of the single or two polarization comb. Interestingly, the best value of the CNR is found close to the PS point. The best comb properties are found when the nonlinear dynamics induced by the comb injection combine with the polarization competition to induce two combs with orthogonal polarizations in a single-mode VCSEL.

In Chapter 7, we have shown that parallel optical frequency comb injection in a single-mode VCSEL can also induce two combs with orthogonal polarizations. Under parallel optical injection, the two polarizations comb area can be suppressed with the decrease of the linear dichroism. By contrast, the size of the two polarizations comb area increases with the decrease of the linear dichroism when the VCSEL is subject to orthogonal optical injection. Compared to the orthogonal optical injection where the two polarization comb dynamics are observed even for large comb spacing, in the case of parallel optical injection, the two polarizations comb is limited to small comb spacing, e.g., in our case $\Omega = 2$ GHz. We have shown experimentally and numerically that this limitation can be overcome when increasing the bias current. Finally, we have found that the CNR is the best at relatively low injected power and as high as 62 dB. Under orthogonal optical injection, the single and two polarization combs show the same performance (bandwidth and CNR), whatever is the bias current. By contrast, in parallel optical injection, the polarization combs are not efficient in terms of number of comb lines at bias current less than two times the threshold current.

8.2 Perspective for future work

- Our theoretically and experimentally investigations have shown that an EEL and VCSEL can exhibit interesting time-periodic dynamics corresponding to the injection locking and new frequency combs. The polarization dynamics in the VCSEL have brought additional degree freedom to broaden the new optical frequency comb over the two-polarization modes. Despite the fact that nonlinear dynamics in the longitudinal mode lasers are less studied compared to the single polarization mode lasers, we believe that frequency comb injection into the longitudinal modes of a diode laser can bring additional dynamics. Furthermore, it would be very interesting to consider the interaction between the longitudinal modes of the cavity, i.e., a multimode laser with a small free spectral range (around 10 GHz). In that case, a long cavity multimode laser must be considered.

- We have shown in chapter 3 that a single electro-optic modulator can not generate a broadband and flat optical frequency comb without fluctuation in the comb lines. A very sophisticated experimental setup involving several phases and intensity modulators must be used to generate a wide and flat frequency comb. However, of particular interest is the injection of a very large number of comb lines in a diode laser. According to our results, we believe that the injection of a large number of comb lines into a single-mode laser can help to improve the comb bandwidth and flatness.

- We have shown that compared to the single-frequency injection, the frequency comb injection can lead to time-periodic dynamics corresponding to the injection locking and new frequency combs. It would be interesting to investigate the bifurcation leading to the new frequency comb dynamics. Several continuation software like AUTO and DDE-BIFTOOL have been used to analyze in-depth the bifurcation underlying optical injection or feedback dynamics, but they have not been used yet for injection of a frequency comb. This will provide a further understanding of the main difference between the single-mode and frequency comb injection dynamics.

- As we introduced in Chapter 3, generation of broad and flat frequency comb using electro-optics modulator requires the association of several phase modulators with intensity modulators. This technique is quite expensive in terms of cost and energy

consumption. We believe that the association of only one phase modulator with cascade DFB laser can improve the bandwidth and the flatness of the frequency comb-based phase modulator.

9

Bibliography

1. Cisco Visual Networking Index: Forecast and Trends, 2017–2022. https://twiki.cern.ch /twiki /pub/HEPIX/TechwatchNetwork /HtwNetworkDocuments/white-paper-c11-741490. *Cisco VNI Global IP Traffic Forecast* (2017–2022).
2. Chen, F.-S. Modulators for optical communications. *Proceedings of the IEEE* **58,** 1440–1457 (1970).
3. Koren, U., Koch, T. L., Presting, H. & Miller, B. InGaAs/InP multiple quantum well waveguide phase modulator. *Applied physics letters* **50,** 368–370 (1987).
4. Winzer, P. J. High-spectral-efficiency optical modulation formats. *Journal of Lightwave Technology* **30,** 3824–3835 (2012).
5. Shannon, C. E. A mathematical theory of communication. *The Bell system technical journal* **27,** 379–423 (1948).
6. Hu, H. & Oxenløwe, L. K. Chip-based optical frequency combs for high-capacity optical communications. *Nanophotonics* **10,** 1367–1385 (2021).
7. Faist, J. *et al.* Quantum cascade laser frequency combs. *Nanophotonics* **5,** 272–291 (2016).
8. Schröder, J. *et al.* Laser frequency combs for coherent optical communications. *Journal of Lightwave Technology* **37,** 1663–1670 (2019).
9. Duill, S. P. Ó., Anandarajah, P. M., Smyth, F. & Barry, L. P. *Injection-locking criteria for simultaneously locking single-mode lasers to optical frequency combs from gain-switched lasers* in *Physics and Simulation of Optoelectronic Devices XXV* **10098** (2017), 100980H.
10. Shortiss, K. J., Shayesteh, M. & Peters, F. H. Modelling the effect of slave laser gain and frequency comb spacing on the selective amplification of injection locked semiconductor lasers. *Optical and Quantum Electronics* **50,** 49 (2018).

11. Moon, H., Kim, E., Park, S. & Park, C. Selection and amplification of modes of an optical frequency comb using a femtosecond laser injection-locking technique. *Applied Physics Letters* **89,** 181110 (2006).

12. Gavrielides, A. Comb Injection and Sidebands Suppression. *IEEE Journal of Quantum Electronics* **50,** 364–371 (2014).

13. Wu, D. S., Richardson, D. J. & Slavık, R. *Selective amplification of frequency comb modes via optical injection locking of a semiconductor laser: influence of adjacent unlocked comb modes* in *Integrated Optics: Physics and Simulations* **8781** (2013), 87810J.

14. Wu, D. S., Slavık, R., Marra, G. & Richardson, D. J. Direct selection and amplification of individual narrowly spaced optical comb modes via injection locking: design and characterization. *Journal of Lightwave Technology* **31,** 2287–2295 (2013).

15. Wu, D. S., Slavık, R., Marra, G. & Richardson, D. J. *Phase noise and jitter characterization of pulses generated by optical injection locking to an optical frequency comb* in *Frontiers in Optics* (2012), FW2A–3.

16. Tistomo, A. S. & Gee, S. Laser frequency fixation by multimode optical injection locking. *Optics Express* **19,** 1081–1090 (2011).

17. Pramod, M. S., Yang, T., Pandey, K., Giudici, M. & Wilkowski, D. Selective injection locking of a multi-mode semiconductor laser to a multi-frequency reference beam. *The European Physical Journal D* **68,** 186 (2014).

18. Shortiss, K., Lingnau, B., Dubois, F., Kelleher, B. & Peters, F. H. Harmonic frequency locking and tuning of comb frequency spacing through optical injection. *Optics Express* **27,** 36976–36989 (2019).

19. Desmet, R. & Virte, M. Laser diodes with modulated optical injection: towards a simple signal processing unit? *Journal of Physics: Photonics* **2,** 025002 (2020).

20. Lingnau, B., Shortiss, K., Dubois, F., Peters, F. H. & Kelleher, B. Universal generation of devil's staircases near Hopf bifurcations via modulated forcing of nonlinear systems. *Physical Review E* **102,** 030201 (2020).

21. Mogensen, F., Olesen, H. & Jacobsen, G. Locking conditions and stability properties for a semiconductor laser with external light injection. *IEEE Journal of Quantum Electronics* **21,** 784–793 (1985).

22. Doumbia, Y., Malica, T., Wolfersberger, D., Panajotov, K. & Sciamanna, M. Optical injection dynamics of frequency combs. *Optics Letters* **45,** 435–438 (2020).

23. Doumbia, Y., Malica, T., Wolfersberger, D., Panajotov, K. & Sciamanna, M. Nonlinear dynamics of a laser diode with an injection of an optical frequency comb. *Optics Express* **28,** 30379–30390 (2020).

24. Doumbia, Y., Malica, T., Wolfersberger, D., Panajotov, K. & Sciamanna, M. *Frequency comb customization by controlling the optical injection dynamics* in *Semiconductor Lasers and Laser Dynamics IX* **11356** (2020), 113560G.

25. Doumbia, Y., Wolfersberger, D., Panajotov, K. & Sciamanna, M. Tailoring frequency combs through VCSEL polarization dynamics. *Optics Express* **29,** 33976–33991 (2021).

26. Doumbia, Y., Wolfersberger, D., Panajotov, K. & Sciamanna, M. *Two Polarization Comb Dynamics in VCSELs Subject to Optical Injection* in *Photonics* **9** (2022), 115.

27. Doumbia, Y., Wolfersberger, D., Panajotov, K. & Sciamanna, M. *Optical Injection Dynamics of VCSEL Frequency Combs* in *The European Conference on Lasers and Electro-Optics* (2021), cb_p_5.

28. Doumbia, Y., Wolfersberger, D., Panajotov, K. & Sciamanna, M. *Nonlinear Polarization Dynamics of VCSEL with Frequency Comb Injection* in *Integrated Photonics Research, Silicon and Nanophotonics* (2021), IF1A–6.

29. Maiman, T. H. *et al.* Stimulated optical radiation in ruby (1960).

30. Einstein, A. Zur quantentheorie der strahlung. *Phys. Z.* **18,** 124 (1917).

31. Haken, H. Analogy between higher instabilities in fluids and lasers. *Physics Letters A* **53,** 77–78 (1975).

32. Scholz, H., Yamada, T., Brand, H. & Graham, R. Intermittency and chaos in a laser system with modulated inversion. *Physics Letters A* **82,** 321–323 (1981).

33. Lodi, V. & Donati, S. Injection modulation in coupled laser oscillators. *IEEE Journal of Quantum Electronics* **16,** 859–864 (1980).

34. Yamada, T. & Graham, R. Chaos in a laser system under a modulated external field. *Physical Review Letters* **45,** 1322 (1980).

35. Weiss, C., Klische, W., Ering, P. & Cooper, M. Instabilities and chaos of a single mode NH3 ring laser. *Optics communications* **52,** 405–408 (1985).

36. Hogenboom, E., Klische, W., Weiss, C. & Godone, A. Instabilities of a homogeneously broadened laser. *Physical review letters* **55,** 2571 (1985).

37. Weiss, C. & King, H. Oscillation period doubling chaos in a laser. *Optics Communications* **44,** 59–61 (1982).

38. Weiss, C., Godone, A. & Olafsson, A. Routes to chaotic emission in a cw He-Ne laser. *Physical Review A* **28,** 892 (1983).

39. Casperson, L. Spontaneous coherent pulsations in laser oscillators. *IEEE Journal of Quantum Electronics* **14,** 756–761 (1978).

40. Lugiato, L., Narducci, L., Bandy, D. & Pennise, C. Breathing, spiking and chaos in a laser with injected signal. *Optics Communications* **46,** 64–68 (1983).

41. Schubert, E. F. *Light-Emitting Diodes (2006)* (E. Fred Schubert, 2006).

42. Thompson, G. H. B. Physics of semiconductor laser devices. *Chichester* (1980).

43. Kroemer, H. A proposed class of hetero-junction injection lasers. *Proceedings of the IEEE* **51,** 1782–1783 (1963).

44. Nathan, M. I., Dumke, W. P., Burns, G., Dill Jr, F. H. & Lasher, G. Stimulated emission of radiation from GaAs p-n junctions. *Applied Physics Letters* **1,** 62–64 (1962).

45. Hall, R. N., Fenner, G. E., Kingsley, J., Soltys, T. & Carlson, R. Coherent light emission from GaAs junctions. *Physical Review Letters* **9,** 366 (1962).

46. Quist, T. M. *et al.* Semiconductor maser of GaAs. *Applied Physics Letters* **1,** 91–92 (1962).

47. Van Tartwijk, G. & Lenstra, D. Semiconductor lasers with optical injection and feedback. *Quantum and Semiclassical Optics: Journal of the European Optical Society Part B* **7,** 87 (1995).

48. Haken, H. *Laser light dynamics, Vol. 2* 1985.

49. Dutta, N., Olsson, N. & Tsang, W. Carrier induced refractive index change in AlGaAs quantum well lasers. *Applied physics letters* **45,** 836–837 (1984).

50. Soda, H., Iga, K.-i., Kitahara, C. & Suematsu, Y. GaInAsP/InP surface emitting injection lasers. *Japanese Journal of Applied Physics* **18,** 2329 (1979).

51. Iga, K., Ishikawa, S., Ohkouchi, S. & Nishimura, T. Room-temperature pulsed oscillation of GaAlAs/GaAs surface emitting injection laser. *Applied Physics Letters* **45,** 348–350 (1984).

52. Iga, K., Kinoshita, S. & Koyama, F. Microcavity GalaAs/GaAs surface-emitting laser with Ith= 6 mA. *Electronics letters* **23,** 134–136 (1987).

53. Jewell, J. *et al.* Low-threshold electrically pumped vertical-cavity surface-emitting microlasers. *Electronics Letters* **25,** 1123–1124 (1989).

54. Lee, Y.-H. *et al.* Room-temperature continuous-wave vertical-cavity single-quantum-well microlaser diodes. *Electronics Letters* **25,** 1377–1378 (1989).

55. Choquette, K. D., Richie, D. & Leibenguth, R. Temperature dependence of gain-guided vertical-cavity surface emitting laser polarization. *Applied physics letters* **64,** 2062–2064 (1994).

56. Yang, 2. M., MacDougal, M. & Dapkus, P. Ultralow threshold current vertical-cavity surface-emitting lasers obtained with selective oxidation. *Electronics Letters* **31,** 886–888 (1995).

57. Hayashi, Y. *et al.* Lasing characteristics of low-threshold oxide confinement InGaAs-GaAlAs vertical-cavity surface-emitting lasers. *IEEE Photonics Technology Letters* **7,** 1234–1236 (1995).

58. Larsson, A. Advances in VCSELs for Communication and Sensing. *IEEE Journal of Selected Topics in Quantum Electronics* **17,** 1552–1567 (2011).

59. Liu, J.-M. *Photonic devices* (Cambridge University Press, 2009).

60. Chang-Hasnain, C. *et al.* Transverse mode characteristics of vertical cavity surface-emitting lasers. *Applied physics letters* **57,** 218–220 (1990).

61. Chang-Hasnain, C. J. *et al.* Dynamic, polarization, and transverse mode characteristics of vertical cavity surface emitting lasers. *IEEE Journal of Quantum Electronics* **27,** 1402–1409 (1991).

62. Chong, C. & Sarma, J. Lasing mode selection in vertical-cavity surface emitting-laser diodes. *IEEE photonics technology letters* **5,** 761–764 (1993).

63. Valle, A., Sarma, J. & Shore, K. Spatial holeburning effects on the dynamics of vertical cavity surface-emitting laser diodes. *IEEE Journal of Quantum Electronics* **31,** 1423–1431 (1995).

64. Valle, A., Pesquera, L. & Shore, K. Polarization behavior of birefringent multi-transverse mode vertical-cavity surface-emitting lasers. *IEEE Photonics Technology Letters* **9,** 557–559 (1997).

65. Choquette, K. D., Schneider, R. P., Lear, K. L. & Leibenguth, R. E. Gain-dependent polarization properties of vertical-cavity lasers. *IEEE Journal of Selected Topics in Quantum Electronics* **1,** 661–666 (1995).

66. Van Exter, M., van Doorn, A. J. & Woerdman, J. Electro-optic effect and birefringence in semiconductor vertical-cavity lasers. *Physical Review A* **56,** 845 (1997).

67. Jansen van Doorn, A., Van Exter, M. & Woerdman, J. Elasto-optic anisotropy and polarization orientation of vertical-cavity surface-emitting semiconductor lasers. *Applied physics letters* **69,** 1041–1043 (1996).

68. Panajotov, K. *et al. Polarization behavior of vertical-cavity surface-emitting lasers: experiments, models and applications* in *AIP Conference Proceedings* **560** (2001), 403–417.

69. Panajotov, K. *et al.* Impact of in-plane anisotropic strain on the polarization behavior of vertical-cavity surface-emitting lasers. *Applied Physics Letters* **77,** 1590–1592 (2000).

70. Peeters, M. *et al. Polarization behavior of vertical-cavity surface-emitting lasers under the influence of in-plane anisotropic strain* in *Vertical-Cavity Surface-Emitting Lasers VI* **4649** (2002), 281–291.

71. Ryvkin, B. *et al.* Effect of photon-energy-dependent loss and gain mechanisms on polarization switching in vertical-cavity surface-emitting lasers. *JOSA B* **16,** 2106–2113 (1999).

72. Martin-Regalado, J., Chilla, J., Rocca, J. & Brusenbach, P. Polarization switching in vertical-cavity surface emitting lasers observed at constant active region temperature. *Applied physics letters* **70,** 3350–3352 (1997).

73. Gatare, I., Sciamanna, M., Nizette, M. & Panajotov, K. Bifurcation to polarization switching and locking in vertical-cavity surface-emitting lasers with optical injection. *Physical Review A* **76,** 031803 (2007).

74. Sciamanna, M. & Panajotov, K. Route to polarization switching induced by optical injection in vertical-cavity surface-emitting lasers. *Physical Review A* **73,** 023811 (2006).

75. San Miguel, M., Feng, Q. & Moloney, J. V. Light-polarization dynamics in surface-emitting semiconductor lasers. *Physical Review A* **52,** 1728 (1995).

76. Sciamanna, M. Nonlinear dynamics and polarization properties of externally driven semiconductor lasers (2006).

77. Ignace, G. G. *Polarization Switching, Locking and Synchronization in VCSELs with Optical Injection* PhD thesis (Citeseer, 2008).

78. Chen, Y., Winful, H. & Liu, J. Subharmonic bifurcations and irregular pulsing behavior of modulated semiconductor lasers. *Applied physics letters* **47,** 208–210 (1985).

79. Tang, M. & Wang, S. Simulation studies of bifurcation and chaos in semiconductor lasers. *Applied physics letters* **48,** 900–902 (1986).

80. Tucker, R. S. High-speed modulation of semiconductor lasers. *IEEE transactions on electron devices* **32,** 2572–2584 (1985).

81. Liu, H.-F. & Ngai, W. F. Nonlinear dynamics of a directly modulated 1.55 mu m InGaAsP distributed feedback semiconductor laser. *IEEE journal of quantum electronics* **29,** 1668–1675 (1993).

82. Tarucha, S. & Otsuka, K. Response of semiconductor laser to deep sinusoidal injection current modulation. *IEEE Journal of Quantum Electronics* **17,** 810–816 (1981).

83. Lee, C.-H., Yoon, T.-H. & Shin, S.-Y. Period doubling and chaos in a directly modulated laser diode. *Applied Physics Letters* **46,** 95–97 (1985).

84. Valle, A., Sciamanna, M. & Panajotov, K. Nonlinear dynamics of the polarization of multitransverse mode vertical-cavity surface-emitting lasers under current modulation. *Physical Review E* **76,** 046206 (2007).

85. Sciamanna, M., Valle, A., Megret, P., Blondel, M. & Panajotov, K. Nonlinear polarization dynamics in directly modulated vertical-cavity surface-emitting lasers. *Physical Review E* **68,** 016207 (2003).

86. Valle, A., Pesquera, L., Turovets, S. & Lopez, J. Nonlinear dynamics of current-modulated vertical-cavity surface-emitting lasers. *Optics communications* **208,** 173–182 (2002).

87. Masoller, C., Torre, M. S. & Shore, K. A. Polarization dynamics of current-modulated vertical-cavity surface-emitting lasers. *IEEE journal of quantum electronics* **43,** 1074–1082 (2007).

88. Lang, R. & Kobayashi, K. External optical feedback effects on semiconductor injection laser properties. *IEEE journal of Quantum Electronics* **16,** 347–355 (1980).

89. Erneux, T., Gavrielides, A. & Sciamanna, M. Stable microwave oscillations due to external-cavity-mode beating in laser diodes subject to optical feedback. *Physical Review A* **66,** 033809 (2002).

90. Erneux, T. *Applied delay differential equations* (Springer Science & Business Media, 2009).

91. Rogister, F. *et al.* Secure communication scheme using chaotic laser diodes subject to incoherent optical feedback and incoherent optical injection. *Optics Letters* **26,** 1486–1488 (2001).

92. Rogister, F., Sciamanna, M., Deparis, O., Mégret, P. & Blondel, M. Low-frequency fluctuation regime in a multimode semiconductor laser subject to a mode-selective optical feedback. *Physical Review A* **65,** 015602 (2001).

93. Sciamanna, M. *et al. High-frequency dynamics in delayed semiconductor lasers with short external cavity* in *Physics and Simulation of Optoelectronic Devices XI* **4986** (2003), 469–479.

94. Sciamanna, M., Mégret, P. & Blondel, M. Hopf bifurcation cascade in small-α laser diodes subject to optical feedback. *Physical Review E* **69,** 046209 (2004).

95. Tabaka, A., Panajotov, K., Veretennicoff, I. & Sciamanna, M. Bifurcation study of regular pulse packages in laser diodes subject to optical feedback. *Physical Review E* **70,** 036211 (2004).

96. Mercier, É., Wolfersberger, D. & Sciamanna, M. Bifurcation to chaotic low-frequency fluctuations in a laser diode with phase-conjugate feedback. *Optics letters* **39,** 4021–4024 (2014).

97. Virte, M., Breuer, S., Sciamanna, M. & Panajotov, K. Switching between ground and excited states by optical feedback in a quantum dot laser diode. *Applied Physics Letters* **105,** 121109 (2014).

98. Lenstra, D., Verbeek, B. & Den Boef, A. Coherence collapse in single-mode semiconductor lasers due to optical feedback. *IEEE Journal of Quantum Electronics* **21,** 674–679 (1985).

99. Ohtsubo, J. *Semiconductor lasers: stability, instability and chaos* (Springer, 2012).

100. Lin, C.-Y., Grillot, F., Naderi, N., Li, Y. & Lester, L. RF linewidth reduction in a quantum dot passively mode-locked laser subject to external optical feedback. *Applied Physics Letters* **96,** 051118 (2010).

101. Grillot, F., Lin, C.-Y., Naderi, N., Pochet, M. & Lester, L. Optical feedback instabilities in a monolithic InAs/GaAs quantum dot passively mode-locked laser. *Applied Physics Letters* **94,** 153503 (2009).

102. Huang, H. *et al.* Analysis of the optical feedback dynamics in InAs/GaAs quantum dot lasers directly grown on silicon. *JOSA B* **35,** 2780–2787 (2018).

103. Dong, B. *et al.* Dynamic and nonlinear properties of epitaxial quantum-dot lasers on silicon operating under long-and short-cavity feedback conditions for photonic integrated circuits. *Physical Review A* **103,** 033509 (2021).

104. Virte, M., Dal Bosco, A. K., Wolfersberger, D. & Sciamanna, M. Chaos crisis and bistability of self-pulsing dynamics in a laser diode with phase-conjugate feedback. *Physical Review A* **84,** 043836 (2011).

105. Tkach, R. & Chraplyvy, A. Regimes of feedback effects in 1.5-μm distributed feedback lasers. *Journal of Lightwave technology* **4,** 1655–1661 (1986).

106. Dal Bosco, A. K., Wolfersberger, D. & Sciamanna, M. Super-harmonic self-pulsations from a time-delayed phase-conjugate optical system. *Applied Physics Letters* **105,** 081101 (2014).

107. Sciamanna, M. & Shore, K. A. Physics and applications of laser diode chaos. *Nature Photonics* **9,** 151 (2015).

108. Sciamanna, M., Rogister, F., Mégret, P. & Blondel, M. *Numerical observation of in-phase and out-of-phase pulses in the polarization modes of a VCSEL operating in the low-frequency fluctuations regime* in *Proceedings Symposium of IEEE/LEOS Benelux Chapter (IEEE, 2002)* (2002), 155–158.

109. Sciamanna, M. *et al.* Bifurcation bridges between external-cavity modes lead to polarization self-modulation in vertical-cavity surface-emitting lasers. *Physical Review A* **65,** 041801 (2002).

110. Masoller, C., Sukow, D., Gavrielides, A. & Sciamanna, M. Bifurcation to square-wave switching in orthogonally delay-coupled semiconductor lasers: Theory and experiment. *Physical Review A* **84,** 023838 (2011).

111. Sciamanna, M. *et al.* Different regimes of low-frequency fluctuations in vertical-cavity surface-emitting lasers. *JOSA B* **20,** 37–44 (2003).

112. Sciamanna, M. *et al.* Fast pulsing dynamics of a vertical-cavity surface-emitting laser operating in the low-frequency fluctuation regime. *Physical Review A* **68,** 015805 (2003).

113. Panajotov, K. *et al.* Residence time distribution and coherence resonance of optical-feedback-induced polarization mode hopping in vertical-cavity surface-emitting lasers. *Physical Review A* **69,** 011801 (2004).

114. Tabaka, A. *et al.* Dynamics of vertical-cavity surface-emitting lasers in the short external cavity regime: Pulse packages and polarization mode competition. *Physical Review A* **73,** 013810 (2006).

115. Sciamanna, M. *et al.* Optical feedback induces polarization mode hopping in vertical-cavity surface-emitting lasers. *Optics letters* **28,** 1543–1545 (2003).

116. Arteaga, M. A. *et al.* Experimental evidence of coherence resonance in a time-delayed bistable system. *Physical review letters* **99,** 023903 (2007).

117. Simpson, T., Liu, J., Huang, K.-F. & Tai, K. Nonlinear dynamics induced by external optical injection in semiconductor lasers. *Quantum and Semiclassical Optics: Journal of the European Optical Society Part B* **9,** 765 (1997).

118. Gavrielides, A. *Nonlinear Optics Center, Phillips Laboratory, PL/LIDN* in *Coherence and Quantum Optics VII: Proceedings of the Seventh Rochester Conference on Coherence and Quantum Optics, held at the University of Rochester, June 7–10, 1995* (2013), 15.

119. Simpson, T., Liu, J.-M., Gavrielides, A., Kovanis, V. & Alsing, P. Period-doubling cascades and chaos in a semiconductor laser with optical injection. *Physical review A* **51,** 4181 (1995).

120. Simpson, T., Liu, J., Gavrielides, A., Kovanis, V. & Alsing, P. Period-doubling route to chaos in a semiconductor laser subject to optical injection. *Applied Physics Letters* **64,** 3539–3541 (1994).

121. Kovanis, V., Gavrielides, A., Simpson, T. & Liu, J.-M. Instabilities and chaos in optically injected semiconductor lasers. *Applied physics letters* **67,** 2780–2782 (1995).

122. Gavrielides, A., Kovanis, V., Varangis, P. M., Erneux, T. & Simpson, T. B. *Subharmonic resonances in an optically injected semiconductor laser* in *Physics and Simulation of Optoelectronic Devices IV* **2693** (1996), 654–665.

123. Wieczorek, S., Simpson, T. B., Krauskopf, B. & Lenstra, D. Bifurcation transitions in an optically injected diode laser: theory and experiment. *Optics communications* **215,** 125–134 (2003).

124. Wieczorek, S., Krauskopf, B., Simpson, T. B. & Lenstra, D. The dynamical complexity of optically injected semiconductor lasers. *Physics Reports* **416,** 1–128 (2005).

125. Altés, J. B., Gatare, I., Panajotov, K., Thienpont, H. & Sciamanna, M. Mapping of the dynamics induced by orthogonal optical injection in vertical-cavity surface-emitting lasers. *IEEE journal of quantum electronics* **42,** 198–207 (2006).

126. Gatare, I., Sciamanna, M., Buesa, J., Thienpont, H. & Panajotov, K. Nonlinear dynamics accompanying polarization switching in vertical-cavity surface-emitting lasers with orthogonal optical injection. *Applied Physics Letters* **88,** 101106 (2006).

127. Valle, A., Gatare, I., Panajotov, K. & Sciamanna, M. Transverse mode switching and locking in vertical-cavity surface-emitting lasers subject to orthogonal optical injection. *IEEE Journal of Quantum Electronics* **43,** 322–333 (2007).

128. Panajotov, K., Gatare, I., Valle, A., Thienpont, H. & Sciamanna, M. Polarization- and transverse-mode dynamics in optically injected and gain-switched vertical-cavity surface-emitting lasers. *IEEE journal of quantum electronics* **45,** 1473–1481 (2009).

129. Gatare, I., Panajotov, K. & Sciamanna, M. Frequency-induced polarization bistability in vertical-cavity surface-emitting lasers with orthogonal optical injection. *Physical Review A* **75,** 023804 (2007).

130. Gatare, I., Buesa, J., Thienpont, H., Panajotov, K. & Sciamanna, M. Polarization switching bistability and dynamics in vertical-cavity surface-emitting laser under orthogonal optical injection. *Optical and quantum electronics* **38,** 429–443 (2006).

131. Nizette, M., Sciamanna, M., Gatare, I., Thienpont, H. & Panajotov, K. Dynamics of vertical-cavity surface-emitting lasers with optical injection: a two-mode model approach. *JOSA B* **26,** 1603–1613 (2009).

132. Pan, Z. G. *et al.* Optical injection induced polarization bistability in vertical-cavity surface-emitting lasers. *Applied physics letters* **63,** 2999–3001 (1993).

133. Sciamanna, M. & Panajotov, K. Two-mode injection locking in vertical-cavity surface-emitting lasers. *Optics letters* **30,** 2903–2905 (2005).

134. Quirce, A. *et al.* Polarization switching and injection locking in vertical-cavity surface-emitting lasers subject to parallel optical injection. *Optics letters* **41,** 2664–2667 (2016).

135. Quirce, A. *et al.* Analysis of the polarization of single-mode vertical-cavity surface-emitting lasers subject to parallel optical injection. *JOSA B* **34,** 447–455 (2017).

136. Denis-le Coarer, F. *et al.* Injection locking and polarization switching bistability in a 1550 nm VCSEL subject to parallel optical injection. *IEEE Journal of Selected Topics in Quantum Electronics* **23,** 1–10 (2017).

137. Colet, P. & Roy, R. Digital communication with synchronized chaotic lasers. *Optics letters* **19,** 2056–2058 (1994).

138. Spitz, O. *et al.* Private communication with quantum cascade laser photonic chaos. *Nature communications* **12,** 1–8 (2021).

139. Argyris, A. *et al.* Chaos-based communications at high bit rates using commercial fibre-optic links. *Nature* **438,** 343–346 (2005).

140. Nguimdo, R. M. *et al.* Fast random bits generation based on a single chaotic semiconductor ring laser. *Optics express* **20,** 28603–28613 (2012).

141. Uchida, A. *et al.* Fast physical random bit generation with chaotic semiconductor lasers. *Nature Photonics* **2,** 728–732 (2008).

142. Argyris, A., Deligiannidis, S., Pikasis, E., Bogris, A. & Syvridis, D. Implementation of 140 Gb/s true random bit generator based on a chaotic photonic integrated circuit. *Optics express* **18,** 18763–18768 (2010).

143. Virte, M., Mercier, E., Thienpont, H., Panajotov, K. & Sciamanna, M. Physical random bit generation from chaotic solitary laser diode. *Optics express* **22,** 17271–17280 (2014).

144. Kim, K. *et al.* Massively parallel ultrafast random bit generation with a chip-scale laser. *Science* **371,** 948–952 (2021).

145. Hargrove, L., Fork, R. L. & Pollack, M. Locking of He–Ne laser modes induced by synchronous intracavity modulation. *Applied Physics Letters* **5,** 4–5 (1964).

146. DeMaria, A., Stetser, D. & Heynau, H. Self mode-locking of lasers with saturable absorbers. *Applied Physics Letters* **8,** 174–176 (1966).

147. Ippen, 5., Shank, C. & Dienes, A. Passive mode locking of the cw dye laser. *Applied Physics Letters* **21,** 348–350 (1972).

148. Diddams, S. A. The evolving optical frequency comb. *JOSA B* **27,** B51–B62 (2010).

149. Ye, J. & Cundiff, S. T. *Femtosecond optical frequency comb: principle, operation and applications* (Springer Science & Business Media, 2005).

150. Parriaux, A., Hammani, K. & Millot, G. Electro-optic frequency combs. *Advances in Optics and Photonics* **12,** 223–287 (2020).

151. Brothers, L., Lee, D. & Wong, N. Terahertz optical frequency comb generation and phase locking of an optical parametric oscillator at 665 GHz. *Optics letters* **19,** 245–247 (1994).

152. Kourogi, M., Enami, T. & Ohtsu, M. A monolithic optical frequency comb generator. *IEEE photonics technology letters* **6,** 214–217 (1994).

153. Fujiwara, M. *et al.* Optical carrier supply module using flattened optical multicarrier generation based on sinusoidal amplitude and phase hybrid modulation. *Journal of lightwave technology* **21,** 2705–2714 (2003).

154. Wu, R., Supradeepa, V., Long, C. M., Leaird, D. E. & Weiner, A. M. Generation of very flat optical frequency combs from continuous-wave lasers using cascaded intensity and phase modulators driven by tailored radio frequency waveforms. *Optics letters* **35,** 3234–3236 (2010).

155. Wu, R., Leaird, D. E., Weiner, A. M., *et al.* Supercontinuum-based 10-GHz flat-topped optical frequency comb generation. *Optics express* **21,** 6045–6052 (2013).

156. Kashiwagi, K. *et al.* Direct generation of 12.5-GHz-spaced optical frequency comb with ultrabroad coverage in near-infrared region by cascaded fiber configuration. *Optics express* **24,** 8120–8131 (2016).

157. Weiner, A. M. Femtosecond pulse shaping using spatial light modulators. *Review of scientific instruments* **71,** 1929–1960 (2000).

158. Murphy, M. *et al.* High-precision wavelength calibration of astronomical spectrographs with laser frequency combs. *Monthly Notices of the Royal Astronomical Society* **380,** 839–847 (2007).

159. Del'Haye, P. *et al.* Optical frequency comb generation from a monolithic microresonator. *Nature* **450,** 1214–1217 (2007).

160. Del'Haye, P. *et al.* Octave spanning tunable frequency comb from a microresonator. *Physical Review Letters* **107,** 063901 (2011).

161. Kippenberg, T. J., Holzwarth, R. & Diddams, S. A. Microresonator-based optical frequency combs. *science* **332,** 555–559 (2011).

162. Grudinin, I. S., Yu, N. & Maleki, L. Generation of optical frequency combs with a CaF 2 resonator. *Optics letters* **34,** 878–880 (2009).

163. Hugi, A., Villares, G., Blaser, S., Liu, H. & Faist, J. Mid-infrared frequency comb based on a quantum cascade laser. *Nature* **492,** 229–233 (2012).

164. Prati, F. *et al.* in *Frontiers in Optics and Photonics* 197–210 (De Gruyter, 2021).

165. Silvestri, C., Columbo, L. L., Brambilla, M. & Gioannini, M. Coherent multi-mode dynamics in a quantum cascade laser: amplitude-and frequency-modulated optical frequency combs. *Optics Express* **28,** 23846–23861 (2020).

166. Villares, G., Hugi, A., Blaser, S. & Faist, J. Dual-comb spectroscopy based on quantum-cascade-laser frequency combs. *Nature communications* **5,** 1–9 (2014).

167. Gioannini, M. & Montrosset, I. Numerical analysis of the frequency chirp in quantum-dot semiconductor lasers. *IEEE Journal of Quantum Electronics* **43,** 941–949 (2007).

168. Gioannini, M., Cedola, A. P., Di Santo, N., Bertazzi, F. & Cappelluti, F. Simulation of quantum dot solar cells including carrier intersubband dynamics and transport. *IEEE Journal of Photovoltaics* **3,** 1271–1278 (2013).

169. Olejniczak, L., Panajotov, K., Thienpont, H. & Sciamanna, M. Self-pulsations and excitability in optically injected quantum-dot lasers: Impact of the excited states and spontaneous emission noise. *Physical Review A* **82,** 023807 (2010).

170. Gioannini, M., Sevega, A. & Montrosset, I. Simulations of differential gain and linewidth enhancement factor of quantum dot semiconductor lasers. *Optical and Quantum electronics* **38,** 381–394 (2006).

171. Olejniczak, L. *et al.* Polarization switching in quantum-dot vertical-cavity surface-emitting lasers. *IEEE Photonics Technology Letters* **21,** 1008–1010 (2009).

172. Gioannini, M. Ground-state power quenching in two-state lasing quantum dot lasers. *Journal of Applied Physics* **111,** 043108 (2012).

173. Olejniczak, L., Panajotov, K., Wieczorek, S., Thienpont, H. & Sciamanna, M. Intrinsic gain switching in optically injected quantum dot laser lasing simultaneously from the ground and excited state. *JOSA B* **27,** 2416–2423 (2010).

174. Saldutti, M., Tibaldi, A., Cappelluti, F. & Gioannini, M. Impact of carrier transport on the performance of QD lasers on silicon: a drift-diffusion approach. *Photonics Research* **8,** 1388–1397 (2020).

175. Veselinov, K. *et al.* Lasing spectra of 1.55 μm InAs/InP quantum dot lasers: theoretical analysis and comparison with the experiments. *Optical and quantum electronics* **40,** 227–237 (2008).

176. Lu, Z. *et al.* An L-band monolithic InAs/InP quantum dot mode-locked laser with femtosecond pulses. *Optics Express* **17,** 13609–13614 (2009).

177. Bardella, P., Columbo, L. L. & Gioannini, M. Self-generation of optical frequency comb in single section quantum dot Fabry-Perot lasers: a theoretical study. *Optics express* **25,** 26234–26252 (2017).

178. Weber, C., Columbo, L. L., Gioannini, M., Breuer, S. & Bardella, P. Threshold behavior of optical frequency comb self-generation in an InAs/InGaAs quantum dot laser. *Optics letters* **44,** 3478–3481 (2019).

179. Lu, Z. *et al.* 312-fs pulse generation from a passive C-band InAs/InP quantum dot mode-locked laser. *Optics Express* **16,** 10835–10840 (2008).

180. Dong, B. *et al.* Frequency comb dynamics of a 1.3 μm hybrid-silicon quantum dot semiconductor laser with optical injection. *Optics letters* **44,** 5755–5758 (2019).

181. Lu, Z. *et al.* High performance InAs/InP quantum dot 34.462-GHz C-band coherent comb laser module. *Optics express* **26,** 2160–2167 (2018).

182. Anandarajah, P. M. *et al.* Phase shift keyed systems based on a gain switched laser transmitter. *Optics Express* **17,** 12668–12677 (2009).

183. Rosado, A. *et al.* Experimental study of optical frequency comb generation in gain-switched semiconductor lasers. *Optics & Laser Technology* **108,** 542–550 (2018).

184. Yoshino, M., Miki, N., Yoshimoto, N. & Kumozaki, K. Multiwavelength optical source for OCDM using sinusoidally modulated laser diode. *Journal of lightwave technology* **27,** 4524–4529 (2009).

185. Peng, P. *et al.* Multiwavelength laser module based on distribute feedback laser diode for broadcast and communication systems. *IEEE Photonics Journal* **8,** 1–8 (2016).

186. Zhou, R., Huynh, T. N., Vujicic, V., Anandarajah, P. M. & Barry, L. P. Phase noise analysis of injected gain switched comb source for coherent communications. *Optics express* **22,** 8120–8125 (2014).

187. Vujicic, V., Anandarajah, P., Zhou, R., Browning, C. & Barry, L. Performance investigation of IM/DD Compatible SSB-OFDM systems based on optical multicarrier sources. *IEEE Photonics Journal* **6,** 1–10 (2014).

188. Shao, T., Martin, E., Prince, A. M. & Barry, L. P. DM-DD OFDM-RoF system with adaptive modulation using a gain-switched laser. *IEEE photonics technology letters* **27,** 856–859 (2015).

189. Ó Dúill, S. P., Anandarajah, P. M., Zhou, R. & Barry, L. P. Numerical investigation into the injection-locking phenomena of gain switched lasers for optical frequency comb generation. *Applied Physics Letters* **106,** 211105 (2015).

190. Quirce, A. *et al.* Nonlinear dynamics induced by optical injection in optical frequency combs generated by gain-switching of laser diodes. *IEEE Photonics Journal* **12,** 1–14 (2020).

191. Prior, E. *et al.* Dynamics of dual-polarization VCSEL-based optical frequency combs under optical injection locking. *Optics letters* **41,** 4083–4086 (2016).

192. Quirce, A., De Dios, C., Valle, A. & Acedo, P. VCSEL-based optical frequency combs expansion induced by polarized optical injection. *IEEE Journal of Selected Topics in Quantum Electronics* **25,** 1–9 (2018).

193. Quirce, A., de Dios, C., Valle, A., Pesquera, L. & Acedo, P. Polarization dynamics in VCSEL-based gain switching optical frequency combs. *Journal of Lightwave Technology* **36,** 1798–1806 (2018).

194. Quirce, A. *et al. VCSEL-Based Optical Frequency Combs: Study of its Polarization Dynamics under Gain Switching and Polarization Selective Optical Injection Locking* in *2018 20th International Conference on Transparent Optical Networks (ICTON)* (2018), 1–4.

195. Minoshima, K. & Matsumoto, H. High-accuracy measurement of 240-m distance in an optical tunnel by use of a compact femtosecond laser. *Applied Optics* **39,** 5512–5517 (2000).

196. Link, S. M., Maas, D., Waldburger, D. & Keller, U. Dual-comb spectroscopy of water vapor with a free-running semiconductor disk laser. *Science* **356,** 1164–1168 (2017).

197. Millot, G. *et al.* Frequency-agile dual-comb spectroscopy. *Nature Photonics* **10,** 27–30 (2016).

198. Quevedo-Galán, C. *et al.* Gain-switched semiconductor lasers with pulsed excitation and optical injection for dual-comb spectroscopy. *Optics Express* **28,** 33307–33317 (2020).

199. Liu, G. *et al.* Passively mode-locked quantum dash laser with an aggregate 5.376 Tbit/s PAM-4 transmission capacity. *Optics express* **28,** 4587–4593 (2020).

200. Marin-Palomo, P. *et al.* Microresonator-based solitons for massively parallel coherent optical communications. *Nature* **546,** 274–279 (2017).

201. Lang, R. Injection locking properties of a semiconductor laser. *IEEE Journal of Quantum Electronics* **18,** 976–983 (1982).

202. Lin, F.-Y. & Liu, J.-M. Chaotic radar using nonlinear laser dynamics. *IEEE Journal of Quantum Electronics* **40,** 815–820 (2004).

203. Simpson, T. Mapping the nonlinear dynamics of a distributed feedback semiconductor laser subject to external optical injection. *Optics Communications* **215,** 135–151 (2003).

204. Marconi, M., Javaloyes, J., Barland, S., Balle, S. & Giudici, M. Vectorial dissipative solitons in vertical-cavity surface-emitting lasers with delays. *Nature Photonics* **9,** 450 (2015).

205. Averlant, E., Tlidi, M., Thienpont, H., Ackemann, T. & Panajotov, K. Vector cavity solitons in broad area vertical-cavity surface-emitting lasers. *Scientific Reports* **6,** 20428 (2016).

206. Denis-le Coarer, F. *et al.* Attractor hopping between polarization dynamical states in a vertical-cavity surface-emitting laser subject to parallel optical injection. *Physical Review E* **97,** 032201 (2018).

207. Rosado, A. *et al.* Numerical and experimental analysis of optical frequency comb generation in gain-switched semiconductor lasers. *IEEE Journal of Quantum Electronics* **55,** 1–12 (2019).

208. Rosado, A. *et al.* Enhanced optical frequency comb generation by pulsed gain-switching of optically injected semiconductor lasers. *Optics express* **27,** 9155–9163 (2019).

209. Davila-Rodriguez, J., Bagnell, K. & Delfyett, P. J. Frequency stability of a 10 GHz optical frequency comb from a semiconductor-based mode-locked laser with an intracavity 10,000 finesse etalon. *Optics letters* **38,** 3665–3668 (2013).

210. Ryu, H. Y., Lee, S. H., Kim, E. B., Suh, H. S. & Moon, H. S. A discretely tunable multifrequency source injection locked to a spectral-mode-filtered fiber laser comb. *Applied Physics Letters* **97,** 141107 (2010).

211. Saha, K. *et al.* Modelocking and femtosecond pulse generation in chip-based frequency combs. *Optics Express* **21,** 1335–1343 (2013).

212. Bordonalli, A. C., Fice, M. J. & Seeds, A. J. Optical injection locking to optical frequency combs for superchannel coherent detection. *Optics Express* **23,** 1547–1557 (2015).

213. Lin, F. & Liu, J. Nonlinear dynamical characteristics of an optically injected semiconductor laser subject to optoelectronic feedback. *Optics Communications* **221,** 173–180 (2003).

214. Bouchez, G., Uy, C.-H., Macias, B., Wolfersberger, D. & Sciamanna, M. Wideband chaos from a laser diode with phase-conjugate feedback. *Optics letters* **44,** 975–978 (2019).

215. Bouchez, G., Malica, T., Wolfersberger, D. & Sciamanna, M. Optimized properties of chaos from a laser diode. *Physical Review E* **103,** 042207 (2021).

216. Malica, T., Bouchez, G., Wolfersberger, D. & Sciamanna, M. Spatiotemporal complexity of chaos in a phase-conjugate feedback laser system. *Optics letters* **45,** 819–822 (2020).

217. Rontani, D., Mercier, E., Wolfersberger, D. & Sciamanna, M. Enhanced complexity of optical chaos in a laser diode with phase-conjugate feedback. *Optics letters* **41,** 4637–4640 (2016).

218. Mercier, É., Wolfersberger, D. & Sciamanna, M. High-frequency chaotic dynamics enabled by optical phase-conjugation. *Scientific reports* **6,** 1–6 (2016).

219. Kelleher, B. *et al.* in *Quantum Dot Devices* 1–22 (Springer, 2012).

220. Hurtado, A. *et al.* Tunable microwave signal generator with an optically-injected 1310nm QD-DFB laser. *Optics express* **21,** 10772–10778 (2013).

221. Li, H., Lucas, T. L., McInerney, J. G. & Morgan, R. A. Transverse modes and patterns of electrically pumped vertical-cavity surface-emitting semiconductor lasers. *Chaos, Solitons & Fractals* **4,** 1619–1636 (1994).

222. Gatare, I., Sciamanna, M., Nizette, M., Thienpont, H. & Panajotov, K. *Excitation of a two-mode limit cycle dynamics on the route to polarization switching in a VCSEL subject orthogonal to optical injection* in *Semiconductor Lasers and Laser Dynamics III* **6997** (2008), 699713.

223. Hurtado, A., Quirce, A., Valle, A., Pesquera, L. & Adams, M. J. Nonlinear dynamics induced by parallel and orthogonal optical injection in 1550 nm vertical-cavity surface-emitting lasers (VCSELs). *Optics express* **18,** 9423–9428 (2010).

224. Al-Seyab, R. *et al.* Dynamics of polarized optical injection in 1550-nm VCSELs: theory and experiments. *IEEE Journal of Selected Topics in Quantum Electronics* **17,** 1242–1249 (2011).

225. Olejniczak, L. *et al.* Polarization switching and polarization mode hopping in quantum dot vertical-cavity surface-emitting lasers. *Optics express* **19,** 2476–2484 (2011).

226. Valle, A., Sciamanna, M. & Panajotov, K. Irregular pulsating polarization dynamics in gain-switched vertical-cavity surface-emitting lasers. *IEEE Journal of Quantum Electronics* **44,** 136–143 (2008).

227. Virte, M., Panajotov, K., Thienpont, H. & Sciamanna, M. Deterministic polarization chaos from a laser diode. *Nature Photonics* **7,** 60 (2013).

228. Lu, Y. *et al.* Directly Modulated VCSELs with Frequency Comb Injection for Parallel Communications. *Journal of Lightwave Technology* (2020).

229. Jerez, B., Martın-Mateos, P., Prior, E., de Dios, C. & Acedo, P. Gain-switching injection-locked dual optical frequency combs: characterization and optimization. *Optics letters* **41,** 4293–4296 (2016).

230. Moskalenko, V., Koelemeij, J., Williams, K. & Bente, E. Study of extra wide coherent optical combs generated by a QW-based integrated passively mode-locked ring laser. *Optics letters* **42,** 1428–1431 (2017).

231. Cotter, W. *et al.* Integrated demultiplexing and amplification of coherent optical combs. *Optics express* **27,** 16012–16023 (2019).

232. Moskalenko, V. *et al.* Record bandwidth and sub-picosecond pulses from a monolithically integrated mode-locked quantum well ring laser. *Optics Express* **22,** 28865–28874 (2014).

233. Quirce, A., de Dios, C., Valle, A. & Acedo, P. *VCSEL-Based Optical Frequency Combs: Expansion of the Optical Span under Arbitrary Polarized Optical Injection* in *2019 21st International Conference on Transparent Optical Networks (ICTON)* (2019), 1–4.

234. Hong, Y., Spencer, P. S., Rees, P. & Shore, K. A. Optical injection dynamics of two-mode vertical cavity surface-emitting semiconductor lasers. *IEEE journal of quantum electronics* **38,** 274–278 (2002).

235. Denis-le Coarer, F. *et al.* Polarization dynamics induced by parallel optical injection in a single-mode VCSEL. *Optics Letters* **42,** 2130–2133 (2017).